eman ta zabal zazu

Universidad del País Vasco
Euskal Herriko Unibertsitatea

Department of Theoretical Physics and History of Science

Characterisation of Cosmic Defects Using Field Theory and Analytical Models

Asier Lopez Eiguren

Ph.D. THESIS
Leioa 2017

eman ta zabal zazu

Universidad del País Vasco
Euskal Herriko Unibertsitatea

Department of Theoretical Physics and History of Science

Characterisation of Cosmic Defects Using Field Theory and Analytical Models

Supervised by Dr. Jon Urrestilla Urizabal
from the University of the Basque Country

Submitted by Asier Lopez Eiguren
for the degree of Doctor of Physics

To whom
that teach me something during my life

"... heriotzak harrapatu gaitzala berarekin dantzatzen... "
McOnak

Acknowledgments

First of all and foremost, I would like to thank Jon Urrestilla, who opened the doors to a career in research for me, and who guided me in the first steps. You introduced me into the research world during my degree thesis, you showed me to admire research during my master's thesis and you tried to teach me everything you know during the PhD. You were the best advisor that I could ever have and a very good friend. Thank you very much for teaching me everything from tthe very beginning *Txo*. Eskerrik asko *Doktore Jauna*!

Secondly, I would also like to thank the collaborators who helped me in every step: Ana Achúcarro, Anastasios Avgoustidis, Jose Juan Blanco-Pillado, Betti Hartmann, Mark Hindmarsh, Martin Kunz, Carlos Martins eta Kepa Sousa. Thank you very much for giving me the opportunity to work with you and for having so much patience to teach me everything you know.

Juan Mari Aguirregabiria and Ínigo Luis Egusquiza also need a special acknowledgment. Their indispensable help makes possible the Basque part of this Thesis. In the same way thank you very much to you two for helping in every small issue I had since the degree epoch.

I would also like to thank the people how made me feel at home when I was traveling. Thank you very much people at the Department of Physics and Astronomy of the University of Sussex, at the Helsinki Institute of Physics, at the Lorentz Institute of Leiden and at the School of Physics and Astronomy of the University of Nottingham. Without your help I wouldn't have learned so much.

I don't want to forget the people at my workplace, the Department of Theoretical Physics at the Science and Technology School. You made me feel very comfortable and you were always very helpful. Thank you very much for being so helpful during this journey: Alex Feinstein, Ruth Lazkoz, Manuel Á. Valle, Juan Luis Mañes, Martín Rivas, Igor Bandos, Michele Modugno, José M. Martín Senovilla and Montserrat Barrio. People who helped me with my first teaching classes need a special acknowledgment: Oscar Ecenarro, David Brizuela, Raül Vera and Iñaki Garay. In this world everything is not related with work, so I would like to thank those people who make my days easier with the lovely coffees every morning; thank you very much Allan, Josu Igartua, Raúl, Luis, Josu Ortega, I nigo, Esti...

I would also like to mention those who I met due to their doc/postdoc character: Carlos, Iñigo, Giussepe, Joao, Iker, Olatz, Unai, Maria, Irene, Santi, Laura, Mikel, Nastassja, Charlotte, Mariam, Sugumi, Jonathan, Jasone, Aitor, Imanol. Between all these people there are three who need an special mention because they became really good friends, thank you Pablo Jimeno, Lluc Garcia and Borja Reina.

Joanes Lizarraga needs a special attention. We started together in this journey; we went to our first conferences together, we had our first teaching experience together, the first.... I'm sure that everything would be different without you; you helped me overcome all the difficulties I have found. Thank you very much for listening to all my bad jokes, and for making them when I was not in the mood. I have won a brother; good luck in your life Joanes!

The Gose Naiz team deserves a very special mention. We were few (Jokin, Julen, Ekhi, Iraultza, Joanes), the team has grown (+ Iagoba, Peio, Aitzol, Iñigo, Mattin, Jon). Although we spend too much time talking about the same things (you know ;)) you are a part of the life that cannot be lost. Lets continue being hungry!!!!

I would also like to mention people not related to the University world. First of all I would like to thank my friends for gdistracting me during the difficult moments. In the same way I would like to thank my second family. I have spent more than the half of my life sharing wonderful moments with you. Thank you very much for making me part of this big and excellent familiy. FORZA ISUNTZA!!!!

Before finishing the acknowledgements I would like to mention my family. You were always with me; in every difficult moment as well as in every good moment. Thank you very much Patxi and Marga for accepting me as your son; and Marga especially for reading the whole Thesis in english and correcting it so wonderfully. Mum and dad, thank you very much for working so hard, for teaching me everything you know and for making me feel so loved in order to reach the point where I am. Ainho, thank you very much for opening the way and helping me every day; you were the best guide for my childhood. Finally, I cannot express my feelings using words, but Ortzi you deserve the biggest appreciation for always being with me and for being the reason for waking up everyday, thank you very much.

Finally, I would like to apologise to the person who has taken this Thesis and who expected to read her/his name in this section. I am sure that you were part of this Thesis. Thank you very much for you too!

Prologue

The work presented in this Thesis characterizes the properties of cosmic defects and explores their observational effects. The different projects that give rise to this Thesis are done in collaboration with my supervisor Jon Urrestilla and our collaborators: A. Achúcarro, A. Avgoustidis, B. Hartmann, M. Hindmarsh, A.M.M. Leite, J. Lizarraga, C.J.A.P. Martins, A.S. Nunes and K. Sousa.

The cosmological standard model and the standard model for particle physics are the main theories to understand the Universe. The standard model for particle physics gives us the high energy description of the universe, while the cosmological standard model provides a successful description for many of the cosmological observations we have nowadays. Nevertheless the connection between these two theories still has some unanswered questions. That is, the physics governing several processes taking place at the early universe which lie in this connection are unknown. Cosmic defects are one of the most promising candidates to answer those questions. They are predicted in many high energy theories and they could be formed in cosmological symmetry breakings that took place in the early universe. They could also survive the cosmological evolution and/or have observational consequences nowadays. Thus the analysis of the properties and observational consequences of cosmic defects would provide the connection between the cosmological standard model and the standard model for particle physics.

This Thesis is divided in two parts: Introduction and Results. In the Introduction (Part I) the theoretical background is given. We will start by describing in **Chapter 1** the cosmological evolution of the universe and pointing out the physical processes where cosmic defects could form. Then, in **Chapter 2** we will describe in detail the cosmic defects. To do so, we will take the most analysed cosmic defect type, the local cosmic string, and we will describe its main characteristics. Then, we will turn to the defect models that we will analyse through this Thesis. These two Chapters are based on previous articles, reviews and books in the literature.

The original research performed during the PhD is presented in Part II, where each Chapter contains the following:

Chapter 3

The work of this Chapter is centered on the survival of the zero modes present on some defect models after coupling them to gravity. Some defect models have a uniparametric family of solutions with the same energy which is associated with a zero mode. Although, the total energy of each of these configurations is the same, the energy density could change. So, taking in mind that gravity is a local property, we analyse if those models preserve the zero mode after coupling them minimally to gravity. The procedure and results of this Chapter are published in the following paper:

- **Gravitating cosmic strings with flat directions**

B. Hartmann, A. Lopez-Eiguren, K. Sousa and J. Urrestilla, JHEP 1303 (2013) 152. arXiv:1212.6502.

Chapter 4

This Chapter analyses the numerical simulations of global monopoles in order to measure their velocities. Global monopoles have some interesting properties, for example, the force between a well separated monopole and an antimonopole is independent of their distance. This example shows offbeat dynamics. For this and other reasons the analysis of them could be of great interest. We perform the biggest and most accurate field theory simulations of global monopoles to date and we extract relevant information. Using this information and a new method to measure velocities, firstly presented here, we give the most accurate values for the global monopole velocities. We also use the information obtained from the simulations to calibrate the analytical models for global monopole evolution. This Chapter is based on the following article:

- **Measuring Global Monopole Velocities, one by one**

  A. Lopez-Eiguren, J. Urrestilla and A. Achúcarro, JCAP01(2017)020. arXiv:1611.09628.

Chapter 5

In this Chapter we characterize the networks of Semilocal strings. Although Semilocal strings share many properties with ordinary local strings, they are not purely topological and will therefore have different properties. For example, this kind of strings can have ends, which behave as global monopoles. Using the biggest and most accurate field theory simulations of semilocal strings to date we characterize and extract detailed information of their properties. In the analysis of these properties the pioneering method to measure monopole velocities, which will be presented in Chapter 4, is also used. The data obtained will be used to calibrate the analytical models of the evolution of semilocal string networks in a future work. The work done in this Chapter can be found in the following two papers:

- **Evolution of semilocal string networks: Large-scale properties**

  A. Achúcarro, A. Avgoustidis, A.M.M. Leite, A. Lopez-Eiguren, C.J.A.P. Martins, A.S. Nunes and J. Urrestilla, Phys. Rev. D89 (2014) no.6, 063503. arXiv:1312.2123.

- **Evolution of semilocal string networks: II. Velocity estimators**

  A. Lopez-Eiguren, J. Urrestilla, A. Achúcarro, A. Avgoustidis and C.J.A.P. Martins, arXiv:1704.00991, Submitted to Phys. Rev. D

Chapter 6

This Chapter presents the energy-momentum correlators and the CMB power spectra for global strings and global monopoles. We perform field theoretical simulations to obtain the energy-momentum correlators and then those are evolved in radiation dominated era, in matter dominated era and across the radiation matter cosmological transition to get the source functions required for the CMB power spectra calculations. Finally the CMB power spectra predictions and the parameter constraints obtained using parameter fitting are shown. The procedure and results of this Chapter are shown in the following paper:

- **Cosmic Microwave Background constraints for global strings and global monopoles**

  A. Lopez-Eiguren, J. Lizarraga, M. Hindmarsh, and J. Urrestilla, In preparation

Chapter 7

Finally, in Chapter 7 we present the general conclusions obtained from the work we carried out during this Thesis.

List of Publications

Published Papers

- **Gravitating cosmic strings with flat directions**

  B. Hartmann, A. Lopez-Eiguren, K. Sousa and J. Urrestilla, JHEP 1303 (2013) 152. arXiv:1212.6502.

- **Evolution of semilocal string networks: Large-scale properties**

  A. Achúcarro, A. Avgoustidis, A.M.M. Leite, A. Lopez-Eiguren, C.J.A.P. Martins, A.S. Nunes and J. Urrestilla, Phys. Rev. D89 (2014) no.6, 063503. arXiv:1312.2123.

- **Measuring Global Monopole Velocities, one by one**

  A. Lopez-Eiguren, J. Urrestilla and A. Achúcarro, JCAP01(2017)020. arXiv:1611.09628.

Submitted Papers

- **Evolution of semilocal string networks: II. Velocity estimators**

  A. Lopez-Eiguren, J. Urrestilla, A. Achúcarro, A. Avgoustidis and C.J.A.P. Martins, arXiv:1704.00991, Submitted to Phys. Rev. D

In Preparation

- **Cosmic Microwave Background constraints for global strings and global monopoles**

  A. Lopez-Eiguren, J. Lizarraga, M. Hindmarsh, and J. Urrestilla, In preparation

- **Evolution of semilocal string networks: III. Segment distribution**

  A. Achúcarro, A. Avgoustidis, A. Lopez-Eiguren, C.J.A.P. Martins and J. Urrestilla, In preparation

- **CMB contraints for O(N) defects**

  M. Hindmarsh, M. Kunz, J. Lizarraga, A. Lopez-Eiguren and J. Urrestilla, In preparation

Proceedings

- **Calibrating Analytical Models for Semilocal Strings**

  A. Lopez-Eiguren, J. Phys. Conf. Ser. 600 (2015) no.1, 012018. arXiv:1412.0432.

Contents

PART I

Introduction

1 Cosmological Evolution

1.1. Introduction

In this first Chapter of the Thesis we will described the Hot Big bang model [48, 113], which describes the evolution of the universe from its initial stages until nowadays. The model is so well tested that now it has become the standard cosmology.

The initial stage from where the model starts its description is not very clear. In the literature several definitions for the Big Bang can be found, but from the point of view of this Thesis the precise initial point of the description is not a crucial aspect. However, the evolution described by the model is of great interest for the analysis of the cosmic defects, because although they are created in the symmetry breakings that take place at early universe, they can last until nowadays.

Therefore, in this Chapter we will start giving some historical precedents of the Hot Big Bang model. Then, we will analyse the dynamics of the universe given by the theory, investigating also some problems that the theory had and how they were solved. Once we will have described the evolution we will give information about the most important events on the history of the universe. Finally, we will study the most used observational tool to analyse the early universe, the Cosmic Microwave background (CMB). The description of the standard cosmological model that we will give in this Chapter will be centered on the information that will be useful for the analysis of the cosmic defects that we will make throughout this Thesis. We will refer the reader interested in other aspects to the detailed analysis in the literature.

1.2. Historical Precedents

Most of the civilisation that has lived in this world has tried to understand the cosmos and give a logical explanation to events related with it. Most early civilisations interpreted the cosmos in an anthropomorphic way, using human characteristics to explain events. For some of them the physical world was animated by wilful beings who could help or obstruct mankind, for others the physical world itself was inanimate but could be manipulated by gods.

The Greeks had their own gods and myths. But they started to identify the causes and effects of events and also to give a description and an explanation to observed phenomena using mathematical or geometrical terms. The identification of cause and effect is still an essential component of scientific theories.

Much of the knowledge acquired by the Greeks was lost to Christian culture during the dark ages, but the restriction of cosmological thinking during the Middle Ages in Europe did not freeze the construction of the mathematical structure of Cosmology. People like Nicolaus Copernicus,

Johannes Kepler and Tycho Brahe gave the indispensable pieces to Isaac Newton, who provided the first theories with the mathematical structure which successfully predict the dynamics of celestial bodies and their orbits.

With the publication of Einstein's general theory of relativity in 1915, cosmology entered a new era. The consistent mathematical description of the entire Universe given by Einstein's theory opened the doors to the study of the Universe as an entity. Cosmology was provided with the ideal mathematical framework to develop a predictable and reliable model for the description of the Universe.

Moreover, in 1929 Edwin P. Hubble discovered that distant galaxies were all moving away from the Milky Way. Not only that, the farther away he observed, the faster the galaxies were receding as it is shown in Fig. 1.1. He found the relationship that shows that the universe is expanding, which is now known as Hubble's law [77]: the recessional velocity of a galaxy is proportional to its distance from us. The equation looks like this:

$$v = Hd, \tag{1.1}$$

where d is the physical distance to the galaxy and H is the Hubble's parameter. At the time that Hubble made this discovery he thought that the proportionality factor H was constant but the precise analysis of the evolution equations of the universe showed that it depends on time, as we will see.

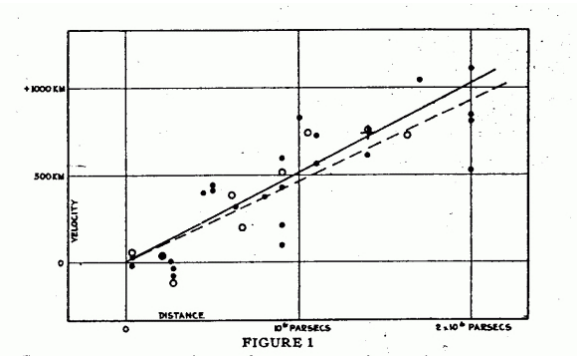

Figure 1.1.: *This figure shows the diagram that Hubble used to explain his discovery, where in the x-axis the distance to the galaxies are displayed and the velocities of those galaxies in the y-axis.*

If the Universe has been expanding it must have been smaller in the past. Consequently, if we extrapolate late enough we will arrive to a very important conclusion: the Universe must have initiated from a singular state, the big bang singularity. The Hot Big Bang model assumes that the current evolution of the Universe started from a very energetic region and evolved and cooled down due to the expansion. This evolution shows an expanding and cooling universe and it is realistic to think that symmetry breakings could have happened during this cooling stages. These symmetry breakings could have given rise to cosmic defects. Therefore, the analysis of the defects could help to reveal the high energy physics of the early universe.

The Hot Big Bang model is based upon a simple assumption, known as the cosmological principle, which says that our large-scale Universe possesses two important properties, isotropy and homogeneity:

- Isotropy: The Universe looks the same in all directions; it has rotational invariance and all directions are equivalent. There are no privileged directions.

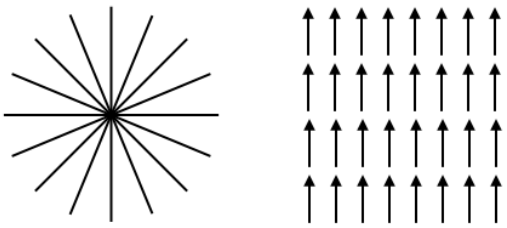

Figure 1.2.: *In this figure we can see two images showing isotropy and homogeneity. The image in the left pane shows isotropy: every direction looks the same from the center. The right pane shows homogeneity: there is translational invariance, all points are equivalent.*

- Homogeneity: The Universe looks the same at each point, this means, it has translational invariance and thus all points are equivalent. There are no privileged points in the Universe

These do not automatically imply each another. For example, a Universe with a uniform magnetic field is homogeneous, as all points are the same, but it fails to be isotropic because directions along the field lines can be distinguished from those perpendicular to them. Alternatively, a spherically-symmetric distribution, viewed from its central point, is isotropic but not necessarily homogeneous. However, if we require that a distribution is isotropic about every point, then that does enforce homogeneity as well. In Fig. 1.2 we show homogeneity and isotropy in a more visual way, as well as the issue that one does not imply the other.

As we have indicated above homogeneity and isotropy are characteristics of the large-scale Universe. This principle does not hold locally and must be considered as a global feature of the Universe at very large scales. Therefore, it is desirable to define our Universe as isotropic and homogeneous except for local irregularities. A very robust evidence of the isotropy and homogeneity of the Universe is given by the Cosmic Microwave Background (CMB), which we will analyse later.

1.3. Dynamics of the Universe

In order to analyse the dynamics of the Universe we have to solve the field equations given by Einstein in his general theory of relativity. These equations describe a geometrical theory, where the space-time is perturbed by the matter content of it, but at the same time the space-time dictates how matter has to move. The Einstein equations are:

$$G_{\mu\nu} = R_{\mu\nu} - \frac{1}{2} R g_{\mu\nu} = 8\pi G T_{\mu\nu}, \tag{1.2}$$

where G is the Newton's constant and $g_{\mu\nu}$ is the metric of the space-time. $G_{\mu\nu}$ is the Einstein tensor, R is the Ricci scalar and $R_{\mu\nu}$ the Ricci tensor, these quantities are calculated using the metric of the space-time. $T_{\mu\nu}$ is the energy-momentum tensor of the constituents of the Universe. We will start by analysing the metric describing the Universe with the properties we have described above. Then we will consider energy-momentum tensors, $T_{\mu\nu}$, that will typically be encountered in cosmology.

A metric is the basic ingredient of the space-time sector of general relativity, which dictates how distances have to be measured. In relativistic cosmology the most general space-time metric

consistent with homogeneity, isotropy and expansion is the Friedmann-Lemaître-Robertson-Walker (FLRW) metric. The line element in FLRW metric reads,

$$ds^2 = -dt^2 + a^2(t)\Big[\frac{dr^2}{1-Kr^2} + r^2\Big(d\theta^2 + \sin^2\theta d\phi^2\Big)\Big], \tag{1.3}$$

where we have used spherical polar coordinates (r, θ, ϕ), since spatial isotropy implies spherical symmetry about every point in each time slice. Note that the signature chosen is $(-,+,+,+)$, which will be used throughout all this Thesis. These coordinates are comoving, which means that distances in these coordinates do not change in time due to the expansion of space. The function $a(t)$ is called the scale factor, which rescales the comoving spacial slices at constant cosmic time of the metric and it is directly related with the expansion. The time coordinate t is the cosmic time measured by a comoving observer, the one at constant spatial coordinates. During this thesis we will also use the conformal time τ, which is obtained by the transformation $dt^2 = d\tau^2/a^2(\tau)$. Using conformal time the comoving distance that light has travel in time τ is simply τ. The metric with conformal time reads,

$$ds^2 = a^2(\tau)\Big[-d\tau^2 + \frac{dr^2}{1-Kr^2} + r^2\Big(d\theta^2 + \sin^2\theta d\phi^2\Big)\Big]. \tag{1.4}$$

The parameter K describes the curvature of the spatial slices at constant cosmic time, see Fig 1.3:

- $K < 0$ Hiperbolic space or open Universe
- $K = 0$ Flat space
- $K > 0$ Spherical or closed Universe

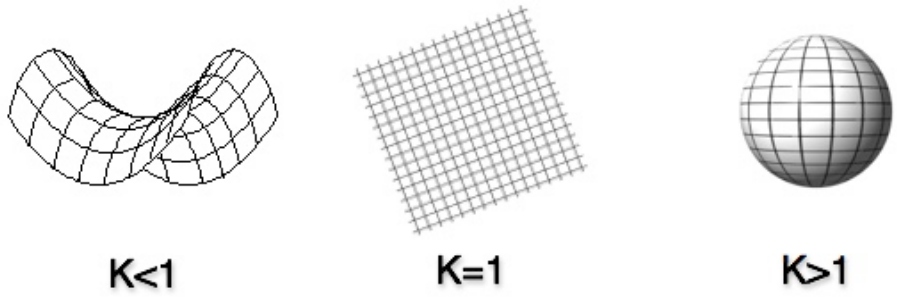

Figure 1.3.: *The different spatial curvatures depending on the value of K.*

For the analysis of the matter content of the Universe we will consider the energy-momentum tensors $T_{\mu\nu}$ of the species that will be typically encountered in cosmology. In order to describe those species the perfect fluid form for the energy-momentum tensor is the most useful one because it is consistent with our previous hypothesis. This form is

$$T_{\mu\nu} = (\rho + p)U_\mu U_\nu + p g_{\mu\nu}, \tag{1.5}$$

where U^μ is the fluid four vector, ρ is the energy density in the rest frame of the fluid and p is the pressure in that same frame. The pressure is necessarily isotropic, for consistency with isotropy

and homogeneity. Similarly, fluid elements will be comoving in the cosmological rest frame, so the normalized four-velocity in the coordinates of (1.3) will be

$$U^{\mu} = (1, 0, 0, 0). \tag{1.6}$$

The energy-momentum tensor thus takes the form

$$T = \begin{pmatrix} -\rho & 0 & 0 & 0 \\ 0 & g_{11}p & 0 & 0 \\ 0 & 0 & g_{22}p & 0 \\ 0 & 0 & 0 & g_{33}p \end{pmatrix}, \tag{1.7}$$

where g_{ii} represents the spatial metric components including the factor of a^2.

Armed with this description of matter and the FLRW metric (1.3), we are now ready to apply Einstein's equations (1.2) to cosmology. Using (1.3) and (1.5), one obtains two equations. The first one is known as the Friedmann equation,

$$H^2 \equiv \Big(\frac{\dot{a}}{a}\Big)^2 = \frac{8\pi G}{3}\sum_i \rho_i - \frac{K}{a^2}, \tag{1.8}$$

where the dot denotes a derivative with respect to cosmic time t and H is the Hubble parameter, which, as we anticipated, generally depends on time. The subindex i refers to all different possible types of energy in the Universe. Using the Hubble parameter one can define the comoving Hubble radius, $(aH)^{-1}$, which is the characteristic length scale of the universe and it can be understood as the distance to galaxies that are receding from as at the speed of light. This equation relates the rate of increase of the scale factor, as encoded by the Hubble parameter, to the total energy density of all matter in the Universe. The second equation, which is an evolution equation, is

$$\frac{\ddot{a}}{a} + \frac{1}{2}\Big(\frac{\dot{a}}{a}\Big)^2 = -4\pi G\sum_i p_i - \frac{K}{2a^2}. \tag{1.9}$$

At this point it is convenient to define, at any given time, a critical energy density,

$$\rho_c \equiv \frac{3H^2}{8\pi G}, \tag{1.10}$$

and the dimensionless energy densities

$$\Omega_i = \frac{\rho_i}{\rho_c}, \tag{1.11}$$

which are defined in terms of the critical energy density. These definitions lead us to write the Friedmann equation as

$$\Omega_{total} - 1 = \frac{K}{(aH)^2}, \tag{1.12}$$

where Ω_{total} counts for all the energy densities. Nowadays it is robustly confirmed by observations that Ω_{total} is certainly within three orders of magnitude of one, so $K = 0$ and the spacial slices at constant cosmic time are flat. In the rest of this Thesis, unless stated otherwise, K will be zero.

Energy conservation is expressed in general relativity by the vanishing of the covariant divergence of the energy-momentum tensor,

$$\nabla_{\mu} T^{\mu\nu} = 0. \tag{1.13}$$

Applying this to the FLRW metric (1.3) and the energy-momentum tensor (1.5) we can obtain a single energy conservation equation,

$$\dot{\rho} + 3H(\rho + p) = 0. \tag{1.14}$$

This equation implies that the expansion of the Universe can lead to local changes in the energy density. Note that there is no notion of conservation of "total energy", as energy can be interchanged between matter and the space-time geometry.

Most of the relevant fluids in cosmology obey the barotropic equation of state: $p = \omega\rho$. A constant ω leads to a great simplification in solving our equations, where the energy density and the scale factor evolve as:

$$\rho \propto a^{-3(1+\omega)}, \tag{1.15}$$

$$a \propto t^{\frac{2}{3(\omega+1)}}. \tag{1.16}$$

The ordinary matter content of the Universe is composed by ultra-relativistic particles or radiation and non-relativistic particles. One can prove that for ultra-relativistic particles $\omega = 1/3$, so (1.15) and (1.16) take the form

$$\rho_r \propto a^{-4}, \tag{1.17}$$

$$a_r \propto t^{1/2} \propto \tau. \tag{1.18}$$

For the non-relativistic matter, the pressure is negligible comparing to the density, and thus $\omega \sim 0$. Therefore,

$$\rho_m \propto a^{-3}, \tag{1.19}$$

$$a_m \propto t^{2/3} \propto \tau^2. \tag{1.20}$$

Equations (1.17) and (1.19) show that the radiation dominates over other species at early times, while non-relativistic matter becomes more important at latter times.

The evolution equations show a Universe that initially was very hot and dense, which then expanded and cooled during its evolution. This picture opens the door to connect the ideas from particle physics and cosmology, which is the main objective behind our research. Matter in the early universe would be described by a unified theory based on a continuous group G. As a result of the extreme temperatures of the early universe, the vacuum state would respect the full symmetry of the Lagrangian. But as the universe cooled the gauged theory would undergo a series of spontaneous symmetry breakings, which schematically can be represented by

$$G \to H \to ... \to SU(3) \times SU(2) \times U(1) \to SU(3) \times U(1). \tag{1.21}$$

The group G is known as the grand unified gauge group and the initial breaking $G \to H$ is expected to have taken place at 10^{16}GeV. The $U(1)$ describes the electromagnetism and its unification with the weak nuclear force gives the electroweak theory which is described by the group $SU(2) \times U(1)$. The strong nuclear force is associated with the group $SU(3)$ and the mathematical theory describing these interactions is known as quantum chromodynamics (QCD).

A direct consequence of these symmetry breakings are cosmic defects, which could be created at those symmetry breakings. Their properties are directly related to the characteristics of the symmetry breaking where they are formed and they evolve, in the cosmological background, until today. Therefore the analysis of their properties will give specific information about symmetry breakings that took place in the early Universe and also about the evolution of the Universe.

1.4. Problems and Solutions

The equations that we have analysed in the previous section describe the evolution of the Universe very well. However, this description leaves a range of crucial questions unanswered. In this section we will describe some of those questions and we will analyse the solutions proposed to solve them.

1.4.1. The concordance model: ΛCDM

Until the mid nineties, the accepted scientific understanding of the Universe said that the cosmos was in a non-accelerated or decelerated expansion. But, in 1998 two independent groups of cosmologists, the Supernova Cosmology Project [112] and the High-Z Supernova Search Team [119], made a startling finding. The Universe is not only expanding, its expansion is also accelerated. They measured the luminosity of distant type Ia supernovas and they found that they were dimmer than predicted by a non-accelerated or decelerated expansion. Nowadays several experiments have confirmed the accelerated expansion; supernovae experiments [58, 63, 68, 126], measurement of cluster properties [21, 22, 53, 134], anisotropies of the CMB [11, 12, 75], cosmic shear measured by weak lensing [116, 132] and Lyman-α forest absorptions [40, 100].

In order to account for the accelerated expansion shown by the measurements, the theory had to be extended because acceleration cannot be explained using ordinary species of the standard model. The most accepted extension of the theory can be done by adding a new ingredient known as dark energy, an energy component with negative pressure that would counteract the gravitational attraction and drive the accelerated expansion.

Dark energy can be simply described adding a term to the Einstein equations. This term (Λ) is known as the cosmological constant and it describes a perfect fluid with $\omega = -1$. The Einstein equations with the cosmological constant read

$$R_{\mu\nu} - \frac{1}{2} g_{\mu\nu} R = 8\pi G T_{\mu\nu} + \Lambda g_{\mu\nu}, \tag{1.22}$$

and consequently the modified Friedmann equations look like

$$\left(\frac{\dot{a}}{a}\right)^2 = \frac{8\pi G}{3} \sum_i \rho_i + \frac{\Lambda}{3}, \tag{1.23}$$

$$\frac{\ddot{a}}{a} + \frac{1}{2}\left(\frac{\dot{a}}{a}\right)^2 = -4\pi G \sum_i p_i + \frac{\Lambda}{3}. \tag{1.24}$$

Using the dimensionless energy densities (1.11) we can rewrite (1.23) as

$$(\Omega_m + \Omega_r + \Omega_\Lambda) - 1 = 0, \tag{1.25}$$

where $\Omega_\Lambda = \Lambda/(3H^2)$ and $\Omega_m = \Omega_b + \Omega_c$ is the sum of the baryonic and dark matter energy densities. Baryonic matter counts for ordinary matter that can interact electromagnetically. Dark matter, on the other hand, was hypothesized to account for discrepancies between the motion of large astronomical objects and theoretical predictions based on ordinary matter composition. Nowadays it is indispensable for the standard model and would account for most of the non-relativistic matter of the Universe, though the fundamental physics behind it is still unknown.

During the last years several dark matter candidates were proposed [60, 80, 140]: the weakly interacting massive particle (WIMP), which would be completely different from the type of matter we know and would only interact gravitationally; the axion, a particle with a very low mass which

does not have charge and only interacts via weak interaction or gravitationally with other matter; the massive astrophysical compact halo object (MACHO), which is composed by ordinary matter but it emits very little to no light and it can be a neutron star, a brown or white dwarf, ... Among the dark matter candidates one can also find cosmic defects [71, 72, 81]. It is worth noting that although the main objective of this thesis is not the characterization of dark matter the analysis and characterization of defects could lead to the understanding of the properties of dark matter.

1.4.2. Inflation

Many of the unanswered questions come under the heading of initial condition problems and require a more complete description of the sources of energy density in the Universe. One of the most severe of these problems eventually led to a radical new picture of the physics of the early Universe: cosmological inflation [61, 93].

The fundamental idea behind inflation is that the Universe undergoes a period of accelerated expansion, defined as a period when $\ddot{a} > 0$, at early times. This can also be understood as $d(H^{-1}/a)/dt < 0$, which says that the Hubble radius, as measured in comoving coordinates, decreases during inflation. At any other time, the comoving Hubble radius increases. Now we will describe shortly the problems arising from the Hot Big Bang model and how inflation can solve them:

- The flatness problem

  Using the definition of the density parameter, the Friedmann equation for any value of K can be written as,

  $$|\Omega - 1| = \frac{K}{(aH)^2}. \tag{1.26}$$

  During the standard big bang evolution, $(aH)^2$ is decreasing, and so Ω moves away from one. For example, in radiation domination $|\Omega - 1| \propto t$ and in matter domination $|\Omega - 1| \propto t^{2/3}$. So $\Omega = 1$ is an unstable critical point. Since we know that today Ω is certainly within three orders of magnitude of one it must have been much closer in the past. Using the appropriate behaviours of matter and radiation eras one can see that at nucleosynthesis ($t \sim 1$ sec) $|\Omega - 1| < \mathcal{O}(10^{-16})$ or at electro-weak scale ($t \sim 10^{-11}$ sec) $|\Omega - 1| < \mathcal{O}(10^{-27})$.

  Inflation solves the flatness problem more or less by definition. This means, if we assume that the early Universe was dominated by the inflaton field, which can be define as a fluid with negative pressure or $\omega = -1/3$, equation (1.23) can be written as,

  $$H^2 \approx \frac{\Lambda}{3}, \tag{1.27}$$

  and solving it we have that,

  $$a(t) = \exp\Big(\sqrt{\frac{\Lambda}{3}}t\Big) \Leftrightarrow |\Omega - 1| \propto \exp\Big(-\sqrt{\frac{4\Lambda}{3}}t\Big). \tag{1.28}$$

  Therefore with the above expression there is no need to fine tune the initial conditions. Regardless of the initial value of the curvature, inflation forces it to be very small.

- The Horizon problem

  Photons emitted from opposite sides of the sky appear to be in thermal equilibrium. The most natural explanation for this is that the Universe has indeed reached a state of thermal

equilibrium, through interactions between the different regions. But unfortunately in the Hot Big Bang model this is not possible. There was no time for those regions to interact before photons were emitted because they were far from each other.

The way to view how inflation solves this problem is to remember that inflation corresponds to a decreasing comoving Hubble length. The Hubble length is ordinarily a good measure of how far things can travel in the Universe; what is telling us that the region of the Universe we can see after inflation is much smaller than the region which would have been visible before inflation started. Hence, casual physics was perfectly capable of producing a large smooth thermalized region.

- The relics problem

  In the initial stages of the universe some objects that are diluted by expansion slower than radiation, as a^{-3} instead of a^{-4}, could form and they could become the dominant material of the Universe, in contradiction to observations.

  The fast expansion of the inflationary stage rapidly dilutes the objects that could dominate the Universe, because the energy density during inflation falls off slower, as a^{-2} or slower, than the density of those objects. Very quickly their density becomes negligible.

  Some cosmic defect types, such as, magnetic monopoles or domain walls, can show this behaviour at the early stages of the universe and they can end dominating the energy density of the universe. But defect networks show a scaling solution, where the fraction of the energy density of the defect remains constant (see Section 2.3.2) and their evolution is cosmologically viable. However, every kind of defect created before inflation will be diluted away. But some inflationary models predict cosmic defects to be created at the end of the inflationary period, and in addition symmetry breakings can take place after inflation.

We have seen that an exponentially accelerated epoch in the early stages of our Universe will solve the problems of the Hot Big Bang model. In order to describe this behaviour with our theory we have to add an extra component, a component with negative pressure, the inflaton. The inflaton is a scalar field and its vacuum energy is responsible to drive the exponential expansion. That is, the inflaton has a self-interacting potential and rolling slowly through it towards its ground state acquires negative pressure.

The theory of inflation does not only solved the problems that we have pointed out. This theory can give a explanation of the origin of density fluctuations that lead to the observed large-scale structure. These fluctuations could also be explained using the creation and evolution of cosmic defects [137], and during some time both theories were in confrontation. But the modern and accurate observations exhibit that inflation contribute the most to the origin of the density fluctuations, as we will see in Section 1.6.

1.5. History of the Universe

After analysing the general aspects of the dynamics of the Universe we will briefly summarise the most important events in the history of the Universe, see Table 1.1.

- Inflation

  As we have described in the previous section inflation is an epoch of exponentially accelerated expansion of the universe driven by a field with a negative pressure. It solves the flatness, horizon and relics problems.

Event	time t	temperature T
Inflation	10^{-34}s (?)	-
Reheating	?	?
Baryogenesis	?	?
EW phase transition	20 ps	100 Gev
QCD phase transition	20 μs	150 MeV
Dark matter freeze-out	?	?
Neutrino decoupling	1 s	1 MeV
Electron-positron annihilation	6 s	500 keV
Big Bang nucleosynthesis	3 min	100 keV
Matter-radiation equality	60 kyr	0.75 eV
Recombination	260-380 kyr	0.26-0.33 eV
Photon decoupling	380 kyr	0.23-0.28 eV
Reionization	100-400 Myr	2.6-7.0 meV
Dark energy-matter equality	9 Gyr	0.33 meV
Present	13.8 Gyr	0.24 meV

Table 1.1.: *The most important events in the history of the Universe in a chronological order.*

- Reheating

  The large potential energy of the inflaton field decays and fills the Universe with particles, starting the radiation dominated era of the universe. (For some, the starting point of the Big Bang.)

- Baryogenesis

  Relativistic quantum field theory requires the existence of anti-particles. Particles and anti-particles annihilate through processes such as $e^+ + e^- \rightarrow \gamma + \gamma$. If initially the Universe was filled with equal amounts of matter and anti-matter then we expect these annihilations to lead to a Universe dominated by radiation. However, we do observe an overabundance of matter over anti-matter in the Universe today. Models of baryogenesis try to derive the observed baryon-to-photon ratio from some dynamical mechanism, without assuming a primordial matter-antimatter asymmetry as an initial condition.

- Electroweak symmetry breaking

  At 100 GeV particles receive their masses through the Higgs mechanism. This leads to a drastic change in strength of the weak interaction.

- QCD symmetry breaking

  While quarks are free at high energies, below 150 MeV, the strong interactions between quarks and gluons become important. Quarks and gluons then form bound quark systems, called baryons and mesons.

- Dark matter freeze-out

  Since dark matter is very weakly interacting with ordinary matter we expect it to decouple relatively early. Choosing natural values for the mass of dark matter particles and their interaction cross sections with ordinary matter reproduces the observed relic dark matter density surprisingly well.

- Neutrino decoupling

  Neutrinos only interact with the rest of the primordial plasma through weak interaction. Estimations show that they decoupled at 0.8 MeV producing the cosmological neutrino background, which is still not measured.

- Electron-positron annihilation

  Electrons and positrons annihilate shortly after neutrino decoupling. The energies of the electrons and positrons gets transferred to photons, increasing the temperature of them. After that, a tiny excess of electrons over positrons were left in equilibrium with photons.

- Big Bang nucleosynthesis

  Neutrons and protons first combine to form D, ^4He, ^3He and ^7Li nuclei. The theory for this is very well developed and agrees very well with a variety of observations.

- Matter-radiation equality

  Transition from radiation dominated Universe to matter dominated Universe happens when the energy densities of radiation and matter became equal.

- Recombination

  At early times the CMB photons are easily energetic enough to ionize hydrogen atoms and therefore the Universe is filled with a charged plasma, and hence opaque. This phase lasts until the photons reshifted enough to allow photons and electrons to combine $e^- + p^+ \rightarrow H + \gamma$, during the era of recombination.

- Photon decoupling

  Before recombination the strongest coupling between photons and the rest of the plasma is through Thomson scattering, $e^- + \gamma \rightarrow e^- + \gamma$. The sharp drop in the free electron density after recombination means that this process becomes inefficient and the photons decoupled in the last scattering surface. They have since streamed freely through the Universe and are today observed as cosmic microwave background (CMB), which we will review in Section 1.6.

- Reionization

  The predominant dark matter begin to collapse into halo-like structures through its own gravitational attraction. Ordinary matter is also pulled into these halos, eventually forming the first stars and galaxies, which, in turn, release large amounts of ultraviolet light. This light is energetic enough to strip the electrons out of the surrounding neutral matter.

- Dark energy-matter equality

  Transition from matter dominated Universe to dark energy dominated Universe happens when the energy densities of matter and dark energy became equal. If this equality took place earlier, structures such as galaxies will never have time to form and life will never have a chance to exist. This is known as the coincidence problem.

- Present

  Baryons and the CMB are entirely decoupled, stars and galaxies have been around a long time and clusters of galaxies are becoming common.

1.6. Cosmic Microwave Background

The primitive radiation we observe in the Universe today has the form of an almost isotropic blackbody spectrum, with temperature approximately 2.7K, known as the Cosmic Microwave Background (CMB). The first measurements of the CMB over the whole sky made by the RELIKT-1 experiment [84] on board the Prognoz 9 satellite and the COBE satellite [124] validate the main assumptions of the Hot Big Bang model: homogeneity and isotropy in large scales of the Universe as it can be seen in the left pane of Fig. 1.4. But most of the information of the CMB is not in its homogeneity and isotropy. The small fluctuations in the temperature of the CMB are the most investigated aspects of it, because they reveal a detailed information about the constituents and mechanisms of the evolution of the Universe. In the right side of Fig 1.4 the temperature anisotropies measured by the Planck mission [10] are shown.

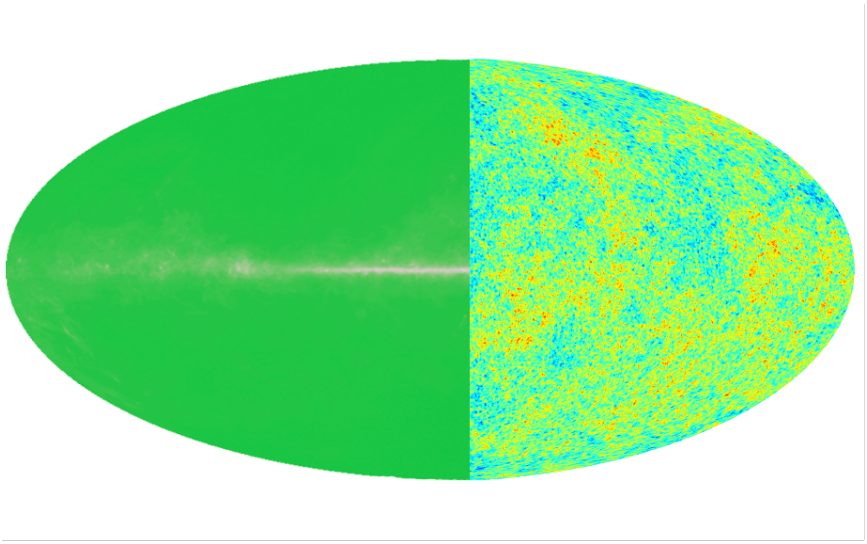

Figure 1.4.: *CMB measurements of the whole sky. In the left side of the figure one can see the measurements made by COBE [124]. This shows that at large scales the homogeneity and isotropy are obeyed. The right side the measurements of Planck mission [10] are shown, where just the anisotropies are shown.*

The origin of the CMB can be explained in terms of Blackbody radiation, a radiation emitted by bodies in thermal equilibrium. The present Universe is certainly not in this state, and so without an evolving space-time we would have no explanation for the origin of this radiation. However, at early times, the density and energy densities in the Universe were high enough that radiation was in approximate thermal equilibrium at each point in space, yielding a blackbody spectrum at early times.

For a blackbody distribution at Temperature T, such as that generated in the early Universe, the energy flux in the frequency range $[\nu, \nu + d\nu]$ is given by the Planck distribution

$$P(\nu, T)d\nu = 8\pi h\Big(\frac{\nu}{c}\Big)^3 \frac{1}{e^{h\nu/kT} - 1} d\nu, \tag{1.29}$$

where h is Planck's constant and k is the Boltzmann constant. Under a rescaling $\nu \to \alpha\nu$, with $\alpha =$constant, the shape of the spectrum is unaltered if $T \to T/\alpha$. It is known that wavelengths are stretched with cosmic expansion, and therefore that frequencies will scale inversely due to the

same effect. We therefore conclude that the effect of cosmic expansion on an initial blackbody spectrum is to retain its blackbody nature, but just at lower and lower temperatures,

$$T \propto 1/a. \tag{1.30}$$

This is what we mean by the Universe is cooling as it expands, as we have anticipated.

The CMB is not a perfectly isotropic radiation bath. Deviations from isotropy (at the level of one part in 10^5) have developed over the last decade into one of our premier precision observational tools in cosmology. The small temperature anisotropies on the sky are usually described by the multipole expansion of the temperature field, which given the spherical symmetry can be expanded in spherical harmonics:

$$\frac{\Delta T}{T}(\hat{n}) = \sum_{l} \sum_{m=-l}^{l} \Theta_{lm} Y_l^m(\hat{n}), \tag{1.31}$$

where l is the multipole moment and $\hat{n}$ is a unitary vector pointing in the line of sight. T is the average temperature and ΔT are deviations from it. The coefficients Θ_{lm} describe the temperature perturbation and obey,

$$\langle \Theta^*_{lm} \Theta_{l'm'} \rangle = \delta_{ll'} \delta_{mm'} C_l, \tag{1.32}$$

where $\delta_{ll'}$ is the Kroenecker's delta function.

In the Gaussian approximation, anisotropies can be fully characterized by the 2-point correlation function of the power spectrum. The power spectrum as a function of the C_l's is written as

$$\left\langle \left| \frac{\Delta T}{T} \right|^2 \right\rangle = \frac{1}{4\pi} \sum_{l=0}^{\infty} (2l+1) C_l. \tag{1.33}$$

The coefficients of the spherical harmonic expansion, Θ_{lm}, are the analogous of the fourier transform coefficients but in spherical surfaces. When we work on small patches of the sky, the curvature can be neglected, thus the relation between angular wavelength and multipole moment simplifies to: $\theta = 2\pi/l$.

The anisotropies of the CMB can be divided in two different types: primary anisotropies and secondary anisotropies. The primary ones are related to processes that took place at the last scattering surface or before, and the secondary ones are related with the processes that occurred between the last scattering surface and the observer.

The primary anisotropies are determined principally by two effects, acoustic oscillations and diffusion damping. Acoustic oscillations come from the photon-baryon plasma in the early Universe. The pressure of the photons tends to erase inhomogeneities, whereas the gravitational attraction of the baryons, moving at speeds much slower than light, makes them tend to collapse to form over densities. These two effects compete to create acoustic oscillations.

On the other hand, secondary anisotropies are produced by effects such as the Sunyaev-Zel'dovich effect, where a cloud of high-energy electrons scatters the radiation, transferring some of its energy to the CMB photons, or the Saechs-Wolfe effect, which causes photons from the CMB to be gravitationally redshifted or blueshifted due to changing gravitational fields.

In Fig. 1.5 one can see a pictorial description of the CMB temperature power spectrum. For large angular scales ($l < 100$), i.e. scales corresponding to super-Hubble modes at the time of decoupling, the angular power spectrum can be estimated as a function of the characteristics of the gravitational potential, which is constant in this regime. This part of the angular spectrum

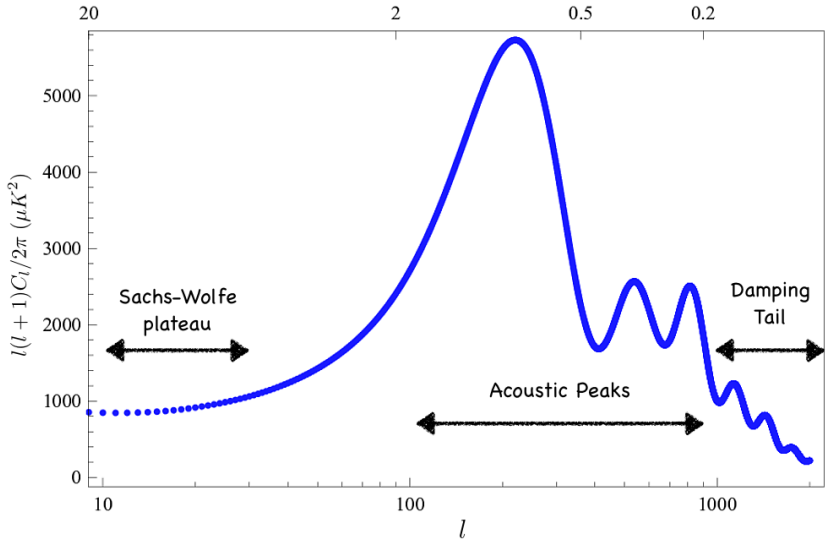

Figure 1.5.: *A pictorial representation of the CMB power spectrum.*

is usually called the Sachs-Wolfe plateau. The peaks of the angular power spectrum $(100 < l < 1000)$ are the acoustic peaks and they contain interesting physical signatures. The angular scale of the first peak determines the curvature of the Universe, the next peak the reduced baryon density and the third one can be used to get information about the dark-matter density. The position of the peaks also give important information about the nature of the primordial density perturbations. On small scales $(l > 1000)$ the free path of photons become of the same order of magnitude as the wavelength of the perturbations, creating the characteristic damping tail.

As we said the analysis of the CMB anisotropies is a precise observational tool. Comparing the observational data with the data coming from theoretical analysis one can analyse the contribution of different processes to the CMB. In order to obtain the theoretical expectation of those different processes, one is required to solve a set of linear differential equations,

$$\mathcal{D}_{ac}(a,\rho,...)\tilde{X}_a = \begin{cases} 0 & \text{Passive (Inflation)} \\ S_c & \text{Active (Defects)} \end{cases} \tag{1.34}$$

where $\tilde{X}_a$ is the Fourier transform of the quantity of interest X_a, $\mathcal{D}_{ac}$ is a differential operator that depends on the cosmic scale factor a, the background density ρ and similar quantities. The perturbations coming form the analysis of (1.34) are classified into density perturbations (scalars), vector perturbations and tensor perturbations or gravitational waves, and they do not mix in linear order. The perturbations created by the quantum fluctuations of the inflaton field are primary, because they produce anisotropies before the last scattering surface and then they evolve passively. On the contrary, perturbations created by cosmic defects are of both types, primary and secondary, because defects create anisotropies during their whole existence.

In the inflationary case the vector perturbations are not considered because they decay very

rapidly. On the other hand, the powers for scalar and tensor perturbations can be expressed as,

$$\mathcal{P}_{\mathcal{R}}(k) = A_s\Big(\frac{k}{k_*}\Big)^{n_s-1}, \tag{1.35}$$

$$\mathcal{P}_t(k) = A_t\Big(\frac{k}{k_*}\Big)^{n_t}, \tag{1.36}$$

where k_* is the pivot comoving wavenumber. A_s and A_t are the scalar and tensor amplitudes, and n_s and n_t represents the spectral index of both power spectra and determine the tilt of it. Note the different definitions for spectral indexes, while $n_s = 1$ gives the Harrison-Zel'dovich model for scale invariant scalar perturbations [62, 141], $n_t = 0$ gives the scale invariance for tensors.

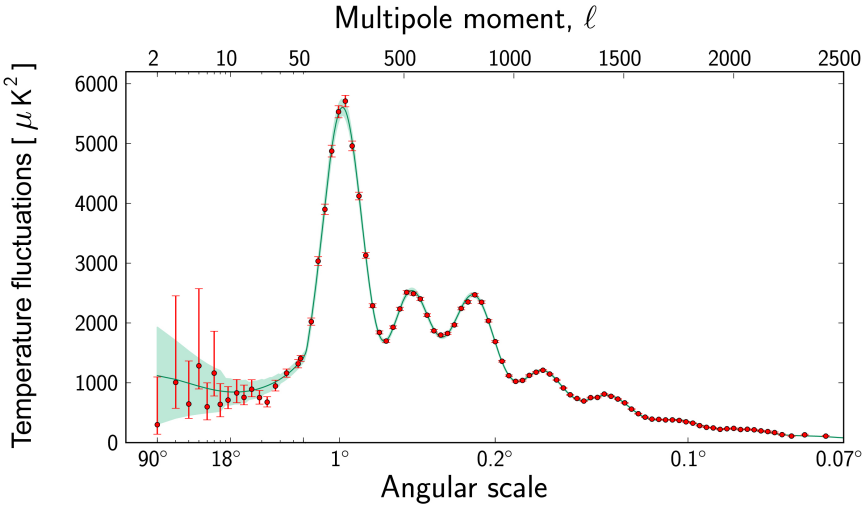

Figure 1.6.: *The temperature power spectra measured by the Planck experiment [10], where the dots represents the measured data with their corresponding error bars and the green curve is the best fit using the ΛCDM model, where the green pale area counts for variations.*

For the case of cosmic defects the power spectra cannot be obtained so easily. In order to solve the equation (1.34) the source functions, which are related with S_a, have to be obtained using numerical simulations of the kind of defect we want to analyse. In Section 2.3.5 we show the procedure that has to be used in order to obtain the source functions from numerical simulations and then how the equations are solved using Einstein-Boltzmann (EB) solvers. Then in Chapter 6 we use this procedure to obtain the power spectra for global O(2) strings and global O(3) monopoles.

However, the power spectra obtained in both cases can be compared with the measured one (see Fig. 1.6) in order to analyse the contribution of each one of the processes. In the left pane of Fig. 1.7 we show an inflationary power spectra, while in the right pane we show a power spectra for the Abelian-Higgs strings, one of the most analysed defect model that we will describe in Section 2.3, obtained by [95]. One can clearly see that the inflationary one recreates the peak distribution of the measured power spectra. On the other hand, the power spectra coming from the Abelian-Higgs case does not show the peak distribution. So, one can think that the contribution of the defects to the measured power spectra should be subdominant. This is shown

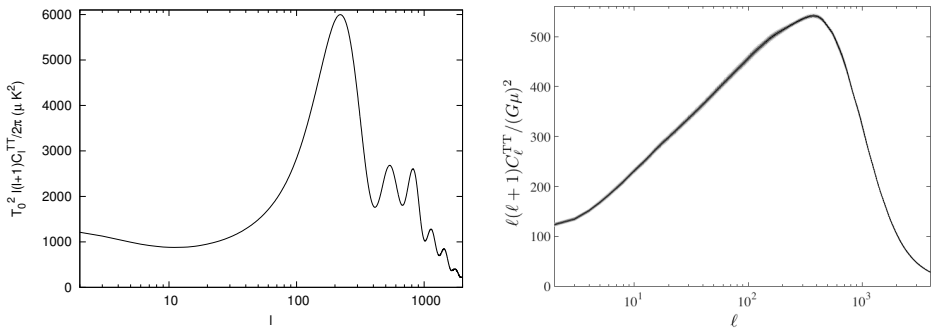

Figure 1.7.: *Temperature power spectrum for inflationary case (left). Temperature power spectrum for Abelian-Higgs strings (rigth), picture courtesy of J. Lizarraga [95]*

in [95], where they calculated that at $l = 10$ the contribution of Abelian-Higgs strings to the measured power spectra is lower than 1.3 %.

It is customary to use 6 parameters to describe a cosmological model describing an isotropic and homogeneous expanding universe. If we want to add the contribution of the defects to the model we have to add a new parameter. In the following, we will analyse the six parameters describing the Hot Big Bang model and we refer the reader to Section 2.3.5, where the analysis of the parameter describing the defect contribution will be done. The six parameters needed to describe the cosmological model without defects are:

1. $\Omega_b h^2$: Physical baryon density.
2. $\Omega_c h^2$: Physical cold dark matter density.
3. θ: Approximation to the ratio of the sound horizon at recombination to the angular diameter distance. It is directly related to the position of the first acoustic peak and is very sensitive to changes in the geometry of the Universe.
4. κ: Reionization optical depth to last scattering. κ provides information about the ionization state of the Universe and gives the probability that a given photon scatters once.
5. n_s: Spectral index of scalar perturbations.
6. A_s: Amplitude of the primordial super-horizon power in the curvature. Usually re-parametrized as $\ln(10^{10} A_s)$

In Table 1.2 we show the values for the parameters described above as determined by the Planck experiment [10].

$\Omega_b h^2$	0.02225 $\pm$ 0.00016
$\Omega_c h^2$	0.1198 $\pm$ 0.0015
$\theta \times 100$	1.04077 $\pm$ 0.00032
κ	0.079 $\pm$ 0.017
n_s	0.9645 $\pm$ 0.0049
$\ln(10^{10} A_s)$	3.094 $\pm$ 0.034

Table 1.2.: *The values of the parameters that describe the Hot Big Bang model determined by the Planck experiment [10], where the parameter accounting for the contribution of defects is not taken into account.*

2 Cosmic defects

2.1. Introduction

In the previous Chapter we have described the standard cosmological model. This model represents a Universe that has expanded from a very dense and hot epoch to a more diluted and cooler era. During this evolution we have seen that symmetry breakings could take place.

One of the most important consequences of these symmetry breakings is the possibility of the creation of cosmic defects[1]. The defects are characterized by the symmetry breaking properties, and as different kind of symmetry breakings could take place, different kind of defects could be created. The properties of the defect are strictly related with the symmetry breaking pattern.

Therefore, the cosmic defect zoo is large and the detailed analysis of each one of the components of this zoo will be a very hard issue. In this Chapter we will consider the most analysed defect model, the Abelian-Higgs model [74, 137], and we will describe its most important properties. We will concentrate on describing the aspects related to this Thesis, and we will refer the reader interested in other aspects to the detailed analysis in the literature.

Once we have described the Abelian-Higgs model we will analyse the models that are relevant for this Thesis. In this description we will highlight the properties that we will later analyse in Part II and we will also try to describe the procedure we will use to do this analysis.

2.2. Spontaneous Symmetry Breaking

The essential features of spontaneous symmetry breaking can be illustrated using a simple model called the Goldstone model [59]. This model is characterised by the following Lagrangian density,

$$\mathcal{L} = (\partial_\mu \phi)^\dagger (\partial^\mu \phi) - \frac{\lambda}{4}(\phi^\dagger \phi - \eta^2)^2, \tag{2.1}$$

where ϕ is a complex scalar field, λ the self-coupling and η is the vacuum expectation value. The potential of the model, the last term in the Lagrangian, is often called the mexican-hat potential and can be seen in Fig. 2.1. The model is invariant under the group U(1) of global phase transformations, $\phi(x) \to e^{i\alpha}\phi(x)$. Global indicates that α does not depend on the space coordinates x. Otherwise, there are other models where the parameter of phase transformations

[1] Note that defects formed in symmetry breakings are usually called "topological" defects, because they are formed due to topological reasons. Since we will analyse some type of defects whose origin is not topological, we will refer to defects formed in cosmological symmetry breakings as "cosmic defects" or just "defects".

$\alpha(x)$ depends on the spacetime location x. This kind of models are called local, due to the fact that $\alpha(x)$ is locally valued.

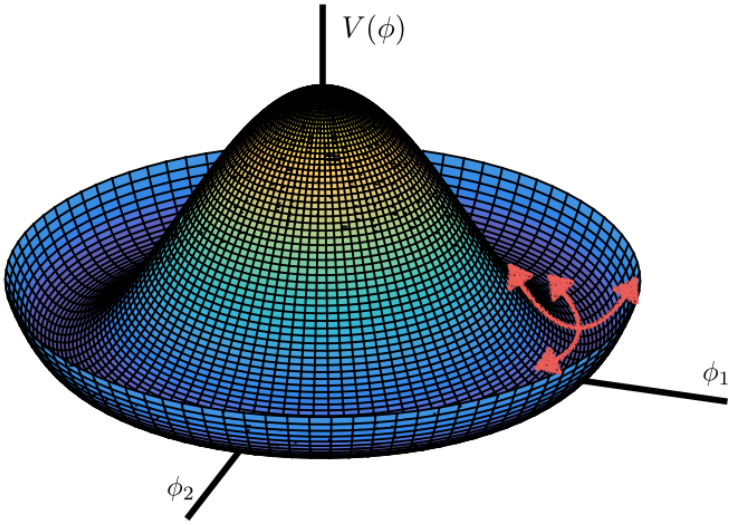

Figure 2.1.: *Mexican Hat potential. The red arrows describe the motion of the ϕ_1 and ϕ_2 fields.*

The minima of the mexican-hat potential lie on a circle in the complex plane, $|\phi| = \eta$, and the vacuum state of the theory is characterized by a non-zero expectation value

$$\langle\phi\rangle = \eta e^{i\theta}, \tag{2.2}$$

with an arbitrary phase θ. Similarly, the local maxima of the potential is located where the field posses a zero expectation value $\langle\phi\rangle = 0$.

The potential shown in Fig. 2.1 is analysed using a fixed value of the temperature, but as we have see in the previous Chapter, the universe in its evolution is expanding and cooling. In order to study the symmetry breaking in terms of an expanding universe we can add thermal corrections to the potential,

$$V_{eff} = \lambda(|\phi|^2 - \hat{\eta}^2(T)) + f(T, \eta). \tag{2.3}$$

The effective vacuum expectation value with temperature corrections up to second order is,

$$\hat{\eta}^2(T) = \eta^2 - \frac{T^2}{6}, \tag{2.4}$$

which as it turns out, it is not positive definite. It actually vanishes when the temperature reaches its critical value, T_c, given by

$$T_c = \sqrt{6}\eta. \tag{2.5}$$

As we can see in Fig. 2.2 at high temperatures $(T > T_c)$, the effective potential has a unique minimum localized at $\phi = 0$. In this case, the vacuum state has the same symmetry as the Lagrangian (2.1) and the symmetry is unbroken as long as the temperature is sufficiently high. When temperature decreases due to the effect of another physical mechanism, such as, for instance, the expansion of the universe, the shape of the potential changes until its minimum is no longer at $\phi = 0$. Then, the field will drop from the state of the unbroken symmetry to a specific vacuum

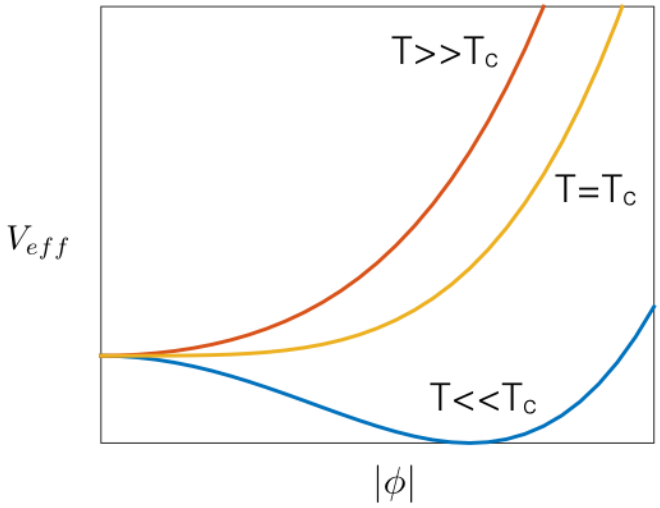

Figure 2.2.: *Dependence of the potential with respect to the temperature.*

state, determined by θ, spontaneously. It is evident that the new vacuum manifold, $\langle\phi\rangle = \eta e^{i\theta}$, is not invariant under the global phase transformation and the symmetry is spontaneously broken.

The broken symmetry vacua with different values of θ are all equivalent, so we can choose one of them to study their properties. Choosing $\theta = 0$ one can represent ϕ as perturbations around the minima as

$$\phi = \eta + \frac{1}{\sqrt{2}}(\phi_1 + i\phi_2), \tag{2.6}$$

where ϕ_1 and ϕ_2 are real fields with zero vacuum expectation values. The re-parametrization (2.6) can be substituted into the Lagrangian (2.1),

$$\mathcal{L} = \frac{1}{2}(\partial_\mu\phi_1)^2 + \frac{1}{2}(\partial_\mu\phi_2)^2 - \frac{1}{2}\lambda\eta^2\phi_1^2 + \mathcal{L}_{int}, \tag{2.7}$$

where the interaction term $\mathcal{L}_{int}$ includes cubic and higher-order terms in ϕ_1 and ϕ_2. Analysing the rearranged Lagrangian one can see that the ϕ_1 field represents a particle with a positive mass, $m_{\phi_1} = \sqrt{\lambda}\eta$, and that ϕ_2 is a massless field. The reason for this is intuitively clear from Fig. 2.1: ϕ_1 corresponds to radial oscillations about a point on the circle of minima, $|\phi| = \eta$, while ϕ_2 corresponds to motion around the circle. The appearance of massless scalar particles, called Goldstone bosons, is a general feature of spontaneously broken global symmetries.

A direct consequence of spontaneous symmetry breakings is the creation of cosmic defects. In the Goldstone model the defects that arise are global strings; lets see how they form. As we have shown, once the symmetry is broken the vacuum expectation value is given by,

$$\langle\phi\rangle = \eta e^{i\theta}, \tag{2.8}$$

where θ may be chosen differently in different regions of space. The requirement that the vacuum expectation value be single valued implies that around any closed curve in space the change $\Delta\theta$ in θ must satisfy,

$$\Delta\theta = 2\pi n, \quad n \in \mathcal{Z}, \tag{2.9}$$

where n is known as the winding number.

If for a given loop we have $n \neq 0$, we can see that any 2-surface bounded by the loop must contain a point where the field ϕ is in the local maximum of the potential. If not we can continuously contract the loop to a point, implying that $n = 0$ which is a contradiction. At the local maximum of the potential the phase, θ, is undefined and $\langle\phi\rangle = 0$. Furthermore, $\langle\phi\rangle$ must be zero all along an infinite or closed curve, since otherwise we can contract our loop without encountering a singularity. We identify this infinite or closed curve of false vacuum as the core of our string. As we have said the state where $\langle\phi\rangle = 0$ can be seen as the unbroken symmetry state and thus strings can be understood as field configurations for which domains exist where the symmetry is left unbroken. Since such configuration does not correspond to a minimum of the potential, it contains a localized energy density around the points where $\langle\phi\rangle = 0$.

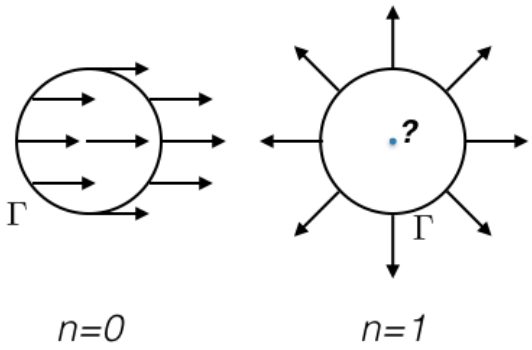

Figure 2.3.: *Field distribution with $n = 0$ (left) and with $n = 1$ (right).*

Another way to understand the formation of strings is representing the field ϕ by an arrow in a complex plane. Then we can draw a closed path Γ in that complex plane and analysing the behaviour of the fields inside the path we can see if we have a string there. Let us consider two different field configurations, as shown in Fig. 2.3; one with $n = 0$ and the other with $n = 1$. In the case where $n = 1$, we can see that inside the closed path Γ there is a singularity, that is, a point where the field cannot be represented by an arrow. On the other hand, in the field distribution with $n = 0$ in all points the field can be represented with an arrow.

In this specific model the cosmic defect that arises is a string, because the vacuum manifold of the theory has non-contractible loops. In general, a field theory with a vacuum manifold $\mathcal{M}$ posses a cosmic defect of some type if the vacuum manifold has a nontrivial homotopy group,

$$\pi_i(\mathcal{M}) \neq 1, \tag{2.10}$$

for some $i = 0, 1, \ldots$. The homotopy group classifies distinct mappings of the n-dimensional sphere S^n in the vacuum manifold $\mathcal{M}$. In Table 2.1 the different cosmic defects types created for different values of i are shown.

However, in some cases even if the topology is not responsible for creating defects energy considerations can give rise to them. In Section 2.4.2 we will analyse the semilocal model. In this model the magnetic field is massive and magnetic flux conserved, which suggest the existence of magnetic flux tubes when the magnetic mass is large.

$\pi_0(\mathcal{M}) \neq 1$	$\mathcal{M}$disconnected	Domain Wall
$\pi_1(\mathcal{M}) \neq 1$	non-contractible loop in $\mathcal{M}$	Cosmic String
$\pi_2(\mathcal{M}) \neq 1$	non-contractible 2-sphere in $\mathcal{M}$	Monopole
$\pi_3(\mathcal{M}) \neq 1$	non-contractible 3-sphere in $\mathcal{M}$	Texture

Table 2.1.: *Different types of cosmic defects.*

2.3. Abelian-Higgs model

In order to illustrate the essential features of cosmic defects we will use the most analysed model, the Abelian-Higgs model [64, 137], which is characterized by the following lagrangian density,

$$\mathcal{L} = (\mathcal{D}_\mu\phi)^*(\mathcal{D}^\mu\phi) - \frac{1}{4}F_{\mu\nu}F^{\mu\nu} - \frac{\lambda}{4}(\phi^\dagger\phi - \eta^2)^2, \tag{2.11}$$

where ϕ is a complex scalar field and the covariant derivatives are given by $\mathcal{D}_\mu = \partial_\mu - ieA_\mu$. The gauge field strength is $F_{\mu\nu} = \partial_\mu A_\nu - \partial_\nu A_\mu$ with A_μ a gauge vector field and e the gauge coupling. The potential of the model, the last term in the lagrangian, is again the mexican-hat potential and can be seen in Fig. 2.1. This model is invariant under the group $U(1)$ of local gauge transformations,

$$\phi(x) \to e^{i\alpha(x)}\phi(x), \quad A_\mu(x) \to A_\mu(x) + e^{-1}\partial_\mu\alpha(x). \tag{2.12}$$

Let us represent ϕ as perturbation around the minima $\phi(x) = \eta + \frac{1}{\sqrt{2}}(\phi_1 + i\phi_2)$, where $\phi_1(x)$ and $\phi_2(x)$ are real scalar fields. In this model we have a freedom to pick a gauge and we can use this freedom to make $\phi_2 = 0$. Using this representation we have,

$$\mathcal{L} = \frac{1}{2}(\partial_\mu\phi_1)(\partial^\mu\phi_1) - \frac{1}{2}\lambda\eta^2\phi_1^2 - \frac{1}{4}F_{\mu\nu}F^{\mu\nu} + \frac{1}{2}e^2\eta^2A_\mu A^\mu + \mathcal{L}_{int}, \tag{2.13}$$

where $\mathcal{L}_{int}$ includes cubic and higher order terms. The term $e^2\eta^2A_\mu^2$ shows that the gauge field A_μ is massive with $m_v = e\eta$, due to its interaction with the constant part of the field ϕ. The $\phi_1(x)$ term of the field ϕ is massive too, with mass $m_s = \sqrt{\lambda}v$, which can be seen as radial oscillations about a point on the circle of minima, $|\phi| = \eta$, see Fig 2.1. In this case there is no massless particle.

Since the vacuum manifold is this model has a non-contractible loop and the symmetry of the Lagrangian is local the cosmic defect that could arise in the spontaneous symmetry breaking of this model is a local cosmic string.

As we have described previously, the Lagrangian of the Abelian-Higgs model has three parameters; η, the vacuum expectation value, e, the gauge coupling and λ, the self coupling. Only some combinations of these parameters are meaningful which can be seen under suitable rescalings given by

$$\phi \to \eta^{-1}\phi, \quad A^\mu \to \eta^{-1}A^\mu, \quad x \to \eta e x. \tag{2.14}$$

Using the rescaling (2.15) the Lagrangian (2.11) takes the following form,

$$\frac{\mathcal{L}}{\eta^4e^2} = (\mathcal{D}_\mu\phi)^*(\mathcal{D}^\mu\phi) - \frac{1}{4}F_{\mu\nu}F^{\mu\nu} - \frac{\beta}{2}(\phi^\dagger\phi - 1)^2 \tag{2.15}$$

where now $\mathcal{D}_\mu = \partial_\mu - iA_\mu$. One can see that the unique parameter governing the model dynamics

is $\beta = \frac{\lambda}{2e^2} = m_s^2/m_v^2$. The equations of motion can be obtained using the Euler-Lagrange equations

$$\frac{\partial(\sqrt{-g}\mathcal{L})}{\partial f_i} - \frac{d}{dx}\Big(\frac{\partial(\sqrt{-g}\mathcal{L})}{\partial f_i'}\Big) = 0, \tag{2.16}$$

where f_i are functions with a single independent variable x and the prime represents a derivative with respect to that variable x. Note that in order to obtain the equations of motion we have to choose the metric. In our case, we will use the FLRW metric (see Section 1.3) with comoving cartesian coordinates and conformal time:

$$ds^2 = a(\tau)^2[-d\tau^2 + dx^2 + dy^2 + dz^2]. \tag{2.17}$$

Substituting the Lagrangian (2.15) into the Euler-Lagrange equations (2.16) and choosing the temporal gauge ($A_0 = 0$) one can obtain the following equations of motion,

$$\begin{aligned} \ddot{\phi} + 2\frac{\dot{a}}{a}\dot{\phi} - \mathcal{D}_j\mathcal{D}_j\phi &= -a^2\frac{\lambda}{2}(|\phi|^2 - \eta^2)\phi, \\ \dot{F}_{0i} - \partial_i F_{ij} &= -2a^2e^2 Im(\phi^*\mathcal{D}_j\phi), \end{aligned} \tag{2.18}$$

where $F_{0i} = \dot{A}_i$, which are supplemented with the Gauss law constraint

$$-\partial_i F_{0i} = -2a^2e^2 Im(\phi^*\dot{\phi}). \tag{2.19}$$

These model accepts a solution for a static cylindrically symmetric straight string with a arbitrary winding number n. The ansatz that gives rise to that solution is

$$\phi = f(r)e^{in\theta}, \quad A_i = \frac{n}{er}v(r)\hat{\theta}_i, \tag{2.20}$$

where r and θ are the radial and azimuthal angle coordinates, respectively. This solution is known as the Abrikosov-Nielsen-Olesen (ANO) vortex line [1, 103], and can be obtained by solving the equations of motion that are calculated substituting (2.20) into (2.18),

$$\begin{aligned} \frac{d^2f}{dr^2} + \frac{1}{r}\frac{df}{dr} - \frac{n^2f}{r^2}(v-1)^2 - \beta f(f^2-1) &= 0, \\ \frac{d^2v}{dr^2} - \frac{1}{r}\frac{dv}{dr} - 2f^2(v-1) &= 0. \end{aligned} \tag{2.21}$$

The equations of motion (2.21) have to be solved subject to appropriate boundary conditions that are obtained by using energy considerations. Moreover, there is no analytic solution to the equations and numerical solvers have to be used in order to obtain solutions. One solution for (2.21) is shown in Fig. 2.4 but we refer the reader interested in how the equations are solved to Chapter 3 where similar equations of motion are treated. Fig. 2.4 shows the profiles for ϕ and A_θ fields for a ANO string centered at $r = 0$ with $n = 1$. The string core is around $\phi = 0$, and far away of the string core, the fields acquire their vacuum expectation value of the broken symmetry phase. Fig. 2.4 also shows that there are two different string core widths. On the one hand, we have the string width related to the field ϕ, the scalar core, $r_s \sim m_s^{-1}$. On the other hand, we have the string width related to the gauge field A_μ, the gauge core, $r_v \sim m_v^{-1}$. Once the profile functions of the fields are obtained it is desirable to analyse the energy per unit length of the

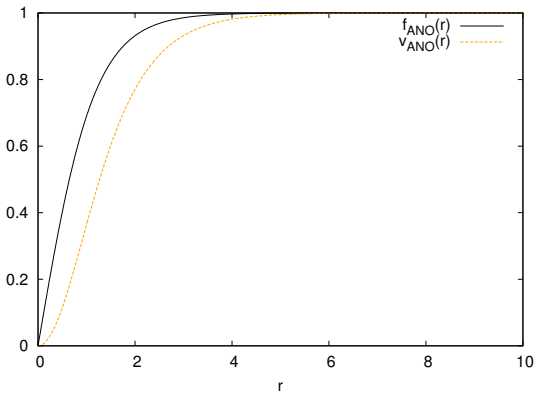

Figure 2.4.: *Profile functions for the ANO case.*

strings:

$$\mu = \eta^2 \int dr\, r\Big((\mathcal{D}_\mu\phi)^*(\mathcal{D}^\mu\phi) + \frac{1}{4}F_{\mu\nu}F^{\mu\nu} + \frac{\beta}{2}(\phi^\dagger\phi - 1)^2\Big), \tag{2.22}$$

where we have used the rescaled functions. One can observe that the energy per unit length is strictly related with the symmetry breaking scale η, so the determination of the string energy could help to obtain information about the energy scale where the symmetry breaking took place. In the same way, it is important to analyse the magnetic flux around the string which is given by,

$$\Phi_B = \int \mathbf{B} d\mathbf{S} = \int_C d\theta\, v = \frac{2\pi n}{e}, \tag{2.23}$$

where $d\mathbf{S}$ describes a two dimensional section perpendicular to the strings and $B_k = \epsilon_{ijk}F_{ij}/2$, where ϵ_{ijk} is the Levi-Civita symbol. C is a closed circle around the string. To obtain the right side term of (2.23) we have used the ansatz for the gauge field (2.20) and one can see that the flux is concentrated around the string and also that it is quantized. This flux quantization is a result of the vanishing of the covariant derivatives, enforced by the boundary conditions (see Chapter 3), which determines v in terms of ϕ.

Using the string properties that we have analysed the strings can be detected in a numerical simulation in three different ways:

- Computing the winding number around a closed path.
- Finding regions with concentration of potential energy.
- Finding regions with concentration of magnetic flux.

For the Abelian-Higgs strings the most used technique to detect strings is the one related to the winding number, however, in other defect types magnetic flux is also used (see Chapter 5).

The stability of the strings depends on the value of β. When $\beta > 1$ the strings are unstable and if $n > 1$ they tend to split into $n = 1$ strings [74, 103]. In this limit, the force between strings is repulsive, because in this case the gauge core is bigger than the scalar core, and the force is governed by the repulsion of the vector fields. On the other hand, vortices with $\beta < 1$ are always stable and the force between strings is attractive, because in this case the scalar core is bigger. When $\beta = 1$, the Bogomol'nyi limit, the strings are neutrally stable and the mass of the scalar field and the mass of the gauge field become identical, which means that the scalar core and the gauge core have the same size and none of the forces dominate.

2.3.1. Strings in Cosmology: Kibble-Zurek mechanism

At this point, it is appropriate to discus how stochastic networks of defects can be formed at cosmological phase transitions. In the cosmological context, the mechanism for the production of defects is known as the Kibble-Zurek mechanism [82, 142, 143], which give a intuitive way to understand the formation. The guiding principle here is causality, which imposes a maximum correlation length: different regions of space that are separated by larger distances than this correlation length are not causally connected and the field can choose different vacuum states in each one of these regions. When the temperature of the expanding universe falls below the critical temperature, T_c, the field ϕ in most regions will have acquired a non-zero expectation value, but the phases in regions separated more than the correlation length will be uncorrelated.

In this process the field does not acquire the unbroken state in all space positions at the same time. Some regions of space will acquire the unbroken phase firstly, in a process known as the bubble nucleation [36, 38, 94], and then these bubbles will grow in size. In this procedure one can expect that the choice of the phase inside each bubble to be the same, but the choice will be different in bubbles separated by more than the correlation length. When two of these bubbles meet, the values of ϕ across the boundary will tend to interpolate between those in the two bubbles. But when three or more bubbles meet, a string could be trapped along their boundary, depending on whether or not the phase change around it is a multiple of 2π or zero. The Kibble-Zurek mechanism also gives an estimate value for the probability of trapping a string in those boundaries.

The process that we have just explained is shown in Fig. 2.5. In the top row of this figure the bubbles are shown, where the white region represents the broken symmetry state and the grey one the unbroken state. The bottom row of the figure shows the corresponding phase choice.

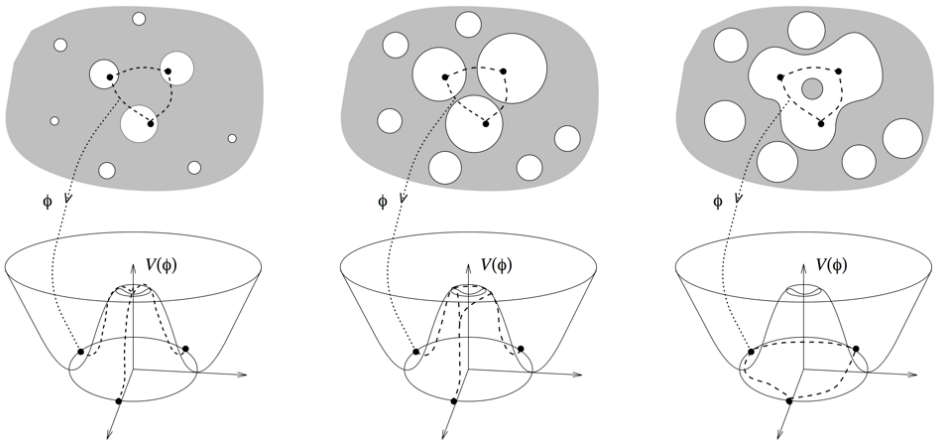

Figure 2.5.: *Pictorial description of the Kibble-Zurek mechanism. Picture courtesy of M. Hindmarsh [74].*

In either case, the result is a random network of strings with some characteristic scale. Among other things this characteristic scale can be the string separation or the total string length. This characteristic scale will be interesting for the analytical model of the defect networks (see Section 2.3.4)[98, 99, 101].

2.3.2. Cosmological viability: Scaling

In Chapter 1, we have shown that the energy density of some cosmological objects could dominate the universe, making these models non viable. Similarly, the energy density of some other objects could be diluted away very rapidly, making these models non measurable. However, the evolution of some type of defects, including local cosmic strings, exhibit a special regime called scaling. In the scaling regime, the characteristic scale, grows linearly with time. In other words, during the scaling regime the fraction of the energy density coming from defects remain constant. Consequently, the defects will not dominate the universe, neither will they disappear.

As mentioned before in the Abelian-Higgs model the strings created should be infinite or closed. In a realistic cosmological evolution for an expanding universe these infinite strings would be stretched. This means that the energy of the strings would be proportional to the scale factor a. In this scenario the energy density of strings is not a constant fraction and the strings would end dominating the universe. However, strings show a scaling behaviour thanks to energy loss mechanisms.

The energy loss mechanisms of string networks are strictly related to the probability of string reconnection when different sections of strings cross. The probability or reconnection for the AH strings was widely studied [102, 121, 133]. So when the infinite strings forming the network intercommute loops can be generated. Soon after these loops are created, they radiate and they decay. Therefore, the energy lost due to loop decays compensates the energy gain coming from the stretching of the infinity strings, enabling the scaling regime.

In order to study networks of defects, numerical simulations are essential (as we will show in Part II of the Thesis). For numerical simulations to be valid tools, scaling is an essential property, since it allows us to use the simulations to analyse the defect properties. On the one hand, it is impossible to perform simulations that cover the whole cosmological evolution of a given defect type. On the other hand, it is very hard to simulate defects at the exact moment that they are created, because it is not clear which model has to be adopted as the underlaying phase transition model. However, scaling allows us to extrapolate numerical simulations to the required cosmological scales. That is, in our simulations we can consider relatively small periods of time and by repeating the simulations obtain a statistical sample of the observables. Then scaling enables the extrapolation of such limited statistics to cosmological scales.

2.3.3. Some observational effects

The analysis of the gravitational properties of cosmic defects is of great interest. Defects interact with cosmological objects mainly via gravitational interaction, and the properties of the observational effects created by them are characterized by the strength of the gravitational field of defects, which is described by the dimensionless parameter $G\mu$. G is the Newton's constant and μ is the string tension for the case of the Abelian-Higgs model. The parameter μ gives information about the energy scale of the symmetry breaking where the defect was produced. Therefore, the determination of the value of $G\mu$ will set the energy scale of the phase transition and help to create the connection between the high energy physics and cosmology that we are looking for.

Let us analyse the gravitational field around a straight string in the Abelian-Higgs model. It is known that in the Newtonian limit the Einstein equations become $\nabla^2\Phi = 4\pi G(\rho + p_1 + p_2 + p_3)$, where Φ is the gravitational potential. For non-relativistic matter $p_i << \rho$, so we can write the Einstein equations as $\nabla^2\Phi = 4\pi G\rho$. In contrast, for a straight string lying in the z-direction, $p_3 = -\rho$ and p_1 and p_2 vanish when they are averaged over the string cross-section obtaining that the Einstein equations takes the form $\nabla^2\Phi = 0$. This solution suggests that straight strings

produce no gravitational force on the surrounding matter in the Newtonian limit.

The gravitational properties of cosmic strings were studied long ago when Vilenkin [136] calculated the gravitational background around an infinitely thin cosmic string in the weak field approximation. He found that the space-time around a cosmic string is conical, that is, Minkowski space minus a wedge,

$$ds^2 = -dt^2 + dr^2 + \left(1 - \frac{\Delta}{2\pi}\right)^2 r^2 d\theta^2 + dz^2, \tag{2.24}$$

where $\Delta = G\mu$ represents the deficit angle. As we have just mentioned to obtain these results Vilenkin made use of two different approximations. The first one, the zero thickness approximation gives rise to the conical singularity at the position of the string, r=0. The second one, the weak field approximation, is only justified for small values of the string tension. However, if one considers the full Einstein-scalar-gauge field equations for the gravitating Abelian-Higgs model, these two problems are resolved. Firstly, the conical singularity is smoothed out by the finite size core of the Abrikosov-Nielsen-Olesen vortex [103] and, secondly, it is possible to show that the deficit angle is approximately proportional to the vortex tension $\Delta \approx \mu G$, and that the metric far from the string core behaves as (2.24). When the string tension μ is sufficiently large, the deficit angle could become larger than 2π. The strings with such tension are called supermassive strings, which are already studied [86, 108], and they have a singularity at a maximal value of the radial coordinate, at which the angular part of the metric vanishes. Strings showing such a large tension in models that can be understood as extensions of the AH model are studied in Chapter 3. Fig. 2.6 shows the 2 dimensional conical space perpendicular to the string is a Minkowski space.

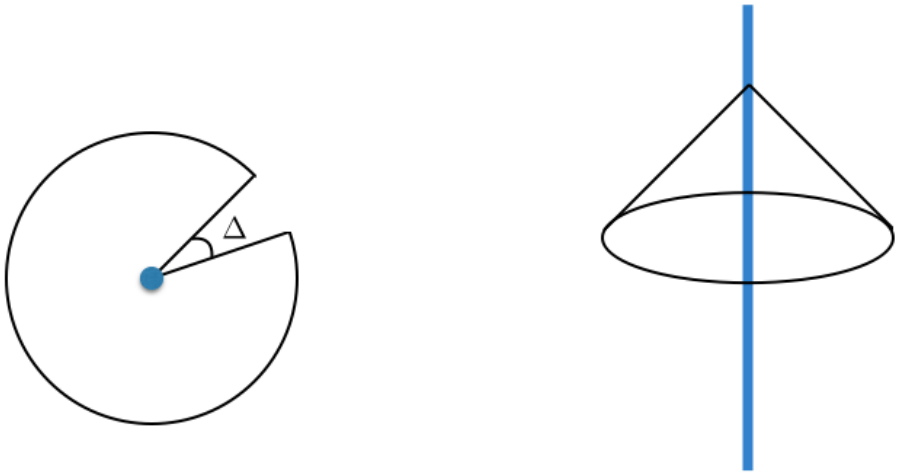

Figure 2.6.: *Illustration of the space around a cosmic string. The blue region represents the string core.*

Due to the conical spacetime of the strings several astrophysical observational signatures have been proposed and studied, such as gravitational lensing, high-energy cosmic rays and gamma ray burst [34, 82, 137], creation of cosmic magnetic fields [47] or generation of non-Gaussian signatures in cosmological perturbations [55, 68, 70, 117]. However, one of the most studied phenomena of defect networks is the generation of CMB anisotropies [29, 30, 95, 127]. As we have said previously, defects can create anisotropies in the primordial photon-baryon plasma, but

they can also create anisotropies during their cosmological evolution. The analysis of the CMB anisotropies could set the value of the dimensionless parameter $G\mu$.

Moreover, in the last few years gravitational waves created by strings have attracted huge interest [2, 46, 76, 105, 123, 131, 135]. As we have mentioned earlier, for the case of the Abelian-Higgs model, the main energy loss mechanism of string networks is the production of loops that soon after their production decay. During the decay of these loops gravitational radiation is emitted[2].

As we have seen, the analysis of the observational effects of defects could give us information to create the connection between high energy physics and cosmology. To obtain that information, in this Thesis, we will make a detailed analysis of the gravitational properties of some kind of defects appearing in extensions of the AH model in Chapter 3. And we will also analyse the CMB anisotropies that global defects could create in others to compare them with the latest observations of the CMB in Chapter 6.

2.3.4. String Dynamics

As we have seen in the analysis of cosmological evolution, cosmic defects could be created very early in the Universe evolution and they could last until today. Therefore, defect evolution is a difficult problem involving physics from different energy scales. In order to deal with these difficulties, two main techniques have been used: numerical simulations and analytical modelling. On the one hand, field theory numerical simulations resolve the equations of motion of a given defect type, under different levels of approximation, for a period of time. They require a high computational cost and have limited accuracy and a limited evolution time. On the other hand, analytical models are effective models that capture the properties of a network of defects into simpler and more tractable evolution equations for a small number of physically meaningful macroscopic quantities that describe the network. In some sense, analytical models concentrate on the thermodynamics of the network instead of on the details of the dynamics. However, the evolution equations have some phenomenological parameters to be determined by the true microphysics of the system. These two techniques can be complementary. On the one hand, the phenomenological parameters appearing on the analytical models have to be calibrated using numerical simulations. On the other hand, the parameter regions that analytical models show that are interesting, can be analysed using numerical simulations.

Field Theory Numerical Simulations

In this section we will explain the procedure to reproduce cosmic strings in realistic cosmological situation using field theory simulations. We will use the Abelian-Higgs model to give a detailed description, but the theory and the procedures explained can be applied to any other scaling defects.

In the previous Section, when we were analysing the properties of the internal structure of strings we have obtained the equation of motion of the AH model in a spatially flat FLRW cosmology with scale factor a and choosing the temporal gauge $(A_0 = 0)$, see Equation (2.18).

In order to analyse the evolution of string networks in a cosmological evolution the equations of motion (2.18) are solved in a discretized lattice. The discretization procedure that we will use is called the lattice link variable method [85, 102]. This method protects the gauge invariance of the equations and recovers the original equations of motion in the limit where the lattice spacing goes

[2] In some models several high energetic and violent events can also occur due to kinks and cusps in the loops giving bursts of gravitational radiation [32, 41–43, 106, 107, 122]

to zero. In this procedure instead of obtaining the equations of motion and then discretising them, the Hamiltonian of the system is discretised and the discrete equation of motion are obtained from it. So lets analyse the Hamiltonian of the Abelian-Higgs model,

$$\mathcal{H} = \Pi^\dagger\Pi + \frac{1}{2}E^iE_i + \frac{1}{4}F_{ij}F^{ij} + (\mathcal{D}^i\phi)^\dagger(\mathcal{D}_i\phi) + \frac{\beta}{2}(|\phi|-1)^2 + E^i(\partial_i A_0) + iA_0(\Pi^\dagger\phi - \phi\Pi), \quad (2.25)$$

where the conjugate momenta are defined as

$$\Pi = \frac{\partial\mathcal{L}}{\partial(\partial^0\phi^\dagger)} = \mathcal{D}_0\phi, \quad (2.26)$$

$$E^i = \frac{\partial\mathcal{L}}{\partial(\partial^0 A_i)} = F_{0i}. \quad (2.27)$$

In order to discretize the Hamiltonian with a lattice spacing l we define the lattice link operator,

$$U_k(x) = e^{-ilA_k(x)}. \quad (2.28)$$

This operator can be understood as the gauge field in the lattice, that is, it takes the nature of gauge fields as affine connections which parallel transport the scalar fields. The link operators will be valued at links, whereas the scalar fields will take values at grid points. Using the link operator the covariant derivatives can be written as,

$$\mathcal{D}_k\phi = \frac{U_k(x)\phi(x+x_k) - \phi(x)}{l}, \quad (2.29)$$

where $x_k = l\hat{k}$. This covariant derivatives acquires the form of the continuum covariant derivatives when $l \to 0$. Using (2.29) the gradient term in the Hamiltonian, $(|\mathcal{D}_k\phi|^2)$, is gauge invariant under the transformation

$$\phi \to A(x)\phi(x), \quad U_k \to A(x)U_k(x)A^\dagger(x+x_k). \quad (2.30)$$

The lattice link operator can be also used to define the plaquette operators

$$Q_{ij} \equiv U_j(x)U_i(x+x_j)U^\dagger(x+x_i)U^\dagger(x), \quad (2.31)$$

which are also gauge invariant. These plaquette operators are important because the expansion for small lattice spacing l of their real part can be related to the term $F_{ij}F_{ij}$,

$$\begin{aligned} Re(Q_{ij}(x)) = \cos[-l(Y_j(x) + Y_i(x+x_j) - Y_j(x+x_i) - Y_i(x))] \simeq \\ 1 - \frac{l^2}{2}(Y_j(x+x_j) - Y_j(x) - Y_i(x+x_j) - Y_i(x)) \end{aligned} \quad (2.32)$$

$$F_{ij}F_{ij} \sim \frac{2}{l^4}(1 - Re(Q_{ij}(x))) \quad (2.33)$$

With all the ingredients that we have analysed we can write our discrete Hamiltonian,

$$\begin{aligned} \mathcal{H} = \Pi^\dagger\Pi + \frac{1}{2}E^iE_i + \frac{\beta}{2}(|\phi|^2-1)^2 + (\mathcal{D}^i\phi)^\dagger(\mathcal{D}_i\phi) \\ + \frac{1}{2l^4}\sum_{i\neq j}(1 - Re(Q_{ij})) + iA_0(\Pi^\dagger\phi - \phi^\dagger\Pi) + E^i(\partial_i A_0). \end{aligned} \quad (2.34)$$

As we have shown previously in Section 2.3 our gauge choice will be $A_0 = 0$, and then, the equation of motion corresponding to this field is a constraint for the evolution, which is the lattice version of the Gauss' law:

$$\Pi(x)^\dagger\phi(x) - \phi^\dagger(x)\Pi(x) = -i\partial_k E^k = \frac{-i}{l}\sum_k (E^k(x) - E^k(x - x_k)). \tag{2.35}$$

In order to discretize time we will use the staggered leapfrog method. In this method the scalar and gauge fields live at integer time steps, whereas the time derivatives of both will live in half integer time steps. We can illustrate this using an arbitrary function $f(t)$:

$$\dot{f}(t + \frac{1}{2}\delta t) = \frac{1}{\delta t}(f(t + \delta t) - f(t)), \tag{2.36}$$

$$\ddot{f}(t + \delta t) = \frac{1}{\delta t}\Big(\dot{f}(t + \frac{3}{2}\delta t) - \dot{f}(t + \frac{1}{2}\delta t)), \tag{2.37}$$

where δt is the time step, and the updating procedure turns into

$$f(t + \delta t) = f(t) + \delta t\dot{f}(t + \frac{1}{2}\delta t), \tag{2.38}$$

$$\dot{f}(t + \frac{3}{2}\delta t) = \dot{f}(t + \frac{1}{2}\delta t) + ... \tag{2.39}$$

Now we will obtain the equations of motion for a string network in a expanding universe with FLRW metric with comoving cartesian coordinates and conformal time (2.17). To do so we will use the discrete Hamiltonian and the staggered leapfrog method. The equations of motion read as follows,

$$\phi(x, \tau + \delta\tau) = \phi(x, \tau) + \delta\tau\Pi(x, \tau + \frac{1}{2}\delta\tau),$$

$$\begin{aligned}\Pi(x, \tau + \tfrac{3}{2}\delta\tau) = \Big(\tfrac{a_{1/2}}{a_{3/2}}\Big)^2\Pi(x, \tau + \tfrac{1}{2}\delta\tau)\\ -\delta\tau\Big(\tfrac{a^2(\tau)}{a_{1/2}}\Big)^2\beta(\phi^\dagger(x, \tau)\phi(x, \tau) - 1)\phi(x, \tau)\\ +\delta\tau\Big(\tfrac{a}{a_{1/2}}\Big)^2\Big(- \tfrac{6}{l^2}\phi(x, \tau) + \tfrac{1}{l^2}\Big[\textstyle\sum_j U_j(x, \tau)\phi(x + x_j, \tau) + U_j^\dagger(x - x_j, \tau)\phi(x - x_j, \tau)\Big]\Big),\end{aligned}$$

$$A_i(x, \tau + \delta\tau) = A_i(x, \tau) + \delta\tau E^i(x, \tau + \frac{1}{2}\delta\tau),$$

$$\begin{aligned}E^i(x, \tau + \tfrac{3}{2}\delta\tau) = E^i(x, \tau + \tfrac{1}{2}\delta\tau)\\ +\delta\tau\Big(- \tfrac{i}{l}\Big(\phi^\dagger(x, \tau)U_i(x, \tau)\phi(x + x_i, \tau) - \phi^\dagger(x + x_i, \tau)U_i^\dagger(x, \tau)\phi(x, \tau)\Big)\\ +\tfrac{a_{1/2}^2}{l^3}\textstyle\sum_{j\neq i}\Big(ImQ_{ij}(x, \tau) - ImQ_{ij}(x - x_j, \tau)\Big)\Big),\end{aligned} \tag{2.40}$$

where a is the scale factor and $a_{1/2}$ and $a_{3/2}$ represents $a(\tau + 1/2\delta\tau)$ and $a(\tau + 3/2\delta\tau)$.

The process to obtain the field values have to be done simultaneously in all L_N^3 lattice points, where L_N is the number of lattices in each space direction, because in the next time step the information of the neighbouring points is necessary in order to solve the spatial derivatives appearing in the equations for the canonical momentum.

The requirement of solving the equations simultaneously in all lattice points implies a huge computational cost. In order to be able to perform simulations big enough to obtain reliable information they have to be parallelized, that is, we have to divide our simulation is small boxes and evolve all of them simultaneously in different processors, but always sharing information of the points in the boundaries of the small boxes. In our case the simulations are parallelized using the LatField2 library for parallel field theory simulations [44], which is based on C++.

The simulation boxes that we use have periodic boundary conditions and one have to notice that there is an upper limit on the time that the system can be evolved before it feels the effects of the periodic boundary conditions. The simulation can only be believed up to half light-crossing time, i.e., if we sent a light ray in opposite directions in the box, the simulation is accurate up to when the two rays meet again. Therefore, there is a clear compromise when choosing the values for the space (Δx) and time (Δt) discretization in the lattice: finer lattice discretization would mean that the solution is more accurate, at the expense of having a smaller dynamical range; whereas if the discretization is coarser, the dynamical range increases, but the equations are not solved accurately enough.

Another subtlety that one can find on the simulations is that the width of the string is a physical constant. So in a simulation box where the physical coordinates are expanding the string width can become very small and the lattice may not be able to resolve it. In order to be able to resolve the string width throughout the whole simulation, we can modify the equation of motion so that the physical width grows. This modification, called the Press-Ryden-Spergel algorithm [115], is obtained by making the coupling constants time dependent in the following form,

$$\lambda = \frac{\lambda_0}{a^{2(1-s)}}, \quad e = \frac{e_0}{a^{(1-s)}}, \tag{2.41}$$

where s is the core growth parameter. Using these expresions the equations of motion (2.18) take the following form

$$\ddot{\phi} + 2\frac{\dot{a}}{a}\dot{\phi} - \mathcal{D}_j\mathcal{D}_j\phi = -a^{2s}\frac{\lambda_0}{2}(|\phi|^2 - \eta^2)\phi, \tag{2.42}$$

$$\dot{F}_{0j} + 2(1-s)\frac{\dot{a}}{a}F_{0j} - \partial_i F_{ij} = -2a^{2s}e_0^2 Im(\phi^*\mathcal{D}_j\phi). \tag{2.43}$$

These equations preserve Gauss's law and one can see that when $s = 1$ we obtain the true field equations. If $s < 1$ the physical width of the string is growing and when $s = 0$ the string width is constant in comoving coordinates. Previous works using the algorithm [31, 45, 95, 101] prove its validity.

As in many field theoretical simulations of defect dynamics the initial conditions are unknown. It would be very hard to simulate the phase transition leading to the formation of the defects, and in many cases it would not be clear which model to adopt as the underlying phase transition model. However, this is not the goal in our case; instead, our aim is to study the asymptotic behaviour of these networks. As we have seen previously the key property for the study of this asymptotic behaviour is scaling. Therefore, it is desirable that our simulations reach scaling as fast as possible. Once scaling is reached the system forgets its initial configuration, therefore, the only importance of the initial configuration is to drive the system to scaling as fast as possible. This way we would have a long dynamical range and we could estimate more accurately the cosmic defect network properties. But the early phases of the simulations contain a huge amount of excess energy induced by the random initial conditions, therefore the field distribution has to be smoothed using a diffusive evolution, with the second derivatives removed from the equations of motion, or introducing a high damping term.

In Fig. 2.7 we show a snapshop of a typical simulation of the AH case.

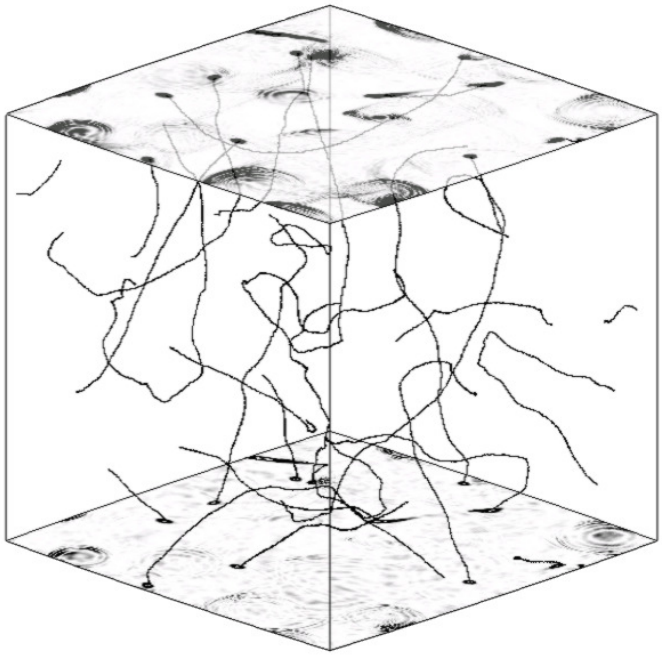

Figure 2.7.: *Typical simulation box of AH network. Picture courtesy of N. Bevis [29]*

Analytical Models:VOS

The first analytical study of topological defects networks was made by Kibble [83]. In the Kibble model, known as 'one-scale' model, the evolution of long-string segments is described using a single meaningful macroscopic quantity, a length-scale which is usually called the 'correlation length'. Solutions for this model were the first ones showing the existence and stability of scaling solutions, subject to conditions on the loop production mechanism, which would be later confirmed by numerical simulations of string network evolutions [16, 25]. In particular, these numerical simulations showed that small scale structure takes a crucial role in the network dynamics. Simulations revealed the existence of a significant amount of small-scale structure on long strings, with loops being predominantly produced at the smallest scales that can be sampled numerically.

Due to these findings Austin, Copeland and Kibble developed a model [20] in order to account for small-scale structure. This model made use of three different length scales: the length-scale used by Kibble, which can be understood as the inter-defect distance; a length-scale which explicitly describes the small structure and a length-scale which introduces the effects of gravitational radiation.

After all these attempts to build a model to describe the evolution of string networks, Martins and Shellard realised that it would be relevant to take into account frictional forces due to particle-string scattering, which are important for some time after the string-forming phase transition. The model proposed by them, known as 'velocity-dependent one-scale' (VOS) model [98, 99, 101], is a simple generalisation of the 'one-scale' model where the average root mean square (RMS) velocity of the string becomes a dynamical variable. The description of the evolution of cosmic string networks that can be obtained using this model is a fully quantitative description of the complete evolution in the early universe.

Let us describe the VOS model for the Abelian-Higgs case presented in [101]. We will start by considering that the network of strings is evolving in $(3+1)$ space-time dimensions with RMS velocity v and that they are non-interacting. Then the momentum per unit length of the strings can be written as

$$p \propto a^{-1} \Rightarrow v\gamma \propto a^{-2}, \tag{2.44}$$

from which we get by differentiation

$$\frac{dv}{dt} + 2H(1-v^2)v = 0. \tag{2.45}$$

Under the above hypotheses, the average number of defects in a fixed comoving volume should be conserved, which implies

$$\rho \propto \gamma a^{-2}, \tag{2.46}$$

and again, differentiating and using the velocity equation, we get

$$\frac{d\rho}{dt} + 2H(1+v^2)\rho = 0. \tag{2.47}$$

The hypotheses made to obtain the equations above are a bit unrealistic but we can use them as the starting point to build the VOS model for the AH networks. The main property describing a network of defects is its characteristic length. Let us start by defining a characteristic length scale for the AH case using the string mass per unit length, μ, as

$$L^2 = \frac{\mu}{\rho}. \tag{2.48}$$

The equations we have obtained above do not count for the energy loss, and as we have seen in Section 2.3.2 it is necessary for the system to achieve the scaling regime. We said that long strings can intersect and produce loops, so in order to describe correctly the evolution of the network, the energy loss due to the loop production has to be taken into account. This process is ensured by a phenomenological term which characterises the loop production as

$$\left(\frac{d\rho}{dt}\right)_{\text{to loops}} = -cv\frac{\rho}{L}, \tag{2.49}$$

where c is the loop chopping efficiency parameter and v is RMS velocity of the string network. The parameter c is expected to remain constant irrespective of the cosmic regime, because it is multiplied by factors which determine the string network self-interaction rate. Its value has to be determined using field theory simulations.

Defects will be slowed down by friction due to particle scattering. This can be characterized by a friction length scale

$$l_f \equiv \frac{\mu}{\theta T^3} \propto a^3, \tag{2.50}$$

where θ is a parameter counting the number of particle species (or degrees of freedom) interacting with the defect.

We can also define an overall damping length which includes both the effect of Hubble damping and that of friction due to particle scattering

$$\frac{1}{l_d} = 2H + \frac{1}{l_f}. \tag{2.51}$$

It is important to compare the relative importance of the two effects. Since the friction length scale will in most circumstances grow faster than the Hubble length, it is expected that friction will be dominant at early times, while Hubble damping will dominate at sufficiently late times.

Putting together all of the above effects, we find the following evolution equation for the characteristic length scale L and RMS velocity v

$$2\frac{dL}{dt} = 2HL + v^2\frac{L}{l_d} + cv, \tag{2.52}$$

$$\frac{dv}{dt} = (1-v^2)\Big(f - \frac{v}{l_d}\Big), \tag{2.53}$$

where in the latter we have included, with the f term, the possibility of further driving forces affecting the defect dynamics. Note that f has the units of acceleration, i.e., it is force per unit mass. For strings this driving force is the local curvature, and we have

$$f \sim \frac{k}{L}. \tag{2.54}$$

We are implicitly assuming that our characteristic length scale is the same as the defect curvature radius. The factor k is another phenomenological parameter that has to be calibrated using numerical simulations.

2.3.5. CMB: UETC approach

As we have shown in Section 1.6 the CMB analysis is a good way to analyse the properties and constituents of the early universe. In order to study the role of cosmic defects in the universe this CMB analysis is also useful. As we have seen, the evolution of cosmic defect networks perturbs the background space-time, and those perturbations evolve and affect the contents of the universe, eventually creating CMB anisotropies. In contrast to the inflationary perturbations, which were seeded primordially, and then evolved passively, defects induce perturbations actively during their whole existence.

In the Section 1.6 we have shown that the CMB analysis is made through two-point correlation functions, and that in order to determine the defect contribution to those correlation functions we are required to solve a set of linear differential equations in which the defect energy momentum tensor components act as source terms $\tilde{S}_a$:

$$\mathcal{D}_{ac}(k, a, \rho, ...)\tilde{X}_a(\mathbf{k}, \tau) = \tilde{S}_c(\mathbf{k}.\tau). \tag{2.55}$$

In the equation above $\tilde{X}_a$ is the Fourier transform of the quantity of interest X_a and it is written in terms of the conformal time τ and the comoving wavevector $\mathbf{k}$. $\hat{\mathcal{D}}_{ac}$ is a differential operator that depends on the cosmology. The equation (2.55) cannot be solved analytically and Eintein-Boltzman solvers, such as CMBeasy [49], have to be used. These solvers give a power spectrum that can be compared with the measured one by "cosmological experiments", such as Planck [10].

The power spectrum at conformal time τ_0 for defects can be described by Green's function $\mathcal{G}_{ac}(\mathbf{k}, \tau_0, \tau)$ as :

$$\langle \tilde{X}_a(\mathbf{k}, \tau_0)\tilde{X}^*_b(\mathbf{k}, \tau_0)\rangle = \int_0^{\tau_0}\int_0^{\tau_0} d\tau d\tau' \mathcal{G}_{ac}(k, \tau_0, \tau)\mathcal{G}^*_{bd}(k, \tau_0, \tau') \times \langle \tilde{S}_c(\mathbf{k}, \tau)\tilde{S}^*_d(\mathbf{k}, \tau')\rangle. \tag{2.56}$$

In the expression above, we can see clearly that the data required to calculate such two-point

correlation functions is the source term, which is strictly related to Unequal Time Correlators (UETC). The UETCs of the energy momentum tensor are defined as follows:

$$U_{\lambda\kappa\mu\nu}(\mathbf{k},\tau,\tau') = \langle \mathcal{T}_{\lambda\kappa}(\mathbf{k},\tau)\mathcal{T}^*_{\mu\nu}(\mathbf{k},\tau)\rangle, \tag{2.57}$$

where $\mathcal{T}_{\alpha\beta}(\mathbf{k},\tau)$ is the energy momentum tensor of the defect.

In principle, considering all possible degrees of freedom of the energy momentun tensor, there seem to be $\frac{1}{2}10(10+1) = 55$ such correlators that would be functions of 5 variables, 3 components of $\mathbf{k}$ and two times. Fortunately, rotational symmetry simplifies the problem considerably and reduces the UETC group to 5 independent correlators (three scalar, one vector and one tensor) that depend on 3 variables: the magnitude of $\mathbf{k}$ (k) and two times (τ and τ').

The relation between the source term $\tilde{S}_a$ and the energy-momentum tensor $\mathcal{T}_{\mu\nu}$, that we anticipated, is,

$$\tilde{S}_a(\mathbf{k},t) = P_a^{\mu\nu}(\mathbf{k})\mathcal{T}_{\mu\nu}(\mathbf{k},\tau'), \tag{2.58}$$

where $P_a^{\mu\nu}(\mathbf{k})$ project onto scalar, vector and tensor parts. In principle there are two of each, but the two vector components are related by parity for symmetric sources like cosmic defects, as well as the two tensor components. Hence, we may consider that the indices a and b take four values corresponding to the independent components of the energy momentum tensor: two scalar, one vector and one tensor. We will denote scalar indices 1 and 2 (corresponding to the longitudinal gauge potentials ϕ and ψ), the vector component with 'v' and the tensor component with 't'.

Thus we can write

$$U_{ab}(\mathbf{k},\tau,\tau') = \frac{\eta^4}{\sqrt{\tau\tau'}}\frac{1}{V}C_{ab}(k,\tau,\tau'), \tag{2.59}$$

where η is the symmetry breaking scale, V a formal comoving volume factor, and the functions $C_{ab}(k,\tau,\tau')$ defined by this equation are dimensionless. Note that the scalar, vector and tensor contributions are decoupled for linearised cosmological perturbations, and therefore cross correlators between them vanish, except in the scalar sector: hence the 5 independent correlators.

A further simplification occurs when the times τ and τ' are both in epochs during which the scale factor grows with the same constant power of conformal time, this is when they are in scaling. In this case the correlation functions do not depend on k, τ and τ' separately, but only on $x, x' = k\tau, k\tau'$. Scaling correlators can be written

$$U_{ab}(\mathbf{k},\tau,\tau') = \frac{\eta^4}{\sqrt{\tau\tau'}}\frac{1}{V}\bar{C}_{ab}(k\tau,k\tau'). \tag{2.60}$$

Here, the overbar represents the scaling form of the UETC in a FLRW background. We will sometimes write $z = k\sqrt{\tau\tau'}$, $r = \tau'/\tau$. During scaling UETCs will depend on k and τ only through the combination x.

In order to insert the UETCs as a source of perturbations into an EB solver we need to take a "square root" of the UETCs as the EB solvers evolve the perturbation variables, not their power spectra. To this end the UETCs, which are real and symmetric, can be decomposed into their eigenfunctions $c_n(k,\tau)$ defined through

$$\int_{\tau_i}^{\tau_0} d\tau' \bar{C}_{ab}(k\tau,k\tau')c_b^n(k,\tau') = \lambda_n c_a^n(k,\tau). \tag{2.61}$$

The scaling UETC is recovered through the sum

$$\bar{C}_{ab}(k\tau, k\tau') = \sum_n \lambda_n c_a^n(k,\tau) c_b^{n*}(k,\tau'). \tag{2.62}$$

Using the eigenfunctions and eigeinvalues the power spectra and cross-correlators of a perturbation in a cosmological variable X_a can be written as

$$\langle \tilde{X}_a(\mathbf{k},\tau)\tilde{X}_b^*(\mathbf{k},\tau')\rangle = \frac{\eta^4}{V}\sum_n \lambda_n I_a^n(k,\tau) I_b^{n*}(k,\tau'), \tag{2.63}$$

where

$$I_a^n(k,\tau_0) = \int_0^{\tau_0} d\tau \mathcal{G}_{ab}(k,\tau_0,\tau)\frac{c_{nb}(k,\tau)}{\sqrt{\tau}}. \tag{2.64}$$

In practice we do not calculate this integral via Green's function; instead we apply a Einstein-Boltzmann integrator, which in our case it is CMBeasy. The power spectrum can then be constructed as the superposition of the results of integrating the source function,

$$s_{an}(k,\tau) = \sqrt{\lambda_n(k)} c_{an}(k,\tau). \tag{2.65}$$

The total power spectra is reconstructed by taking the sum of the power spectra obtained for each source function:

$$C_l^{Tot} = \sum_n \lambda_n^S C_{l,n}^S + \sum_n \lambda_n^V C_{l,n}^V + \sum_n \lambda_n^T C_{l,n}^T. \tag{2.66}$$

However, it should be noted that the above discussion requires a small change because scaling is broken near the time of radiation-matter equality τ_{eq}, since τ_{eq} is a second dimensional scale which enters the problem. We are required to take the UETC data in both the radiation and matter eras, although the matter era data dominates the CMB results, and we then use interpolation in order to model the transition.

Ideally, in order to compare the data obtained from the defects with the observed one, we will expand the parameter space of the cosmological standard model and add a seventh parameter related with the string contribution. Then using a Monte Carlo Markov Chain (MCMC) analysis [91] we will estimate the best value of those parameters. In order to do this, we will have to solve the equation (2.55) for every different choice of the parameters describing the cosmological evolution which is time and computationally very consuming. But as we have anticipated in Chapter 1 the contribution of the strings to the measured CMB spectra is subdominant and it can be treated as perturbations of the theory. Instead of solving the EB for each different choice of the seven parameters, we will solve it for the best values of the six parameters given by Planck, see Chapter 1. Once we have the power spectra for the contribution of the defects we will use the MCMC to obtain the best fit for the seven parameters, where the seventh one is the amplitude of the power spectra of the defect contribution. All in all, using this approach we will solve the EB for defects just once and then we will assume that the shape of the defect power spectra will not change and that the unique difference will be the amplitude of it. In Chapter 6 we use this approach to obtain the contribution of the global O(N) defects to the CMB.

2.4. Defect models relevant for the Thesis

Now we will describe the defect models that we will use in Part II of this Thesis, using the description of the AH string properties from this Chapter.

2.4.1. Global O(N) Defects

In this section we will analyse a model with a global symmetry O(N) where the defects are created when the global O(N) symmetry spontaneously broke down to O(N-1). The simplest Lagrangian that gives rise to these kind of defects is the following one,

$$\mathcal{L} = \frac{1}{2}\partial_\mu \Phi^i \partial^\mu \Phi^i - \frac{1}{4}\lambda(|\Phi|^2 - \eta^2)^2, \tag{2.67}$$

where $|\Phi^i| \equiv \sqrt{\Phi^i \Phi^i}$ and λ and η are real constant parameters. Φ^i, where $i = 1, ..., N$ are real fields. The potential of the model, the last term in the Lagrangian, is similar to the potential term in the Goldstone model, but depending on the number of real fields N the dimensions of that potential are different and the defect type formed will be different too. For example the $N = 2$ case is the Goldstone model presented in Section 2.2.

During this Thesis we will analyse two kinds of Global O(N) defects; global cosmic strings $N = 2$ and global monopoles $N = 3$:

O(2) Global Strings

This model is the one we have used to describe the spontaneous symmetry breaking in Section 2.2. The massless particle that has appeared in the symmetry breaking is responsible for the large range interactions that global strings have. In contrast to the Abelian-Higgs case and due to the long range interactions, the total energy of the strings is not confined to a finite region and the energy density diverges when moving away from the center of the string. Although this could lead to think that the energy density of global strings could rapidly dominate over the energy of the universe that is not the case. The presence of other defects creates a cut off in the divergent energy density and the network of global strings acquires the scaling regime.

Due to the different evolution of global strings compared with the Abelian-Higgs ones, we use field theory simulations of the global string model to analyse the CMB contribution of global strings for the first time. In Chapter 6 we obtain this contribution using the procedure we described in Section 2.3.5.

O(3) Global Monopoles

When $N = 3$ we have a Global Monopole model. The model has a global $O(3)$ symmetry spontaneously broken down to $O(2)$. The set of ground states is the two sphere $|\Phi| = \eta$ and, since $\pi_2(S^2) = \mathbf{Z}$, there are field configurations with non-trivial topological charge. For example, a global monopole of unit topological charge can be described by the "hedgehog" configuration $\phi^i = \phi(r)\hat{x}^i$, where $\hat{x}^i$ is a radial unit vector and outside the monopole core $\phi(r) \approx \eta$, which can be seen in Fig. 2.8.

The analysis of the broken vacua leads to two Goldstone bosons and one scalar excitation with $m_s = \sqrt{2\lambda}\eta$. Due to the presence of the Goldstone bosons the energy of a monopole is divergent with radius but in a cosmological situation this divergence is not catastrophic, since there is always

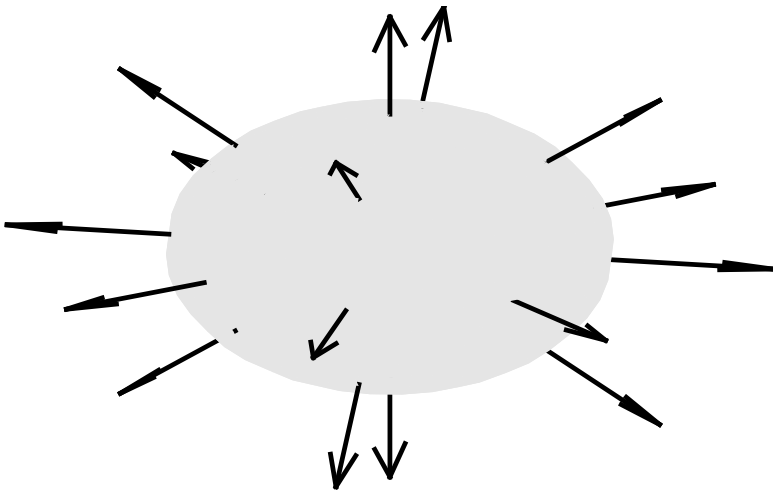

Figure 2.8.: *Hedgehog field configuration of a monpole.*

an antimonopole around that cuts-off the energy divergence. However, the force between a well-separated monopole and anti-monopole is approximately independent of their distance [111]. For example, simulations often show how a monopole-antimonopole pair that are nearby 'repel' each other, since they have found another partner to annihilate with somewhere else.

In the study of the stability of the global monopoles it was shown that if the core of the monopoles was artificially fixed, they were unstable towards concentrating all the gradient energy in the, say, north pole, and then decaying into the vacuum [57], pointing towards an instability[3]. However, if the core of the monopole is free to move, it was argued in [118] that the core would move upwards so as to compensate the increase of the concentration of gradients in the north pole, and therefore there is no instability, just the translation of the monopole core.

In the monopole case we can also see a different evolution compared with the Abelian-Higgs case. Therefore, we also use field theory simulations of the global monopole model to analyse the CMB contribution of global monopoles for the first time. This analysis is also done in Chapter 6, where the contribution is obtained using the procedure we described in Section 2.3.5.

Moreover, the analysis of the evolution of the global defects can be made also using VOS types models. The model for global monopoles was firstly presented in [97] where the equations for the length scale, L, and the RMS velocity, v, were obtained using a similar procedure as the one we have presented in Section 2.3.4. In this case the the velocity and the density will depend on the scale factor as

$$v\gamma \propto a^{-1} \quad \rho \propto \gamma a^{-3} \tag{2.68}$$

and the characteristic length scale is defined using the mass of the monopoles as

$$L^3 = \frac{M}{\rho}. \tag{2.69}$$

Using the same procedure as in Section 2.3.4 the characteristic length scale, L, and the RMS

[3]Global monopoles were proven to be stable to axisymmetric normalizable perturbations [3], though (surprisingly) the energy barrier between different cosmic defects is *finite*.

velocity, v, are described by the following equations,

$$3\frac{dL}{dt} = 3HL + v^2\frac{L}{l_d} + cv, \tag{2.70}$$

$$\frac{dv}{dt} = (1-v^2)\Big[\frac{k}{L}\Big(\frac{L}{d_H}\Big)^{3/2} - \frac{v}{l_d}\Big]. \tag{2.71}$$

The parameters H and d_H are the Hubble parameter and the Hubble horizon size, and t is the physical time. As in the local string case, the overall damping length which includes both the effect of Hubble damping and of friction due to particle scattering is parametrised by l_d, and c and k are the parameters governing the phenomenological terms, which have to be calibrated using numerical simulations.

In the case of global monopoles, the term involving c is associated with energy losses from monopole-antimonopole annihilation; in some sense, it depends on short distance physics. The term involving k is the acceleration due to the forces among monopoles. These forces are approximately independent of distance but, because global monopoles have linearly divergent gradient energy, the "mass" at a given scale L grows linearly with L. The resulting acceleration term is of the form $\sim k/L$, and is corrected by a $1/\sqrt{\mathcal{N}}$ factor to account for the combined effect of interactions with multiple monopoles. In [97] the authors considered how sensitive the solutions are to the modelling of the parameters, and found that the final characterization of the network is much more dependent on details of the term involving k than those of the term involving c.

This analytical model has two different solution branches; one for luminal velocities and the other one for subluminal velocities. In the literature one can find the first attempt to estimate the velocities of global monopoles, which is done by Yamaguchi [139]. The averaged values for the global monopoles velocities in radiation- and matter-dominated eras given by Yamaguchi are $v_r = 1.0 \pm 0.3$ and $v_m = 0.8 \pm 0.3$, respectively. The method used in that work had a rather large error, big enough that one cannot determine if the velocities were luminal or subluminal. To determine whether the velocities of the global monopoles are luminal or subluminal is of great interest for the determination of the VOS model solution branch. Due to this interest, in Chapter 4 we perform numerical simulations, following the procedure described in Section 2.3.4, for global monopoles and using a nobel method to measure velocities we present more precise values of the velocities.

As we have said, the parameters c and k governing the phenomenological terms have to be calibrated by numerical simulations. The first attempt to calibrate those parameters was done in [97] but that time it was not clear if the velocities of the monopoles were luminal or subluminal. So after our precise measurement of the global monopole velocities we will use the data obtained from the numerical simulations to calibrate the VOS model for global monopoles also in Chapter 4.

2.4.2. Extensions of AH

Semilocal Strings

Semilocal strings [4, 66, 129] were introduced as a minimal extension of the Abelian Higgs model with two complex scalar fields—instead of just one—that make an $SU(2)$ doublet. This leads to $U(1)$ flux-tube solutions even though the vacuum manifold is simply connected. The strings of this extended model have some similarities with ordinary local $U(1)$ strings, but they are not purely topological and will therefore have different properties. For example, since they are not topological, they need not be closed or infinite, and can have ends. These ends are effectively

global monopoles (that we have just analysed) and they can make the segments grow or shrink.

The relevant Lagrangian for the simplest semilocal string model, the one we will use during this thesis, reads

$$\mathcal{L} = (\mathcal{D}_\mu \Phi)^* (\mathcal{D}^\mu \Phi) - \frac{1}{4} F_{\mu\nu} F^{\mu\nu} - \frac{\lambda}{4} (\Phi^\dagger \Phi - \eta^2)^2, \tag{2.72}$$

where $\Phi = (\phi_1, \phi_2)$ and $F_{\mu\nu} = (\partial_\mu A_\nu - \partial_\nu A_\mu)$ is the gauge field strength. The covariant derivatives are given as $\mathcal{D}_\mu = \partial_\mu - ieA_\mu$. It can be easily seen that when setting one of the two scalar fields to zero, we recover the Abelian Higgs model (2.11).

The symmetry breaking pattern that leads to the formation of strings in this model is $SU(2)_{\text{global}} \times U(1)_{\text{local}} \to U(1)_{\text{global}}$ so this model can be thought of as a particular limit of the Glashow-Weinberg-Salam electroweak model in which the SU(2) symmetry is global, i.e. the Weinberg angle is $\cos\theta_W = 0$ and there are no SU(2) gauge fields. The vacuum manifold is the three sphere, so one would not expect strings to form if the dynamics is dominated by the potential energy. On the other hand, the magnetic field is massive and magnetic flux is conserved, which would suggest the existence of magnetic flux tubes when the magnetic mass is large.

The stability of the strings is not trivial, and it will depend on the value of the parameter $\beta = \lambda/2e^2$: for $\beta < 1$ the network is stable, for $\beta > 1$ it is unstable, and for $\beta = 1$ it is neutrally stable [66, 129]. The $\beta = 1$ limit is known as the Bogomoln'yi limit. It is shown in [66] that in this limit, the model has a zero mode, i.e. a uniparametric family of solutions with the same total energy. Although the total energy is the same, the value of the parameter related with the zero mode will change the distribution of the energy density. As we have shown in Section 2.3.3 the gravitational properties of defects are of great interest, and it is known also that gravity is a local property. Taking everything into account one can realize that the analysis of the gravity coupling of this model will be interesting. Therefore, in Chapter 3 after showing more precisely the presence of the zero modes in the semilocal model, we coupled it minimally to gravity in order to analyse the solutions.

Theoretical expectations, confirmed by numerical simulations, indicate that the dynamics of semilocal string segments are different from those of local strings [4, 27]. While some segments disappear, there is also a significant probability that segments merge and form longer segments. This is due to the long range interactions of global monopoles at the end of the segments. As we have pointed out in Section 2.3.4 the evolution of networks can be made in a simpler and more tractable way by using analytical models of VOS type. In a recent paper [104] two different analytical models describing the evolution of semilocal strings were presented.

These models focus on the behavior of the network as a whole, starting from the premise that the semilocal network can be treated as a network of local strings attached to global monopoles. Therefore previously analysed VOS models in Sections 2.3.4 and 2.4.1 for each of these cases can be applied, with suitable changes, to this case. The models for the evolution of these networks are based on explicitly modelling the dynamics and interactions of the monopoles. This is justified since (as has been shown in work [8]) it is indeed the monopoles that control the evolution of the network. The VOS model that capture the nature of the semilocal string networks can be described by the following equations

$$\frac{dl_s}{dt} = Hl_s - v_s^2 \frac{l_s}{l_d}, \quad \frac{dv_s}{dt} = (1 - v_s^2)\Big[\frac{k}{l_s} - \frac{v_s}{l_d}\Big], \tag{2.73}$$

where l_s is the length of the segment under consideration, v_s is the root mean square (RMS) velocity, k a free parameter describing string curvature (to be calibrated), H the Hubble parameter and l_d is the string damping length. Then those equations are modified in two possible

phenomenological ways:

Scale-dependent Behaviour:

A simple generalisation of the equations (2.73) would be

$$\frac{dl_s}{dt} = Hl_s - v_s^2\frac{l_s}{l_d} + \sigma\Big(1 - \frac{L}{l_s}\Big)v_m^2, \qquad \frac{dv_s}{dt} = (1-v_s^2)\Big[\frac{k}{l_s} - \frac{v_s}{l_d}\Big], \tag{2.74}$$

where L is the characteristic scale of the monopoles, σ is a free parameter controlling the importance of the newly introduced term and v_m is the velocity of the string ends (monopoles). The new term was added on phenomenological reasoning that, to a first approximation, small segments should shrink and large ones should grow and merge [67]. This can be intuited as a competition between two characteristic timescales. Each segment will have an annihilation timescale, and each monopole will have a characteristic timescale in which to find its (anti)partner and annihilate, thereby producing a longer segment. The second process is expected to become relatively more likely as the segment size increases.

Balance Equation:

The following modification for the evolution equations is considered

$$\frac{dl_s}{dt} = Hl_s - v_s^2\frac{l_s}{l_d} + dv_s\Big(\frac{l_s}{L} - 1\Big), \qquad \frac{dv_s}{dt} = (1-v_s^2)\Big[\frac{k}{l_s} - \frac{v_s}{l_d}\Big]. \tag{2.75}$$

In these we are assuming that the network of string segments has a Brownian distribution, something that can be tested in numerical simulations. The new term (including new free parameter, d) accounts for the probability that different segments intersect, which depends both on the length/number density and velocity of the segments.

Therefore, there are two different models proposed to describe the evolution of the semilocal strings networks, and in addition, each one of the models has two parameters to be calibrated using numerical simulations. In Chapter 5 we will show how we characterize the main properties of the semilocal strings networks, such as the segment length, the segment velocity or the velocity of string ends (where we implement what we have learnt from the monopole case), using field theory simulations that we construct using the procedure we have described in Section 2.3.4. In a future work we will use the data obtained from these simulations to calibrate the parameters governing the phenomenological terms in the analytical models and also to specify which one of the models describe the semilocal network evolution better.

Axionic strings

The model in question is a supersymmetric Abelian-Higgs model with a D-term potential coupled to an axion-dilaton multiplet [114, 138]. However, axionic strings [33] arise in the low energy effective theory of this supersymmetric model. The strings in question are axionic D-term strings which are identified with the D-strings of type II string theory. The study of the original model is beyond the scope of this work and we start our analysis from the bosonic part of the action of the effective theory, that is,

$$\mathcal{L}^A = -|\mathcal{D}_\mu\phi|^2 - K_{S\bar{S}}|\mathcal{D}_\mu S|^2 - \frac{1}{4}e^{-2}F^{\mu\nu}F_{\mu\nu} - \frac{1}{2}e^2(\xi + 2\delta K_S - q|\phi|^2)^2, \tag{2.76}$$

where ϕ is the tachyonic field and $S = s + ia$ where s is the dilaton and a the axion. The model depends on three continuous parameters: the gauge coupling e, the charge of the axio-dilaton δ, and ξ which determines the expectation value of the fields. K represents the Kähler potential

and K_S and $K_{S\bar{S}}$ the derivatives of the Kähler potential with respect to the fields S and $\bar{S}$. The choice of the Kähler potential in this case is

$$K = -M_p^2 \log(S+\bar{S}), \quad K_S = -M_p^2 \frac{1}{S+\bar{S}}, \quad K_{S\bar{S}} = M_p^2 \frac{1}{(S+\bar{S})^2}. \tag{2.77}$$

The covariant derivatives in this case take the form,

$$\mathcal{D}_\mu \phi = \partial_\mu \phi - iqA_\mu \phi, \quad \mathcal{D}_\mu S = \partial_\mu S - 2i\delta A_\mu, \tag{2.78}$$

where q is an integer which represents the $U(1)$ charge of the tachyon. The associated Abelian field strength is $F_{\mu\nu} = \partial_\mu A_\nu - \partial_\nu A_\mu$. Taking all this into account our Lagrangian takes the form,

$$\mathcal{L} = -|\mathcal{D}_\mu \phi|^2 - \frac{M_p^2}{(S+\bar{S})^2}|\mathcal{D}_\mu S|^2 - \frac{1}{4e^2}F^{\mu\nu}F_{\mu\nu} - \frac{1}{2}e^2(q|\phi|^2 + 2\delta \frac{M_p^2}{(S+\bar{S})} - \xi)^2. \tag{2.79}$$

Depending on the field that winds giving rise to trapped magnetic flux, this model can accommodate three different kind of strings:

- ϕ-strings (tachyonic strings): The tachyon field winds.
- s-strings (axionic strings): The axio-dilaton winds.
- Hybrid: Both fields wind.

One can see that the above Lagrangian (3.23) is similar to the semilocal model Lagrangian (2.72). Axionic strings, as well as the semilocal strings in the limit $\beta = 1$, have a uniparametric family of solutions with the same energy, so the analysis of the survival of the zero mode after coupling the model to gravity will be of great interest. However, there is a main difference between them; in the semilocal case, both fields are the same type but in the axionic case they are different. This is the reason for having three different string types. This difference will create some different behaviours on the properties of strings arising form the both models, but in general the behaviour will be very similar. The analysis of the survival of the zero modes as well as the comparison between the models is made in Chapter 3.

PART II

Results

3 Gravitating Cosmic Strings with Flat Directions

As we have seen in Chapter 2, the analysis of the gravitational properties of defects is of great interest. We have pointed out that the effects created by the gravitational properties of defects are characterized by the dimensionless parameter $G\mu$. Moreover, the parameter μ contains information about the energy scale of the symmetry breaking and, therefore, the determination of $G\mu$ will help in the analysis of the connection between high energy physics and cosmology.

We have also seen that defect models with flat directions exist: these kind of models admit a uniparametric family of solutions with the same energy which is directly related with the zero mode. In this Chapter, we study field theoretical models for cosmic strings with flat directions in curved space-time. More precisely, we consider minimal models with semilocal, axionic and tachyonic strings, respectively. In flat space-time, isolated static and straight cosmic strings solutions of these models have a flat direction. We analyse the survival of these zero modes, and study the role of the flat direction, when coupling the string to gravity. Even though the total energy of the solution is the same, and thus the global properties of the family of solutions remain unchanged, the energy density, and therefore the gravitational properties, will be different.

The Chapter is structured as follows: in Section 3.1 we describe the models in flat space-time and we analyse their flat directions. Then in Section 3.2 we minimally couple the models to gravity and we obtain the equations of motion. Finally, in Section 3.3 we discuss the numerical results obtained solving the equations of motion and conclude in Section 3.4.

3.1. The Models and Their Flat Directions

In this section we will introduce our models, and we will analyse their static straight string configurations without coupling the model to gravity in order to show their main characteristics, specially the existence of families of configurations with the same energy.

The action for matter configurations in flat space-time reads,

$$S = \int d^4x \sqrt{-\det g}\mathcal{L}_m, \tag{3.1}$$

where g is the metric consistent with static cylindrically symmetric configurations invariant under boosts along the axis of symmetry which, without loss of generality, we can choose to be the z-axis. The line element consistent with these symmetries that we will use is:

$$ds^2 = -dt^2 + dr^2 + r^2 d\theta^2 + dz^2, \tag{3.2}$$

where (r, θ, z) are cylindrical coordinates.

As we have mentioned before, we will study two types of matter Lagragians $\mathcal{L}_m$ with zero modes: the semilocal model [4, 129] and the axionic D-term model [33], both presented in Section 2.4.2. It is known that for stationary field configurations with a translational symmetry along the z-axis, the definition of energy per unit length is the following:

$$E = \int d^2x \sqrt{-\det g} T_0^0, \tag{3.3}$$

where T_0^0 is the 00 component of the energy-momentum tensor defined as

$$T_{\mu\nu} = -2\frac{\partial \mathcal{L}_m}{\partial g^{\mu\nu}} + g_{\mu\nu}\mathcal{L}_m. \tag{3.4}$$

Taking this into account, the energy (3.3) can be expressed as,

$$E = -\int \mathrm{drd}\theta \mathrm{r}\mathcal{L}_{\mathrm{m}}. \tag{3.5}$$

3.1.1. Semilocal Strings

In this Chapter we will analyse the semilocal model that we have presented in Section 2.4.2, which is described by the Lagrangian (2.72):

$$\mathcal{L}_m^{SL} = -|\mathcal{D}_\mu \Phi|^2 - \frac{1}{4}F_{\mu\nu}F^{\mu\nu} - \frac{\lambda}{2}(|\Phi|^2 - \eta^2)^2, \tag{3.6}$$

where $\Phi = (\phi_1, \phi_2)^T$ and $\phi_1, \phi_2 \in \mathbb{C}$. $\mathcal{D}_\mu = \partial_\mu - ieA_\mu$, $F_{\mu\nu} = \partial_\mu A_\nu - \partial_\nu A_\mu$ and A_μ is an Abelian $U(1)$ gauge field. The parameter η gives the symmetry breaking scale, e denotes the gauge coupling, and λ the self-coupling. As we have mentioned in Chapter 2, it is convenient to reduce the number of parameters governing the model, in order to obtain meaningful information about them. To do so we can use the following rescaling:

$$r = \frac{\hat{r}}{\eta e}, \quad A_\mu = \eta \hat{A}_\mu, \quad \Phi = \eta\hat{\Phi}. \tag{3.7}$$

This rescaling reveals that the only significant parameter in the model is the ratio of the Higgs and vector masses, $\beta \equiv m_s^2/m_v^2 = \lambda/2e^2$ (see Section 2.4.2):

$$\frac{\mathcal{L}_m^{SL}}{\eta^4 e^2} = -|\mathcal{D}_\mu \Phi|^2 - \frac{1}{4}F_{\mu\nu}F^{\mu\nu} - \beta(|\Phi|^2 - 1)^2. \tag{3.8}$$

where now $\mathcal{D}_\mu = \partial_\mu - iA_\mu$. The parameter β governs the stability of the semilocal string solutions [66, 67], as we have seen in Section 2.4.2.

In order to study the energy of a static vortex configuration with a translational symmetry along the z-axis, we drop the z dependence and set $A_z = 0$. Therefore, the vortex energy for the semilocal case can be written using (3.5) as

$$E = \int dr d\varphi r\Big(|\mathcal{D}_r\Phi|^2 + \frac{1}{r^2}|\mathcal{D}_\theta\Phi|^2 + \frac{1}{2r^2}F_{r\theta}^2 + \beta(|\Phi|^2 - 1)^2\Big). \tag{3.9}$$

Significant advances in understanding the mathematical properties of vortices have arisen by considering the critical coupling limit in which the Higgs and vector masses become identical,

$\beta = 1$. The main simplification, realised by Bogomol'nyi [35], is that the energy (3.9) can be rearranged in such a way that the second order field equations reduce to a more tractable first order system.

One can rewrite the vortex energy (3.9) using the following identities,

$$|\mathcal{D}_r\Phi \pm \frac{i}{r}\mathcal{D}_\theta\Phi|^2 = |\mathcal{D}_r\Phi|^2 + \frac{1}{r^2}|\mathcal{D}_\theta\Phi|^2 \mp \frac{1}{r}(\partial_r J_\theta - \partial_\theta J_r) \mp \frac{1}{r}F_{r\theta}(|\Phi|^2 - 1), \tag{3.10}$$

$$\frac{1}{2}\Big(\frac{F_{r\theta}}{r} \pm (|\Phi|^2 - 1)\Big)^2 = \frac{F_{r\theta}^2}{2r^2} + \frac{1}{2}(|\Phi|^2 - 1)^2 \pm \frac{1}{r}F_{r\theta}(|\Phi|^2 - 1), \tag{3.11}$$

where J_μ is the current defined as

$$J_\mu = \frac{i}{2}\Big(\Phi(\mathcal{D}_\mu\Phi)^* - \Phi^*(\mathcal{D}_\mu\Phi)\Big) + A_\mu. \tag{3.12}$$

Using the identities above the vortex energy (3.9) takes the Bogomol'nyi form [35]:

$$\begin{aligned} E = \int dr\ d\theta\ r\Big\{ \Big|(\mathcal{D}_r \pm \frac{i}{r}\mathcal{D}_\theta)\Phi\Big|^2 + \frac{1}{2}\Big(\frac{F_{r\theta}}{r} \pm (|\Phi|^2 - 1)\Big)^2\Big\} \\ \pm \int dr\ d\theta\ \mathcal{F}_{r\theta} \\ + \frac{1}{2}(\beta - 1)\int dr\ d\theta\ r\ (|\Phi|^2 - 1)^2, \end{aligned} \tag{3.13}$$

where we have defined $\mathcal{F}_{\mu\nu} = \partial_\mu J_\nu - \partial_\nu J_\mu$ as the auxiliary field strength of the current (3.12). The first integrand in (3.13) is positive definite. Considering that in the critical coupling limit ($\beta = 1$) the last term vanishes, the second integrand implies a lower bound for the energy

$$E \geq \pm \int dr\ d\theta\ \mathcal{F}_{r\theta}. \tag{3.14}$$

One can realize that the expression for the energy is very similar to the expression for the magnetic flux we have analysed in Equation (2.23). Depending on the direction of the flux the integral will be positive or negative, so the choice of the sign in the expression (3.14) is to ensure that the energy is positive in whatever direction of the flux. Clearly, this bound will be saturated if, and only if, the first integrand in (3.13) vanishes, implying the following first-order equations, known as Bogomol'nyi equations:

$$(\mathcal{D}_r \pm \frac{i}{r}\mathcal{D}_\theta)\Phi = 0, \quad \frac{F_{r\theta}}{r} \pm (|\Phi|^2 - 1) = 0. \tag{3.15}$$

The most general ansatz for a static straight semilocal cosmic string lying along the z-axis is

$$\Phi = (f(r)e^{in\theta}, h(r)e^{im\theta}), \quad A_\theta = v(r), \tag{3.16}$$

with all the other components of the gauge fields set to zero. Here n and m are the winding numbers of the fields ϕ_1 and ϕ_2, respectively. In our case, without loss of generality, we will assume that the winding numbers are positive and $n > m$; so the Bogomol'nyi equations (3.15) have to be solved using the upper sign. The case $n = m$ can always be rotated into a Nielsen-Olesen string using a $SU(2)$ transformation as shown in [4]. Using the ansatz (3.16) the Bogomol'nyi

equations (3.15) take the from:

$$f' + \frac{v-n}{r} f = 0, \quad h' + \frac{v-m}{r} h = 0, \quad \frac{v'}{r} + (f^2 + h^2 - 1) = 0. \tag{3.17}$$

In order to obtain string-like solutions, we have to solve the Bogomol'nyi equations (3.17) subject to appropriate boundary conditions. On one hand, we want finite energy configurations, so we have to require that far away from the center of the string, the fields are in the vacuum, and that the covariant derivatives of the fields vanish

$$|\Phi|^2\big|_{r\to\infty} = 1, \quad \mathcal{D}_\mu \Phi\big|_{r\to\infty} = 0. \tag{3.18}$$

On the other hand, we want regularity of our solutions at the origin. Imposing both requirements we have the following boundary conditions,

$$f_\infty^2 + h_\infty^2 = 1, \quad v_\infty = n, \tag{3.19}$$

$$f(0) = 0, \quad v(0) = 0, \quad h'_{m=0}(0) = 0 \text{ or } h_{m\neq 0}(0) = 0, \tag{3.20}$$

where the subscript $_\infty$ denotes $r = \infty$. We choose, without loss of generality, that the magnetic flux trapped in the core of the string will be induced by the winding of the ϕ_1 field, but due to the symmetry of the equations the same results would be obtained if the winding responsible for the trapped magnetic flux was in ϕ_2.

As mentioned, the stability of semilocal strings was analysed by Hindmarsh [66, 67], where he checked the stability of the solutions to small perturbations in h, by looking for negative-eigenvalue solutions to the Schrödinger-like equation for a small perturbation around $h = 0$. In the Bogomol'nyi limit, $\beta = 1$, he discovered that there is a zero-eigenvalue solution for the Schrödinger type equation, i.e., a zero mode. This indicates that there is a degeneracy in the solutions to the Bogomol'nyi equations, that is, there is a solution for any $h(r)$ and not just $h = 0$.

The existance of the degeneracy in the solutions can be shown directly analysing the Bogomol'nyi equations (3.17). The first two equations imply that the profile functions f and h must be related to each other:

$$\log h = \log f - (n-m)\log r + \kappa \Rightarrow h = c\, f\, r \exp(m-n), \tag{3.21}$$

and therefore, there is a one-parameter family of solutions characterized by a real constant $\kappa = \log c$. In this work, we will analyse the case $m = 0$, in which case the profile function of ϕ_2, $h(r)$, can be non-zero at the core creating a "condensate". Actually, the value of $h(r = 0)$ will be the free parameter related to κ and it is strictly related with the width of the string. The total energy does not depend on the value of $h(r = 0)$, as can be checked by inserting the ansatz for the gauge boson (3.16) and its boundary conditions in (3.14)

$$E = \pm \int dr\, d\theta\, \mathcal{F}_{r\theta} = \int d\theta A_\theta|_{r=\infty} = 2\pi n. \tag{3.22}$$

In Fig. 3.1 the behaviour of the profile functions is shown, where we have chosen the value of $h(r = 0) = 0.5$. As we can see the profile functions for f and v are similar to the f_{ANO} and v_{ANO} functions of the Abelian-Higgs model (Figure 2.4). In this case, however, there is an extra function h which is responsible for the condensate.

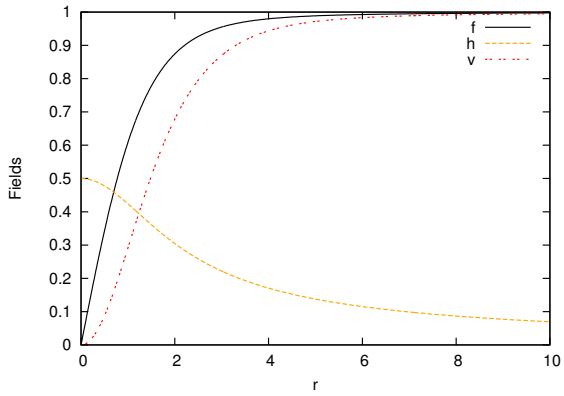

Figure 3.1.: *Profile functions for semilocal string solutions where $n = 1$ and $m = 0$. The value of $h(r = 0)$ is the free parameter related to κ. In this case we choose $h(r = 0) = 0.5$ in order to show the behaviour of the functions but any choice of the value of $h(r = 0)$ will have the same total energy.*

3.1.2. Axionic Strings

In this section we will analyse the axionic string model. As we have said in Section 2.4.2, these strings arise in a low energy effective model of the supersymmetric Abelian-Higgs model with a D-term potential coupled to an axion-dilaton multiplet. The study of the supersymmetric model is beyond the scope of this work, so we will start our analysis with the bosonic part of the Lagrangian of the effective theory (2.76) that reads,

$$\mathcal{L}^A = -|\mathcal{D}_\mu\phi|^2 - \frac{M_p^2}{(S+\bar{S})^2}|\mathcal{D}_\mu S|^2 - \frac{1}{4e^2}F^{\mu\nu}F_{\mu\nu} - \frac{1}{2}e^2\left(q|\phi|^2 + 2\delta\frac{M_p^2}{(S+\bar{S})} - \xi\right)^2. \quad (3.23)$$

As we did with the semilocal case, we are going to rescale the fields in order to obtain a meaningful combination of the parameters in the model,

$$\phi = \sqrt{\frac{\xi}{q}}\hat{\phi}, \quad s = \frac{\delta M_p^2}{\xi}\hat{s}, \quad a = \frac{2\delta}{q}\hat{a}, \quad A_\mu = e\sqrt{\frac{\xi}{q}}\hat{A}_\mu, \quad x = (e\sqrt{\xi q})^{-1}\hat{x}. \quad (3.24)$$

After dropping the hats, the Lagrangian (3.23) reads:

$$\frac{\mathcal{L}^A}{e^2\xi^2} = -|\mathcal{D}_\mu\phi|^2 - \frac{1}{4}\frac{\alpha^2}{s^2}|\mathcal{D}_\mu S|^2 - \frac{1}{4}F^{\mu\nu}F_{\mu\nu} - \frac{1}{2}(|\phi|^2 + s^{-1} - 1)^2, \quad (3.25)$$

with $\mathcal{D}_\mu\phi = \partial_\mu\phi - iA_\mu\phi$, $\mathcal{D}_\mu S = \partial_\mu S - 2iA_\mu$, $S = \alpha^{-2}s + 2ia$ and $\alpha^2 = \xi/(qM_p^2)$. α is the only meaningful parameter of the theory.

To study the energy of straight vortices along the z-direction, we drop the z dependence and set $A_z = 0$. With all this we can write the vortex energy (3.5) as

$$E = \int drd\theta r\Big(|\mathcal{D}_r\phi|^2 + \frac{1}{r^2}|\mathcal{D}_\theta\phi|^2 + \frac{1}{4}\frac{\alpha^2}{s^2}(|\mathcal{D}_r S|^2 + \frac{1}{r^2}|\mathcal{D}_\theta S|^2) + \frac{1}{2r^2}F_{r\theta}^2 + \frac{1}{2}(|\phi|^2 + s^{-1} - 1)^2\Big). \quad (3.26)$$

As in the semilocal case, we can use the following identities to rewrite the vortex energy in the

Bogomol'nyi form

$$|\mathcal{D}_r\phi \pm \frac{i}{r}\mathcal{D}_\theta\phi|^2 = |\mathcal{D}_r\phi|^2 + \frac{1}{r^2}|\mathcal{D}_\theta\phi|^2 \mp \frac{1}{r}(\partial_r J_\theta - \partial_\theta J_r) \mp \frac{1}{r}F_{r\theta}(|\phi|^2 - 1), \tag{3.27}$$

$$|\mathcal{D}_r S \pm \frac{i}{r}\mathcal{D}_\theta S|^2 = |\mathcal{D}_r S|^2 + \frac{1}{r^2}|\mathcal{D}_\theta S| \mp \frac{1}{r}(\partial_r I_\theta - \partial_\theta I_r) \mp \frac{1}{r\alpha^2}F_{r\theta}s, \tag{3.28}$$

$$\frac{1}{2}\Big(\frac{F_{r\theta}}{r} \pm (|\phi|^2 + s^{-1} - 1)\Big)^2 = \frac{1}{2}\frac{F_{r\theta}^2}{r^2} + \frac{1}{2}(|\phi|^2 + s^{-1} - 1)^2 \pm \frac{F_{r\theta}}{r}(|\phi|^2 + s^{-1} - 1), \tag{3.29}$$

where J_μ and I_μ can be understood as the currents of ϕ and S fields, respectively. These currents are defined as

$$J_\mu = \frac{i}{2}\Big(\phi(\mathcal{D}\phi)^* - \phi^*(\mathcal{D}_\mu\phi)\Big) - A_\mu, \tag{3.30}$$

$$I_\mu = \frac{i}{8\alpha^2}(S(\mathcal{D}_\mu S)^* - S^*(\mathcal{D}_\mu S)). \tag{3.31}$$

Using the identities above, the vortex energy in the Bogomol'nyi form is rewritten as follows,

$$E = \int dr\ d\theta\ r\Big\{|(\mathcal{D}_r \pm \frac{i}{r}\mathcal{D}_\theta)\phi|^2 + \frac{1}{4}\frac{\alpha^2}{s^2}|(\mathcal{D}_r \pm \frac{i}{r}\mathcal{D}_\theta)S|^2 + \frac{1}{2}\Big(\frac{F_{r\theta}}{r} \mp (|\phi|^2 + s^{-1} - 1)\Big)^2\Big\} \pm \int dr d\theta \mathcal{F}_{r\theta}, \tag{3.32}$$

where we have defined the composite vector field $\mathcal{A}_\mu$ and its field strength as

$$\mathcal{A}_\mu = \frac{i}{2}\Big(\phi(\mathcal{D}\phi)^* - \phi^*(\mathcal{D}_\mu\phi)\Big) + \frac{i\alpha}{2s^2}(S(\mathcal{D}_\mu S)^* - S^*(\mathcal{D}_\mu S)) - A_\mu, \quad \mathcal{F}_{\mu\nu} = \partial_\mu\mathcal{A}_\nu - \partial_\nu\mathcal{A}_\mu. \tag{3.33}$$

This $\mathcal{A}_\mu$ can be understood as the overall current of the string.

As in the semilocal model, if we restrict ourselves to finite energy configurations, we have to impose that far away from the string core the fields are in the vacuum, and that the covariant derivatives vanish

$$(s^{-1} + |\phi|^2)|_{r\to\infty} = 1 \quad \mathcal{D}_\mu\phi|_{r\to\infty} = 0, \quad \mathcal{D}_\mu S|_{r\to\infty} = 0. \tag{3.34}$$

With these boundary conditions we find a lower bound for the energy similar to (3.14),

$$E \geq \pm \int dr d\theta \mathcal{F}_{r\theta} = \pm \int dr d\theta F_{r\theta}. \tag{3.35}$$

The choice of the sign in the above integral will be to ensure that the energy is positive. The corresponding Bogomol'nyi equations, which ensure that the energy bound is saturated are,

$$(\mathcal{D}_r \pm \frac{i}{r}\mathcal{D}_\theta)\phi = 0, \quad (\mathcal{D}_r \pm \frac{i}{r}\mathcal{D}_\theta)S = 0, \quad \frac{F_{r\theta}}{r} \pm (|\phi|^2 + s^{-1} - 1) = 0. \tag{3.36}$$

In order to solve the Bogomol'nyi equations we use the ansatz for the matter fields proposed in [33], which represents a static straight cosmic string along the z-axis:

$$\phi = f(r)e^{in\theta}, \quad s^{-1} = h(r)^2, \quad a = m\theta, \quad A_\theta = v(r). \tag{3.37}$$

Substituting this ansatz into the Bogomol'nyi equations (3.36) we have,

$$f' + \frac{v - |n|}{r} f = 0, \quad h' + \alpha^2 \frac{v - |m|}{r} h^3 = 0 \quad \frac{v'}{r} + (f^2 + h^2 - 1) = 0. \tag{3.38}$$

The signs of the winding numbers n and m are fixed by requiring $f(r)$ to be regular and $h^2(r) > 0$ for $r \to 0$. In this case, we can also use the first two Bogomol'nyi equations to find a relation between the tachyon and the dilaton field

$$\frac{1}{(\alpha h)^2} = -2(|m| - |n|) \log r - 2 \log f + k, \tag{3.39}$$

and therefore the solutions are parametrized by an arbitrary constant κ, showing a existence of a one-parameter family of solutions.

As we did in the semilocal case, in order to obtain string-like solutions we have to solve the Bogomol'nyi equations (3.38) subject to appropiate boundary conditions. So using the energy condition from (3.34) we have the following boundary conditions

$$(f_\infty^2 + h_\infty^2) = 1, \quad f_\infty(v_\infty - |n|) = 0, \quad h_\infty(v_\infty - |m|) = 0. \tag{3.40}$$

Actually, we can see that the boundary conditions can be fulfilled by three different choices of the field values at $r \to \infty$. In this case, the fields in the model are not the same type as in the semilocal model, so the symmetry does not imply that the three different choices give the same result. Therefore, the model admits three different families of cosmic string solutions:

ϕ-strings (tachyonic)

In this type of strings the magnetic flux trapped in the core is induced by the winding of the tachyon field, which must satisfy $|n| > |m|$ in order to solve the Bogomol'nyi equations. The profile functions have the following asymptotic behaviour

$$f_\infty \to 1, \quad h_\infty \to 0, \quad v_\infty \to |n|, \tag{3.41}$$

so that the tachyon field acquires a non-vanishing expectation value far from the core while the function $h(r)$ tends to zero. For the solutions to be regular we also have to impose the following boundary conditions at the core of the strings $r \to 0$:

$$f(0) = 0, \quad v(0) = 0, \quad h'_{m=0}(0) = 0 \quad \text{or} \quad h_{m\neq 0}(0) = 0. \tag{3.42}$$

For tachyonic strings we will only consider the case $m = 0$, where the profile function of the axion-dilaton, $h(r)$, can be non-zero at the core creating a "condensate". Actually, the value of $h(r = 0)$ will be a free parameter related to κ, which determines the width of the string. This family of solutions is degenerated in energy because the vortex energy is independent of h, as we can show by inserting the ansatz for the gauge boson (3.37) and its boundary conditions in (3.32)

$$E = \pm \int dr d\theta \mathcal{F}_{r\theta} = \int d\theta A_\theta|_{r=\infty} = 2\pi|n|. \tag{3.43}$$

In Fig. 3.2 the profile functions of tachyonic strings can be seen, where the value of the free parameter is chosen to be $h(r = 0) = 0.1$. Here also, the f and h functions are similar to the f_{ANO} and v_{ANO} functions of the Abelian-Higgs model (see Figure 2.4).

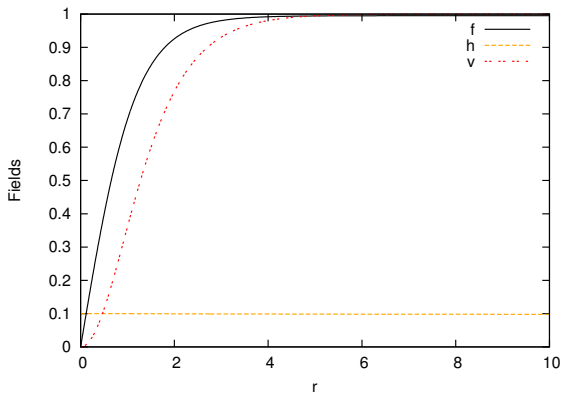

Figure 3.2.: *Profile functions of tachyonic strings with $n = 1$ and $m = 0$. With this choice of n and m the value of $h(r = 0)$ is a free parameter and it could take any value without changing the value of the total energy. In this figure we choose $h(r = 0) = 0.1$. ($\alpha = 1$)*

s-strings (axionic)

In this case the magnetic flux inside the strings is induced by the winding of the axio-dilaton, S. The behaviour at infinity is

$$f_\infty \to 0, \quad h_\infty \to 1, \quad v_\infty \to |m|. \tag{3.44}$$

It is now the dilaton which acquires a non-zero expectation value far from the core, while the tachyonic field tends to zero far from the core. Thus, the role of the tachyonic and the dilatonic field is exchanged. These strings are solutions to the Bogomol'nyi equations provided $|n| < |m|$. Regularity at the origin imposes the following boundary conditions

$$h(0) = 0, \quad v(0) = 0, \quad f'_{n=0} = 0, \quad \text{or} \quad f_{n\neq 0}(0) = 0. \tag{3.45}$$

For axionic strings we will discuss the properties of this family of solutions for the case $n = 0$, where the value of the profile function of the tachyon at the center of the string, $f(r = 0)$, is a free parameter related to κ and, as we will see, it is related with the width of the string. Again, this family of solutions is degenerated in energy

$$E = \pm \int dr d\theta \mathcal{F}_{r\theta} = \int d\theta A_\theta|_{r=\infty} = 2\pi|m|. \tag{3.46}$$

In Fig. 3.3 the profile functions of axionic strings are shown, where $f(r = 0) = 0.5$. The profiles in this case are a bit different compared to the Abelian-Higgs model. The function v is still similar to the v_{ANO} function of Abelian-Higgs case but due to the presence of the h^3 factor the h function has a slightly different behaviour compared to the f_{ANO} function in the Abelian-Higgs case (see Figure 2.4).

Hybrid-strings

In this case, both the tachyon and the dilaton field contribute to cancel the scalar potential far away from the core, i.e., they both acquire a finite vacuum expectation value for $r \to \infty$. This can only happen provided the windings satisfy $|n| = |m|$. Thus, in this case we have the following

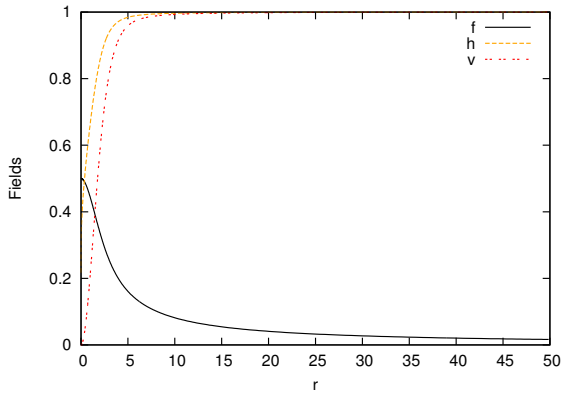

Figure 3.3.: *Profiles of a typical axionic string with $n = 0$ and $m = 1$. As we can see the $f(r = 0) = 0.5$ takes a non-zero value at the core of the string creating a condensate. ($\alpha = 1$)*

boundary conditions at infinity

$$f_\infty^2 + h_\infty^2 = 1, \quad v_\infty = |n| = |m|, \tag{3.47}$$

Provided the previous constraints are satisfied the value of f_∞, for example, can be a free parameter, which will be again related to κ. In this case κ, is related to the relative contributions of the tachyonic and the axionic string to the tension of the string. The corresponding boundary conditions at the core of the string are given by

$$f(0) = 0, \quad v(0) = 0, \quad h(0) = 0. \tag{3.48}$$

The zero mode associated with the parameter κ is not normalizable and thus we will not discuss it any further in this research. Indeed, if we promote the parameter κ to be time dependent the corresponding effective action for the zero mode gets a quadratically divergent contribution Λ^2, where Λ is a cutoff which, in a cosmological setting, could be given by the distance to the closest cosmic string.

3.2. Coupling to Gravity

Once we have revisited the models and their zero modes, we will analyse the survival of these zero modes and the role of the flat directions when coupling the models minimally to gravity. The models we have described in the previous section will be minimally coupled to gravity using the following action:

$$S = \int d^4x \sqrt{-\det g}\Big(-\frac{1}{2} M_p^2 R + \mathcal{L}_m \Big), \tag{3.49}$$

where the gravitational strength coupling is given in terms of the reduced Plank mass $M_p^{-2} = 8\pi G$, where G is the Newton constant. R is the Ricci scalar.

As in the previous section, we are interested in static cylindrically symmetric configurations invariant under boosts along the axis of symmetry which, without loss of generality, we can take to be the z-axis. The most general line element in curved space-time consistent with these symmetries is:

$$ds^2 = -N^2(r)dt^2 + dr^2 + L^2(r)d\varphi^2 + N^2(r)dz^2, \tag{3.50}$$

where we have chosen $g_{tt} = -g_{zz}$ due to the boost symmetry of the solution. $N(r)$ and $L(r)$ are functions to be determined.

Using the non-vanishing components of the Ricci tensor one can compute the components of the Einstein tensor (1.2), which read as follows:

$$G_t^t = \frac{-N^2 L''}{L}, \quad G_r^r = \frac{N'^2 - NN''}{N^4}, \quad G_\theta^\theta = \frac{L^2(N'^2 - NN'')}{N^4}, \quad G_z^z = \frac{N^2 L''}{L}, \tag{3.51}$$

where the prime denotes the derivative with respect to r. In the same way, using (3.4) the components of the energy-momentum tensor can be computed

$$T_r^r = T_\varphi^\varphi = 0, \quad T_t^t = \mathcal{L}_m, \quad T_z^z = -\mathcal{L}_m. \tag{3.52}$$

Thus, we have the following Einstein equations,

$$\frac{-N^2 L''}{L} = -M_p^{-2}\mathcal{L}_m, \quad \frac{N'^2 - NN''}{N^4} = 0, \quad \frac{L^2(N'^2 - NN'')}{N^4} = 0, \quad \frac{N^2 L''}{L} = M_p^{-2}\mathcal{L}_m. \tag{3.53}$$

We have to impose regularity at the origin to solve these equations. This regularity will be guaranteed by the conditions $L(0) = N'(0) = 0$ and $L'(0) = N(0) = 1$. Making use of them the metric functions take the next form,

$$N(r) = 1, \quad \frac{L''(r)}{L(r)} = M_p^{-2}\mathcal{L}_m. \tag{3.54}$$

As we have shown in Section 2.3.3, the metric around a infinitely long straight string is a Minkowski space minus a wedge, which is described by the deficit angle. For this type of metrics, it is shown in [137] that the deficit angle, Δ, is determined by the asymptotic value of $L(r)$ as $\Delta = 2\pi(1 - L'|_{r=\infty})$, as we will see.

In order to discuss the existence of zero-modes in these theories we need an appropriate definition of the energy which will be valid for our cases. That is, we have to ensure that the equations that are obtained from the Bogomol'nyi procedure are the equations of motion of the entire system, our models coupled to gravity, and consequently that they will extremize the action of the system. We can use the definition in [52] where the appropriate energy is obtained by adding a Gibbons-Hawking term to the action (3.49),

$$E = -S - S_{GH}, \quad E = \int_{\mathcal{M}} \sqrt{-\det g}\Big(-\frac{1}{2}M_p^2 R + \mathcal{L}_m\Big) + M_p^2 \int_{\partial\mathcal{M}} \sqrt{-\det h}\tilde{R} \tag{3.55}$$

where $\tilde{R}$ is the Gaussian curvature at space-time boundary $\partial\mathcal{M}$ at $r = 0$ and $r = \infty$ on which the metric is h. For the metric (3.50),

$$\sqrt{-\det g} = L(r), \quad \sqrt{-\det g}R = 2L''(r), \quad \sqrt{-\det h}\tilde{R} = L'(r), \tag{3.56}$$

and thus the energy can be written as,

$$E = \int d^2x\sqrt{\det g}\mathcal{L}_m - M_p^2 \int dr d\theta L''(r) + M_p^2 \int d\theta L'(r)|_{r=\infty} - M_p^2 \int d\theta L'(r)|_{r=0}. \tag{3.57}$$

Clearly the term in the energy related to the Ricci curvature will be suppressed by the Gibbons-

Hawking term. Then, the energy for our field configurations can be taken to be

$$E = \int d^2x \sqrt{-\det g} T_0^0. \tag{3.58}$$

3.2.1. Semilocal Strings

In order to obtain the energy of the semilocal stationary string we use the rescaling (3.7), the semilocal model lagrangian (3.7) and the explicit form of the metric (3.50). But before putting everything together we have to realised that now the metric function $L(r)$ has to be rescaled as $L(r) = \hat{L}(r)/\eta e$ and that the metric function $N(r)$ is equal to one, $N(r) = 1$. Taking everything into account the energy of the semilocal stationary string with a translational symmetry along the z-axis is:

$$E = \int dr d\varphi L(r) \Big(|\mathcal{D}_r \Phi|^2 + \frac{1}{L^2} |\mathcal{D}_\theta \Phi|^2 + \frac{1}{2L^2} F_{r\theta}^2 - \beta (|\Phi|^2 - 1)^2 \Big). \tag{3.59}$$

One can see that the energy configuration that we have obtained for semilocal strings coupled to gravity is almost equal to the energy configuration that we have obtained for the uncoupled case (3.9). The only difference is that, in the coupled case, the metric function $L(r)$ appears in the place of the radial coordinate r in the uncoupled case. Therefore, all we learnt from the flat case can be used here to obtain the Bogomol'nyi equations that read:

$$f' + \frac{(v-n)}{L} f = 0, \quad h' + \frac{(v-m)}{L} h = 0, \quad \frac{v'}{L} + (f^2 + h^2 - 1) = 0, \tag{3.60}$$

which have to be solved subject to appropriate boundary conditions that result from imposing (3.18) and regularity at origin as in the flat case

$$f_\infty^2 + h_\infty^2 = 1, \quad v_\infty = |n|, \quad f(0) = 0, \quad v(0) = 0, \quad h'_{m=0}(0) = 0 \; or \; h_{m\neq 0}(0) = 0. \tag{3.61}$$

The first two Bogomol'nyi equations (3.60) imply that the profile functions f and h must be related to each other,

$$\log h = \log f - (n-m) \int \frac{dr}{L(r)} + \kappa \quad \rightarrow \quad h = cf \exp\Big((m-n) \int \frac{dr}{L(r)} \Big), \tag{3.62}$$

and therefore, there is a one-parameter family of solutions characterised by a real constant $\kappa = \log c$. In the present work we are considering the $m = 0$ case, where the profile function of ϕ_2, $h(r)$, can be non-zero at the core creating a "condensate". Actually, the value of $h(r = 0)$ is the free parameter related to κ and, as we will see, its value is related to the width of the string. This family is degenerated in energy, i.e. the total energy does not depend on the value of $h(r = 0)$,

$$E = \pm \int d\varphi A_\varphi|_{r=\infty} = 2\pi n, \tag{3.63}$$

showing that the zero mode still exists after coupling the model to gravity. From this expression we can also see that, in the Bogomol'nyi limit, the energy density, which will be very useful for our analysis, is closely related to the magnetic field $F_{r\theta}$,

$$\mathcal{E} = \frac{v'(r)}{L}. \tag{3.64}$$

Once we have obtained the equations of motion we need the expression for the metric function

$L(r)$ in order to solve them. Using (3.54) and by rescaling both sides of the equation, we obtain the following,

$$\frac{L''}{L} = \alpha^2\Big(|\mathcal{D}_r\Phi|^2 - \frac{1}{L^2}|\mathcal{D}_\theta\Phi| + \frac{1}{2L^2}F_{r\theta}^2 - \beta(|\Phi-1|^2)^2\Big), \tag{3.65}$$

where $\alpha = M_p^{-1}\eta$ is the vacuum expectation value of Φ measured in Plank masses. It is easy to show that applying the identities (3.10,3.11), where r is substituted by $L(r)$, and taking into account that we are working on the Bogomol'nyi limit, this equation can be represented as

$$\frac{L''}{L} = \alpha\mathcal{F}_{r\theta} = \alpha^2\partial_r J_\theta. \tag{3.66}$$

By integrating both sides of the equation above, we have the following expression,

$$L' = 1 \pm \alpha^2 J_\theta. \tag{3.67}$$

In the context of supergravity theories this equation is known as the gravitino equation [52]. Here the integration constant is fixed by the boundary conditions (3.61), since regularity also requires that $J_\theta(0) = 0$. Using the ansatz (3.16)

$$L' = 1 - \alpha^2((n-v)f^2 + (m-v)h^2 + v). \tag{3.68}$$

Using the formula above and the boundary conditions (3.61) one can directly derive that the deficit angle $\Delta = 2\pi(1 - L'|_{r=\infty})$, which is

$$\Delta = 2\pi n\alpha^2. \tag{3.69}$$

Note that if the vacuum expectation value of Φ measured in Plank masses is sufficiently large, corresponding to very heavy strings, the deficit angle becomes larger than 2π. The solutions with the deficit angle greater than 2π are the so-called "supermassime strings" [86, 108], and possess a singularity at the maximal value of the radial coordinate, at which the angular part of the metric vanishes.

Once we have the equations of motion we can analyse their form in the limiting cases. Close to the core, the profile functions have the same form as in Minkowski background:

$$L(r) \approx r + ..., \quad f(r) \approx f_0 r^n + ..., \quad h(r) \approx h_0 r^m + ..., \quad v(r) \approx \frac{1}{2}r^2 + ... \tag{3.70}$$

However, far away from the core, $r \to \infty$, the metric takes the form

$$ds^2 \approx -dt^2 + dr^2 + (1 - n\alpha^2)^2 r^2 d\varphi^2 + dz^2. \tag{3.71}$$

Comparing this result with the space-time around a cosmic string we have shown in Section 2.3.3, one can see that the equation above represents a conical space-time with a deficit angle $\Delta = 2\pi n\alpha^2$, ensuring that the deficit angle can be directly obtained using the value of the metric function L at infinity. The behaviour of the profile functions in the same limit is given by the following asymptotic expansion:

$$f(r) \approx 1 - \frac{1}{2}\Big(\frac{r}{r_0}\Big)^{\frac{2(m-n)}{1-|n|\alpha^2}} + ..., \quad h(r) \approx \Big(\frac{r}{r_0}\Big)^{\frac{m-n}{1-n\alpha^2}} + ..., \quad v(r) \approx n - (n-m)\Big(\frac{r}{r_0}\Big)^{\frac{2(m-n)}{1-n\alpha^2}}, \tag{3.72}$$

where r_0 is a parameter related with h_0 which determines the width of the string core. Setting

the constant $\alpha = 0$ we will recover the expansions in flat space.

As we have said, the energy density in the Bogomol'nyi limit has a simple form $\mathcal{E} = v'(r)/L$ and thus it is trivial to find the limiting form of the energy density

$$\mathcal{E}(r \to 0) \approx \frac{1}{2} + ..., \quad \mathcal{E}(r \to \infty) \approx \frac{2(n-m)^2}{(1-n\alpha^2)^2 r^2}\Big(\frac{r}{r_0}\Big)^{\frac{2(m-n)}{1-n\alpha^2}} + ... \,. \tag{3.73}$$

3.2.2. Axionic and Tachyonic strings

Using the same rescaling as in (3.24), and rescaling the metric function as $L(r) = (e\sqrt{\xi q})^{-1}\hat{L}(r)$ we can write the energy of the axionic stationary string with a translational symmetry along the z-axis as,

$$E = \int dr d\varphi L(r)\Big(|\mathcal{D}_r\phi|^2 + \frac{1}{L^2}|\mathcal{D}_\theta\phi|^2 + \frac{1}{4}\frac{\alpha^2}{s^2}(|\mathcal{D}_r S|^2 + \frac{1}{L^2}|\mathcal{D}_\theta S|^2) + \frac{1}{2L^2}F_{r\theta}^2 + \frac{1}{2}(|\phi|^2 + s^{-1} - 1)^2\Big). \tag{3.74}$$

Once again, one can realise that the only difference is that in the coupled case there is a $L(r)$ appearing in the places where the coordinate r appears in the flat case. So using the same procedure as in the flat case, one can obtain the following Bogomoln'yi equations

$$f' + \frac{(qv - |n|)}{L}f = 0, \quad h' + \alpha^2 q\frac{(v - |m|)}{L}h^3 = 0, \quad \frac{v'}{L} + (f^2 + h^2 - 1) = 0. \tag{3.75}$$

One can use the first two equations to find a relation between the tachyon and the dilaton field

$$\frac{1}{(\alpha h)^2} = 2(|n| - q|m|)\int \frac{dr}{L(r)} - 2\log f + \kappa, \tag{3.76}$$

and therefore the solutions are parametrized by an arbitrary constant κ. Before analysing the three different families of cosmic string solutions we will analyse the equation for the metric function L. As we did for the semilocal case, rescaling both sides of the equation (3.54) we get,

$$\frac{L''}{L} = \alpha^2\Big(|\mathcal{D}_r\phi|^2 + \frac{1}{L^2}|\mathcal{D}_\theta\phi|^2 + \frac{1}{4}\frac{\alpha^2}{s^2}(|\mathcal{D}_r S|^2 + \frac{1}{L^2}|\mathcal{D}_\theta S|^2) + \frac{1}{2L^2}F_{r\theta}^2 + \frac{1}{2}(|\phi|^2 + s^{-1} - 1)^2\Big). \tag{3.77}$$

One can observe that applying the identities (3.27, 3.28, 3.29), where r is substituted by $L(r)$, the equation takes the form,

$$\frac{L''}{L} = \alpha^2\mathcal{F}_{r\theta} = \alpha^2\partial_r\mathcal{A}_\theta, \tag{3.78}$$

from where we can obtain a first integral to the Einstein equations

$$L' = 1 \pm \alpha^2\mathcal{A}_\theta, \tag{3.79}$$

which in the context of supergravity theories is known as the gravitino equation [52]. The integration constant is also fixed by the boundary conditions (3.34), since regularity also requires that $\mathcal{A}_\theta(0) = 0$. Using the ansatz (3.37),

$$L' = 1 - \alpha^2((|n| - v)f^2 + (|m| - v)h^2 + qv). \tag{3.80}$$

Finally, we will analyse the behaviour of the Bogomol'nyi and Einstein equations that we have obtained in the two different families of cosmic string solutions that we will analyse:

ϕ-strings (tachyonic)

This family of solutions is degenerated in energy

$$E = \pm \int d\varphi A_\varphi|_{r=\infty} = 2\pi|n|, \tag{3.81}$$

and therefore the zero-mode survives the coupling to gravity. Using the expression (3.80) and substituting the boundary conditions (3.41) we can obtain the deficit angle $\Delta = 2\pi(1 - L'(\infty))$,

$$\Delta = 2\pi|n|\alpha^2. \tag{3.82}$$

In this case we can also obtain supermassive strings when the value of α is sufficiently large.

These solutions share many properties with semilocal strings, the main difference being the factor h^3 in the equation (3.75) instead of the h in equation (3.60). This translates into the function h tending to zero logarithmically. The tachyonic field f is responsible for the formation of the string, whereas h is responsible for the condensate. Close to the core of the string the profile functions behave as in flat space-time [33], in particular

$$f(r) \approx f_0 r^{|n|} + ..., \quad h(r)^{-2} \approx h_0^{-2} - 2\alpha^2|m| \log r + ..., \quad v(r) \approx \frac{1}{2} r^2 + ... \,. \tag{3.83}$$

The value $h(0)$ is a free parameter, related to the string width, which leaves the total energy unchanged and modifies the field configurations slightly. Actually, all the profile functions approach their values at infinity logarithmically, as can be seen from their asymptotic expansions,

$$\begin{aligned} h^2(r) \approx \frac{(1 - |n|\alpha^2)}{2\alpha^2(|n| - |m|)\log r} + ..., \quad f(r) \approx 1 - \frac{(1 - |n|\alpha^2)}{4\alpha^2(|n| - |m|)\log r} + ..., \\ v(r) \approx |n| - \frac{(1 - |n|\alpha^2)^2}{4\alpha^2(|n| - |m|)\log^2 r} + ... \,. \end{aligned} \tag{3.84}$$

The term in the numerator of the three expressions $(1 - |n|\alpha^2)$ was not obtained in the flat space-time analysis done in [33], since this is a consequence of the asymptotic form, the conical form, of the space-time metric

$$ds^2 \approx -dt^2 + dr^2 + (1 - |n|\alpha^2)^2 r^2 d\varphi^2 + dz^2. \tag{3.85}$$

Comparing (3.85) with the expression for the metric around a infinity straight AH string obtained in Chapter 2 the deficit angle can be derived directly, $\Delta = 2\pi|n|\alpha^2$. From (3.85) we can immediately extract the form of the energy density far away from the core:

$$\mathcal{E}(r) \approx \frac{M_p^2(1 - |n|\alpha^2)}{2(|n| - |m|)r^2 \log^3 r} + ... \,. \tag{3.86}$$

s-strings (axionic)

Again, this family of solutions is degenerated in energy

$$E = \pm \int d\varphi A_\varphi|_{r=\infty} = 2\pi|m|, \tag{3.87}$$

and thus the zero-mode still exists after coupling the model to gravity. Substituting the behaviour of the fields at infinity (3.44) at (3.80) the deficit angle is,

$$\Delta = 2\pi|m|\alpha^2. \tag{3.88}$$

In this case we can also obtain supermassive strings when the value of α is sufficiently large.

For this type of strings, the roles played by the tachyon field f and the dilaton field h are interchanged, the latter being responsible of the formation of the strings, and the former giving a measure of the width of the string. Close to the core, the approximate form of the profile functions is also given by (3.83), but in this case $|m| > |n|$. $f(0)$ plays the role of the free parameter which fixes the width of the string. The following asymptotic expansion shows the behaviour of the profile functions in the limit $r \to \infty$

$$f(r) \approx \Big(\frac{r}{r_0}\Big)^{\frac{|n|-|m|}{1-|m|\alpha^2}} + ..., \quad h(r) \approx 1 - \frac{1}{2}\Big(\frac{r}{r_0}\Big)^{\frac{2(|n|-|m|)}{1-|m|\alpha^2}} + ..., \quad v(r) \approx |m| - \frac{|n|-|m|}{\alpha^2}\Big(\frac{r}{r_0}\Big)^{\frac{2(|n|-|m|)}{1-|m|\alpha^2}} \tag{3.89}$$

This result is slightly different than the one obtained in a Minkowski background [33], as can be seen from the factor $(1-|m|\alpha)$ in the exponents. From this factor the deficit angle can be obtained directly, $\Delta = 2\pi|m|\alpha^2$. As in the case of the tachyonic strings, this correction is related to the form of the space-time metric far away from the core of the string:

$$ds^2 \approx -dt^2 + dr^2 + (1-|m|\alpha^2)^2 r^2 d\varphi^2 + dz^2. \tag{3.90}$$

Using (3.89) we obtain the asymptotic expansion of the energy density far away from the core:

$$\mathcal{E}(r) = \frac{2M_p^2(|n|-|m|)^2}{(1-|m|\alpha^2)^2 r^2}\Big(\frac{r}{r_0}\Big)^{\frac{2(|n|-|m|)}{1-|m|\alpha^2}} + \dots . \tag{3.91}$$

The energy density of these strings is similar to the semilocal or tachynic strings. There is a concentration of energy next to the core, although at much shorter distances than in those cases. The origin of this effect is in the factor $Re(S)^{-2}$ of the kinetic terms of the axio-dilaton field, which is responsible for the divergence of $Re(S)$ at the center of the s-strings.

3.3. Numerical Results

As seen in the previous section, all the cases that are being studied have a system of four coupled differential equations. In order to solve these equations numerically, we use a Fortran code named *colsys*, written by Uri M. Ascher, J. Christiansen and Robert D. Russell [19]. Colsys is a code for computing solutions for systems of ordinary differential equations with boundary conditions. This code compute approximate solutions on a sequence of meshes until a user-specified tolerance is satisfied.

In the *colsys* code one can choose the mesh distribution. In our case, the code uses 400 points in the mesh, and we choose these points to be equidistant from each other. One can also choose the range of integration depending on the information that one needs. We integrate our equations up to where the fields acquire, or are very close to, their vacuum expectation value. This point changes depending on the model and the free parameter related to the zero mode, therefore we have to choose the correct range in each of the different solutions.

3.3.1. Semilocal Strings

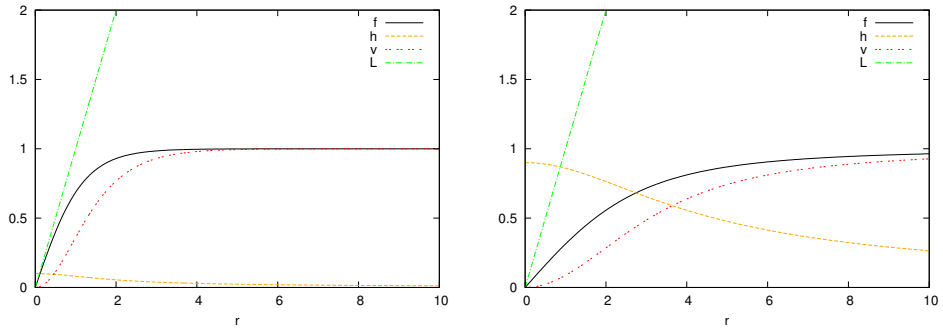

Figure 3.4.: *Profiles of a typical $n = 1$ semilocal string solution uncoupled to gravity, with different values of the free parameter: $h(0) = 0.1$ (left) and $h(0) = 0.9$ (right)*

Fig. 3.4 shows two typical $n = 1$ cosmic string solutions to this model, when the value of α is $\alpha = 0$. The metric function takes the form $L \equiv r$ and we recuperate the flat-space solutions (see Fig. 3.1). These figures illustrate the effect of varying the value of the condensate h at the center of the string $r = 0$, the free parameter of the family of degenerate solutions. For larger values of $h(r = 0)$ the profile functions reach their asymptotic values farther away from the string center and thus, the width of the string core increases.

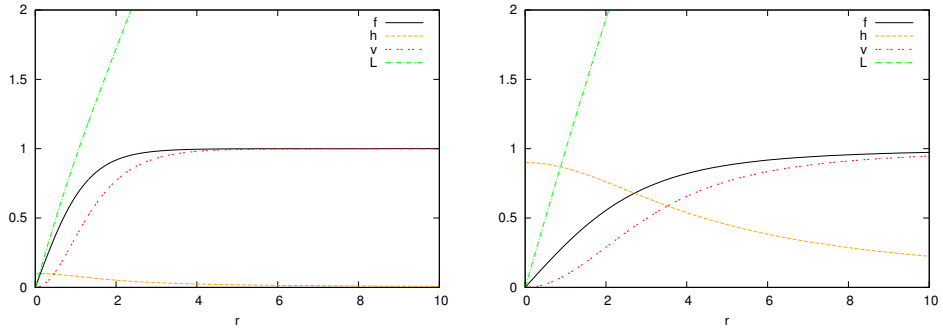

Figure 3.5.: *The profiles of a gravitating $n = 1$ semilocal string when we couple it to gravity ($\alpha = 0.5$) with the value of the free parameter: $h(0) = 0.1$ (left) and $h(0) = 0.9$ (right)*

The form of the profiles when coupling to gravity, can be seen in Fig. 3.5. The figures show that the metric function L does indeed depend on the value of the condensate. We can see the dependence more clearly in the left plot of Fig. 3.6 where we have displayed the metric function L for different values of the condensate keeping the value α constant. In the right plot of Fig. 3.6 we show the profile function L in different cases where we keep the value of the condensate constant and vary the value of the α parameter. Note that the deficit angle (3.69) increases with increasing α, and also that as α approaches zero, the space-time becomes Minkowski, where $L(r) = r$.

One way of understanding this phenomenon is by looking at the energy density for each one of these configurations, as shown in Fig. 3.7, where we only vary the value of the condensate. Even though the total energy (the area below these lines) is the same, the energy density is different, and affects the metric function with different strength. Indeed, since the width of the string core increases with the condensate, the energy density spreads and the metric profile function L reaches its asymptotic behaviour farther away from the string. Also keep in mind that the deficit

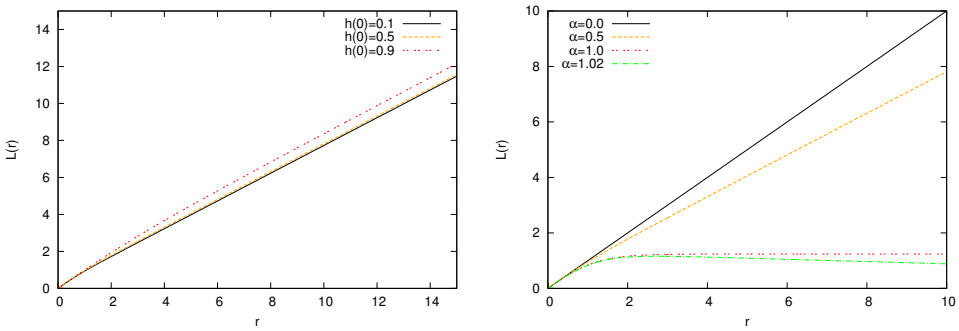

Figure 3.6.: *The function L for different configurations. On the left,* $\alpha = 0.5$ *while we vary the value of* $h(0)$*; on the right* $h(0) = 0.5$ *while we vary the values of* α *.*

angle for each of the configurations is exactly the same, and therefore the slope of the profile function L in the limit $r \to \infty$ should be the same regardless of the value of the condensate.

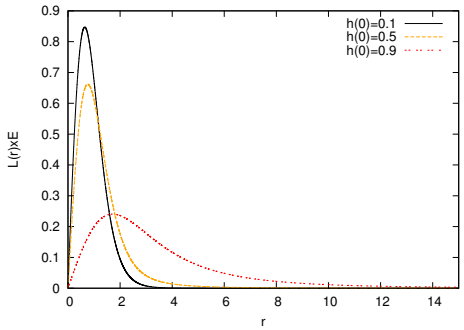

Figure 3.7.: *Energy density for different values of the free parameter* $h(0)$*, with fixed* $\alpha = 0.5$

A dramatic effect happens when considering supermassive strings. In this case the string is massive enough to make the function L turn around and become zero at some finite value of r^* (see Fig. 3.6 for the case with $\alpha = 1.02$), in other words, the deficit angle Δ becomes larger than 2π. The value of the condensate in the core determines the extent to which this solution exist; it decides the "size" of the universe. Once again, the total energy does not change, i.e., the integral for the energy density curve from $r = 0$ up to the other point r^* where $L(r^*) = 0$ is independent of the value of $h(r = 0)$. In Fig. 3.8 we have depicted the values of r^* for a fixed coupling constant with respect to the value of the condensate at the core $h(r = 0)$. As the value of the condensate increases the string core (where space-time is approximately Minkowski) becomes wider. In the limiting case where $h(r = 0) \to 1$ the space-time becomes Minkowski everywhere and the point r^* tends to infinity.

3.3.2. ϕ-strings (tachyonic)

As we have seen in the previous section, the tachyonic string solutions share many properties with semilocal strings, although there is a significant difference in the presence of the factor h^3 in the equation (3.75) instead of the h in equation (3.60). The presence of this term makes the function h tend logarithmically to zero as we can see in Fig. 3.9. In this figure the profile functions for the tachyonic strings are shown for two different values of $h(r = 0)$, the free parameter related to the zero mode.

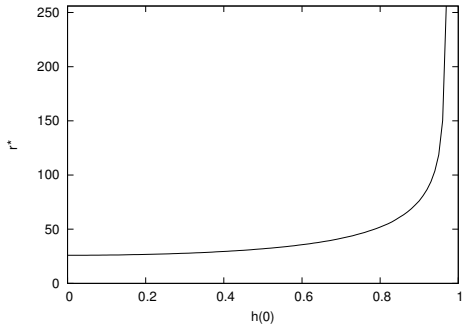

Figure 3.8.: *Values r^* at which the function $L = 0$ for a given coupling constant $(\alpha = 1.02)$ with respect to the value of the condensate at the core $h(0)$.*

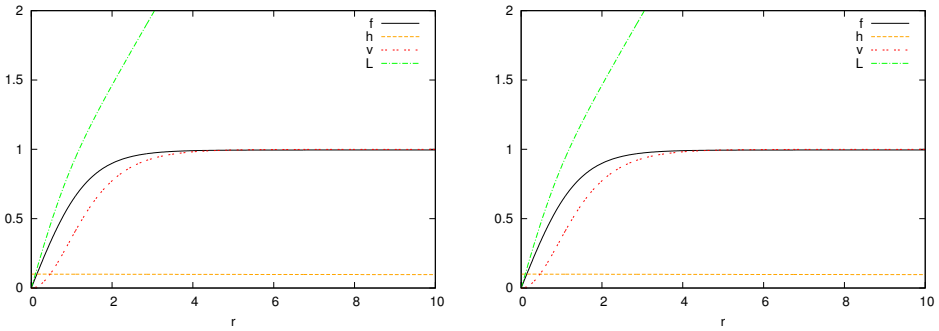

Figure 3.9.: *Profiles of a gravitating tachyonic string $(\alpha = 0.5)$ with the value of the free parameter $h(0) = 0.1$ (left) and $h(0) = 0.9$ (right).*

The effect created by the h^3 factor in the equations is not only visible in the profile functions. This factor also affects the behaviour of the energy density at infinity. As one can see in Fig. 3.10 the energy density reaches zero farther away from the core compared with the semilocal case. The difference in the behaviour at infinity of the energy density does not affect the total energy of the strings. The energies, for the three different values of $h(r = 0)$, shown in Fig. 3.10 have the same global value.

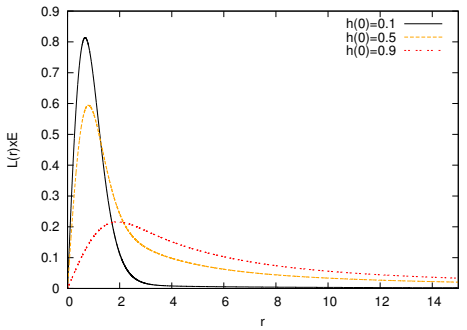

Figure 3.10.: *Energy density for different values of the free parameter $h(0)$ with fixed $\alpha = 0.5$.*

The fact that the global energy, and thus the deficit angle, are independent of the value $h(r = 0)$ implies that the slope of L remains unchanged for large values of r. But as we have shown, in the case of the tachyonic strings, the energy density is more spread and also the presence of

the condensate spreads it more. This is why that the behaviour of the metric profile function L changes close to the core, and in particular reaches its asymptotic behaviour farther away from the string center (see Fig. 3.11).

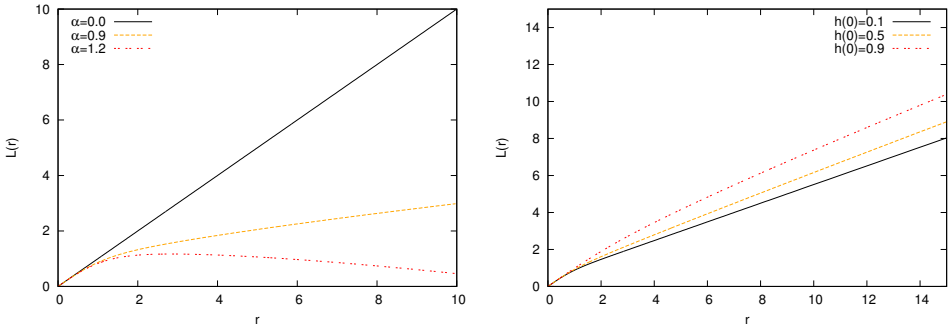

Figure 3.11.: *The function L for different models: left, $h(0) = 0.5$ and various α; right, $\alpha = 0.5$ and various $h(0)$.*

Once again, the deficit angle increases with α, and in the supermassive string case, the metric field develops a zero far from the core, making the space-time closed. Fig. 3.12 depicts the points r^* where the L develops a second zero for different values of the condensate at the core, keeping α value fixed.

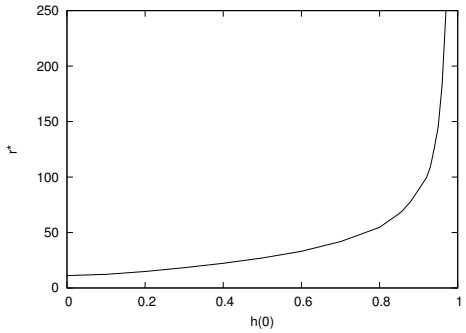

Figure 3.12.: *Values of the point r^* at which the function $L = 0$ for a given coupling constant $\alpha = 1.1$ with respect to the value of the condensate at the core $h(0)$.*

3.3.3. s-strings (axionic)

In order to analyse the behaviour of the profile functions of the axionic strings we have to keep in mind that the roles played by tachyon field f and the dilaton field h are interchanged. In this case, the dilaton field h is responsible for creating the string. As we have pointed out in the previous section there is an h^3 factor in (3.75) that creates the most significant difference between these kinds of strings and the semilocal ones. In the axionic case this difference can be clearly seen in the behaviour of the field h near the core of the string (see Fig. 3.13).

It is also clear that the swap of the roles of tachyon field and the dilaton field creates some differences between the behaviour of the tachyonic string profile functions (see Fig. 3.9) and the axionic string profile functions (see Fig 3.13). However, the main characteristics of the solutions obtained from both cases are almost equal. The global energy of these configurations does not change in respect to the value of the condensate at the core, the zero mode survives. This is why,

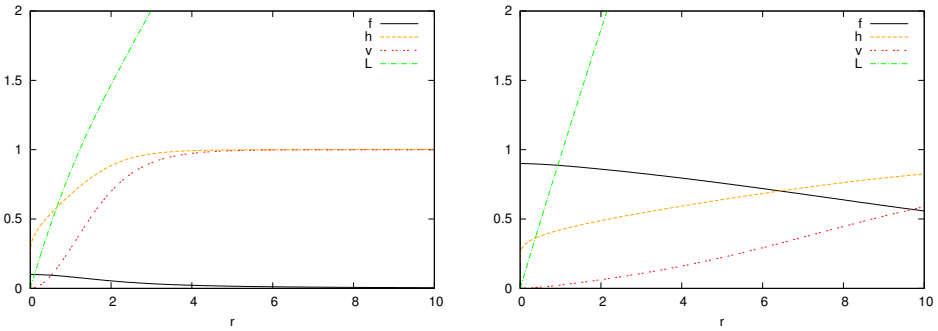

Figure 3.13.: *The profiles of a gravitating axionic string* $(\alpha = 0.5)$ *with the value of the free parameter* $f(0) = 0.1$ *(left) and* $f(0) = 0.9$ *(right)*

the slope of L does not change for large values of r, although it can change close to the core. Solutions for supermassive strings that have a closed space-time associated with them can also be obtained, and the dependency of the values r^* at which the closing occurs can be found in Fig. 3.14.

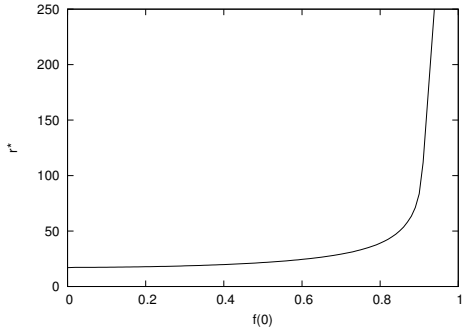

Figure 3.14.: *Values of the points* r^* *at which the function* $L = 0$ *for a given coupling constant* $\alpha = 1.1$ *with respect to the value of the condensate at the core* $f(0)$.

3.4. Conclusions and Discussion

In this Chapter we have studied field theoretical models for cosmic strings with flat directions in curved space-time. Specifically we have considered the effects of the coupling to gravity on the models with semilocal, axionic and tachyonic strings, which were known to have flat directions in flat space-time. In this research we have focused on solutions of a single static cylindrically symmetric string with invariance under boosts along the axis of symmetry. Although the models studied here are very different in character, some of the solutions obtained are quite similar. We have proven that the zero mode survives the coupling to gravity in all three cases. We have found numerical solutions to the Bogomol'nyi equations for the three types of strings, paying special attention to the space-time metric, and in particular, we have characterised its dependence on the value of the family-parameter and the string energy.

The cosmic string solutions have been found using a Bogomol'nyi-type of argument, which consists in minimising an energy functional appropriate for static cylindrically symmetric field configurations in a gravitational theory. The field configurations saturate the corresponding Bo-

gomol'nyi bound when the fields satisfy a set of first order differential equations, similar to those found for Minkowski space. We have shown that, if these conditions are met, then the energy momentum tensor acquires a very simple form, which allows to find a first integral to the Einstein equations. This result is also interesting in the context of supergravity theories, where this first integral is known as the gravitino equation, and it is known to exist whenever the cosmic string configuration preserves a fraction of the supersymmetries. However, since the derivation we have presented here makes no reference to supersymmetry, our results show that cosmic string solutions saturating a Bogomol'nyi bound can satisfy a gravitino-type of equation, regardless of the fraction of supersymmetries of the model that is broken by the string.

We have seen that the free parameter related to the zero mode changes where the fields acquire their vacuum expectation value. This is, the bigger the value of the free parameter at $r = 0$ the further the fields acquire their vacuum expectation value, increasing the width of the string. Due to this behaviour the shape of the energy density also depends on the value of the free parameter, that is, the energy density is more spread for wider strings. However, the free parameter does not change the total energy, and therefore, neither the deficit angle of the string.

Since gravity depends on energy density (not only on the global value of it), the energy distribution changes the metric function L. Basically, this change happens near the core of the string, because, as we just said, the slope of the metic function L at infinity is closely related with the deficit angle and it does not vary. That is, the metric function L will reach its asymptotic value farther away from the string center when the string is wider but its slope, at this asymptotic value, will be always the same. Thus, we show that different values of the zero mode do change the local metric properties, even though they do not change the global characteristics.

The change created by the parameter related with the zero mode in the metric properties becomes very apparent when the string is massive enough to have a deficit angle larger than 2π. In those cases the L function turns around and becomes zero at some finite value of the radial coordinate, rendering the spatial directions transverse to the string closed. As the free parameter associated with the zero mode changes the shape of the L function, the value acts as a modulus which fixes the size of the compact space-time dimension.

4 Measuring Global Monopole Velocities

4.1. Introduction

In Section 2.3.4 we have described two different ways to analyse the networks of topological defects: numerical simulations, which solve the discrete equations of motion of the system under different levels of approximation; and VOS type analytical models, which describe the system using evolution equations for macroscopic quantities. This two approaches are complementary, as we will show in this Chapter: we study global monopole networks using the largest and most accurate field theory simulations, and use the data obtained to determine the parameters of the VOS model.

In Section 2.4.1 we have described the VOS model for global monopoles which was presented in [97]. The careful analysis of this model shows that there are two different branches of solutions. One of this branches is related with luminal velocities of monopoles, while the other is related with subluminal velocities. In order to use the correct branch in the analysis of global monopoles networks their velocity has to be determined. This determination must be done by numerical simulations. The first attempt to estimate the velocities of monopoles using numerical simulations was made by Yamaguchi [139], where he obtained $v_r = 1.0 \pm 0.3$ and $v_m = 0.8 \pm 0.3$ for radiation dominated era and matter dominated era, respectively. Clearly, the method used had a large error, big enough that the luminal and subluminal branches cannot be distinguished. Therefore a more accurate measurement of the velocities of global monopoles seems to be necessary.

We develop a new method that determines the velocity of each one of the monopoles in the simulation box at every time-step. We also implement the method proposed by Yamaguchi [139], and an extension of the method proposed by Hindmarsh et al. [69].

Moreover, the phenomenological terms appearing in the analytical model have parameters that have to be calibrated using the numerical simulations. We use the data obtained from the simulations to perform the calibration. All in all, in this work we will determine more accurately the values of the parameters for the monopole VOS model, and also give a measure of the accuracy of each velocity estimator, as well as the accuracy of the numerical approximations used for the simulations.

Before starting the description of the procedure to measure the global monopole velocities it is desirable to comment that these simulations are not only interesting for networks of global monopoles. In fact, as we have shown in Section 2.4.2, global monopoles are also present in the semilocal string model [4, 66, 129]. These strings are non-topological, and thus can have ends. The field configuration around the ends of the strings could be identified with some sort of global monopole. Therefore, the new method proposed here can be used to characterise the semilocal string model, as we will see in Chapter 5.

The rest of the Chapter is organised as follows. In Sect. 4.2 we describe the field theory simulations that we performed. We then present three different velocity estimators in Sect. 4.3, including our new estimator. We report the results obtained from those methods in Sect. 4.4. In Sect. 4.5 we use the results obtained to calibrate the analytical model for global monopoles. Finally we conclude in Sect. 4.6.

4.2. Field Theory Simulations of Global Monopoles

4.2.1. Simulations and Scaling

The defects that we will analyse in this section are global monopoles which are created in an $O(3)$ model when the $O(3)$ symmetry spontaneously breaks down to $O(2)$. In Section 2.4.1 we have analysed the properties of this model in detail, where we have said that this model can be described by the following Lagrangian (2.67),

$$\mathcal{L} = \frac{1}{2}\partial_\mu \Phi^i \partial^\mu \Phi^i - \frac{1}{4}\lambda(|\Phi|^2 - \eta^2)^2, \tag{4.1}$$

where $|\Phi| \equiv \sqrt{\Phi^i \Phi^i}$ and λ and η are real constant parameters. In the monopole case $i = 1, 2, 3$ and Φ^i are real fields. Since our aim is to study the dynamics of a network of global monopoles in an expanding universe, we consider, as in the AH case, a flat Friedmann-Robertson-Walker space-time with comoving coordinates:

$$ds^2 = a(\tau)^2\Big(- d\tau^2 + dx^2 + dy^2 + dz^2\Big), \tag{4.2}$$

where $a(\tau)$ is the cosmic scale factor and τ is conformal time.The equations of motion can be derived from the Lagrangian (4.1) for global monopoles and they are,

$$\ddot{\phi}^i + 2\frac{\dot{a}}{a}\dot{\phi}^i - \nabla^2\phi^i = -a^2\lambda(\phi^2 - \eta^2)\phi^i, \tag{4.3}$$

where the dots represent derivatives with respect to the conformal time τ.

It is also convenient to perform rescalings to reduce the number of parameters governing the behaviour of the model,

$$\begin{aligned} \Phi^i &\rightarrow \tilde{\Phi}^i = \frac{\Phi^i}{\eta}\,, \\ x^\mu &\rightarrow \tilde{x}^\mu = \sqrt{\lambda_0\eta^2}x^\mu\,. \end{aligned} \tag{4.4}$$

Substituting (4.6) in (4.3), we now have:

$$\ddot{\phi}^i + 2\frac{\dot{a}}{a}\dot{\phi}^i - \nabla^2\phi^i = -a^2(\phi^2 - 1)\phi^i. \tag{4.5}$$

At this point we can observe that the monopole size $\delta \approx (\sqrt{\lambda}\eta)^{-1}$, which is a fixed physical length scale, rapidly decreases in comoving coordinates. Thus, in order to obtain a representative network, extreme care is needed when setting the parameters controlling the evolution of the simulations. Otherwise the monopole size could be too small to be resolved during the simulation, or too large initially and monopole cores could be overlapping. As we have pointed out in

s	Cosmology	$\tau_{\rm dif}$	$\tau_{\rm ini}$	$\tau_{\rm end}$	τ_s
0	Mat&Rad	12.5	150	510	5 for $\tau < 200$, otherwise 10
1	Rad	25	210	510	10
1	Mat	25	250	510	10

Table 4.1.: *Description of the time parameters for every different simulation, as explained in the text.*

Chapter 2, this is a well-known issue in lattice simulations, and that difficult is overcome by the use of the Press-Ryden-Spergel algorithm [115]. The algorithm proposes to turn the coupling constant into a time-dependent variable:

$$\lambda = \lambda_0 a^{-2(1-s)}. \tag{4.6}$$

In order to perform numerical simulations of this model we use the procedure we have described in Section 2.3.4. We have simulated the system in 2048^3 lattices for radiation and matter dominated eras, with two different values of the s parameter: $s = 0$ and $s = 1$. We have performed five production simulations for each case which, given the high number of monopoles in each simulations, give us appropriate statistics. As a good compromise, for the computing power available to us, we chose $\Delta x = 0.5$ and $\Delta t = 0.25$, where Δx and Δt are lattice and time spacings measured in units of $[\eta^{-1}]$, respectively.

We found that Vachaspati-Vilenkin [130] type initial conditions are a good choice in our case to obtain the scaling regime as fast as possible: the scalar field velocities are set to zero and scalar fields are chosen to lie in the vacuum manifold, but have randomly chosen orientations. This field configuration has to relax into a network of scaling monopoles and we achieve this by using a period of diffusive evolution, with the second derivatives removed from the equations of motion.

Depending on the nature of the simulation (cosmological era and value of s) the system needs to undergo different periods of diffusion $\tau_{\rm dif}$ in order to aid in reaching the scaling regime. After the diffusion regime, the equations of motion are solved. The scaling regime is obtained at different stages in each case, and bearing that in mind, we start extracting data from time $\tau_{\rm ini}$ until $\tau_{\rm end}$. It is numerically very expensive to analyze the system every single time-step, but it needs to be analysed often enough to obtain meaningful results. The compromise between these two situations is reached by analyzing the system every τ_s time-units. The parameters and details of each case can be found in Table 4.1.

It is of great importance to test the scaling regime of the system before starting to acquire meaningful results. We test it by monitoring that a characteristic length of the network grows linearly in time. In fact, we use two different characteristic lengths in this work:

On the one hand, we can define a velocity-one-scale (VOS) type length-scale [98, 99]

$$\Big(\frac{V}{\mathcal{N}}\Big)^{1/3} = \gamma_m \tau\,, \tag{4.7}$$

where V is the volume of the simulation box, $\mathcal{N}$ is the number of monopoles[1] in the simulation box, and γ_m is a proportionality constant. In Fig. 4.1 we show that, after a burn in period, the simulation reaches a regime where $(V/\mathcal{N})^{1/3}$ is approximately linear with respect to τ.

On the other hand, we can obtain the characteristic length scale of the network from the

[1]We will refer to monopoles *and* antimonopoles as just monopoles, for simplicity, unless the distinction is meaningful, where we will revert to distinguishing them.

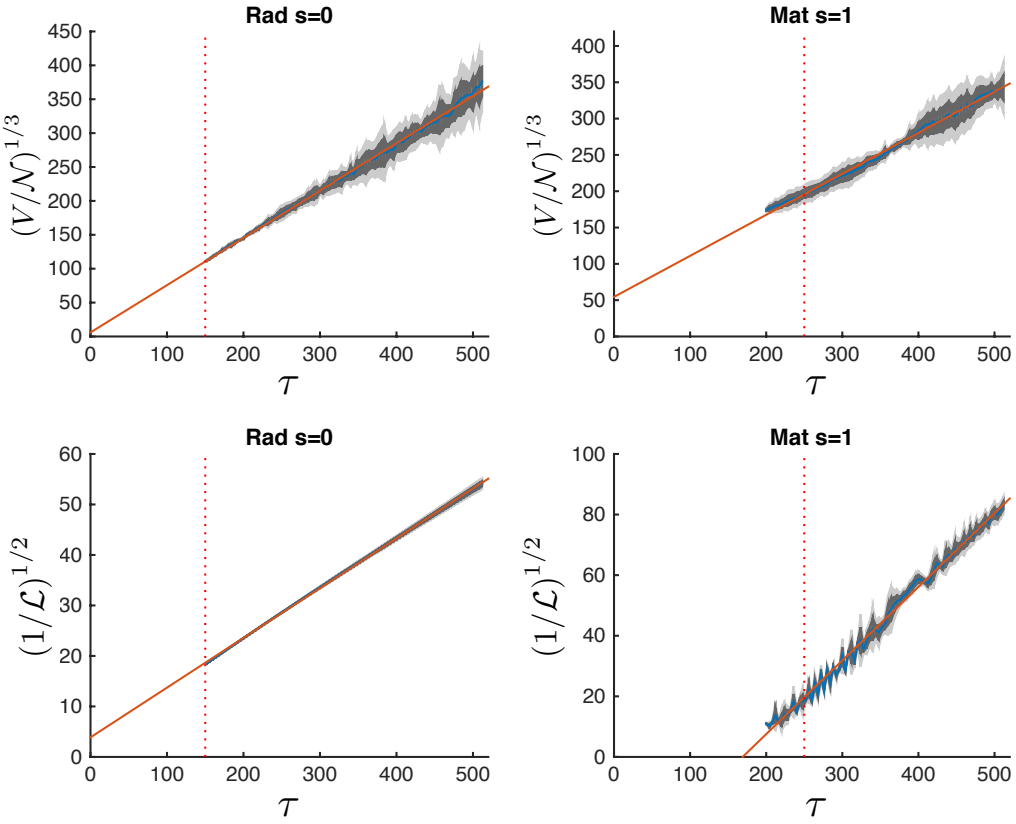

Figure 4.1.: *Scaling regions computed using the monopole number ($\mathcal{N}$) and the Lagrangian density ($\mathcal{L}$) as the characteristic lengths of the network. The two extreme cases are shown: radiation era with $s = 0$, where the system reaches a smooth scaling regime in a comparatively long period of time; and Matter era with $s = 1$, where the scaling regime is not so smooth and in a shorter time interval.*

	γ_m		$\gamma_{\mathcal{L}}$	
s	Radiation	Matter	Radiation	Matter
0	0.72 ± 0.06	0.65 ± 0.04	0.1± 0.05	0.20 ± 0.05
1	0.76 ± 0.03	0.58 ± 0.03	0.1±0.05	0.25 ±0.05

Table 4.2.: *Values of γ_m and $\gamma_{\mathcal{L}}$ for matter and radiation eras. Note that for a given era, the values obtained for different s are compatible.*

Lagrangian [29],

$$\left(\frac{\eta^2}{-\mathcal{L}}\right)^{1/2} = \gamma_{\mathcal{L}}\tau\,, \tag{4.8}$$

where $\gamma_{\mathcal{L}}$ is another proportionality constant. Fig. 4.1 shows also that the quantity $(\eta^2/-\mathcal{L})^{1/2}$ reaches a region where it is approximately linear in τ. The two proportionality constants, γ_m and $\gamma_{\mathcal{L}}$, refer to two different quantities in the simulations: the former refers to the number of monopoles in the network while the second refers to the typical intermonopole distance. The values of γ_m and $\gamma_{\mathcal{L}}$ for each different type of simulation are shown in Table 4.2.

We achieve scaling for all different cases simulated, though at different stages. The cases with $s = 0$ are the ones which reach scaling fastest, and therefore, have the longest dynamical range simulated. For the $s = 1$ case, the radiation simulations achieve scaling earlier than the matter case. Besides, in the matter $s = 1$ case, the lagrangian measure of scaling has much more structure than the other cases, i.e., there are some small spikes along the straight line. As an example, we plot the scaling regime for the two extreme cases in Fig. 4.1: radiation era with $s = 0$, which reaches scaling fastest and the scaling line is rather smooth, and the Matter era with $s = 1$, which has the latest onset of a bumpier looking scaling. In the other two cases the scaling regime is as smooth as in radiation era with $s = 0$ but in the case of radiation era with $s = 1$, scaling is reached later.

Note that the $s = 1$ case is the closest to the real equations of motion, but the dynamical range obtained is shorter than that of the $s = 0$ case. Therefore, we have more 'realistic' data with $s = 1$, though with shorter dynamical range and less statistics; and data obtained from modified equations of motion with $s = 0$ (and therefore with a higher level of modelling), but with higher dynamical range and more statistics. We will show in the following sections that both approaches give compatible results. This can also be seen in Table 4.2, where the values of γ_m and $\gamma_{\mathcal{L}}$ for each different types of simulation are shown to be compatible within the same cosmological era.

Once the system reaches scaling, quantities of interest can be measured: for example, monopole velocities. There are several systematic errors that the reader should be aware of. On the one hand, there are numerical errors inherent to the simulation of the dynamics of the system. By these we mean errors arising form the discretisation of the equations, errors due to the limited dynamical range and errors coming from the Press-Ryden-Spergel algorithm. On the other, there will be errors coming from the procedure used in tracking each monopole's trajectory, as explained in the next section.

4.3. Monopole velocity estimators

The magnitude of interest in this work is the averaged network velocity of the monopoles. There are two procedures proposed in the literature to obtain the network velocity, which we will revisit momentarily. But first, we will describe in detail the novel procedure proposed in this work, called

the *Monopole–Tracking* Method.

4.3.1. Monopole-Tracking Velocity

In this method we calculate the monopole velocity by measuring directly the distance traveled by a monopole in a specific period of time. In order to do so, we need to pinpoint where each monopole is at every time step, we need to determine where it moves to at the following step and we need to track all the steps of each monopole.

Note that we are evolving field values in each lattice point, and not point-like global monopoles. For this reason every time step we have to identify monopole positions within the lattice; that is, we have to translate the information from field values to monopole positions. In this case the translation is done by working out the topological charge in each one of the lattice points. The topological charge of monopoles is given by the surface integral [137]

$$N = \frac{1}{8\pi} \oint dS^{ij} |\Phi|^{-3} \epsilon_{abc} \Phi^a \partial_i \Phi^b \partial_j \Phi^c. \tag{4.9}$$

Thus, in order to determine the location of a monopole, we calculate whether the integral (4.9) has a non-zero value. Actually, since we are in a discretized environment, we do not use directly formula (4.9), but rather a discrete version of it. We identify monopoles in a lattice by generalizing the well known "geodesic rule" used in most cosmic-string lattice based simulations [130].

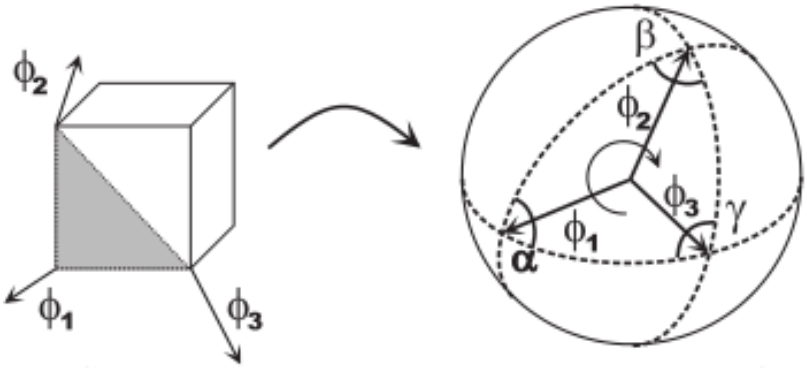

Figure 4.2.: *The monopole charge in a cubic cell is identified by projecting the field-vectors at every corner onto a unit sphere. Each triangle on the faces of the cube is thus mapped into a spherical triangle (the one with the smallest surface is chosen). The sum of the surface of all these triangles, divided by 4π, is then taken as defining the monopole charge inside cubic cell. Picture courtesy of M. Kunz [18].*

We count the winding of the field-vectors around each unit cell in our grid by using a "smallest area" assumption. For this we triangulate the faces of each lattice cube and then map the $O(3)$ field-vectors at all corners onto the unit sphere. We can do this due to the fact that the presence of a monopole depends only on the orientation of the field and not on its norm. Each triangular element in the cube's surface defines a solid angle on the unit sphere, see Fig. 4.2, where the sign of the solid angle is taken according to the handedness of the corners. Its value Θ can be calculated thanks to a formula that relates the area of the spherical triangle, defined by three vectors on a unit sphere, to the angles between the geodesic sides of the triangle:

$$|\Theta| = \alpha + \beta + \gamma - \pi. \tag{4.10}$$

Adding the solid-angles corresponding to all 12 triangles in the cube's surfaces, we obtain $\sum \Theta = 4\pi n$ where n is an integer taken to be the charge of the monopole inside the lattice cube.

Using this method we are able to detect positions in the lattice with non-zero topological charge; i.e., we detect the positions of both monopoles (positive topological charge) as well as anti-monopoles (negative topological charge). As mentioned before, the monopole number $\mathcal{N}$ will be given by

$$\mathcal{N} = m + \bar{m}, \tag{4.11}$$

where m refers to the number of monopoles and $\bar{m}$ to the number of anti-monopoles in the simulation.

The detection of monopoles is performed during run-time, together with the evolution of the equations of motion. In principle one would like to detect monopoles every time step. However, the topological charge calculation is very time consuming, and instead of computing it for every time step, we only computed it for every τ_s time interval. Table 4.1 shows the values of τ_s for every case. At early times a finer τ_s is necessary because the density of monopoles is higher, and at later times a coarser search is enough. We have checked in a few simulations that the results obtained using these τ_s gives the same result as performing it at every single time step.

Once all monopoles in all time steps have been detected, we start the reconstruction of the world line of each monopole. In order to do so, we need to identify where each monopole has travelled from time τ_1 to time τ_2; or in other words, we have to identify all monopoles at time τ_1 with all monopoles at time τ_2. This matching procedure is achieved by computing the distances between monopoles at time τ_1 and those at time τ_2; and pairing the ones that are closest to each other. We are aided by these two considerations: first, we check that the topological charge of the two monopoles to be paired is the same, that is, a monopole does not turn into an antimonopole as it moves, or viceversa. The other consideration is that of maximum distance: we do not want a monopole to travel much faster than the speed of light.

This second consideration needs some explanation. Imagine the following situation: a monopole just met an antimonopole in the simulation just after time τ_1. Thus, in the next time step to be analyzed (τ_2) they have both annihilated each other. However, our procedure is unaware of the annihilation and would still find the monopole at time τ_2 that is closest to the monopole at τ_1 under consideration. Since that monopole is nowhere to be found in τ_2, it will pair it with another monopole, with the one that is the closest, even though that would be another monopole. If we did not account for this kind of event, we would obtain extremely high velocities when annihilation events happen. In order to avoid these, we suppress all monopole pairings that mean velocities higher than 1.5 times the speed of light[2]. We allow for speeds higher than the speed of light since previous works [139] measured velocities compatible with superluminal velocities.

Once the monopoles (and antimonopoles) have been paired, we then start reconstructing their path. First we match all monopoles at time τ_1 with those at time τ_2; then we match those at time τ_2 with those at time τ_3; and so forth. This way we can obtain the whole worldline of each monopole in the simulation box. In Fig. 4.3 the whole process to obtain a worldline of one specific monopole in the simulation box is shown.

There is, however, another subtlety: since we are in a discretized situation, there are instances when a monopole is not inside a dx^3 cube, but it is moving through the face that divides two dx^3 cubes (see Fig. 4.4), and the algorithm fails to detect it. In those instances, the corresponding

[2]We also checked the results with a cutoff of c, $2c$ and $3c$. We found out that a cutoff of c gave the same results as $1.5c$, but decided to keep the higher cutoff to show explicitly that we were allowing for superluminal velocities. In the higher cutoff cases ($2c$ and $3c$) the velocities obtained were higher, but in all cases it was due to monopoles being matched to the wrong monopole; not because their actual velocity was superluminal.

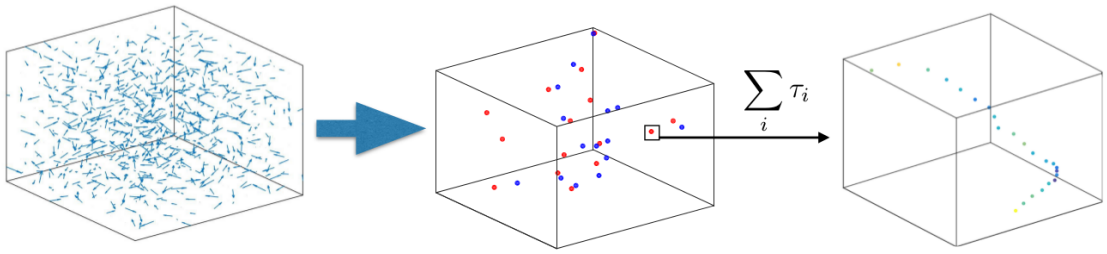

Figure 4.3.: *In this figure we show the procedure to obtain the traveling path of a monopole. In the left figure the box is shown as we output it from the simulation. This means that we only have information of the fields and not of monopole positions. In the middle figure one can see the simulation box after computing the topological charge in each lattice site using (4.9), where blue the dots represent monopoles and red ones antimonopoles. Finally in the right figure a path described by a single monopole is shown. In order to obtain this worldline we have to analyse every time step and match the positions of the same monopole in each one of them.*

monopole at a previous time-step remains unmatched, and the monopole at the following time-step may seem to have appeared from thin air. In order to account for this problem, whenever a monopole failed to be matched with a monopole from the *previous* step, we looked at two time steps back to match it with a monopole there. With this method we observe that all instances of monopoles coming out of nowhere were solved.

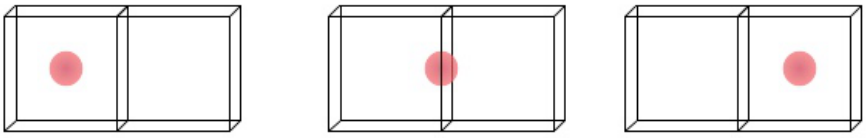

Figure 4.4.: *In this set of images a monopole moving through the face that divides two dx^3 cubes can be seen. In the left figure we will measure a topological charge of one unit in the left cube and zero charge in the right cube. In the right figure we will have zero topological charge in the left cube and a unit topological charge in the right one. The monopole will be located in both cases. But, in the middle image the monopole is crossing through the face that divides both of the dx^3 cubes and in this case we will have zero topological charge in both of them and the monopole will not be detected.*

Once we have the paths of all the monopoles in the simulation box, the velocities can be obtained straightforwardly by dividing the distance traveled by the monopole by the time lapsed to travel that distance. Then we can average over all the velocities of the monopoles to obtain a network average velocity. This number can be used for the calibration of the effective model of global monopoles; and it can also be used to compare with the velocities obtained with the other network velocity estimators explained below.

4.3.2. Local Velocity Estimator

This method was proposed by Yamaguchi [139] to estimate global monopole network velocities using field values. It relies on the fact that all the information about the global monopoles

is included in the scalar fields. We summarize the method, that we will refer to it as the Local Velocity Estimator (LVE), in the following lines and direct the interested reader to [139] for details. Then we will explain a change we made to the original method.

Let us assume that the monopole at τ_0 is located at $\mathbf{x_0}$, and at a sufficiently close time τ is at $\mathbf{x}$. Let us expand the scalar fields $\phi^i(\mathbf{x},\tau)$ around $\phi^i(\mathbf{x_0},\tau_0)$ up to first order,

$$\phi^i(\mathbf{x},\tau) \simeq \phi^i(\mathbf{x_0},\tau_0) + \nabla\phi^i(\mathbf{x_0},\tau_0)(\mathbf{x}-\mathbf{x_0}) + \dot{\phi}^i(\mathbf{x_0},\tau_0)(\tau-\tau_0)\,. \tag{4.12}$$

Bearing in mind that the position of the monopole means that the scalar fields vanish, we have that at times τ_0 and τ both $\phi^i(\mathbf{x_0},\tau_0)=0$ and $\phi^i(\mathbf{x},\tau)=0$, which lead us to

$$\nabla\phi^i(\mathbf{x_0},\tau_0)(\mathbf{x}-\mathbf{x_0}) + \dot{\phi}^i(\mathbf{x_0},\tau_0)(\tau-\tau_0) = 0\,. \tag{4.13}$$

These equations can be solve by Cramer's formula [139]. Let us first define the matrix M as

$$M = \begin{vmatrix} A^1_x & A^1_y & A^1_z \\ A^2_x & A^2_y & A^2_z \\ A^3_x & A^3_y & A^3_z \end{vmatrix}\,, \tag{4.14}$$

where $\mathbf{A}^i = \nabla\phi^i(\mathbf{x_0},\tau_0)$. Defining $B^i = \dot{\phi}^i(\mathbf{x_0},\tau_0)$ we have that

$$\frac{(\mathbf{x}-\mathbf{x_0})_j}{\tau-\tau_0} = -\frac{\det(\mathbf{M}_j)}{\det(\mathbf{M})}\,, \tag{4.15}$$

where $\mathbf{M}_j$ is the matrix formed by replacing the j-th column of $\mathbf{M}$ by the column vector B. For example $\mathbf{M}_2$ takes the following form:

$$\mathbf{M}_2 = \begin{pmatrix} A^1_x & B^1 & A^1_z \\ A^2_x & B^2 & A^2_z \\ A^3_x & B^3 & A^3_z \end{pmatrix}\,. \tag{4.16}$$

The velocity of global monopoles can thus be estimated as

$$v = \frac{|\mathbf{x}-\mathbf{x_0}|}{\tau-\tau_0}\,. \tag{4.17}$$

As explained in [139], one main source of errors for LVE comes from the fact that a monopole does not generally lie just on the lattice point in a simulation, but the actual zero of the fields is between lattice points, and therefore the LVE approximation is not accurate. Thus, the monopole detection algorithm used in [139] was prone to errors, and at some lattice points the velocities obtained were extraordinarily large, even at points that had nothing to do with a monopole core [139].

In order to reduce these errors we have refined Yamaguchi's approach. Since we do have the information (at run-time) of the location of the monopoles via their topological charge, we only compute velocities using LVE at the eight vertices of the cubic cell where the monopole is located. We then average the velocity over the eight points. This improves the prediction, but still the error in the velocity of each individual monopole is quite significant, and we still get situations with velocities that are very high. We then disregard instance where the value is greater than 1.5 and average over all monopoles to obtain a meaningful estimate. Thus, we will report only the average velocity of the monopole network.

4.3.3. Average Velocity Field Estimator

This method was originaly proposed by [69, 73] for Abelian Higgs cosmic strings, but it can readily be used for global monopoles [65]. As LVE, the Average Velocity Field Estimator (AVFE) uses the values of the fields at each lattice point to estimate network velocities. In the AVFE, the velocity is obtained directly by the local values of the derivatives of the fields, more precisely, using the fact that in a moving defect solution, the canonical scalar momentum $\mathbf{\Pi} = \partial_0 \mathbf{\Phi}$ is given by Lorentz boost of the static field configuration.

In order to compute the velocity from the expression of the Lorentz boost we will consider that all the energy in the field is in the form of a global monopole. We will denote with the subscript s all the variables measured in the local rest frame, for example, $\mathbf{x}_s$ will be the rest frame coordinates. Under this considerations the fields of a monopole moving with velocity $\dot{\mathbf{x}}$ are

$$\mathbf{\Pi}(\mathbf{x}, \tau) = \gamma \dot{\mathbf{x}} \partial \mathbf{\Phi_s}(\mathbf{x}_s), \tag{4.18}$$

$$\partial \mathbf{\Phi}(\mathbf{x}, \tau) = \gamma \hat{\mathbf{v}} (\hat{\mathbf{v}} \partial \mathbf{\Phi}_s(\mathbf{x}_s)) + \hat{\partial} \mathbf{\Phi_s}(\mathbf{x}_s), \tag{4.19}$$

where $\hat{\mathbf{v}}$ is a unit vector in the direction of the velocity, $\gamma = 1/\sqrt{1 - \dot{\mathbf{x}}^2}$ is the boost factor, and $\partial \mathbf{\Phi}(\mathbf{x}, \tau)$ and $\hat{\partial} \mathbf{\Phi_s}(\mathbf{x}_s)$ are 3-vectors. The components of $\hat{\partial} \mathbf{\Phi_s}(\mathbf{x}_s)$ are,

$$\hat{\partial}_i \mathbf{\Phi_s}(\mathbf{x}_s) = (\delta_{ij} - \hat{v}_i \hat{v}_j) \partial_j \mathbf{\Phi}_s(\mathbf{x}_s). \tag{4.20}$$

Once we know the expressions for the boosted field configurations we can use them to write the kinetic, (E_Π) and gradient, (E_∂) energies in the following way:

$$E_\Pi = \int d^3x |\mathbf{\Pi}|^2 = \int \frac{d^3 x_s}{\gamma} |\gamma \dot{\mathbf{x}} \partial \mathbf{\Phi}_s|^2, \tag{4.21}$$

$$E_\partial = \int d^3x |\partial \mathbf{\Phi}|^2 = \int \frac{d^3 x_s}{\gamma} |\gamma \hat{\mathbf{v}} (\hat{\mathbf{v}} \partial \mathbf{\Phi}_s(\mathbf{x}_s)) + \hat{\partial} \mathbf{\Phi_s}(\mathbf{x}_s)|^2, \tag{4.22}$$

where we have used $\mathbf{x}_s = \mathbf{x} + \hat{\mathbf{v}} \gamma (\hat{\mathbf{v}} \mathbf{x} - v\tau)$ ($\mathbf{v} = \dot{\mathbf{x}}$). These expressions can be rearranged,

$$E_\pi = \frac{\dot{\mathbf{x}}^2 \gamma}{3} \int d^3 x_s |\partial \mathbf{\Phi_s}|^2, \tag{4.23}$$

$$E_\partial = \int d^3 x_s \frac{(\gamma^2 - 1)}{\gamma} |\hat{\mathbf{v}} \partial \mathbf{\Phi_s}|^2 + \int \frac{d^3 x_s}{\gamma} |\partial \mathbf{\Phi_s}|^2 = \frac{(\gamma^2 + 2)}{3\gamma} \int d^3 x_s |\partial \mathbf{\Phi_s}|^2. \tag{4.24}$$

So, if we divide E_π with E_∂ we can obtain the following expression,

$$\frac{E_\Pi}{E_\partial} = \frac{\dot{\mathbf{x}}^2 \gamma^2}{\gamma^2 + 2} = \frac{\dot{\mathbf{x}}^2}{3 - 2\dot{\mathbf{x}}^2}. \tag{4.25}$$

From the expression above one can directly obtain the velocity. Since we are interested in the velocities of the monopoles, we want our estimator to pinpoint regions with monopoles. In order to do so, we weight the derivates of the fields with the potential energy, since the potential energy peaks at sites where the fields are close to zero, denoting (mostly) the core of the monopole. We denote the weighting of a field $\mathcal{X}$ with respect of the potential energy $\mathcal{V}$ as

$$\mathcal{X}_\mathcal{V} = \frac{\int d^3x \; \mathcal{X} \; \mathcal{V}}{\int d^3 x \; \mathcal{V}} \, . \tag{4.26}$$

Using this definition for a *weighted average*, the ratio $R_{\mathcal{V}} = E_{\Pi\mathcal{V}}/E_{\partial\mathcal{V}}$ read

$$R_{\mathcal{V}} = \frac{E_{\Pi\mathcal{V}}}{E_{\partial\mathcal{V}}} = \frac{\int d^3x E_{\Pi}\mathcal{V}}{\int d^3x E_{\partial}\mathcal{V}} \tag{4.27}$$

Thus, using the expression for $R_{\mathcal{V}}$, we can obtain our AVFE $\langle \dot{\mathbf{x}}^2 \rangle$ as:

$$\langle \dot{\mathbf{x}}^2 \rangle = \frac{3R_{\mathcal{V}}}{1 + 2R_{\mathcal{V}}} \,. \tag{4.28}$$

We can obtain a visual confirmation that this algorithm indeed succeeds in selecting the regions where there are monopoles. In Fig. 4.5 a configuration of monopoles as detected by calculating topological charge is plotted, and also the values of the potential energy that are greater than a threshold. It is clear that the potential energy mimics the monopole positions satisfactorily. We observe, however, that even though all the monopoles are recovered, there are some regions that do not correspond to a monopole (in cyan, in the figure). Those points would correspond to, for example, a monopole-antimonopole pair that have annihilated, and there is still considerable potential energy in the region, even though there is no topological charge. It could also be the case that the monopole is crossing a face of a cube, and thus we do not detect it by the topological charge, but the potential energy is able to pinpoint it. In any case, we will see in Section 4.4 that the effects of these regions are very small.

4.4. Velocity Results

We have used the previously described three methods to estimate the velocity of the network of monopoles. Two of the methods, the *Local Velocity Estimator* and the *Average Velocity Field Estimator* are able to give us a network average velocity only; whereas our new estimator, the *Monopole–Tracking Velocity* estimator, is able to obtain velocities of single monopoles, which can be obviously averaged over to obtain a network velocity estimator.

We used Monopole–Tracking Velocity to compute the velocities of each one of the monopoles in the simulation box for every time step. This information can be presented in two different manners. In Fig. 4.6 we have depicted the case for radiation era and $s = 0$ as an example; the behaviour is similar for the other case. In the left panel we consider the average velocity of each monopole, and plot a histogram where the bins are 20 equally spaced bins in the $[0, 1]$ range. To obtain the velocity of each monopole, we track the path of each monopole and divide the total length of the path of each monopole by the time it took to cover that distance. In the right panel, we average over the instantaneous velocity of all the monopoles for every time step, i.e., at every time-step we calculate the velocity of each monopole, and take the average of all monopoles in the box.

The values of the velocities obtained for every case can be found in Table 4.3. We have included the velocities obtained by a) the average velocity of each monopole, as obtained by dividing the total length travelled by the time taking to cover it (Total-length) and b) the average of all instantaneous velocities (Instantaneous). We also take two types of averages: a) averaging over the absolute value of the velocities ($\sum_{i=0}^{\mathcal{N}} |v_i|/\mathcal{N}$), and b) using the root mean square (RMS) of the ensemble ($\sqrt{\sum_{i=0}^{\mathcal{N}} v_i^2/\mathcal{N}}$).

Our results show that the global monopole velocity is sub-luminal; not a single monopole velocity (in any of the cases studied) was measured to be higher than 1. The average velocity is consistent with a constant velocity, and that velocity coincides with the mode of the velocity

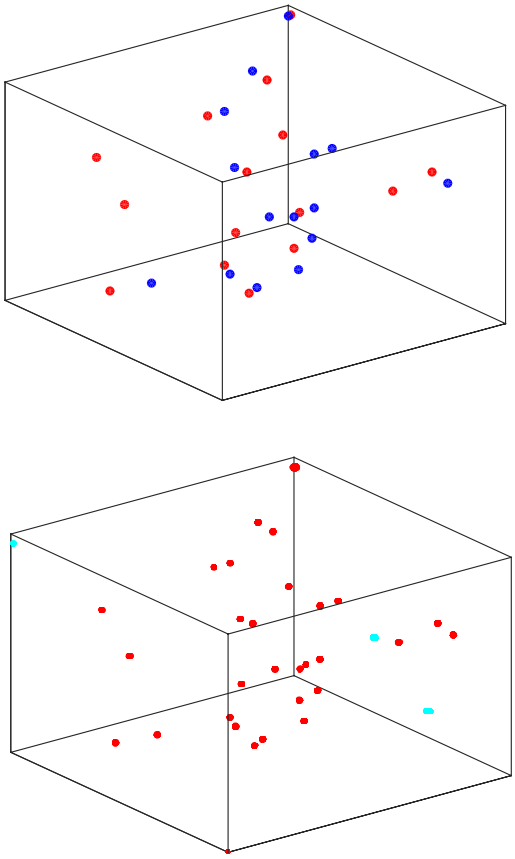

Figure 4.5.: *In the left pane the simulation box is shown after working out the topological charge in each point of the box: red dots represent antimonopoles (points where the topological charge is -1), and blue dots represent monopoles (points where the topological charge is 1). The right pane show the same simulation at the same time, but in this case regions where the value of the potential energy is high are shown. It is clear that all the monopoles and antimonopoles in the left pane have been recovered (red dots). There are few regions (in cyan) that do not correspond to a monopole detected by measuring the topological charge. These can be regions where a monopole-antimonopole pair has just annihilated, or monopoles that are crossing the face of a lattice cell, and even though they are not detected by the topological charge, they are detected by the potential energy.*

distribution (see the histogram in Fig. 4.6). The values of the velocities obtained for every case can be found in Table 4.3, both averaging over the absolute value of the velocities, and also by the RMS velocity of the ensemble.

The errors quoted include statistical errors as well as an estimation of the systematic errors. These systematic errors come mainly from the identification method: we are assuming that the monopole is at a specific point in the lattice, whereas in reality it can be anywhere inside the dx^3 cube specified by that lattice point; therefore, there is an error in the length of the path due to the discretization of the lattice. Another possible ingredient that might be included into the errors is the correlation between the measurement of individual monopole velocities. Monopoles are interacting with each other, and it is not surprising to think that there might be some correlation between the errors; but we expect this to not change drastically the error budget.

The monopole–tracking method also allows to study the velocity history of individual monopoles,

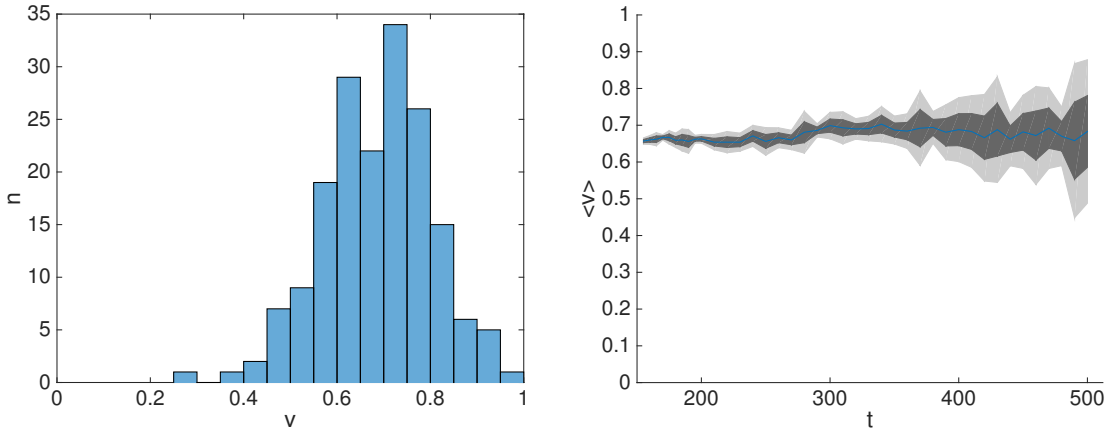

Figure 4.6.: *Values of the velocities for radiation era with $s = 0$. In the left plot the number of monopoles is divided in velocity intervals: the intervals are 20 equally spaced bins in the $[0, 1]$ range. These velocities are obtained by dividing the total length travelled by the time it takes. In the right plot we show the average of the instantaneous velocity over all monopoles in each time step. Note that even though we allow for monopoles to have velocities up to $1.5c$, we have not observed any monopole with $v > 1$ in any of the simulations we have performed.*

	Radiation		Matter	
	$s = 0$	$s = 1$	$s = 0$	$s = 1$
	Average of absolute velocities			
Total-length	0.70 ± 0.05	0.70 ± 0.05	0.62 ± 0.05	0.55 ± 0.05
Instantaneous	0.70 ± 0.09	0.70 ± 0.09	0.62 ± 0.09	0.55 ± 0.09
	Root mean square velocities			
Total-length	0.71 ± 0.07	0.70 ± 0.09	0.63 ± 0.07	0.55 ± 0.09
Instantaneous	0.72 ± 0.07	0.72 ± 0.07	0.65 ± 0.07	0.59 ± 0.06
Total	0.71 ± 0.05	0.72 ± 0.06	0.64 ± 0.05	0.57 ± 0.05

Table 4.3.: *Values of the velocities for matter and radiation eras, and for $s = 0$ and $s = 1$ cases, using the Monopole–Tracking method (Track) estimator. We report velocities obtained by considering the average velocities of the monopoles obtained by the time spent in travelling the length of their path (total-length) and by the average of the instantaneous velocities of the monopoles in each time-step (Instantaneous). We also report the average of the absolute value of the velocities, and RMS velocity value. We can see that the values given by the different methods are compatible with each other, including the values for $s = 0$ and $s = 1$. The last row shows the combined RMS velocities, combining both averaging and instantaneous velocities. Typical velocities during matter domination are somewhat slower, consistent with the higher Hubble damping.*

showing that the situation is much richer than a single network average can show. For example, Fig. 4.7 shows the path of a typical monopole, with the value of its velocity in each time step. It can be seen that the velocity history of the monopole is highly non-trivial. The monopole travels in a more-or-less straight line, then reduces its velocity to change directions, and then continues in another straight line. This can be understood by considering that the monopole may be travelling to meet an antimonopole, but before it gets there, the antimonopole has annihilated with another monopole. The field configuration around the first monopole then reorganises and the monopole

heads towards another antimonopole.

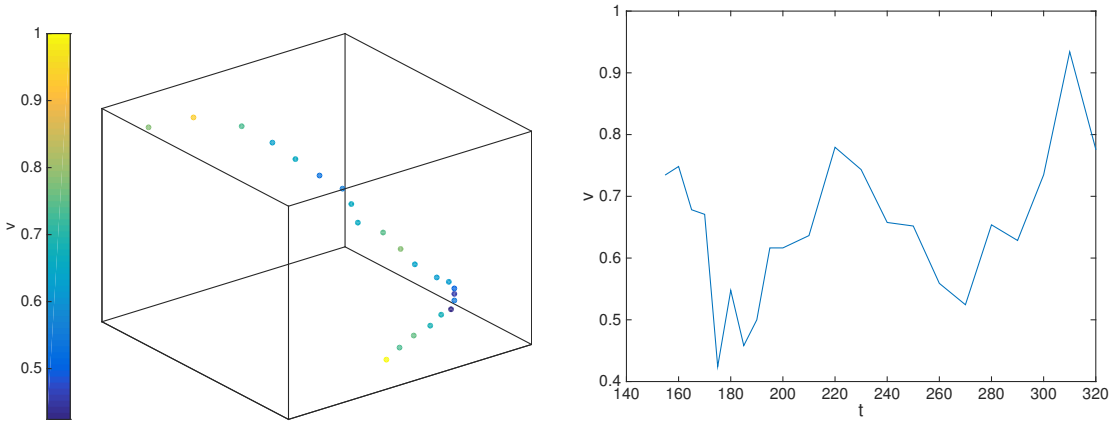

Figure 4.7.: *The left pane shows the path described by a monopole during its evolution. The initial time step is located at the bottom of the box, so the path travelled by the monopole has to be understood to go from bottom to top. The color indicates the velocity of the monopole at each time step, which can be better viewed in the right pane, showing the non-trivial velocity history of the monopole.*

We also used our improved version of the Local Velocity estimator (LVE) and the Average Velocity Field Estimator (AVFE) to obtain an average network velocity. Table 4.4 shows the values of velocities obtained with all different methods and configurations. The errors for the LVE and AVFE methods are just statistical errors. As in the previous case we are assuming that the measurements are independent, though clearly there may be some correlation between them.

	s=0			s=1		
	Track	LVE	AVFE	Track	LVE	AVFE
Radiation	0.71 ± 0.05	0.7 ± 0.1	0.85 ± 0.06	0.72 ± 0.06	0.7 ± 0.1	0.90 ± 0.09
Matter	0.64 ± 0.05	0.6 ± 0.1	0.76 ± 0.08	0.57 ± 0.05	0.6 ± 0.1	0.80 ± 0.09

Table 4.4.: *Values of the RMS velocities for matter and radiation eras using the methods described in the text: the Monopole–Tracking method (Track), the Local Velocity estimator (LVE) and the Average Velocity Field estimator (AVFE). The monopole–tracking values quoted here are the average of the RMS velocities obtained by a combination of 'average' and 'instantaneous' averages (see Table 4.3). We can see that the values given by the different methods are compatible with each other, including the values for $s = 0$ and $s = 1$.*

We see that the results obtained using the three different methods are compatible with each other (within $1-\sigma$ for $s = 0$ and $2-\sigma$ for $s = 1$); and in all cases the velocities are subluminal. We also see that the velocity of monopoles in the radiation era is higher than in the matter era, consistent with the lower Hubble friction in radiated–dominated expansion.

The agreement between the Tracking and the LVE methods is remarkable. The Average Velocity Field Estimator, however, tends to overestimate the velocity of the monopoles, but this is not surprising since the weighting method encapsulates points in the simulation which have some velocity but are not monopoles. For example, the AVFE includes regions where a monopole-antimonopole have annihilated and have left some temporary residual potential energy, before it decays away like radiation. It is reasonable to think that those regions would contribute with high velocity to the average.

We can also see that the results obtained using the $s = 0$ and $s = 1$ cases are very similar. Bear in mind the dilemma in deciding what procedure to use: either we simulated for a longer dynamical range with modified equations of motion; or we simulated the equations of motion but for a shorter dynamical range. Our results show that both methods render results that are compatible with each other. Therefore, it seems appropriate to take advantage of both the larger dynamical range and the fact that the true equations of motion can be simulated to report the velocity of the global monopoles combining all simulations together.

The average velocities of a network of global monopoles, combining the $s = 0$ and $s = 1$ simulations, together with the three velocity estimation methods described above, for radiation and matter dominated epochs, respectively, are

$$v_r = 0.76 \pm 0.07\,, \qquad v_m = 0.65 \pm 0.08\,. \tag{4.29}$$

The errors are obtained by averaging over all the data (three methods, five simulations and both values of s). We have been conservative in the errors quoted, bearing in mind that the measurements may not be totally uncorrelated, and that there may be some (small) changes due to correlations.

4.5. Calibration of the VOS model for global monopoles

Using the data obtained from our simulations we can determine the phenomenological parameters in the analytical model for global monopoles we have describe in Section 2.4.1. First of all, we will remind the reader how the length scale, L, and the RMS velocity, v, are described by the following equations

$$3\frac{dL}{dt} = 3HL + v^2\frac{L}{l_d} + cv, \tag{4.30}$$

$$\frac{dv}{dt} = (1-v^2)\Big[\frac{k}{L}\Big(\frac{L}{d_H}\Big)^{3/2} - \frac{v}{l_d}\Big]. \tag{4.31}$$

The parameters H and d_H are the Hubble parameter and the Hubble horizon size, and t is the physical time (as opposed to the conformal time in Eq. (4.3)). The overall damping length which includes both the effect of Hubble damping and of friction due to particle scattering is parametrised by l_d. Finally, c and k are the parameters governing the phenomenological terms, and these are the parameters that we will calibrate using our data.

We are interested in identifying the scaling solutions for this model. In order to do so, we first observe that in our simulation the characteristic length of the network (see Eq. 4.7) is proportional to time[3] and that the velocities are constant:

$$L = \epsilon t\,, \qquad v = v_0 = const. \tag{4.32}$$

As shown in [97], for expansion rates of the form $a(t) \propto t^\lambda$ with $\lambda < 3/4$ (which includes matter– and radiation–domination), the equations (4.30) - (4.31) admit two branches of scaling solutions: an ultrarrelativistic one with $v_0 = 1$ and a subluminal one with $v_0 < 1$. We will not study the values of the parameters for the luminal branch, since our simulations show no evidence

[3]Note that the parameter ϵ is the analogous to the parameter γ_t in Eq. 4.7, but time is now physical instead of conformal.

of its existence. For the subluminal branch we can read off the values of c and k[4],

$$\epsilon = \frac{cv_0}{3(1-\lambda) - \lambda v_0^2}\,, \qquad k = \frac{\lambda v_0}{(1-\lambda)^{3/2}\epsilon^{1/2}}. \tag{4.33}$$

	s=0			s=1		
	ϵ	c	k	ϵ	c	k
Radiation	1.42± 0.09	2.5±0.2	0.76 ± 0.02	1.53 ± 0.04	2.6±0.2	0.92 ± 0.02
Matter	1.97 ±0.09	2.2± 0.2	1.55 ± 0.04	2.00 ±0.06	2.7± 0.2	1.42± 0.02

Table 4.5.: *Values of the analytical parameters for matter ($\lambda = 2/3$) and radiation ($\lambda = 1/2$) and for $s = 0$ and $s = 1$.*

In Table 4.5 we show the results obtained using equations (4.33) and our numerical results. To obtain the values for ϵ we have used the slopes of the scaling curves, as given in Table 4.2. As for the values for the velocity, we have used the velocity obtained by averaging over all three methods of RMS velocity estimation discussed in section 4.4 and shown in Table 4.4.

Since the velocity results for both $s = 0$ and $s = 1$ are compatible with each other, and they complement each other, we could also try to combine all simulations with different s to obtain an estimate of parameters c and k. This way we obtain a more conservative value of the errors on the parameters. The values obtained averaging over all simulations, both with $s = 0$ and $s = 1$, can be seen in Table 4.6.

	ϵ	c	k
Radiation	1.47 ± 0.09	2.6 ± 0.3	0.9 ± 0.1
Matter	1.98 ± 0.07	2.5 ± 0.3	1.6 ± 0.2

Table 4.6.: *Values of the analytical parameters for matter and radiation averaging over all simulations with $s = 0$ and $s = 1$. We first average over all velocities, and then use that average (with errors) to obtain the value of c and k.*

We see that the values of c in radiation and matter are compatible with each other, but even when treating the errors conservatively, there is tension on the value of k from the radiation and matter simulations. We will discuss this further in the next section.

We can compare our results with the values of the parameters previously given in [97], where they used two different sets of simulations to determine the value of their parameters. On the one hand they use the results due to the work by Yamaguchi [139], to obtain both the values of ϵ and the velocity:

$$\begin{aligned} \epsilon_r &\sim 1.3 \pm 0.4\,, \qquad & c_r &\sim 1.3 \pm 0.7\,, \\ \epsilon_m &\sim 1.6 \pm 0.1\,, \qquad & c_m &\sim 1.2 \pm 0.6\,. \end{aligned} \tag{4.34}$$

On the other, they use the values of ϵ from the work by Bennett and Rhie [26], combined with

[4] In the first version of the paper related with this Chapter there is an error on the expression of c. We gratefully thank the authors of [125] for pointing out the mistake.

the velocities obtained by Yamaguchi (Bennett and Rhie do not give estimates for the velocities):

$$\begin{aligned} \epsilon_r &\sim 1.3 \pm 0.2\,, \qquad & c_r &\sim 1.3 \pm 0.5\,, \\ \epsilon_m &\sim 1.9 \pm 0.2\,, \qquad & c_m &\sim 1.4 \pm 0.7\,. \end{aligned} \tag{4.35}$$

The uncertainties in v_0 were such that it was not possible to determine whether monopoles move subluminally or luminally. Likewise, due to the uncertainties it was not possible to determine the k parameter (from Eq.(4.33)) in [97].

4.6. Conclusions and discussion

In this work we have obtained the most accurate values of the average network velocity of a network of global monopoles to date. These values have then been used to complete the characterization of the phenomenological "velocity–dependent one-scale" (VOS) model proposed by [97]. This model admits two branches of scaling solutions, one with $v_0 = 1$ (luminal) and one with $v_0 < 1$ (subluminal). The velocities measured in our work make it possible to determine, for the first time, that only the subluminal branch is physically realized.

In order to obtain the velocities, we have implemented a new method (the monopole–tracking method) to measure global monopole velocities in a network. This method has two main steps: first, we translate from field values to monopole positions, i.e., we calculate the topological charge in field space, and translate it into a position in space. The second step identifies monopoles in each time slice, thus following the evolution of each monopole in time. This last step can be applied to any evolution of point like particles in the lattice, so our method is not specific for global monopoles and it can be used in many other situations.

The monopole–tracking method has been used to calculate the average velocities of global monopoles in a network. Nevertheless, since we can obtain the behaviour of each one of the monopoles in the box throughout the whole evolution, this method can also be used to analyse and understand the complex mechanism governing annihilation (and choice of annihilating partner) in global monopole models. We have observed how a monopole travels to meet with an antimonopole, but this antimonopole annihilates with a third monopole before the first one reaches it. Then, the monopole slows down, changes direction, and starts speeding up towards another monopole. These peculiar behaviours are interesting and are left for future work.

We have also implemented two other methods previously proposed in the literature. One of them was introduced to measure global monopoles using local variables in [139], and we call it Local Velocity Estimator (LVE). It was known that that method was prone to have high errors. We have improved the approach, as well as perform simulations in bigger lattices, to obtain results with more reasonable errors. The other method was proposed in [69, 73] (the Average Velocity Field Estimator (AVFE)) for the case of cosmic strings and uses weighted averages of field quantities to estimate directly the average network velocity. We have adapted it for the case of global monopoles and we used it in our simulations.

It is interesting to compare these two types of methods. The monopole–tracking method follows the position of the monopole over their evolution; it is a method in spacetime. The other methods, the LVE and AVFE, extract the information from field-space at every time-step. These two approaches are in principle very different, but we have showed that the results coming from LVE and AVFE agree with the results obtained using our new monopole–tracking method.

Actually, the (improved) LVE method agrees surprisingly well with the results obtained from our methods. The other method, the AVFE, also agrees, but only within 1-σ or 2-σ. The differences

come from systematic errors that can be understood from physical considerations. For example, regions that contribute to the velocity estimation in AVFE may not be from monopole position, but can be from the remnants of a monopole-antimonopole annihilation. In any case, this is a good test to show that the approaches made by considering field-theory information, and which are much easier to implement, work well.

We were also able to compare the results obtained using the so-called Press-Ryden-Spergel algorithm [115] with the *true* simulations for the case of global monopoles. The former allows for a rather larger dynamical range, but does not evolve the *true* equations of motion; instead it evolves some artificially modified equations. In the latter one has to pay the price of a short dynamical range for the benefit of simulating the true equations of motion. We show that in both cases the results obtained are compatible. This result could be extrapolated to cases where unfortunately the true equations of motion cannot be solved, and gives some reassurance that the Press-Ryden-Spergel algorithm is a reasonable approximation.

Finally, with the data obtained from the different velocity estimations, we obtain the average network velocity for global monopoles to be (4.29)

$$v_r = 0.76 \pm 0.07\,, \quad v_m = 0.65 \pm 0.08\,,$$

for radiation and matter domination epochs, respectively.

We can compare the results obtained in this work with the velocities obtained in the literature. For example, Yamaguchi [139] used the LVE to obtain the velocity values for global monopoles as:

$$v_r = 1.0 \pm 0.3\,, \qquad v_m = 0.8 \pm 0.3\,, \tag{4.36}$$

where r stands for radiation era and m for matter era. Our results are compatible with those of Yamaguchi's, but with much smaller errors. Note how Yamaguchi's numbers were not accurate enough to discard the ultrarelativistic branch.

The fact that we get such an improvement on the velocity estimation has many reasons. Our monopole–tracking method is much more accurate than those previously in the literature. Also, our simulation is much bigger than those previously used. Besides, we also use combined the monopole–tracking methods with an improved version of the LVE and with the AVFE. Actually, had we used just the improved LVE method, we would have got much smaller errors than in the original work by Yamaguchi, since the improved version tries to minimize the known sources for errors, and also, as mentioned above, because we used bigger simulations, increasing the statistical significance.

Our new velocity estimations allow us to determine that the physical branch of solutions of the analytical model presented in [97] is the subluminal one. Actually, we have not found any monopole going close to or above the speed of light in our simulations. We can use our velocity numbers, together with the network scaling numbers reported earlier, to calibrate the analytical model for global monopole networks in radiation and matter domination, respectively (see Table 4.6):

$$\begin{aligned} c_r &= 2.6 \pm 0.3\,, \qquad k_r = 0.9 \pm 0.1\,, \\ c_m &= 2.5 \pm 0.3\,, \qquad k_m = 1.6 \pm 0.2\,. \end{aligned} \tag{4.37}$$

The values of c are compatible within 1σ and 2σ with those previously reported, but the errors have been reduced. The values of k were never reported before, due to the uncertainties in previous simulations to determine whether the subluminal or the luminal branch was the one preferred by monopoles.

Maybe more interestingly, the values of c we obtain for radiation and matter domination are compatible with each other, even with the reduced error bars. However, there is tension on the values of k from radiation and matter domination simulations. Already in the original paper for global monopole VOS model [97] the authors comment on the different physics involved in the approximations, and how the term involving c is more robust than the one involving k. Our simulations support their conclusions.

The reason why the values of k depend on the simulation may be due to the approximations about the force between monopoles. The VOS model supposes the field configuration of a monopole to be spherically symmetric, and thus the mass of the monopole to grow linearly with distance. The model also asumes that the force between monopoles is independent of distance. Moreover, the presence of other monopoles in the vicinity is factored in by adding and *ad hoc* $1/\sqrt{\mathcal{N}}$ factor. These assumptions should be revisited: the typical field configuration of a monopole in a network is unlikely spherical; the force between monopoles is independent of distance only if the monopoles are far from each other, it is not clear what the force is when the cores are involved; and the fact that there are other monopoles and antimonopoles distort the field configuration substantially. Our results point at a possible direction where the VOS model could be improved. In any case, one should also be cautious and bear in mind that there are different numerical errors in the simulations: there are errors due to the Press-Ryden-Spergel algorithm, due to our algorithms to detect and estimate velocities, or even due to the inherent errors of the discretization.

The method described in this Chapter can be used also to characterize other types of defect networks. For example, a direct application will be to calibrate the analytical models for semilocal strings, as we will do in Chapter 5, where the knowledge obtained in this work about the treatment of the evolution of point like particles will be invaluable to track the velocities of the string ends.

5 Evolution of Semilocal String Networks

5.1. Introduction

In the previous Chapter we have seen that numerical simulations are essential in order to build a reliable VOS type analytical model for cosmological defect networks. The detailed characterisation of defect properties that one can obtain from the numerical simulations is very important to analyse the behaviour of the network of defects, as well as the behaviour of individual defects. Moreover, the analysis of this behaviour can be used to decide which are the characteristic scales of the network that the analytical model has to describe or which assumptions have to be made in order to build a reliable model. Once the analytical model is constructed the free parameters related to the phenomenological terms have to be calibrated using the data obtained from the simulations.

In Section 2.4.2 we have seen that the strings arising from the semilocal model have some peculiar features. Due to the fact that this kind of strings are not purely topological they can have ends that behave like global monopoles, and the networks of this kind of strings can be understood as networks of local strings attached to monopoles. Furthermore, taking also into account that in the semilocal model there are two complex scalar fields, it is not clear which field winds or whether the windings actually gives the position of the string. Therefore, the magnetic field has been used to detect the positions of the strings in numerical simulations. This algorithm gives a three dimensional representation of the strings making very difficult the detail analysis of the behaviour of segments in the network.

Therefore, in this work we give the description of the detailed characterisation of the semilocal string properties we have made. Now we are able to give a one dimensional representation of the semilocal segment cores and we are also able to detect the segment ends as monopoles. Using this representation, we measure the lengths of the segments and we calculate the velocities of string segments as well as the velocities of the string ends (global monopoles) using the similar procedure we have presented in Chapter 4. Moreover, the one dimensional representation of segments lets us to analyse the behaviour of each one of the segments in the box.

In [104] the VOS-type analytical models for semilocal strings were presented. The authors of this work used the fact that the semilocal string networks can be seen as networks of local strings attached to global monopoles and the analytical models they have presented are mixtures of the VOS type analytical models of local strings and global monopoles. Using this mixture two different models were presented. Each one of these models uses a different approach to account for the phenomenological terms as we can see in Section 2.4.2. The analysis of the behaviour of the segments presented in this Chapter will be used in a future work to study if the initial assumptions made to construct the VOS-type analytical models hold. In such case we will then calibrate the parameters of the model.

At this point it is worth to mention that this Chapter is based on two different articles:

- **Evolution of semilocal string networks: Large-scale properties**

  A. Achúcarro, A. Avgoustidis, A.M.M. Leite, A. Lopez-Eiguren, C.J.A.P. Martins, A.S. Nunes and J. Urrestilla, Phys. Rev. D89 (2014) no.6, 063503. arXiv:1312.2123.

- **Evolution of semilocal string networks: II. Velocity estimators**

  A. Lopez-Eiguren, J. Urrestilla, A. Achúcarro, A. Avgoustidis and C.J.A.P. Martins, arXiv:1704.00991, Submitted to Phys. Rev. D

In the first one, the large-scale properties of the semilocal networks were studied and in the second one, the new characterisation, as well as the length and velocity data is introduced.

The rest of the Chapter is structured as follows. In Section 5.2 we describe the field theory simulations of semilocal string networks that we have performed. We then, in Section 5.3, present the algorithms to measure the segment lengths and velocities as well as the monopole positions and their velocities. Some of these algorithms have already been used in the literature and some are introduced here for the first time and are specific to semilocal strings. In Section 5.4 the caveats and difficulties of the algorithms are explained. We report the results obtained from these algorithms in Section 5.5. Finally we conclude in Section 5.6.

5.2. Field Theory Simulations and Scaling

The defect networks that we will analyse in this Chapter are semilocal string networks. As we have seen in Section 2.4.2 (where a detailed description of the model is given), semilocal strings can be seen as a minimal extension of the Abelian Higgs model with two complex scalar fields that make the $SU(2)$ doublet. This leads to $U(1)$ flux-tube solutions even though the vacuum manifold is simply connected. Taking the Lagrangian (2.72) and appling suitable rescalings to it, the simplest semilocal string model lagrangian has the following form,

$$\mathcal{L} = (\mathcal{D}_\mu \Phi)^\dagger (\mathcal{D}^\mu \Phi) - \frac{1}{4} F_{\mu\nu} F^{\mu\nu} - \frac{\beta}{2} (\Phi^\dagger \Phi - 1)^2, \tag{5.1}$$

where $\mathcal{D}_\mu \Phi = (\partial_\mu - i A_\mu)\Phi$ and $F_{\mu\nu} = \partial_\mu A_\nu - \partial_\nu A_\mu$. As one can see the only parameter governing the behaviour of the model is β and as we have seen in Section 2.4.2 the stability of the strings depends on it. Since our aim is to characterize the dynamics of a network of semilocal strings in the early universe, we consider a spatially flat Friedmann-Lemaître-Robertson-Walker space-time (see Section 1.3) with comoving coordinates:

$$ds^2 = a(\tau)^2 \Big(- d\tau^2 + dx^2 + dy^2 + dz^2 \Big), \tag{5.2}$$

where τ is conformal time and $a(\tau)$ is the cosmic scale factor.

The equations of motion for the semilocal model in temporal gauge $(A_0 = 0)$ read

$$\begin{aligned} \ddot{\Phi} + 2\frac{\dot{a}}{a}\dot{\Phi} - \mathbf{D}^2 \Phi + a^2 \beta (|\Phi|^2 - 1)\Phi &= 0, \\ \partial^\mu F_{\mu\nu} - i a^2 (\Phi^\dagger D_\nu \Phi - D_\nu \Phi^\dagger \Phi) &= 0, \end{aligned} \tag{5.3}$$

together with

$$\partial_i F_{0i} = i a^2 (\dot{\Phi}^\dagger \Phi - \Phi^\dagger \dot{\Phi}), \tag{5.4}$$

which is Gauss's law. Note that the equations of motion we have just obtained are almost equal to (2.18). In (5.3) Φ represents two complex scalar fields while in (2.18) ϕ represents just one complex scalar field.

As we have seen in Section 2.3.4, simulating a network of defects in expanding backgrounds has another problem: the physical size of the defects is fixed throughout the simulation, but the size of the box is growing in time. The same argument would be that the comoving box size is kept constant, but the actual (physical) size of the defects shrinks. Again this would point to the necessity to simulate the system in bigger lattices, which is not feasible. Instead, there is an algorithm by Press-Ryden-Spergel (PRS) [115] (see Section 2.3.4) by which the defect cores are made to grow comovingly during the simulation. As we have seen, this is achieved by promoting the parameters of the model into time varying variables [101], and the (continuum) equations of motion (5.3) get modified to:

$$\begin{aligned} \ddot{\Phi} + 2\frac{\dot{a}}{a}\dot{\Phi} - \mathbf{D}^2\Phi + a^{2s}\beta(|\Phi|^2 - 1)\Phi &= 0, \\ \partial^\mu \left(a^{2(1-s)}F_{\mu\nu}\right) - ia^2(\Phi^\dagger D_\nu \Phi - D_\nu \Phi^\dagger \Phi) &= 0, \end{aligned} \tag{5.5}$$

where the parameter s gives the level of modelling with the PRS algorithm: $s = 1$ corresponds to the true equation of motion, whereas $s = 0$ correspond to defects whose core size is constant.

In order to perform numerical simulations of this model we use the procedure we have described in Section 2.3.4. We have simulated the system in 1024^3 lattices for radiation and matter eras with $s = 0$. As a good compromise for the computing power avalilable to us, we chose $\Delta x = 0.5$ and $\Delta\tau = 0.2$, where Δx and $\Delta\tau$ are lattice and time spacings measured in units of $[\eta^{-1}]$, respectively. The simulations were performed at the COSMOS Consortium supercomputer and i2Basque academic network computing infrastructure.

We found that the initial conditions used in [9] are a good choice in our case to obtain the scaling regime as fast as posible: the gauge field, gauge field velocities and scalar field velocities are set to zero. The scalar fields are chosen to lie in the vacuum manifold, but have randomly chosen orientations [130].

We want to simulate strings that are stable and long enough, such that we can get a statistical ensemble of them in our simulations. As mentioned in Section 2.4.2, semilocal strings are stable for values of $\beta < 1$, and our simulations are performed for $\beta = 0.04, 0.09, 0.15, 0.20, 0.25, 0.30, 0.35$. Higher values of β show a much more scarce network [8], and it would be much harder to get a numerous ensemble of semilocal strings. Lower values of β are also not optimal, since the scalar string cores start to be too big for our simulation parameters.

For every value of β, and for both cosmologies (radiation and matter), we have performed 7 different simulations, in order to increase our statistics. It is very expensive to analyse and output the simulation at every time-step; instead, the information is output every 20 time steps once the network has reached scaling. The times chosen to output the data range from $\tau = 96$ until $\tau = 256$; times earlier than $\tau = 96$ the system has not setteled into scaling well enough, and $\tau = 256$ is our limit due to the boundary conditions[1].

In this case the scaling regime, the regime where the characteristic scale grows with time, can be analysed using two different VOS-type characteristic scales. On the one hand, we can use the

[1]For a couple of cases the information has been output more frequently also, in order to check that the time spacing between outputs was correct, and also to pinpoint some issues that we will discuss later.

characteristic scale related to the segment length

$$\xi^s \equiv \sqrt{\frac{V}{\mathcal{L}}} = \gamma_{\mathcal{L}}\tau, \tag{5.6}$$

where V is the horizon volume and $\mathcal{L}$ is total string length. $\gamma_{\mathcal{L}}$ is a VOS-type length scale parameter (see Section 2.3.4). The total string length can be measured in two different ways. Firstly, an estimation of $\mathcal{L}$ can be obtained using local field theory estimators, where using the 00 component of the energy momentum tensor, T_{00}, and the energy per unit length of the string,μ, the length can be obtained in the following way,

$$\mathcal{L} = T_{00}/\mu. \tag{5.7}$$

Secondly, the total string length can be derived by directly measuring the comoving length of each string.

On the other hand we can also use the characteristic scale related with the number of string ends (monopoles),

$$\xi^m \equiv \left(\frac{V}{\mathcal{N}}\right)^{1/3} = \gamma_{\mathcal{M}}\tau, \tag{5.8}$$

where V is the horizon volume and $\mathcal{N}$ is the total number of monopoles. In this case the VOS-type length scale parameter, $\gamma_{\mathcal{M}}$, is related with the number of string ends (monopoles).

In Section 2.3.4 we have seen that an accurate measurement of segment lengths, segment velocities and monopole velocities is of great interest to obtain the correct analytical model describing semilocal string networks, and as we have just seen some of those quantities are also of great interest to measure the scaling of the network. Therefore, in this Chapter we will introduce algorithms for estimating string length, string velocities and monopole velocities; some of these algorithms have already been used previously in the literature and some are introduced here for the first time.

The fact that semilocal strings are not topological makes it much more difficult to numerically detect their location in a simulated lattice compared to the AH strings. As we have seen in Section 2.3 three different procedures can be used to detect the position of the strings in the AH case. However, the procedure related to the winding of the fields was widely used in the literature, because, among other reasons, it gives a one dimensional characterisation of the string.

In the semilocal case, there are twice as many scalar fields, and just one gauge field. It is not clear then which field one has to choose to follow the windings, or whether these windings actually give the position of the string. Besides, the field does not have to be zero when there is a winding. Unlike in the AH case, *one* field can be winding around a site, but the *other* field may still fulfil the requirements to be in the vacuum of the potential energy. Therefore, we can have a field winding, but no concentration of potential or magnetic field.

5.3. Algorithms to measure lengths and velocities

In previous works [7–9, 104], the criterion used to decide whether a point in the lattice belongs to a semilocal string was based on the concentration of magnetic field (we will describe this method in more detail below). The procedure gives a collection of points that can be grouped into segments by proximity, *i.e.* we end up with a *volume* of points, which is subsequently used to estimate length. Moreover, the number of segments is also a good estimator for the number of monopoles,

i.e. segment ends. It has always been understood that this was just a first approach to obtain the length of strings, and will shall show later that this estimator was seriously underestimating the string length.

Instead of a volume characterization of the strings, one would rather get a one-dimensional representation of strings, using, for example, the position of the core of the string. We will introduce a new estimator using field windings that will produce such a one-dimensional characterization of the string. This will be invaluable for the estimators of velocity we will describe later, and will enable us to determine individual segment velocities for semilocal strings for the first time.

We have also detected monopoles directly from the simulation for the first time. The number and velocity of monopoles are also important quantities for characterising our system. For example, from the total number of monopoles, $\mathcal{N}$, an independent measurement of the number of segments can be inferred.

In the following we will describe the algorithms used to obtain lengths of segments, number of segments, number of monopoles; velocities of segments, monopoles and the network velocity; and magnitudes to monitor scaling.

5.3.1. Estimation of segment lengths using the threshold of the magnetic field

One criterion for deciding whether a lattice-point in the simulation is part of a semilocal string is the following: points where the magnetic field density is higher than a given threshold are considered to belong to a semilocal string. In order to get a meaningful threshold, for a given β, we consider the corresponding Abelian Higgs string, and calculate the maximum of its magnetic field $B_{\max}$. We also calculate the radious of the Abelian Higgs string $r_{\rm AH}$, defined as the radious at which the magnetic field $B_{threshold}$ (absolute value) drops to 30% of $B_{\max}$. Armed with the value $B_{\max}$, the whole simulation grid is scanned at every time-step, the value of the magnetic field is calculated at each grid point, and if the magnetic field is higher than 30% of $B_{\max}$, the position of that point is output. One typical snapshot of the network after scanning the rid points with magnetic field greater than the threshold is shown in Fig. 5.1.

Once all the points have been output, they are distributed into segments. In order to do that, the points that are in contact with each other are grouped into one segment. Thus, a collection of points forming the volume of a segment is obtained. Dividing that volume by the cross-section area of the string (calculated from $r_{\rm AH}$ assuming a circular cross-section), the length of the segment is estimated. From this procedure a distribution of segment lengths is obtained at every time step. In Fig. 5.1 one can see the network after the segment rearrangement, where different segments are plotted with different colour. Adding up all the segments, the total length of string in every time step $L(t)$ can also be obtained.

The segments in the network are mostly tube-like, but some are sphere-like instead of tube-like, i.e., they are *blobs* of energy. These can be formed, for example, after a segment has collapsed into itself. We do not wish to count these blobs as part of our network, so another cut-off can be introduced: those segments that are not longer than a given factor (α) times the typical radius of a string are considered to be blobs, and are discarded. In Fig. 5.1 can also be seen the differentiation between structures that we consider *blobs* and *proper* semilocal string segments.

As mentioned earlier, the number of monopoles can be directly read from the number of segments. Some of the segments will in fact form a closed loop, so monopoles would be slightly overcounted by this procedure. Besides, even though we tried to factor out the energy blobs, some of them escaped the algorithm, and we are still counting those blobs as segments, and thus overcount monopoles again. Finally, the definition of segment is somewhat arbitrary, since those

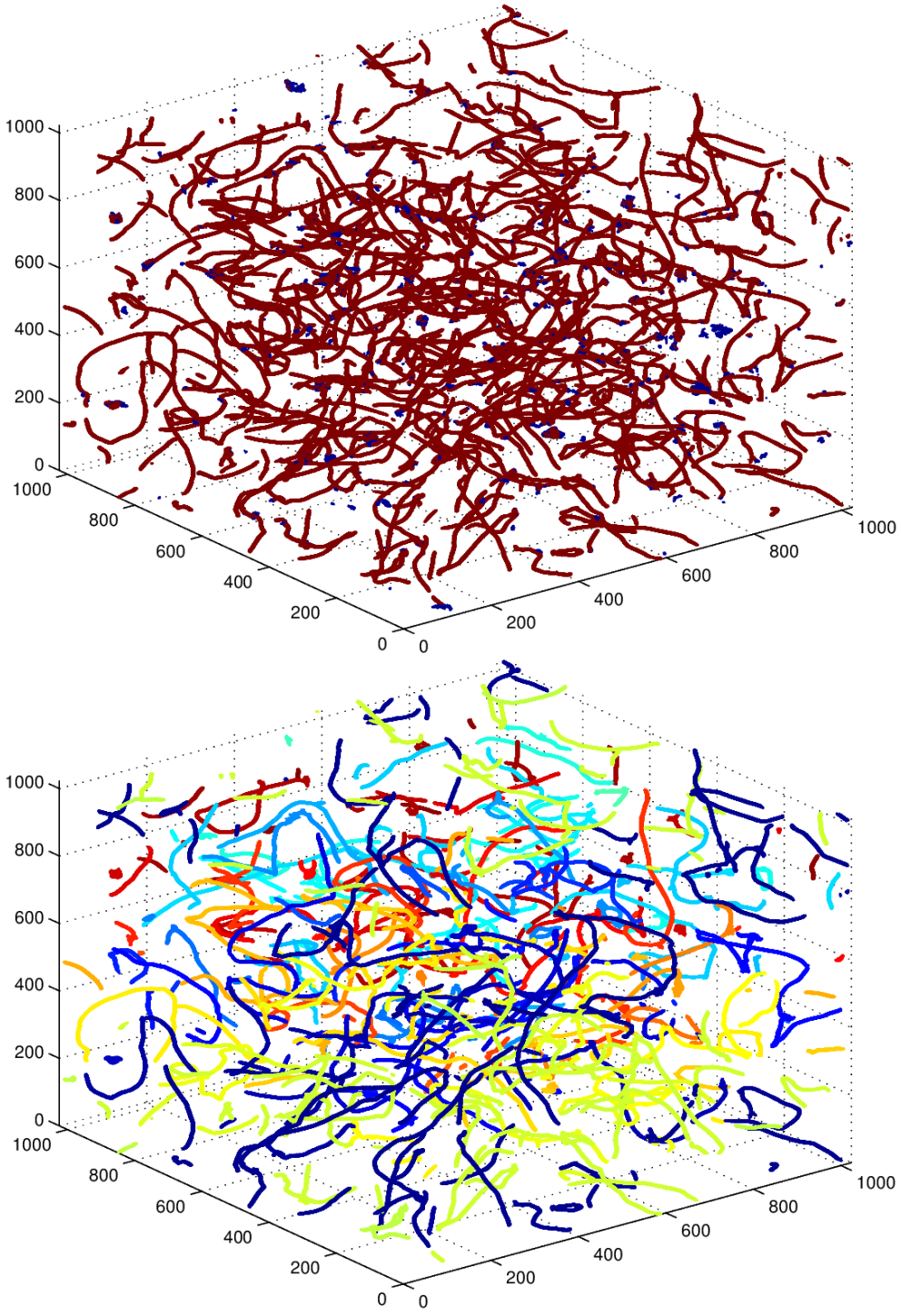

Figure 5.1.: *Semilocal string network, in matter domination with $\beta = 0.04$. The top figure shows two types of structures: on the one hand we have tube-like structures (proper strings) and on the other short blobs. These blobs we disregard in our analysis. The bottom figure shows the network without blobs, and also each segment has been identified and plotted with a different color. As there number of segments is large, the colours are unfortunately used for more than one string segment. Note also that the blob removal procedure does sometimes fail to identify some sphere-like structures, since their volume is large.*

	Radiation		Matter	
β	$\gamma_{\mathcal{L}}$	$\gamma_{\mathcal{M}}$	γ_{L}	$\gamma_{\mathcal{M}}$
0.01	0.29 ± 0.04	0.6 ± 0.2	0.30 ± 0.05	0.56 ± 0.08
0.04	0.30 ± 0.04	0.5 ± 0.1	0.30 ± 0.03	0.5 ± 0.1
0.09	0.33 ± 0.05	0.5 ± 0.1	0.33 ± 0.06	0.46 ± 0.08

Table 5.1.: *Values of the VOS-type length estimators for the total length of segments $\gamma_{\mathcal{L}}$ and the total number of monopoles $\gamma_{\mathcal{M}}$ (5.6, 5.8) obtained in [9].*

segments that are not longer than α times the typical radius of a string are discarded. Different choices for α can give different number of segments.

In the paper we have analysed the large-scale properties of the semilocal networks [9], we analysed the scaling regime of semilocal string networks for $\beta = 0.01, 0.04, 0.09$ using this procedure. In that work we have shown that values of α between 3 and 8 give compatible results. Moreover, for values of α lower than 3 we are still counting to many *blobs* and for values greater than 8 we start discarding to many *proper* segments. We have also obtained the values for the VOS-type scaling parameters that can be seen in Table 5.1[2].

5.3.2. Estimation of segment lengths using the windings of the scalar fields

This is a new length estimator which allows us to obtain a one-dimensional characterization of the segments. In order to do so, it uses the windings in either or both of the scalar fields (ϕ_1 and ϕ_2) in the model.

The procedure is defined as follows: During the simulation, the winding of fields ϕ_1 and ϕ_2 is calculated at every point, and if this winding is different from zero, that position is output together with the value of the magnetic field at that point. The value of the magnetic field is needed because having the fields winding around some plaquette does not necessarily mean that that point belongs to a string segment; it is only when the non-zero winding happens in a region with a high concentration of magnetic field that the position is regarded as the core of a string. The position of the core is given by the non-zero winding of either (or both) of the scalar fields (within the cloud of points with magnetic field), and following the points with winding one can map the 1-D array of points defining the centre of the string.

Actually, since there is no topological constraint, as we are following the points with non-zero windings of one of the fields, the points may stop belonging to a semilocal string segment (because there may not be a high concentration of magnetic field), or the sequence of points with windings may abruptly stop. It is worth noting that, in principle, for a point to be part of a semilocal string it is enough that one of the fields winds in a region with high magnetic field. It is not necessary that the second field winds[3]. On the other hand, sometimes both fields may be winding inside a cloud of magnetic field, but (due to discretization issues) not exactly on the same plaquette and they may be displaced by one lattice unit. In order to overcome these two nuisances, the points of non-zero windings of both fields are combined, and those that are in contact are grouped to obtain segments. Every segment is thus formed of a (1 dimensional) collection of points where either (or both) of the scalar fields have a non-zero winding and magnetic field is above some threshold.

[2] In this table we give the values for γ_{L} and $\gamma_{\mathcal{M}}$ that will be useful for compare with the data in the work we analyse the velocity estimators.

[3] Although we will show later on that both fields seem to wind inside the string core.

Figure 5.2 shows the string positions, taking into account the concentration of magnetic field (blue) and the points where the fields are winding (ϕ_1 with red, ϕ_2 with cyan and both with black).

Since our fields are discretized in a lattice, the determination of the centre of the string suffers from the Metropolis effect: the center of the segment is not a a smooth curve, but it is actually formed by a collection of unit steps. A smooth version of the position of the cores would be beneficial as the estimation of both the length and the velocity of the segment would improve. Thus, the points in the string segments are smoothed by averaging the position over nearest neighbours. After trials using different number of neighbours, averaging over 4 neighbours at each side seems optimal: the position of the core is smooth enough, and the structure of the segment is not lost (as would happen by averaging over too long distances).

The outcome of this procedure is a collection of segments, given by a one-dimensional list of the smoothed position of their core. The right panel of Fig. 5.2 depicts a zoom into a portion of a segment, showing how the averaged version of the core of the string, obtained by smoothing, nicely interpolates between the points with non-zero windings.

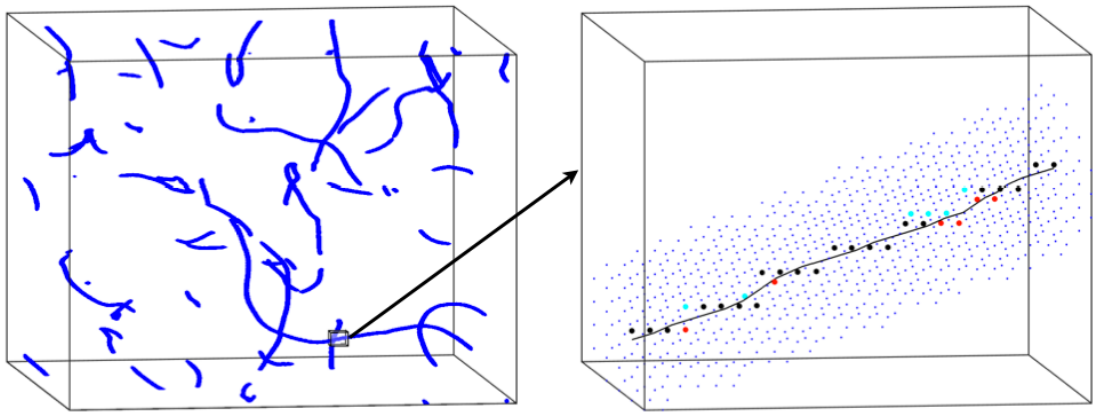

Figure 5.2.: *In the left panel, the string segments in a typical simulation boxed are shown; the blue points are points with a magnetic field higher than the threshold described in the text. The right panel is a zoomed portion of one segment. The blue dots correspond again to points with high magnetic field, and the red, cyan and and black points correspond to points where the windings of the scalar fields ϕ_1, ϕ_2 or both (respectively) are non-trivial. Notice how these dots are not nicely aligned in a smooth curve, but jitter around (this is the Metropolis effect). Performing the smoothing over four nearest neighbours on each side of each point renders the black line, which is the smoothed version of the centre of the core of the segment. Actually, the black line is also formed of points, but here those points have been joint by a line to show how they interpolate between the lattice–points with winding.*

5.3.3. Estimation of the velocity of the segments

Once the segments have been characterized by a smooth one-dimensional array of positions, this set of data can be used to track the history of each segment in time, and also estimate its (transverse) string velocity.

Consider a string segment at time τ_1, and the same segment at a later time τ_2. If one is able to estimate where each point in the segment has moved from τ_1 to τ_2, we can get an ensemble average. This can be done in the following way: choose a point x_1 in the core of a segment at

time τ_1, and find its distance to all points belonging to the segments' core at τ_2. The point at time τ_2 that is closest to x_1 is identified as the point where x_1 has moved to from τ_1 to τ_2. The velocity of point x_1 is then estimated by merely dividing the distance it has travelled by the time interval $\tau_2 - \tau_1$. Performing this with every point belonging to a given segment at every time step allows us to obtain a segment velocity (an average of $|v|$ over all the points in the segment). The average of all the segment velocities would then be the network average velocity.

Although this procedure has some subtleties, which we will describe in the next section, the benefits are manifold: one can obtain individual segment velocities at every time step. We can thus record the history of the velocity evolution of each segment in the simulation. Moreover, a by-product of this procedure is that one can create a map of which segments merge with which.

It is clear that for this procedure to work a one-dimensional characterization of the string segment is necessary, and therefore the velocity determination of segments relies on the string length characterization given by the windings.

5.3.4. Estimation of number and velocity of string-ends (monopoles)

As explained in Section 2.4.2, the field configurations at the ends of the segments can be understood as global monopoles [4] and, as such, they can be detected in a simulation directly from the fields. The whole simulation lattice is scanned point by point to check whether monopoles are present. In order to do so, following [4], the field configuration at the string ends are recast from the 4 real scalar fields with SU(2) symmetry into three scalar fields, establishing an analogy to $O(3)$ global monopoles, through

$$\Psi \sim \Phi^\dagger \vec{\sigma} \Phi, \tag{5.9}$$

where $\vec{\sigma}$ are the Pauli matrices. Actually, the field configuration thus obtained is still quite noisy to clearly detect monopoles, and we clean it further by

$$\Psi \longrightarrow \tilde{\Psi} = \Psi - \nabla \times (\nabla \times \Psi) .$$

Once the field configuration has been treated, the location of a monopole is determined using the procedure we have described in Section 4.3.1.

When spanning the simulation box, if the topological charge is different than zero, the position of the monopole together with its topological charge is output. One can then directly obtain the number of monopoles (or string ends) in the simulation lattice, which is an independent way of measuring the number of string segments: the number of segments would be roughly $N/2$; not exactly because some segments can be closed loops and thus have no ends. Moreover, the number of monopoles is another estimator for checking the scaling regime.

Since the position of the monopoles (and their topological charge) is known at every time-step, the velocity of monopoles can also be estimated following the procedure we have described in detail in Section 4.3.1: A monopole M_1 is chosen at time τ_1, and its distance with respect to all monopoles at the next time τ_2 is calculated. Then, M_1 is identified with the closest monopole at time τ_2. Repeating this procedure at all times, the history of M_1 can be tracked and an estimate of its velocity can be obtained by merely diving the distance it has travelled by the corresponding time interval.

Monopole velocity estimations also have their issues (see Section 4.3.1), but once again the benefits are manifold: one can obtain individual monopole velocities, both at each time step and as the average velocity during the life of the monopole. By averaging over all monopoles, a monopole-network velocity can be obtained too.

5.3.5. Estimation of the network velocity using local lattice variables

There are also other types of velocity estimators for the whole network, based on local field quantities as described in [69, 73]. As we have seen in Section 4.3.3, these estimators are computed by considering a defects at rest, and performing a Lorentz boost to it. For the global monopole case we have just one estimator, but in the semilocal case due to the presence of gauge fields another estimator can be added. Using a similar procedure as in Section 4.3.3 we can obtain the following estimators:

$$\begin{aligned} \langle v^2 \rangle_F &= \frac{\mathbf{E}^2_{\mathcal{W}}}{\mathbf{B}^2_{\mathcal{W}}}, \\ \langle v^2 \rangle_G &= \frac{2R_{\mathcal{W}}}{1+R_{\mathcal{W}}}, \end{aligned} \tag{5.10}$$

where,

$$R_{\mathcal{W}} = \frac{E_{\Pi\mathcal{W}}}{E_{\partial\mathcal{W}}}. \tag{5.11}$$

The subscript $\mathcal{W}$ denotes weighting by some appropriate physical quantity (see Section 4.3.3). In the present case, a magnetic energy weighting was used, because this automatically ensures that only regions with non-vanishing magnetic energy contribute to velocities. Regions with semilocal strings have higher concentration of magnetic energy, and thus those regions contribute most to the above integrals. During the simulation, the quantities needed to obtain these velocity estimators are output.

Note that these field velocity estimators give information of the network as a whole, whereas the previously described methods for segments (and monopoles) give information about each individual segment (or monopole). Besides, the estimators (5.10) average over all regions with some magnetic energy, and thus both segments and monopoles contribute, as well as regions where a segment may have disappeared (or is it about to disappear) and a temporary magnetic field density is left-over.

5.4. Caveats and difficulties of the algorithms and the numerical setup

In this section we will describe some caveats and difficulties we encountered in the simulations. These, on the one hand, have to be dealt with in order to obtain physically valuable solid results, and on the other, are really interesting to give us an insight into how to reformulate the analytical model for semilocal strings in a more realistic way.

5.4.1. Comparison between the two length estimators

In the previous sections, two different procedures for obtaining the length of string segments have been described: one using the threshold of the magnetic field and the other using the windings of the scalar fields. We did expect some mismatch between these two procedures, mostly because the method of obtaining segment lengths by counting points above a magnetic field threshold and diving the *volume* by the *cross-section area* was a rather crude algorithm. This algorithm was used in previous works [8, 9, 104] due to the difficulty of defining a semilocal string otherwise (with windings or zeros of the scalar field), and was believed to be a good first approximation.

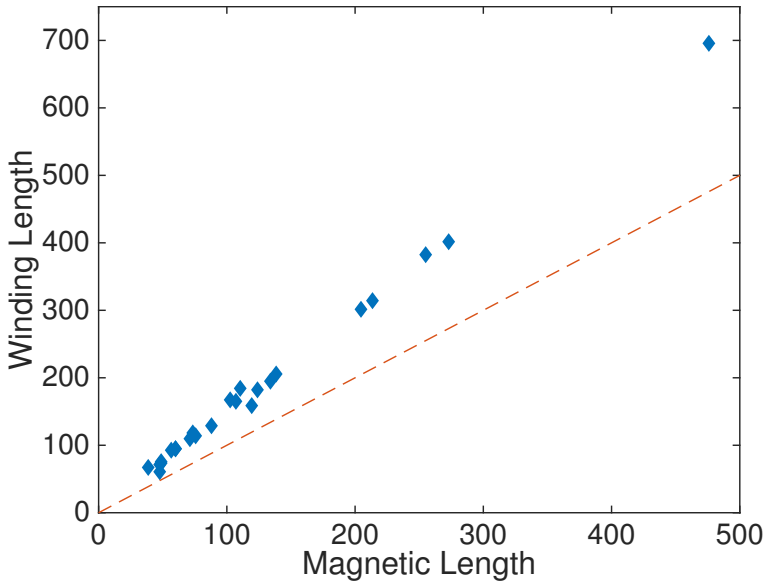

Figure 5.3.: *In this figure the relation between the two length-measuring approaches is shown. In the x axis the lengths measured with the magnetic field approach, and in the y axis the lengths measured with the winding approach, are shown. Every diamond represents a segment in a simulation box for $\beta = 0.20$ at time $t = 256$. It is clear that the proportionality is almost the same for all the segments in the network.*

Fig 5.3 shows the relation between the lengths of the segments measured by using the magnetic flux ($\alpha = 5$) and the winding approach for $\beta = 0.20$ at $t = 256$. The ratio between these two procedures is almost the same, and it is roughly a (surprisingly large) factor of 1.5 for most values of β both in the matter and radiation cases. The factor is a bit different for shorter segments, which is presumably due to the fact that the segment ends play a stronger role for shorter segments, but this is not relevant for the whole network length, which is dominated by long segments.

There are several possible sources of uncertainty that can help us understand the difference in the string length obtained with the different procedures. There are two possible physical effects to take into account: one is Lorentz contraction of the segments due to their velocities, making segments narrower than the estimated cross-section of the string; the other is that segments are not straight, and when they bend the strings can be considerably narrower.

There is also a clear numerical uncertainty in the procedure of obtaining the cross-section of the string. Remember that the cross-section of the semilocal strings in the simulations are defined to be the same as those of a straight AH string at rest. The typical radius for AH strings range from $r_{04} = 2.36$ for $\beta = 0.04$ to $r_{35} = 1.71$ for $\beta = 0.35$. The lattice spacing we are using is $\Delta x = 0.5$ which already gives us a considerable error on the string radius: we consider that points with magnetic field higher than 30% of the maximum magnetic field belong to the string. Imagine a string centered at a lattice-point, with radious, say, 1.4. The string radious is then shy of reaching 3 lattice units ($3 * \Delta x > 1.5$), and therefore there are only 2 lattice points which *qualify* as points of strings, but the volume of strings obtained like that will nevertheless be divided by the *true* radious, clearly underestimating the string length. Moreover, a string will typically not be centered around a lattice–point, but it will be located anywhere within a lattice–cell, making this effect more important. Thus, the points that we *numerically* decide that belong to the string are *fewer* than what a more sophisticate procedure would get. We can get an estimation of the

	Radiation		Matter	
β	$L_{winding}$	$L_{magnetic}$	$L_{winding}$	$L_{magnetic}$
0.04	6166.44	3895.33	12303.07	8014.28
0.09	6903.84	4673.61	10780.82	7266.59
0.15	5246.97	3476.99	9267.51	6099.45
0.20	5221.27	3546.95	7447.93	4865.46
0.25	4450.95	2948.52	6147.42	3853.46
0.30	2546.31	1585.21	4562.78	2901.85
0.35	2095.5	1173.86	3405.10	2119.90

Table 5.2.: *The total lengths in $\tau = 256$ for every β we simulated and for Radiation and Matter epochs. $L_{winding}$ denotes the length estimator using the windings of the scalar fields, whereas $L_{magnetic}$ denotes the length estimator using a threshold of magnetic field.*

maximum errors for the two extreme β as follows:

$$\frac{r_{04}^2}{(r_{04}-\Delta x)^2} = 1.60\,, \qquad \frac{r_{35}^2}{(r_{35}-\Delta x)^2} = 1.99\,.$$

This numerical bias seems to account for most of the discrepancy between the two length estimation procedures, and the Lorentz factor and the fact that strings are not straight do not seem to be so important. Actually, the Lorentz contraction of the segments is clearly not a factor to take into account since the velocity values we obtain later on are rather low to obtain a Lorentz factor capable of explain the difference. In Table 5.2, the total length in segments for every β is shown. We conclude then that the string segments length we estimated in previous work has been overestimated by roughly a factor of 1.5 (the average ratio between the values in Table 5.2 are 1.56 for Radiation and 1.55 for matter).

Moreover, with the new winding approach, the problem of how to remove blobs has disappeared. In any case, we have checked that the number of monopoles obtained by the winding approach, and by the magnetic field approach (removing blobs) is very similar.

One very nice check that our new length estimators work fine can be found in Figure 5.4. There, we plot the positions of the strings obtained by the winding procedure, and the positions of the monopoles obtained by calculating the monopole charge. In principle, these two procedures are independent, but the positions of the strings and monopoles (string–ends) are aligned very nicely.

As we have seen in (5.6,5.8) from the length estimators (of both monopoles and strings) two different VOS-type lengthscale parameters can be obtained, γ_L and $\gamma_{\mathcal{M}}$. We show the values of those parameters in Table 5.3 in Section 5.5, but we would like to point out that these values are compatible (within errors) with the values obtained in [9] and shown in Table 5.1, for both γ_L and $\gamma_{\mathcal{M}}$. Note that for γ_L the values in Table 5.1 should be corrected by a $\frac{1}{\sqrt{1.5}}$ coming from the factor 1.5 difference in the length estimator, but even without the factor, the values lie within the 1-σ errors of the values.

In the rest of this work, we will only use the length estimator which uses the windings approach. The reason for calculating segment lengths using the threshold of the magnetic field was for ease with comparing with previous works, and it will be of no use for the rest of this paper.

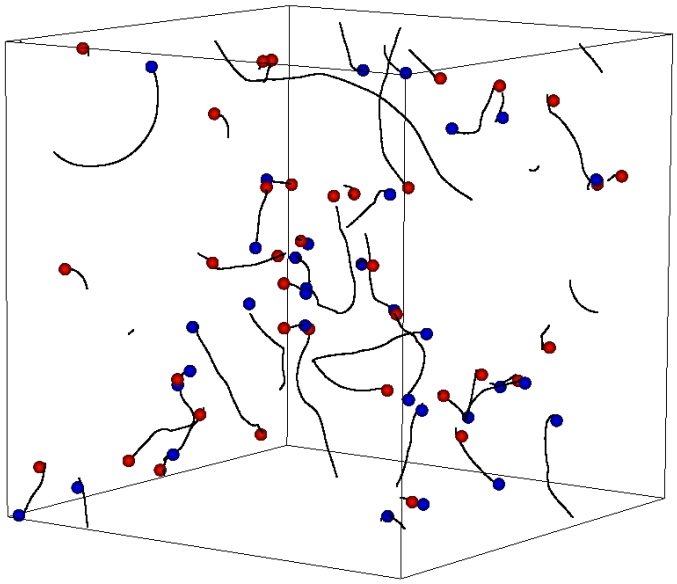

Figure 5.4.: *In this figure one can see the box after the characterization. The black lines represent the string segments detected using the windings, where each point is smoothed using the four nearest neighbours in each direction. The red dots represent the antimonopoles and the blue ones the monopoles.*

5.4.2. Identification of semilocal segments

As it has been already explained, the position of a semilocal string is difficult to pinpoint because there is no topological obstruction for the string to acquire a non-zero value around a winding (one field may wind and the other may climb the potential) and there is no requirement for semilocal strings to be closed or infinite. Actually, it is *finite semilocal string segments* that we are studying.

One way of detecting the strings, explained above, is by following the windings of both scalar fields ϕ_1 and ϕ_2, and checking where those windings happen within regions of high magnetic field. In the top panel of Fig (5.5) we show the windings of both fields in the simulation box, without taking into account the values of the magnetic field: windings of ϕ_1 in blue and of ϕ_2 in green. Actually, there are several regions where the two fields wind in the same plaquette (or at a difference of 1 plaquette), and those are plotted in red.

The first thing we notice is that each of the fields, ϕ_1 and ϕ_2, creates a network of closed or infinite 'strings', very much like an Abelian Higgs network. But unlike in the Abelian Higgs case, a winding of a scalar field does not necessarily mean that there is a string forming; there is not necessarily a corresponding concentration of magnetic or potential energy. Where do semilocal strings form then? In the bottom panel we plot the same windings, but also the regions where there is a high concentration of magnetic field. This shows that semilocal strings are actually the regions where *both* fields wind, which makes sense because in that case the scalar field has to be approximately zero there and therefore the magnetic field can be large in those regions.

One could consider this network as formed from points with windings of ϕ_1, points with windings of ϕ_2 (both with no corresponding physical concentration of energy associated with them), and semilocal strings. This could be reminiscent of a p-q string network, where the Y-junctions actually correspond to monopoles.

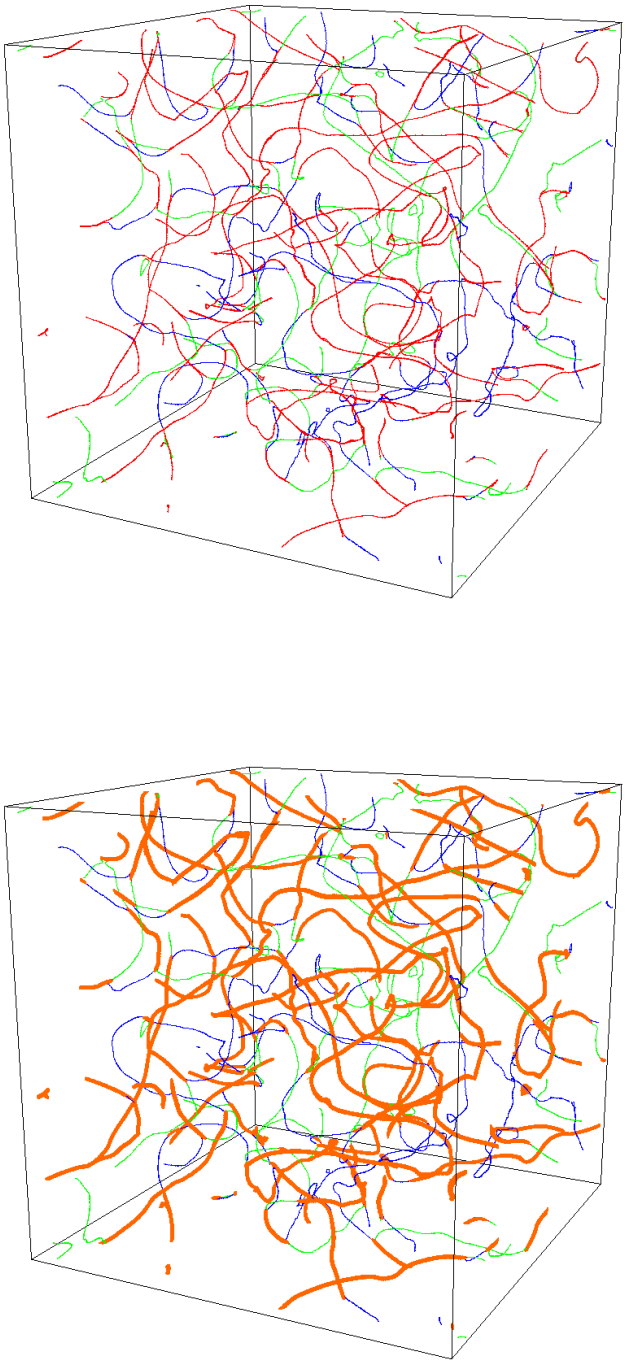

Figure 5.5.: *In the left pane the windings of both fields are shown, without taking into account the magnetic field: blue for windings of ϕ_1, green for windings in ϕ_2 and red for windings in both. As one can see each one of the fields creates a network of closed or infinite strings. On the right panel, we plot the same windings, but also the regions where there is concentration of magnetic field (orange). This figure shows that semilocal strings are actually the regions where both fields wind.*

5.4.3. Apparent superluminal velocities

The preliminary results on velocities (for both segments and monopoles) obtained by most of the direct algorithms, as well as from estimators based on local field quantities (5.10) give rather modest velocities. However, on a few occasions, we obtained values higher than the speed of light c; on some very few extreme cases as large as $10c$. It is clear that this is a numerical issue or a breakdown of the approximations used in the algorithm, as the dynamics is local and causal at the level of the fields.

This prompted a more detail analysis, and we found out that the superluminal values for velocities were only obtained when using the estimators (described above) which try to track the segments and the monopoles in each time step as the network evolves. We also found out that the procedure needed some more careful handling, due to the following caveats:

- Segment velocities:

  Imagine a segment that has closed into a loop at time τ_1, and disappears before the next time τ_2 when the box will be re-analysed. Then, all the points belonging to the loop at time τ_1 will not have a close-by point to match with at τ_2. However, our code will find the closest segment at time τ_2, even though that will correspond to another segment, presumably further than causality allows. Therefore, the calculated velocity for the loop will be very high, but clearly it is not physical; it is a shortcoming of the procedure. One way of dealing with this is by applying a cut-off, and disregarding all velocities higher than that cut-off, but this has the danger of possibly losing some dynamics (if the cutoff is too strict), or considering too many unphysical cases (if the cutoff is too weak). Another possibility to avoid these problems is by performing the identification between segments at different times backwards, i.e., choosing a point at τ_2 and looking at all points at τ_1 to match it to.

  However, if we revert to the *backward* identification, we may run into another problem: Imagine now a segment that is going to join to another segment, and for the sake of explaining this issue assume that with the exception of the segments ends (which are traveling towards each other) the string is at rest. At time τ_1 the two segments are separated by some distance, but at time τ_2 all that distance is filled with string. All the points that have filled that gap at time τ_2 will have their closest point at the ends of the segments at time τ_1 and therefore the velocity we get for those points is not the velocity of the segment. If at all, that velocity will be related to the segment end (monopole) velocity. This is avoided by calculating velocities *forward* (from τ_1 to τ_2).

  Clearly, choosing the forward or backward approach may solve one of the two previous problems, but not both.

- Monopole velocities[4]:

  Throughout the simulation monopole-antimonopole pairs annihilate: if a monopole M_1 annihilates with an antimonopole between times τ_1 and τ_2, our procedure will not have the information to know that monopole M_1 has annihilated. Instead, the procedure will try to match it to another monopole (the one nearest to it), and the velocity obtained will be incorrect (and possibly supeluminal).

  Other types of mis-identification issues may also occur occasionally: There are some detection problems when a string segment collapses into itself, as the fields are reconfiguring to

[4]Note that these caveats are analysed in detail in Section 4.3.1, but we are explaining them here for completeness.

the new situation and radiating energy away. In this case, the field configuration at the string ends is related to the merging of a monopole and an antimonopole, and our detection algorithm fails (both by detecting spurious monopoles, or failing to detect any charge at all).

Moreover, if at the moment when the identification algorithm is run a monopole passes through a face of the lattice, the algorithm may miss to detect it, because the topological charge will be divided into two different cells of the lattice. The way we have chosen to overcome this difficulty is by checking whether the monopole can be matched to a monopole in a subsequent time-step τ_3, and to compare the distances obtained. If the distance to the monopole at τ_3 is smaller than to that at τ_2 (and is actually physical), the intermediate step is by-passed. The fact that the charge of the monopole is recorded is of help when there are monopoles and antimonopoles nearby: the topological charge of a monopole does not change during its evolution, *i.e.* a monopole does not become an antimonopole, and therefore the number of possible candidates to match to a given monopole is halved.

After this refinement of segment and monopole velocity estimators, most of the instances where superluminal velocities were obtained have been cured. However, there remains some cases where superluminal velocities appear, still corresponding to the same merging of segments as mentioned above; but not too all cases, just a few.

We pinpointed those cases, in order to determine whether those high velocities where physical or had their origine only on the shortcomings of our algorithms, and found that the reason for these apparently superluminal velocities was the following: on these occasions, the field configuration between the two monopoles that are about to merge is such that it is energetically favourable for a new segment to form in-between the two advancing ones. In some sense, a new segment appears out of thin air, such that it seems that the monopole has instantaneously moved considerably. The monopole does not pull from the string and creates string as it moves; instead, a *chunk* of string has been formed and the monopole has made a jump forward. One way to understand this is to think about the field dynamics in the plane orthogonal to the string that is about to form (see [6]). Consider the extreme case of a z-independent field configuration that is going to become a straight string in the z axis. Initially the magnetic field in the $x-y$ plane is dispersed over a relatively large area, so its value is below the threshold where our algorithm would recognize the presence of a string, and it is accreting into a smaller area around the z axis –a region with a lower value of the scalar field than the surroundings. At some point the magnetic field grows above the threshold and we see the whole string appear in a single timestep.

In other words, the points of windings of ϕ_1 and ϕ_2 are almost parallel, and it is favourable for a collection of points to become part of a string all together. Since our simulation only takes snapshots every 20 timesteps, this process can remain unnoticed, and the end result is that the segment has apparently grown superluminaly, whereas the reality is that a new segment has been formed.

It is worth reminding the reader at this stage that we are *not* simulating segments and monopoles, we are simulating fields, and the monopoles and segments are consequences of them. Thus, a monopole does not really *move*, it is the movement of the fields which render the apparent movement of the monopole. When a new segment forms, the physics of the fields are causal, but the consequence may seem to be a monopole moving ultrarelativistically, when, in essence, it is a different monopole.

Figure 5.6 shows one such situation. The two fragments showed belong to segments that were behaving nicely (i.e., not ultrarelativistically), until they get ready to merge. When they are close

to each other, the dynamics of the fields try to perform the merging as soon as possible: on the one hand, that segment-ends grow by creating small segments in the ends, and even in between the segments a new string is formed (shown as single points in the figure). Our algorithm is not able to catch these instances, and instead, velocities faster than light are reported.

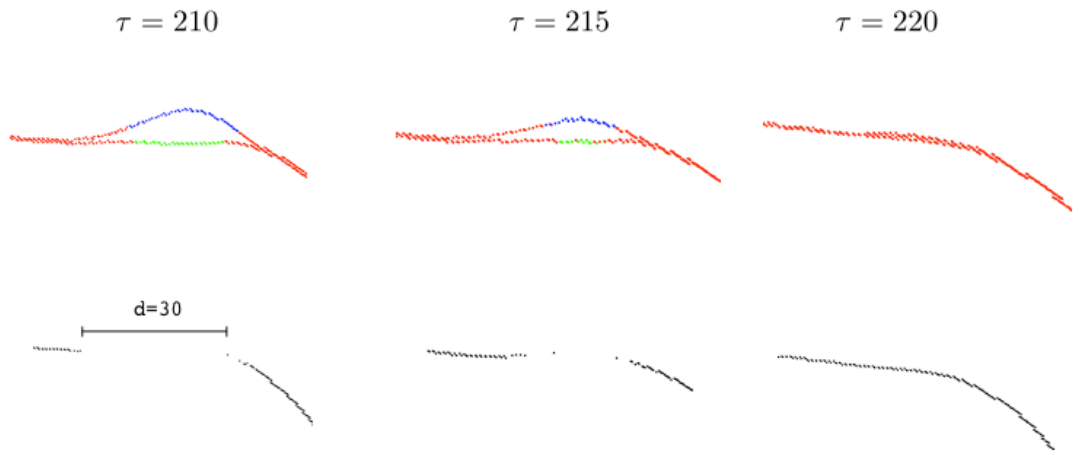

Figure 5.6.: *In this figure we show the mergining of two string segments, in what our algorithm would report as ultrarelativistic velocities. Initially the separation between both string-ends is $d = 30$ and in less than $\Delta\tau = 10$ both segments have merged. This process can be understood as small string segments being formed both close to the string ends, as well as in between both strings (depicted by those single points in between strings).*

The question remains now on how to automatically factor out those instances, which would clearly corrupt the estimator and give much higher velocities than the true physical one. Learning from our previous experience on segment velocities, we apply the following method to disregard those unphysical velocities: For points that move very fast (in practice we chose velocities faster than 0.5c), the velocities obtained by going "forward" (from τ_1 to τ_2) and "backward" (from τ_2 to τ_1) are compared. If the difference is higher than 50% of the value of either of the velocities, we disregard it. This is preferable than setting a hard cut-off, because the results clearly do depend on the cutoffs, and we do not want to artificially enforce that the velocities be sub-luminal in case this should result form the physics.

5.5. Numerical results

In this section we report on the results obtained from our simulations, after carefully filtering out the caveats described in the previous section.

We first checked that the simulations reached the scaling regime. Scaling can be checked by the evolution of the energy of the system, as mentioned earlier, by checking that $T_{00}^{-1/2}$ is linear with time τ. This is a measure that depends only on the values of the fields as simulated, without further treatment. We show the scaling on our simulations using the energy as a measure of scaling in Fig. 5.7.

There are also two other ways that check for scaling that depend on the total length of string $\mathcal{L}$ and the total number of monopoles $\mathcal{N}$. One can obtain a VOS-type length scale by the following combinations $\sqrt{\frac{V}{\mathcal{L}}}$ and on $\left(\frac{V}{\mathcal{N}}\right)^{1/3}$. These two magnitudes are derived magnitudes, meaning that

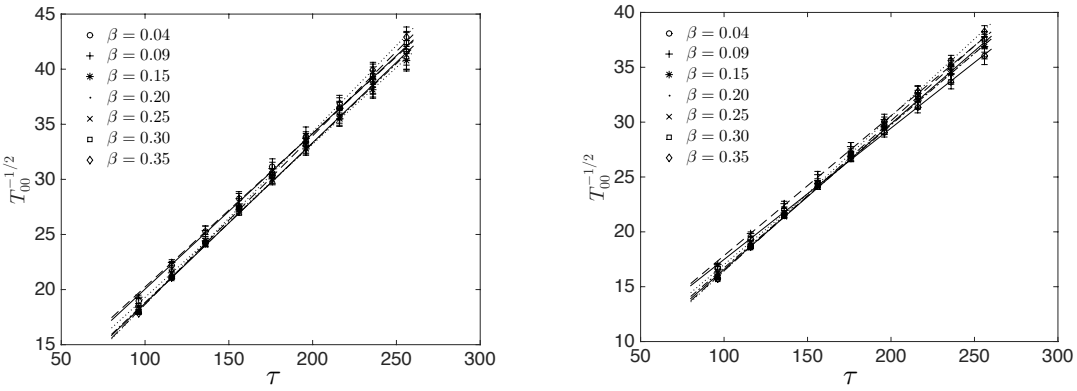

Figure 5.7.: *This figure shows that our simulations reach a scaling regime. The left panel shows the case, for all β, of radiation domination; and the right panel the case of matter domination.*

one has to extract this information from the simulation using estimators, and therefore, in some sense, they are more indirect than using the Energy to check for scaling. We show the behaviour of those parameters in Figure 6.1 for two extreme cases (radiation and $\beta = 0.04$) and (matter and $\beta = 0.35$). These curves show that the system does indeed reach scaling fairly early. The slope of the curves related to $\mathcal{L}$ and $\mathcal{N}$ is what was used above (5.6, 5.8) to determine the VOS-type scaling parameters. The values of $\gamma_{\mathcal{L}}$ and $\gamma_{\mathcal{N}}$ can be found in table 5.3 for every β studied.

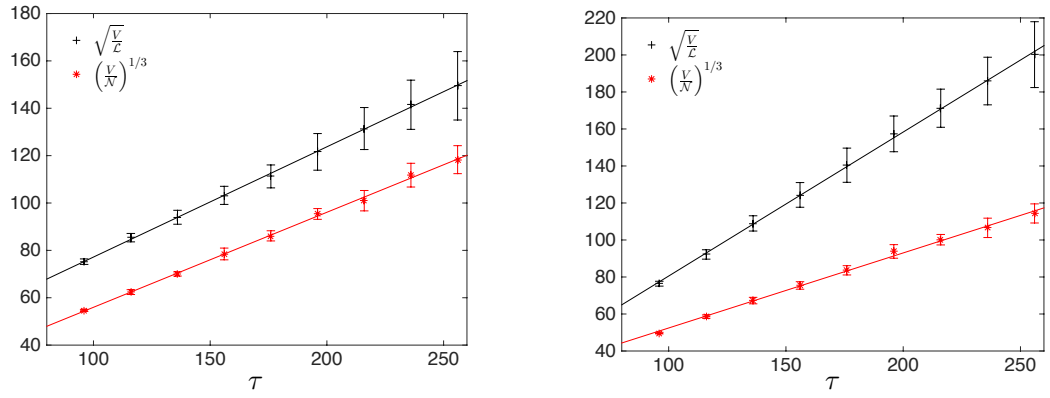

Figure 5.8.: *Scalings in total string length and monopole number for $\beta = 0.15$ in radiation era (left) and for $\beta = 0.35$ in matter era (right).*

One main result obtained in this work is the values of the velocities of the semilocal network, both for strings and for monopoles, using our different estimators. In Table 5.4 we show the velocity values for every β in Radiation and Matter epoch obtained by following the positions of each string segment and monopole, and averaging over all cases (the errors given are statistical errors). Overall one can see that the velocities in radiation are somewhat higher than the velocities in matter, as expected due to a lower damping term in the former. More interestingly, there does not seem to be a strong dependency on the velocities on β; one can try to hint some tendency, but all those numbers are equivalent within the errors.

In Table 5.5 we show the velocities obtained by local field estimators (5.10). Note that these estimators do not distinguish between string and monopoles, and give one number for the average

	Radiation		Matter	
β	$\gamma_{\mathcal{L}}$	$\gamma_{\mathcal{M}}$	$\gamma_{\mathcal{L}}$	$\gamma_{\mathcal{M}}$
0.04	0.38 ± 0.05	0.48 ± 0.04	0.28 ± 0.02	0.41 ± 0.02
0.09	0.40 ± 0.04	0.43 ± 0.02	0.33 ± 0.02	0.38 ± 0.02
0.15	0.47 ± 0.09	0.40 ± 0.02	0.40 ± 0.04	0.35 ± 0.03
0.20	0.52 ± 0.08	0.41 ± 0.04	0.46 ± 0.04	0.37 ± 0.02
0.25	0.61 ± 0.09	0.42 ± 0.05	0.54 ± 0.06	0.37 ± 0.02
0.30	0.81 ± 0.09	0.46 ± 0.05	0.65 ± 0.09	0.37 ± 0.03
0.35	1.06 ± 0.09	0.49 ± 0.05	0.78 ± 0.09	0.41 ± 0.03

Table 5.3.: *Values of the VOS-type length estimators for the total length of segments $\gamma_{\mathcal{L}}$ and the total number of monopoles $\gamma_{\mathcal{M}}$ (5.6, 5.8) in the box for every β.*

	Radiation		Matter	
β	$v_{\mathcal{L}}$	$v_{\mathcal{M}}$	$v_{\mathcal{L}}$	$v_{\mathcal{M}}$
0.04	0.345 ± 0.010	0.574 ± 0.010	0.266 ± 0.010	0.505 ± 0.010
0.09	0.338 ± 0.010	0.583 ± 0.010	0.265 ± 0.010	0.510 ± 0.010
0.15	0.337 ± 0.010	0.600 ± 0.012	0.262 ± 0.011	0.509 ± 0.010
0.20	0.337 ± 0.010	0.591 ± 0.010	0.260 ± 0.010	0.519 ± 0.010
0.25	0.337 ± 0.010	0.591 ± 0.010	0.261 ± 0.010	0.520 ± 0.010
0.30	0.342 ± 0.014	0.596 ± 0.010	0.259 ± 0.010	0.524 ± 0.010
0.35	0.337 ± 0.013	0.600 ± 0.012	0.262 ± 0.011	0.521 ± 0.012

Table 5.4.: *Velocities for segments ($v_{\mathcal{L}}$) and monopoles ($v_{\mathcal{M}}$) obtained by following the positions segments and the monopoles during the simulation. The error are statistical errors obtained by averaging. The velocities in radiation are somewhat higher than in matter; but there does not seem to be a strong dependence on β for the velocities.*

network velocity for semilocal strings as a whole. Once again, we obtain that velocities during radiation are faster than in matter; and we also note that both local field estimators give equivalent velocities. In this case there seems to be a trend, and velocities seem to decrease for increasing β.

The procedure of following the positions of the string segments and of the monopoles does not only allow us to obtain a network velocity, but it also allows us to obtain the velocity of each segment and monopole, and to follow the history of each segment and monitor whether they merge with another segment, they disappear, or they just continue to flow in the network. This is very interesting information from the point of view of the VOS model, because we can now tell if there is a correlation between string segment size and its velocity, for example.

We show in Figs. 5.9 and 5.10 the velocity versus length distribution for some time-steps and $\beta = 0.04$ in radiation domination. The situation with other β and matter domination is analogous; figures for other values of β can be found in Appendix A. In those figures, each point corresponds to a segment, which are distributed according to their length-per-time (x axis) and velocity (y axis) for three different times (τ =116, 176, 236). Those segments have been divided into two groups: On the one hand, in Fig. 5.9 we plot the segments which do not interact with other string segments in the next time step, i.e., segments which *flow* through the network. On the other hand, in Fig. 5.10 we show the segments that do merge with other segments before the next time

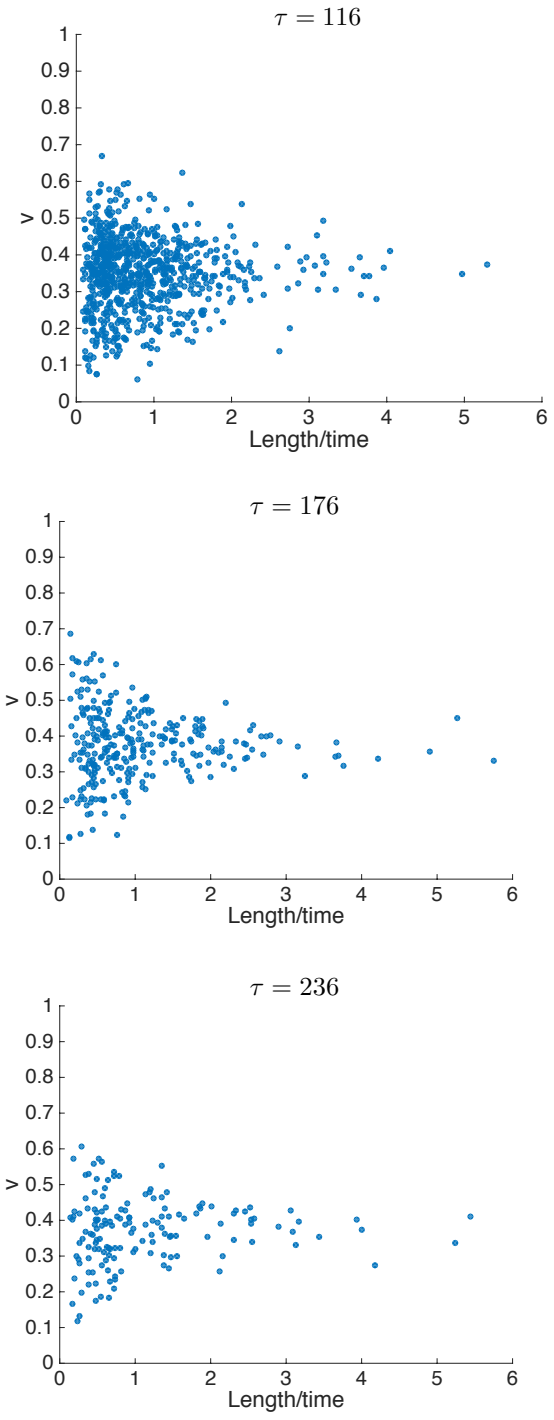

Figure 5.9.: *This plot shows the distribution of segments with respect to velocity for simulation in radiation domination and $\beta = 0.04$. Each point represents a segment in the network, where in the x-axis the length of the segment divided by time is shown and its velocity in the y-axis. This is the case where segments flow through the network, i.e., they do interact with any other segment in the next time step.*

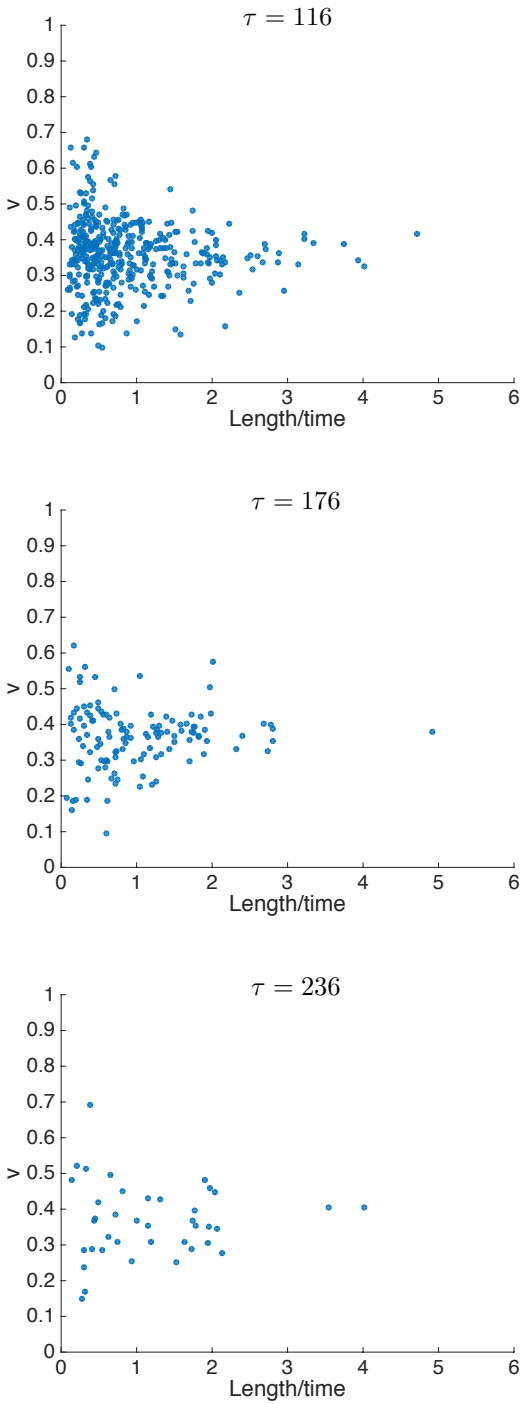

Figure 5.10.: *This figure is similar to Fig. 5.9, but in this case the segments that are plotted are those that merge with other segments before the next time step.*

	Radiation		Matter	
β	v_F	v_G	v_F	v_G
0.04	0.57 ± 0.02	0.55 ± 0.02	0.41 ± 0.01	0.41 ± 0.01
0.09	0.57 ± 0.02	0.56 ± 0.02	0.42 ± 0.01	0.41 ± 0.01
0.15	0.55 ± 0.02	0.55 ± 0.01	0.41 ± 0.01	0.41 ± 0.01
0.20	0.53 ± 0.02	0.53 ± 0.02	0.40 ± 0.01	0.40 ± 0.01
0.25	0.51 ± 0.02	0.51 ± 0.02	0.39 ± 0.01	0.39 ± 0.01
0.30	0.49 ± 0.02	0.50 ± 0.02	0.38 ± 0.01	0.38 ± 0.01
0.35	0.47 ± 0.02	0.48 ± 0.02	0.36 ± 0.02	0.37 ± 0.02

Table 5.5.: *Velocities obtained from local field estimators (5.10) for all β and radiation and matter dominations. Velocities in radiation domination are higher than in matter domination. There are stronger hints that the velocity of the network decreases for increasing β.*

step.

It is worth mentioning that the points are scattered around a central value, which is roughly the same for all times and all lengths. The scatter is larger around short segments, mainly because there are many more short than long segments. This is rather clear in the *flow* case, because there are more segments in this case than in the *merge* case; though we could say that this is generic for all cases.

This information can be shown also, maybe in a more compact way, in form of histograms; which are in some sense the marginalized distribution functions of Figures 5.9 and 5.10. For example, in the top panel of Fig. 5.11 we show distribution of the length-per-time of the number of segments during the evolution for $\beta = 0.04$ in radiation domination. The segments are binned in 10 bins with uniform width, and we show together three cases: in blue we depict the segments which are *flowing*, in green the ones that are *merging* and in yellow we show the segments that *collapse* before the next time step. Note that in the last time step we have no information whether the segments which flow, merge or collapse, so we just choose to show them as flow segments. In the bottom panel we show the same histogram, but instead of showing the number of segments in each bin, we also account for the length-per-time of the strings; we add up the total length-per-time of the segments in each bin, and show that length-per-time in each bin.

The histograms with information about velocities can be seen in Fig. 5.12. The top panel shows the distribution of number of segments per velocity, for $\beta = 0.04$ in radiation domination. The bottom panel shows the corresponding distribution for monopoles. This velocities are computed instantaneously, i.e., they are the velocities obtained by measuring the distance traveled by monopoles between two adjacent time-steps (not by averaging over the whole history of the monopole). Note that there is no information for time $\tau = 256$ because we have no "next time step" to compute the velocity with. The color-code is the same is in the previous figure: in blue we depict the strings (segments or monopoles, correspondingly) which are flowing, in green the ones that are merging and in yellow we show the strings that *collapse* before the next time step.

The histograms show a scaling behaviour, where roughly the segment distribution follows the same pattern independently of time. The length distribution show that, logically, only short segments collapse before the next time step; but mergings happen for all string lengths. There is no preference on the velocity of the collapsing segments; there are collapsing segments with a wide variety of velocities. The velocity distribution have some kind of Gaussian distribution, centered in the average velocity, corresponding to the velocities of Table 5.4.

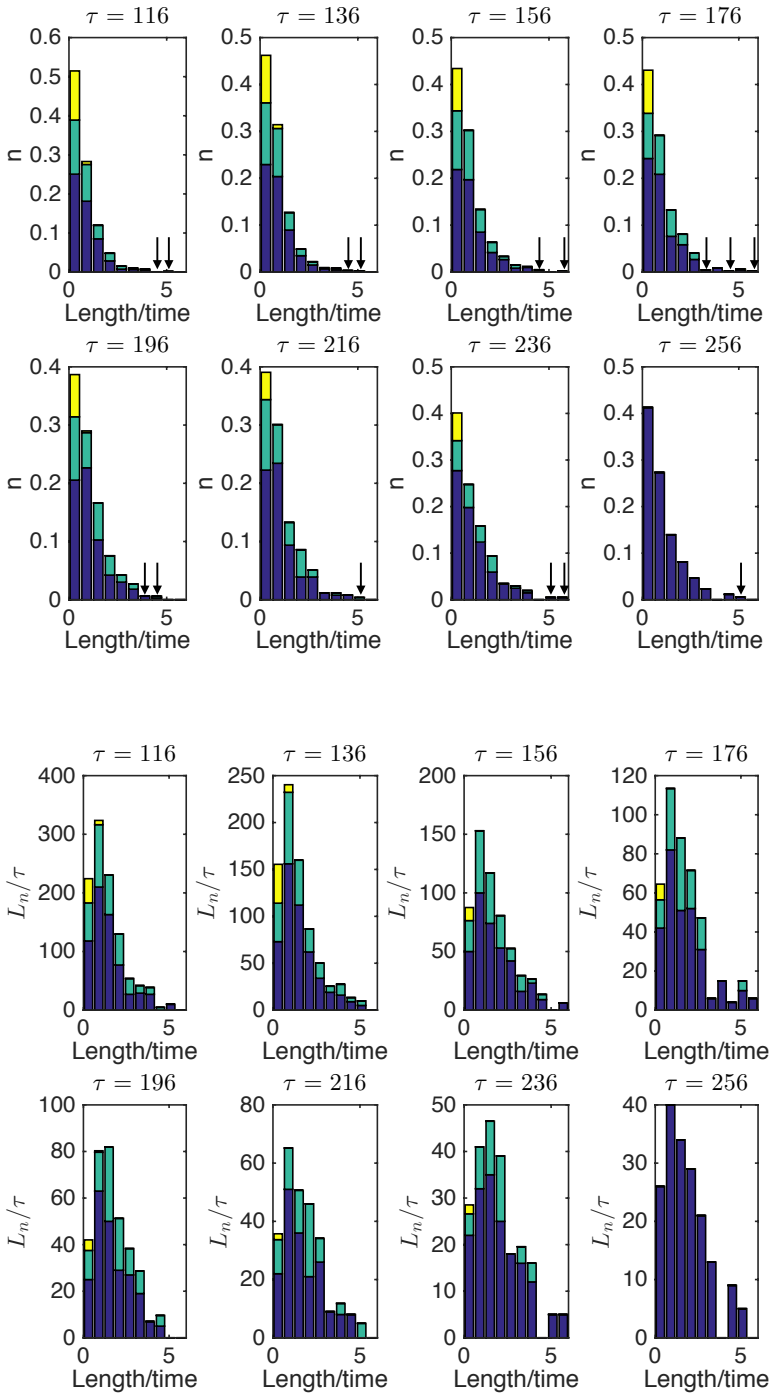

Figure 5.11.: *These histograms show the distribution of the segments during the evolution for $\beta = 0.04$ in radiation domination, where the segments are binned in 10 bins with uniform width. The top figure shows the distribution of the number of segments with respect to length-per-time, whereas the bottom figure shows the same distribution, but where the total length-per-time of the segments in each bin has been added. The colors represent different type of segments, depending on their future behaviour: in blue segments which are flowing, in green segments that are merging and in yellow segments that are collapsing before the net time-step. We write arrows to remark that in those instances, there are a few (one or two) segments in that bin, which are hard to see in the top plot, but can be seen in the bottom plot. Note that in the last time step we have no information whether the segments will flow, merge or collapse, so we just choose to show them as flow segments.*

The monopole-velocity histograms show also a (wider) gaussian-like distribution, with instances in which monopoles approach $v = 1$ (though this may be an artefact of our algorithms, as explained in Section 5.4.3). It is easy to convince oneself that the average of these velocities agree with the ones in Table 5.4. It is worth noticing that the velocities of monopoles that are about to collapse are rather high, most of the times higher than the average velocities of the segments. Therefore, even though the segment velocities for collapsing segments have no preference, the monopole velocities do. This could be understood by realizing that the monopole velocity only takes into account the string-ends, whereas in the segment velocity, the whole segment contributes; and apparently only the segment ends get high velocities in collapse.

Finally, it is interesting to investigate what the pattern of merging of different segments is. In order to do so, we chose one of the largest segments at the last time-step for $\beta = 0.04$, and traced back its history to see what where its "constituents". This information can be found in Fig. 5.13, in the form of a "family tree". This shows that at very early times, many mergings happen. This does not mean that many segments have joined at the same time; most likely the segments have been joining by pairs, but our choice time-step to measure the network is too coarse to distinguish all these mergings. The sum of the length of the constituents does not match the final segment; clearly, this is because segments can grow or shrink in their evolution. Also, there are some segments that remain quite solitary for most of their life. This exercise of following the family history of a segment highlights once more the complicated dynamics that semilocal strings have.

5.6. Conclusions and discussion

In this work we have investigated a network of semilocal strings using field theoretical simulations. We have estimated the length and velocity of the semilocal strings (including the string-ends, that can be understood as global monopoles) using different estimators; coming from both direct field theory based estimators and by estimators that use the position of the strings. As well as characterizing the network of defects, these measures are indispensable to obtain a VOS-type effective model for semilocal strings. Before this work, the velocities of semilocal strings (both as a network and as individual segments, as well as the monopoles) were unknown.

The VOS-type length estimators for string segments and monopoles (5.6, 5.8) can be found in Table 5.3. These values had already been computed in a previos work [9] using a different technique. In [9] the semilocal string segments were defined as collections of points in contact with a magnetic field higher than some threshold, and that volume of points was divided by an estimate of the cross-section of the strings to get a length. In this work we reproduced those calculation, and compared it to the new length estimator, which is based on following the points with windings in the simulation. We found that these two length estimators do not match, and that there is roughly a factor 1.5 difference between the two length estimators. We identified the source of error as a numerical error on the estimation of the string cross-section, and therefore the values for the length estimators that we obtain in the present work can be considered as corrections to the ones in [9]. However, the differences obtained lie within the 1-σ error level. It should also be noted that the length corresponding to the monopoles $\gamma_{\mathcal{N}}$ is roughly equivalent in both works, since the number of segments (monopoles) does not depend on the error corresponding to the cross-section of the strings.

One big advantage of being able to characterize the semilocal strings by the points (plaquettes) with winding is that we get a one-dimensional description for the position of the strings. This allows us to follow string segments and monopoles throughout the simulation, map their history,

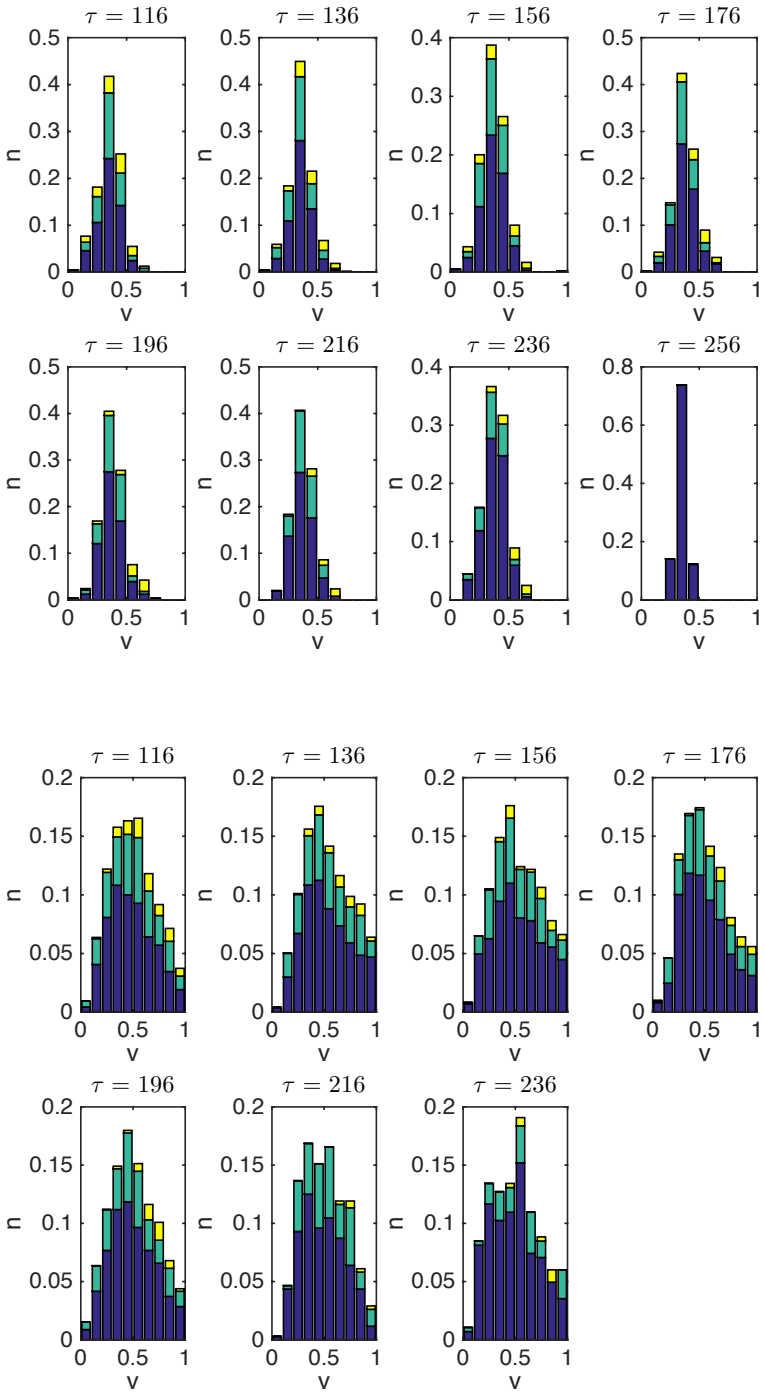

Figure 5.12.: *These histograms show the velocity distribution of the segments (top) and monopoles (bottom) during their evolution, for radiation and $\beta = 0.04$. The velocities are binned in 10 bins with uniform width. The color code is analogous to the previous figure: blue corresponds to strings that do not interact with other strings before the next time-step (flow), green is for strings which merge with other segments and yellow is for strings that disappear before the next time-step because the segment collapses. Note that in the last time step we have no information whether the segments will flow, merge or collapse, so we just choose to show them as flow segments. Note also that in the monopole velocity case we do not have information to compute the velocity at the last time step.*

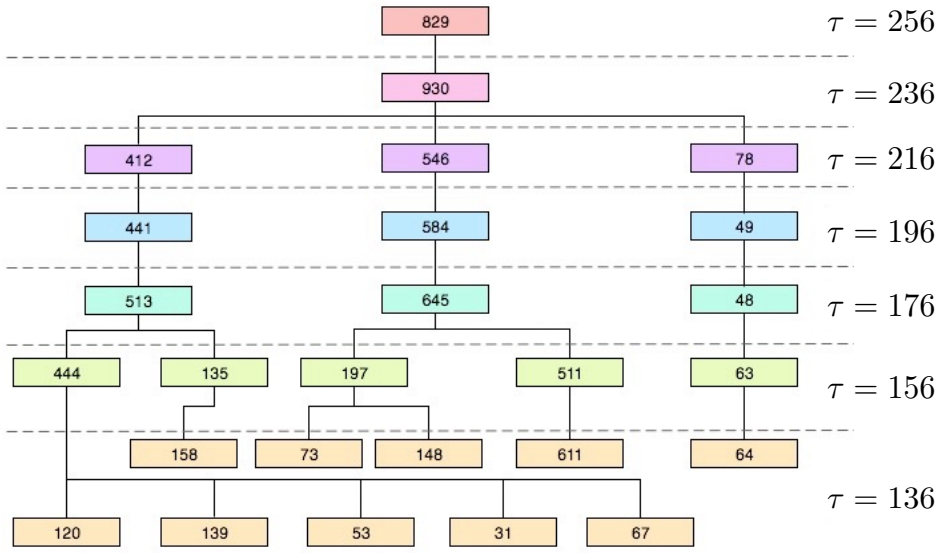

Figure 5.13.: *The "family tree" of a segment for $\beta = 0.04$ in radiation. The number inside the box denotes the length of each segment, and time runs upwards.*

and get an estimate on the velocity. Table 5.4 shows the network velocities of segments and monopoles for radiation and matter eras, for all β under study. The velocities for radiation domination are higher than the corresponding velocities in matter domination, for all β. It is worth pointing out that there is little dependence on β for these numbers, specially for the velocity of the segments. Even though some trend could be hinted, bearing in mind the errors for the estimates makes it hard to claim any such trend.

The velocities can also be estimated using field-theoretical estimators (5.10), and the result can be found in Table 5.5. The velocities obtained with both local-field estimators agree with each other, and as in the previous case, the velocities in radiation are higher than in matter. These values obtained from the field-estimators are somewhat different from the ones obtained form the positions of the defects. In fact, the field-estimators do not distinguish between strings and monopoles, and they give a single number for the whole network. It is not surprising, maybe, that in all cases the values lie in between the velocities of strings and monopoles.

Contrary to the velocities obtained from the positions, the values in Table 5.5 show a trend with β. One cannot but speculate that this difference is the result of several magnitudes in the simulation box: the ratios of densities of strings and monopoles depend on β (for lower β strings are longer), the mass of the strings (for lower β strings are lighter), the tendency of strings to collapse or merge... Moreover, it has been noted before that the estimation of velocities of defects using directly the position of the defects underestimates the velocities [73, 96, 101], and the reason for this is not completely clear.

Even though there are some discrepancies in the values of the velocities, one huge advantage of being able to follow the positions of the strings is that we can obtain the history and the velocities for individual segments. Figures 5.9 and 5.10 show the scatter plot of segment length versus segment velocity, for cases when the segments do not interact with other segments in the following time-step, and for cases where the segments merge with other segments, respectively.

It was somewhat surprising to see that the values of the velocities where scattered around a central value for all values of the length of the strings. In other words, we found no correlation between the length and the velocity of the segments. This is a hint that the VOS effective model may need to be revisited to take this into account. Moreover, one could have wondered whether it is more preferable for short segments to collapse and for longer ones to merge. These plots show that mergings happen for all segment sizes, not only for longer ones.

The histograms where the length of the strings per bin are depicted (Figure 5.11 bottom) shows that actually most of the string length is not in the shortest segments; there is more length in the second and/or third bins. This histogram also shows more clearly that there are very long segments which do merge with other ones. This interesting behaviour is also shown in the family tree-like figure Fig. 5.13. There we can se many mergings at the beginning of the simulation, then some quiet period, before mergings happen also towards the end of the simulation. The lengths of the segments that take part in mergings are very varied, and there is no correlation between segments size and their future behaviour.

Monopole velocities show, however, that segments that are going to collapse do it generally at somewhat higher velocities. The distribution is not so clearly gaussian, there is more noise, and some monopoles are very fast. One has to be cautious here and remember all the caveats we have to overcome to obtain velocities of segments. The instances where monopole velocities were very close to one (and sometimes faster than one) are due to the merging/collapsing of segments, and the shortcomings of our algorithm or interpretation of those event.

One of the most challenging aspects in this work has been, actually, the correct estimation of the velocity of segments and monopoles close to mergings. The naïve estimators of velocity gave

instances of extremely high velocities. After we corrected for the obvious caveats (such as trying to get the velocity of a segment that had collapsed by trying to find the (collapsed) segment in the next time step and obviously failing) many of those very fast segments disappeared. But there were still some cases where the velocity was too high, higher than what one would naively expect from the causality of the field equations, and from what the field-estimators for velocities were showing.

The reason for this apparently superluminal behaviour is that, close to segment mergings, if the field configuration was favourable, new string segments appeared 'out of the blue'. It was not a case of a monopole moving towards an antimonopole and creating string as it evolved; it was rather a new segment appearing, and giving the illusion of a very fast movement of the monopole/segment; whereas in reality it was a new monopole altogether, and the *old* monopole had annihilated with the newly formed antimonopole. This behaviour is completely consistent with causal dynamics; it is the effect of the magnetic field accreting to form the new string segment. It has been studied in two-dimensional simulations in [5, 6] and is also seen in the case of a global monopole whose cores are pinned down while letting the radial field gradients bunch into a string-like region that subsequently decays and disappears, taking the monopole with it [3, 26, 57].

This is something that may prompt revisiting the VOS analytical model for semilocal strings: if we consider that network velocities are subliminal, the effective model has to account for the possibility of segments growing out of thin air, because otherwise the speed at which segments merge and collapse may be underestimated.

Another possible idea prompting some revision on the VOS analytical model for semilocal strings comes from the realization that semilocal strings happen roughly when both fields are winding; even though in theory it would be enough that one of them wind and the other was not in its vacuum value, so as to allow for some concentration of magnetic energy. This picture is reminiscent of a network of p-q strings [39, 51], with monopole playing the rôle of the Y-junctions. However, the analogy might end there, since the "constituents" of either p- or q-strings are actually massless (they are virtually formed of field configurations in their vacuum manifold), spoiling the analogy between semilocal string networks and p-q networks.

This work about characterization of semilocal string has highlighted even more how rich the dynamics of this model is, and how complicated the life of a semilocal network can be.

6 Cosmic Microwave Background constraints for global strings and global monopoles

6.1. Introduction

As we have seen in Section 1.6, the evolution of a defect network perturbs the background space-time; and those perturbations evolve and affect the contents of the universe, eventually creating CMB anisotropies. In contrast to the inflationary perturbations, which were seeded primordially and then evolve "passively", defects induce perturbations actively during their whole existence.

The analysis of the CMB gives a good opportunity to study early Universe models. Therefore the CMB signature of cosmic strings in gauge theories has been widely analysed. In these analyses different approaches were used. Some approaches computed full-sky maps of defects [17, 87, 88, 109]. Many other approaches, however, relied on the use of Green functions or of unequal time correlators (UETC) [110], where the knowledge of the defect stress tensor evolution during the cosmological expansion is required. Using the UETC approach, CMB signatures of cosmic strings have been analysed for different levels of modelling, that is, using effective models [14, 15, 24, 89, 90] or using the field-theory model describing the defect [29, 31, 128]. In the last few years significant advances in the study of the CMB power spectrum using the UETC approach for Abelian-Higgs strings were performed; using the biggest simulation boxes up to date [45] and, among other improvements, studying the behaviour of the correlators cross cosmological transitions [95]. However, there are other defect models that have also been studied but they have attracted less attention. For example, the imprints of semilocal strings were studied in [127].

In the same way, global defect models, O(N), have been also studied. For the analysis of the CMB power spectrum of these kind of models the large-N limit and the non-linear sigma model were used [28, 50, 109]. Using this approaches gravitational wave imprints were also calculated [54, 78]. However, in [56], where the GW imprints for O(N) models using field-theory simulations were analysed, was showed that for $N > 4$ the large-N prediction worked rather well, but it failed to capture the dynamics of lower Ns.

Global string and monopole networks have been analysed for other reasons, but the CMB signature for O(2) and O(3) models have never been studied, even though the analysis of the CMB power spectrum generated by global strings and monopoles would be of great interest. For example, in [101] the evolution of global string networks in large-scale numerical simulations were studied and in Chapter 4 of this Thesis the network velocities of global monopoles are studied in detail. As we have previously mentioned the large-N predictions for GW does not fit with O(2) and O(3) direct calculations. Therefore it is important to perform O(2) and O(3) field theory simulations to check whether they follow the CMB predictions from O(N) with large-N. Moreover, due to the difference in behaviour between global defects and local defects that we

have mentioned in Section 2.4.1 this analysis will bring different results.

In this work we perform field-theory simulations of O(2) and O(3) global models and using the UETC approach we calculate the CMB power spectrum. This power spectrum will be used to compare with the predictions given by the large-N limit and also with the spectrum coming from the analysis of the Abelian-Higgs model. We perform a Monte Carlo analysis using Planck data [12] and the results obtained in this Chapter.

The rest of the Chapter is structured as follows: In section 6.2 we give an overview of the model. Then, we describe the procedure to obtain the UETCs from the simulations in section 6.3 and the computation of the source function in section 6.4. Once we have the source functions we present the power spectra in section 6.5. Finally, in section 6.6 we show the fits and constraints and we conclude in section 6.7.

6.2. Model overview

The defects that we will analyse in this section are global strings and global monopoles. These defects are created in a global $O(N)$ model when the $O(N)$ symmetry spontaneously breaks down to $O(N-1)$, where $N=2$ for global strings and $N=3$ for global monopoles. The properties of these models are analysed in detail in Section 2.4.1, where we have said that these models can be described by the following Lagrangian (2.67),

$$\mathcal{S}=\int d^4x\sqrt{-g}\Big(\frac{1}{2}\partial_\mu\Phi^i\partial^\mu\Phi^i-\frac{1}{4}\lambda(|\Phi|^2-\eta^2)^2\Big), \tag{6.1}$$

where $|\Phi|\equiv\sqrt{\Phi^i\Phi^i}$ and λ and η are real constant parameters. Φ^i are real fields where $i=1,2$ for global strings and $i=1,2,3$ for global monopoles. Since our aim is to study the dynamics of a network of global defects in an expanding universe, we consider a flat Friedmann-Lemaitre-Robertson-Walker space-time with comoving coordinates (see Section 1.3):

$$ds^2=a^2(\tau)(-d\tau^2+dx^2+dy^2+dz^2), \tag{6.2}$$

where $a(\tau)$ is the cosmic scale factor and τ is conformal time. The equations of motion derived from (6.1) are

$$\ddot{\phi}^i+2\frac{\dot{a}}{a}\dot{\phi}^i-\nabla^2\phi^i=-a^2\lambda(\phi^2-\eta^2)\phi^i, \tag{6.3}$$

and the dots represent derivatives with respect to the conformal time τ.

Since the size of the defect is given by their mass ($\delta\sim m_s^{-1}$), it is a fixed length in physical units, which means that in comoving coordinates the size of the defects rapidly decreases. Thus, as we have done in Chapters 4 and 5, we will use the Press-Ryden-Spergel algorithm [115], where the width of the defect transforms into controllable by turning the coupling constant into a time-dependent variable, $\lambda=\lambda_0 a^{-2(1-s)}$. That is, when $s=0$ the defect size is fixed in comoving coordinates and when $s=1$ we obtain the true case where the size of the defect is fixed in physical length.

6.3. UETCs from the Simulations

In this section we present the details of the numerical simulations from which the UETC data were collected. The scaling UETCs are the inputs for the next section, in which the eigenvector decomposition method is described.

	$O(2)$	$O(3)$
$\tau_{\rm ini}$	50	0
$\tau_{\rm diff}$	70	20
$\tau_{\rm ref}$	150	60
$\tau_{\rm end}$	300	250
$n_{\rm out}$	50	60

Table 6.1.: *The values of the time-related parameters, given in units where $\eta = 1$. The simulations start at time $\tau_{\rm ini}$ and there is a period of diffusion until $\tau_{\rm diff}$; the data are taken from $\tau_{\rm ref}$ until $\tau_{\rm end}$ every $n_{\rm out}$ time-steps.*

6.3.1. Simulation details

In order to simulate the evolution of the global defects in a discrete box we use the procedure described in Section 2.3.4. Our simulation lattice, which is a 1024^3 lattice, has a comoving spatial separation of $\Delta x = 0.5$ and time steps of $\Delta\tau = 0.1$, in units where $\eta = 1$. The simulation volume therefore has comoving size $L = 512$. The coupling was chosen to be $\lambda = 2$, and thus the mass of the scalar fields $m_s = \sqrt{2}e\eta$. These simulations were performed in Sisu, a Massively Parallel Processor (MPP) supercomuter managed by CSC-IT center for science. We performed 5 individual runs in pure radiation and in pure matter dominated eras with $s = 0$ to determine the scaling form of the UETCs. We also performed runs across the radiation-matter cosmological transitions using the same parameters and initial conditions.

For the radiation and matter simulations we are interested in the scaling regime of the defect network, not on the details of the phase transition. Thus, the initial condition (at time $\tau_{\rm ini}$) used in the numerical simulation is not used to extract data; its mere functionality is to drive the system to scaling as soon as possible in order to get as large as possible dynamical range. We have found that for the present work a satisfactory initial field configuration is given by the scalar field velocities set to zero and the scalar fields set to be stationary Gaussian random fields with power spectrum

$$P_\phi(\mathbf{k}) = \frac{A}{1 + (kL_\phi)^2}, \tag{6.4}$$

with A chosen so that $\langle|\phi^2|\rangle = \eta^2$, and $L_\phi = 5\eta^{-1}$.

The UETCs cannot be calculated until after the defects are formed and reach their scaling configuration. These early phases contain a huge amount of excess energy induced by the random initial conditions, therefore we smooth the field distribution by applying a period of diffusive evolution, with the second derivatives removed from the equations of motion and with time steps of $\Delta\tau = 1/30$, in units where $\eta = 1$. Depending on the model we are simulating we have to impose the diffusive evolution in a different time period ($\tau_{\rm diff}$).

After the diffusion period, the system relaxes into scaling, and we start to collect data from $\tau_{\rm ref}$ until the end of the simulation $\tau_{\rm end}$. We measure the UETC by recording the mean value of $C_{ab}(k, \tau_{ref}, \tau)$ for wavevectors binned in the range $2\pi(n-1)/L < |\mathbf{k}| \leq 2n/L$ $(1 \leq n < N_b)$, with $N_b = 886$, and n_{out} logarithmically-spaced times between τ_{ref} and τ_{end}. The wavenumber of the nth bin k_n is set to the mean value of $|\mathbf{k}|$ in that bin. Table 6.1 shows the values of these parameters.

We also record the equal time correlators (ETCs) at each time the UETC is evaluated, with which we can monitor the quality of scaling. Perfect scaling would mean that the ETCs collapse

to a single line when plotted against $x = k\tau$.

6.3.2. Scaling

In order to track both the state of the system and scaling, it is convenient to define a length scale of the network. We will define two different length scales, one for each case of defect under study, *i.e.* one for strings and another one for monopoles.

For the case of strings the comoving string separation $\xi^{\rm s}$ has been identified as a useful quantity to determine compatible simulation stages [45]. The string separation is defined in terms of the mean string length ℓ_s in a horizon volume $\mathcal{V}$ as

$$\xi^{\rm s} = \sqrt{\frac{\mathcal{V}}{\ell_s}}. \tag{6.5}$$

The mean string length, ℓ_s, is usually derived by directly measuring the comoving length of each string (see details in [29, 31, 79, 120]). One way of obtaining the length of strings is by summing the number of plaquettes pierced by strings [79]. Such plaquettes are identified calculating the winding of the field in each plaquette of the lattice. We denote the string separation computed in this way as $\xi^{\rm s}_{\rm w}$.

An alternative way is to use local field theory estimators to get the above ratio [45]. In our case we use the energy weighted by the potential V ($E_{\rm V}$) and the energy per unit length ($\mu_{\rm s,V}$) also weighted with the potential,

$$\ell_s = \frac{E_{\rm V}}{\mu_{\rm s,V}}, \tag{6.6}$$

to obtain $\xi^{\rm s}_{\rm L}$.

In order to obtain the potential weighted energy per unit length of global strings, $\mu_{\rm s,V}$, we have solved numerically the equations of motion for a static straight string lying on the z-axis [137]. From the values of the profile functions we have calculated the weighted energy per unit length.

As we can see in Fig. 6.1 the scaling information given by both approaches (*i.e.* length estimations counting windings or using field estimators) are compatible. However, the computational cost of the field estimators is considerably lower.

Monopole networks can be characterized using the comoving monopole separation $\xi^{\rm m}$. The monopole separation is defined in terms of the monopole number in a horizon volume $\mathcal{V}$ as

$$\xi^{\rm m} = \Big(\frac{\mathcal{V}}{\mathcal{N}}\Big)^{1/3} \tag{6.7}$$

where $\mathcal{N}$ is the monopole number in the volume $\mathcal{V}$[1]. The monopole number can be computed by directly obtaining the topological charge in each lattice cell of the simulation box [18] (see Section 4.3.1) and also using local field theory estimators the number of monopoles can be obtain in the following way,

$$\mathcal{N} = \frac{E_{\rm V}}{\mu_{\rm m,V}}, \tag{6.8}$$

where $\mu_{\rm m,V}$ is a energy of a monopole weighted with the potential V and $E_{\rm V}$ is the energy weighted with the potential. The weighted energy is computed in a similar way in which we have computed the weighted energy per unit length of global strings. That is, we have solved the

[1] We will not make any distinction between monopoles and antimonopoles in this work, since for our purposes they are equivalent. Therefore, we will denote as $\mathcal{N}$ the sum of monopoles and antimonopoles.

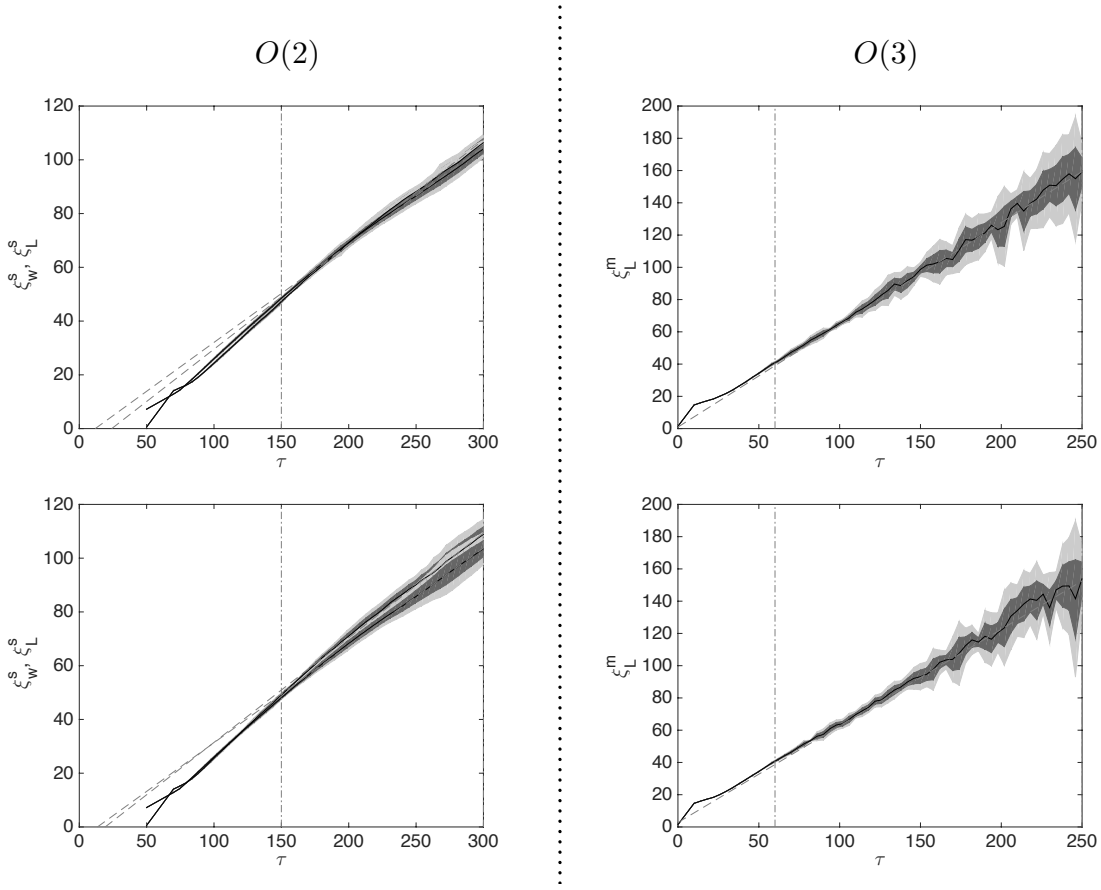

Figure 6.1.: *In the left column: String separation $\xi^{\rm s}$ from simulations in radiation era (top figure) and matter era (bottom figure), with $\xi^{\rm s}_{\rm w}$ obtained from the winding length measure and $\xi^{\rm s}_{\rm L}$ from the Lagrangian length measure. In the right column: Monopole separation $\xi^{\rm m}_{\rm L}$ from simulations in radiation era (top figure) and matter era (bottom figure), obtained using Lagrangian separation measure.*

	$\beta_{\rm w}^{\rm s}$	$\beta_{\rm L}^{\rm s}$	ζ	$\beta_{\rm L}^{\rm m}$
Radiation	0.36 $\pm$ 0.01	0.38 $\pm$ 0.01	1.7 $\pm$ 0.1	0.63 $\pm$ 0.03
Matter	0.36 $\pm$ 0.02	0.39 $\pm$ 0.02	0.72 $\pm$ 0.08	0.60 $\pm$ 0.02

Table 6.2.: *Numerical values of the slopes of different length estimators in scaling. $\beta_{\rm w}^{\rm s}$ is the slope related with the length estimator for strings computed using the length of strings obtained from the number of windings , $\beta_{\rm L}^{\rm s}$ is related with the length estimator for strings computed using the weighted energy and $\beta_{\rm L}^{\rm m}$ with the length estimator for monopoles computed using the weighted energy.*

equations of motion for a static monopole [137] using a relaxation method and then, using the profile functions we have calculated the weighted mass.

In order to compute number of monopoles directly one has to solve a surface integral which involves the information of the fields in the eight corners of each simulation cell (and all this have to be done during runtime) [18] (see Chapter 4). Therefore, considering the compatibility of both approaches for global strings, we restrict the analysis of the scaling regime to the study of the information provided by local field estimators.

As it was found in previous works, the asymptotic behaviour of the separations for both type of defects is very close to linear,

$$\xi \to \beta(\tau_{\rm sim} - \tau_{\rm offset}), \tag{6.9}$$

where $\tau_{\rm offset}$ is the time offset of the ξ curve (see Fig. 6.1). We have managed to choose initial conditions such that the time offset is almost zero in all realisations. Although the ξ are almost equal in all runs, we define the mean slope β as the average of all different slopes from different realisations. Numerical values of the slopes can be found in Table 6.2.

The Table 6.2 shows clearly that the values of β for strings obtained using both procedures are compatible. Moreover, we can translate these values to the form of parameters used in [101]. In this paper the authors used the parameter ζ to analyse the scaling behaviour of the simulations,

$$\zeta = \frac{E_V}{\mu_s} t^2 \tag{6.10}$$

where t is the physical time. The translation of our values of β to ζ can be seen in Table 6.2. These values are compatible with the values given in [101] where they obtained $\zeta = 2.0 \pm 0.5$ for the radiation era.

The values for the slope, $\beta_{\rm L}^{\rm m}$, for the monopole case can also be seen in Table 6.2. These values are compatible with the values obtained in Chapter 4 where we found that $\beta_{\rm r} = 0.72 \pm 0.06$ in radiation era and $\beta_{\rm m} = 0.65 \pm 0.04$ in the matter era.

As an alternative test of scaling we can use the ETCs. In Fig. 6.2 we show the ETCs for global strings and global monopoles in radiation era for the whole period of time recorded: the ETC at reference time in black, the ETC at $\tau_{\rm end}$ in blue and the rest between those two limits in green. The behaviour in the matter era is similar to the behaviour in the radiation era. The figures show that at small scales the ETCs collapse to a single line, though this behaviour is not so clear at low-kτ's.

All in all, since the offset is zero in our simulations, we can directly average the UETCs obtained from different realizations, without the need of correcting each run with its own offset. Figure 6.3 shows the averaged Matter UETCs for global strings, and Fig. 6.4 shows the corresponding one for global monopoles.

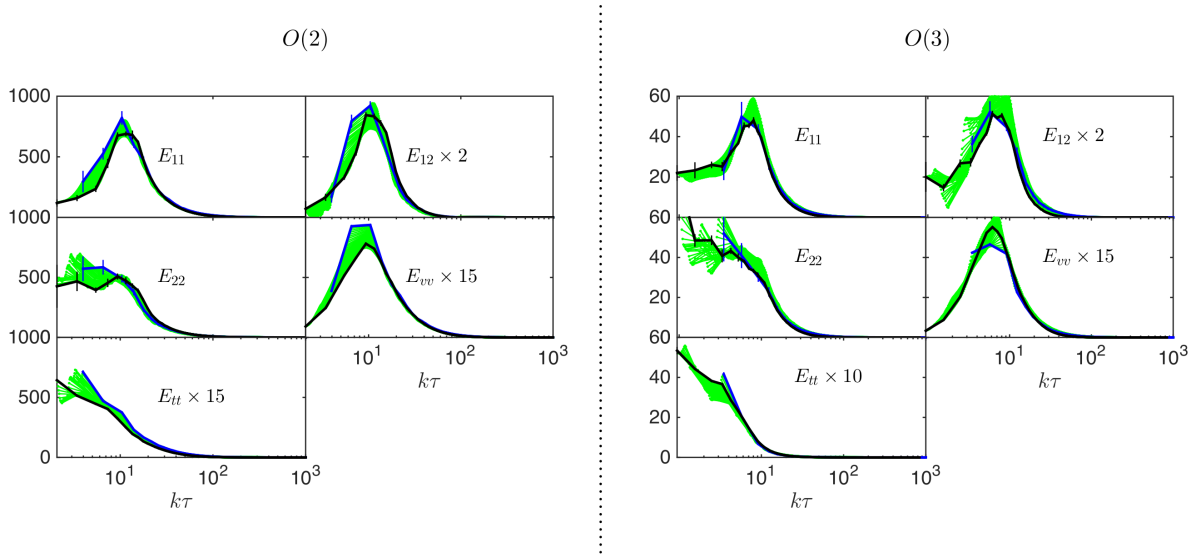

Figure 6.2.: *ETCs for global strings and for global monopoles in radiation era, where we have plotted ETC at reference time in black, the ETC at $\tau_{\rm end}$ in blue and the rest between those two limits in green.*

Figures 6.3 and 6.4 show that the amplitudes of the correlators of O(2) strings are much bigger than the amplitude of O(3) UETCs. Similarly, if we compare global string correlators with the UETCs obtained from simulations of the Abelian-Higgs model presented in [45], we observe that the general shape is similar while the amplitude is slightly higher for the global case. In both cases the normalisation used is the canonical normalisation; however, note that the normalisation is applied differently for complex and scalar fields.

6.4. Computation of source functions

It has been established in the previous section that global strings and monopoles evolve in the scaling regime for most of the time reproduced by our simulations. As it is known, and also mentioned in Section 2.3.2, the scaling can be used to extrapolate results derived from numerical simulations of different type of defects to the required cosmological scales. The universe undergoes two transitions during times of interest, the transition from radiation-dominated era to matter-dominated era and the transition from matter-domination to Λ-domination. In this work we will not consider the transition from matter-domination to Λ-domination, since its effect is rather small, as shown in [95]. Therefore, perfect scaling is not a feature of networks evolving in our universe, this is why the scales imposed by the transitions must be also considered.

UETCs must also depend on the scales imposed by the transitions. This means that in general the correlators will depend explicitly on $\tau_{\rm eq}$, in other words, the true (non-scaling) UETCs are functions of three different dimensionless variables, *e.g.* $C_{ab}(k\tau, k\tau', \sqrt{\tau\tau'}/\tau_{\rm eq})$. One has to determine a method which captures the information of the transitions and includes it in the computation of the source functions. There are several proposals in the literature for performing

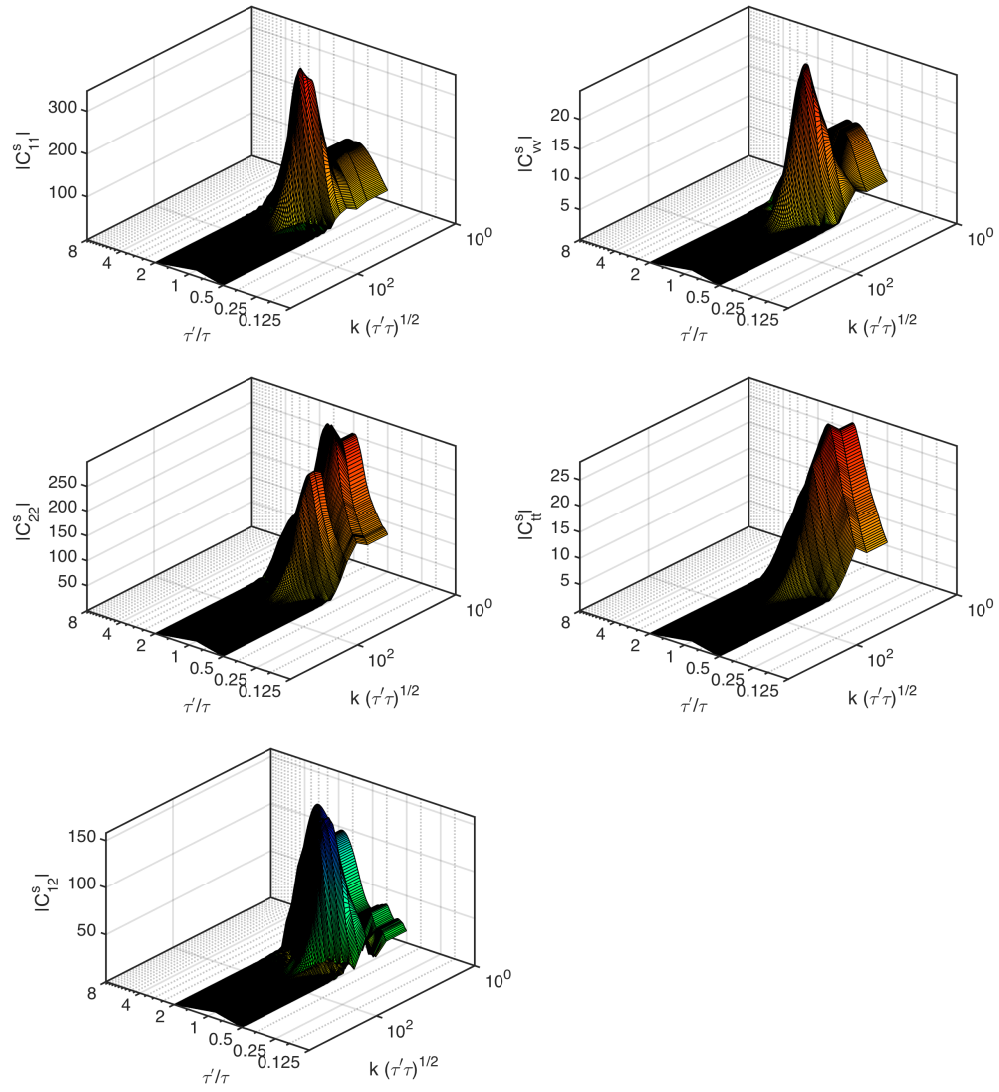

Figure 6.3.: *Full set of scaling O(2) UETCs for the matter era, calculated averaging over 5 runs.*

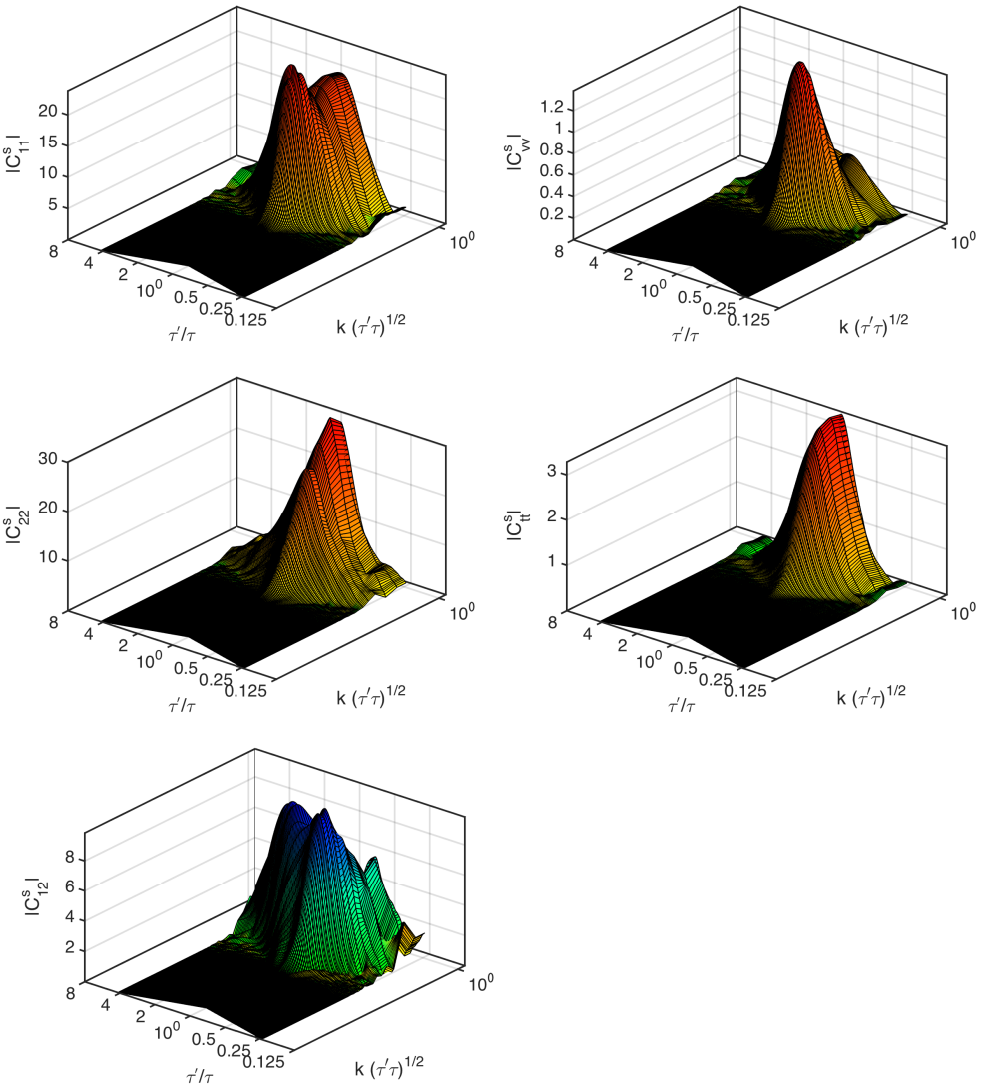

Figure 6.4.: *Full set of scaling O(3) UETCs for the matter era, calculated averaging over 5 runs.*

this estimation [31, 45, 54, 95], all of which were compared in [45].

In this work we will follow the *Fixed-k interpolation* method proposed in [45]: the UETCs are thought of as symmetric functions of τ and τ' for a given k. This approach has several advantages: it preserves orthogonality of the source functions during defects' whole existence and reproduces better the UETCs at cosmological transitions. Moreover, it also fits very well into the scheme used by Einstein-Boltzmann codes, which solve the perturbation equations with an outer loop over k and an inner time integration for fixed values of k. For further details we refer the reader to [45].

The true UETCs $C_{ab}(k,\tau,\tau')$ are constructed from the mixture of the scaling matter and radiation correlators, extracted from our simulations, at each value of k. The relative mixture of matter and radiation UETCs is determined by $\tau/\tau_{\rm eq}$ and $\tau'/\tau_{\rm eq}$. An explicitly symmetric proposal for the UETCs which models this behaviour across the radiation-matter transition is the following [45]:

$$C_{ab}(k,\tau,\tau') = f\left(\frac{\sqrt{\tau\tau'}}{\tau_{eq}}\right)\bar{C}^{M}_{ab}(k\tau,k\tau') + \left(1-f\left(\frac{\sqrt{\tau\tau'}}{\tau_{eq}}\right)\right)\bar{C}^{R}_{ab}(k\tau,k\tau'). \tag{6.11}$$

It approximates the UETC in the entire region by the linear combination of pure radiation and pure matter era scaling correlators balancing the contribution of each by an interpolating function f. At extreme values of τ/τ_{eq} we recover functions that correspond to matter ($\tau/\tau_{\rm eq} \gg 1$) and radiation ($\tau/\tau_{\rm eq} \ll 1$) dominations.

We note that the source functions for the EB integrators at a given k are now just the eigenvectors of these model UETCs, multiplied by the square root of the associated eigenvalues, and so they are indeed orthogonal, see Eq. (2.65).

In order to establish the form of the interpolating function, we perform numerical simulations of O(2) and O(3) defects at cosmological transitions. The interpolating function can be defined in the following way in terms of the equal-time correlators (ETC) $E_{ab}(k,\tau) = C_{ab}(k,\tau,\tau)$ [54]:

$$f_{ab}(k,\tau) = \frac{E^{\rm RM}_{ab}(k,\tau) - \bar{E}^{\rm M}_{ab}(k\tau)}{\bar{E}^{\rm R}_{ab}(k\tau) - \bar{E}^{\rm M}_{ab}(k\tau)} \quad \forall k, \tag{6.12}$$

where $\bar{E}^{\rm R}(k\tau)$ and $\bar{E}^{\rm M}(k\tau)$ are the scaling ETCs in the radiation and matter eras respectively, and $E^{\rm RM}(k,\tau)$ is the true ETC measured from the simulations performed during the transition.

We extracted ETCs from the simulations with $\tau_{\rm eq} = 3,\ 10,\ 40,\ 150$ and 300 (see Table 6.3), and used Eq. (6.12) to compute the function. Fig. 6.5 shows the results obtained for E_{11} correlators for global strings (left panel) and global monopoles (right panel), the transition functions for the rest of the correlators are similar to those shown in the figure. The five grey shaded regions represent the raw transition functions obtained during the five transition periods simulated. The two grey levels indicate 1σ and 2σ deviations from the mean value calculated averaging over a set of wavevectors: $1.5 < |\mathbf{k}| < 3.5$ and $3 < |\mathbf{k}| < 5$ respectively.

The interpolating functions derived from our simulations confirm what previous analysis of the behaviour of the energy-momentum correlators at cosmological transitions showed: scale independence of the interpolating function. The deviations from the mean value represented by two grey levels, though they are somewhat bigger for monopoles, are not significant in either case. This demonstrates that the interpolating functions can be considered to be dependent only of time ($f(\tau)$) to a very good approximation. The rest of the correlators (not shown) support the scale independence statement.

$\tau_{\rm eq}$	300	150	40	10	3
$\tau_{\rm ref}/\tau_{\rm eq}$	0.5	1.0	3.75	15	50
$\tau_{\rm end}/\tau_{\rm eq}$	1.00	2.0	7.5	50	100
$\alpha(\tau_{\rm ref})$	1.09	1.17	1.44	1.76	1.91
$\alpha(\tau_{\rm end})$	1.17	1.29	1.60	1.86	1.95

Table 6.3.: *Selected parameters for simulations across the radiation-matter transition. The parameters are the conformal time of matter-radiation equality, $\tau_{\rm eq}$, in units of η^{-1}, the ratio of the reference time $\tau_{\rm ref}$ for UETC data taking and the simulation end time $\tau_{\rm end}$ to $\tau_{\rm eq}$, and the expansion rate $\alpha = d\ln a/d\ln\tau$ at $\tau_{\rm ref}$ and $\tau_{\rm end}$.*

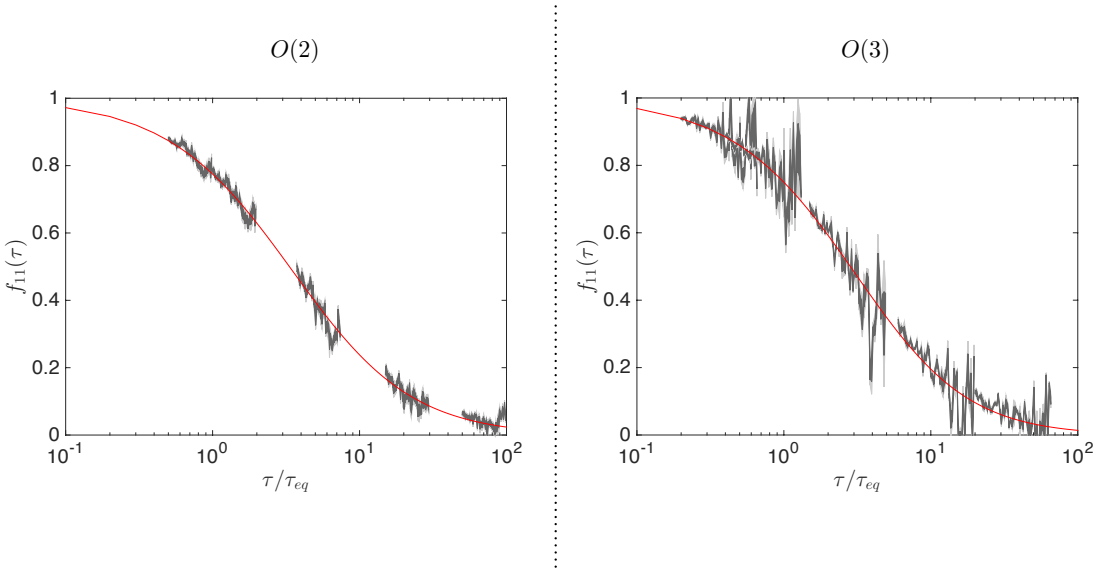

Figure 6.5.: *UETC interpolation functions derived from simulations performed during the radiation-matter transition corresponding to global strings (left panel) and global monopoles (right panel)(thick grey line). The five patches correspond to simulations with $\tau_{\rm eq} = 3,\ 10,\ 40,\ 150$ and 300. The shaded regions represent the 1σ and 2σ deviations from the mean value of the function obtained from Eq. (6.12) calculated from averaging over k, while the red line corresponds to the best-fit given by the function expressed in Eq. (6.13). In both panels the correlator used is E_{11}.*

	γ	κ
O(2)	0.26 $\pm$ 0.03	-1.15 $\pm$ 0.02
O(3)	0.23 $\pm$ 0.05	-1.4 $\pm$ 0.2

Table 6.4.: *Mean values together with the standard deviations for parameters γ and κ of Eq. (6.13) needed to reproduce the radiation-matter transition.*

We fit the data using the same form used in [45, 54], which reads as:

$$f(\tau) = \left(1 + \gamma \frac{\tau}{\tau_{eq}}\right)^{\kappa}, \tag{6.13}$$

where γ and κ are the parameters to be determined by the fitting process.

Table 6.4 shows the mean values and standard deviations for the parameters of Eq. 6.13. The mean and standard deviations are obtained averaging over different realizations and over different correlators, since it has been observed that in a good approximation the interpolating function is the same for all correlators. The best-fit obtained fitting data is also included in Fig. 6.5.

Comparing the interpolating function we have obtained here with the ones previously obtained in [54] and [45] we can confirm that the interpolation function is not universal across defect models. Although in [54] it was said that the interpolation function should be universal, in [45] the first hints of its non universality were given. The form is the same but the values of the parameters differ. The values of the parameter γ we have obtained are compatible with the values obtained in the two previous analysis, but the values of the exponent κ differ from numbers obtained in previous works. None of the values of the exponent are compatible with the values obtained for the Abelian-Higgs strings or for the large-N limit. However for bigger N's the value of κ is bigger, which might be a sign of a trend. It would be interesting to test whether increasing the value of N we eventually get the value proposed in [54].

Finally, having determined how the transitions has to be performed for the two defects analysed in this paper, we diagonalise the true non-scaling UETCs Eq. (6.11) and obtain the source functions Eq. (2.65) that will be used for the CMB power spectra calculation, as we describe in the next section.

6.5. Power Spectra

In the previous section we have defined the source functions for the global strings and monopoles. Inserting these functions into a source enabled Einstein-Boltzmann (EB) solver we can compute the contributions to CMB power spectra due to the presence of global defects. In our case the EB solver we have used is the source enabled version of CMBEASY [49], *i.e.* the code has been additionally modified to handle source functions as we have explained in Section 2.3.5.

The cosmological parameters used for these calculations are the best-fit values obtained by the Planck collaboration [12] (see Section 1.6): $h = 0.6726$, $\Omega_b h^2 = 0.02225$, $\Omega_\Lambda = 0.6844$ and reionization optical depth $\tau_{re} = 0.079$. After diagonalisation, the total contribution of defects to temperature and polarization anisotropies is calculated summing the contribution of each individual source functions, where 130 source functions are summed in each case.

Fig. 6.6 shows the temperature and polarization power spectra obtained for the global string case (black lines). Moreover, in the same figure we have plotted the power spectra obtained for

N	peak (L-N)	peak (S)	peak Ratio (S/L-N)	l_{10} (L-N)	l_{10} (S)	l_{10} Ratio (S/L-N)
2	40.99	799.34	19.5	32.01	373.61	11.67
3	18.22	37.88	2.08	14.23	22.75	1.60

Table 6.5.: *Values of $l(l+1)C_l^{TT}$ for $N = 2$ and $N = 3$ where $l = 10$, l_{10}, and at the peak of the power spectra. S means the values obtained from our simulations and L-N values obtained in [54] using the large-N limit.*

Abelian-Higgs strings in [95] (red lines). Note that μ is the following one:

$$\mu = \pi\eta^2, \tag{6.14}$$

where η is the vacuum expectation value of the scalar fields. However, in each case μ has a different meaning. For the AH case it represents the string tension, while in the global string case it can be seen as the tension in the core of the string. The figure shows that the amplitude of the signal of global strings is bigger, whereas the shape of both are very similar.

Fig. 6.7 in turn shows the temperature and all polarization power spectra obtained for global monopoles. For global monopoles μ is related with the mass in the core of the monopole. Comparing with the O(2) case we can see that the signal given by the O(2) model is much bigger than the one given by O(3) monopoles. Furthermore, although the overall shape is similar in both cases, the O(3) case shows a more bumpy distribution.

The power spectra for global strings and monopoles can be compared with that obtained in [54] for O(N) defects, in the large-N limit. It can be noted that all spectra share a similar overall shape. Nevertheless, the spectrum obtained from the large-N limit shows a clearer bumpy distribution, which evidences the oscillatory behaviour for models with bigger N's. Moreover, comparing the values of the power spectra we have obtained with the ones obtained in [54] we can say that the large-N limit underestimates the values. In table 6.5 we show the values of the power spectra obtained in our analysis (S)and using large-N (L-N), at the peak of the power spectra and at $l = 10$. In those values we can see that for $N = 2$ the ratio between our values and the ones obtained in [54] is bigger than 10, while the ratio for $N = 3$ is greater than 1.6. Note also that the ratio is not the same in both points showing that the large-N limit does not capture well the details of the shape of the power spectra. In these values we can see a similar behaviour to the one shown in [56]; that is for bigger values of N the ratio between the measured value and the theoretical one tend to agree more.

Fig. 6.8 shows the contribution of scalars, vectors and tensors to the temperature channel for the both cases O(2) and O(3). In this figure we can see that the contribution of scalars is the dominant one for temperature, followed by the vector contribution and lastly by the tensor contribution. The contribution scheme in both models, O(2) and O(3), is almost the same.

6.6. Fits and constraints

The CMB anisotropy predictions obtained from field theoretical numerical simulations of global string and global monopoles are compared with the latest CMB data released by the *Planck* collaboration [12], in order to put limits on the allowed fraction of those defects. We consider the whole *Planck* CMB dataset and analyzed them using the publicly available likelihoods (TT, TE, EE + lowTEB) provided by the collaboration [13]. The Monte Carlo analysis has been performed

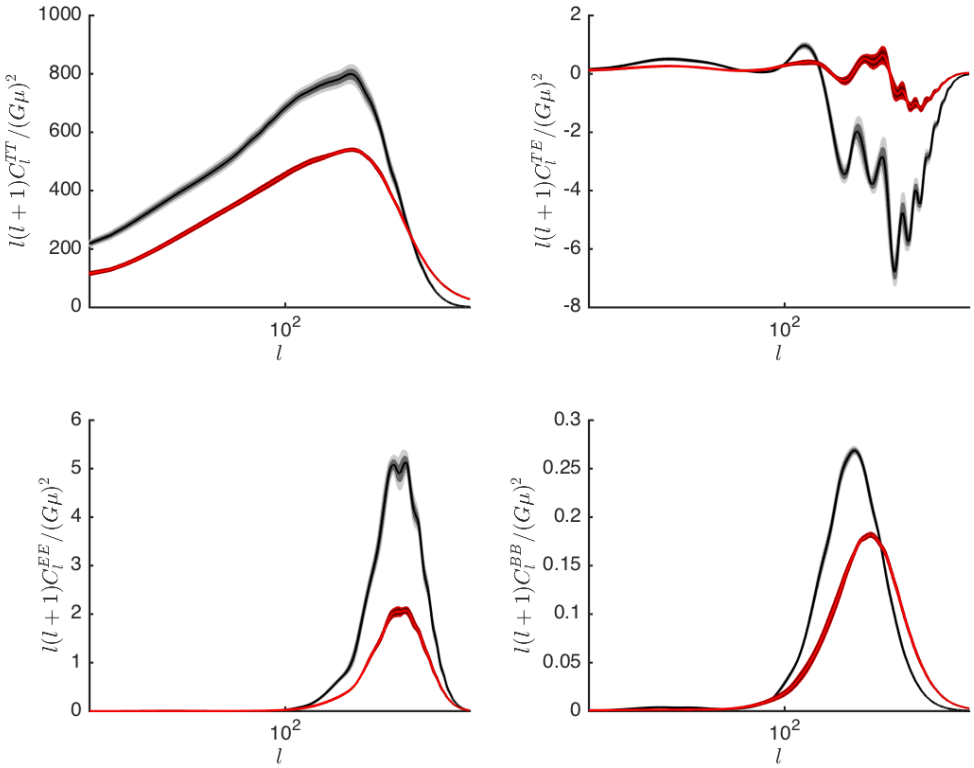

Figure 6.6.: *Temperature and all polarization channels for the CMB of O(2) (black line) and Abelian-Higgs (red line). Black lines (red for AH) correspond to the mean spectra while grey regions (pale red for AH) represents 1σ and 2σ confidence limits obtained by bootstrapping 10 times over 5 radiation and 5 matter realizations for UETCs (over 7 radiation and 7 matter realizations in the UETC merging process for AH) [95]. Note that $\mu = \pi\eta^2$, where η is the vacuum expectation value of the scalar fields. However, in each case μ has a different meaning. For the AH case it can be seen as the string tension, while in the global string case it can be seen as the tension in the core of the string.*

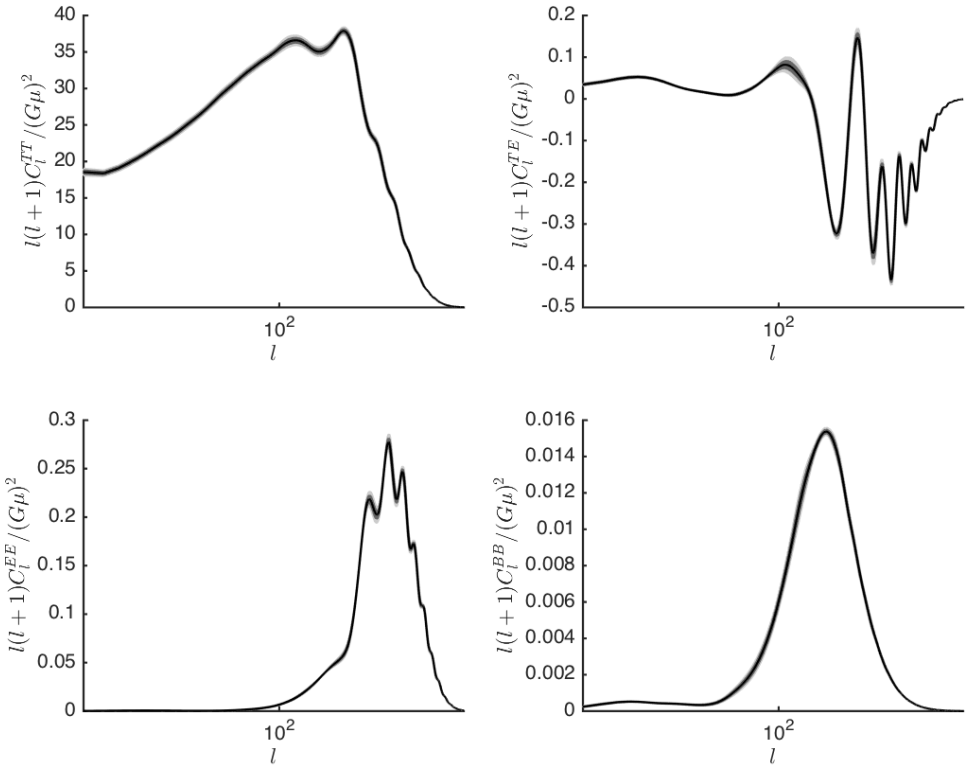

Figure 6.7.: *Temperature and all polarization channels for the CMB of O(3). Black lines correspond to the mean spectra while grey regions represents 1σ and 2σ confidence limits obtained by bootstrapping 10 times over 5 radiation and 5 matter realizations for UETCs. Note that in this case μ is related with the mass in the core of the monopole.*

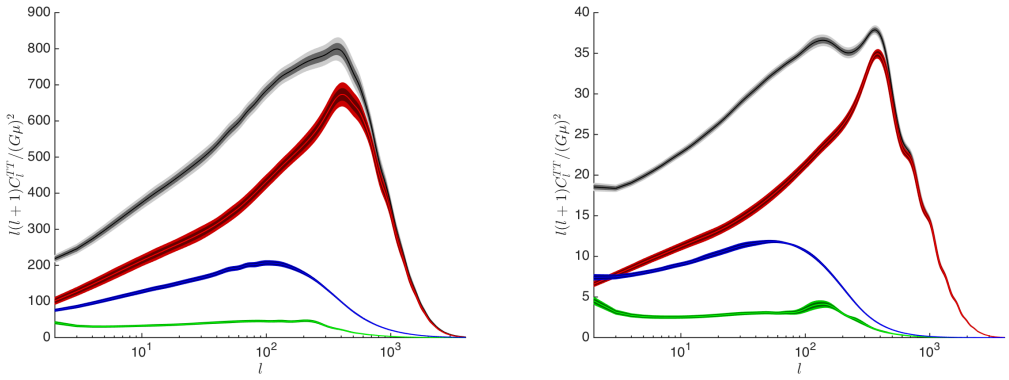

Figure 6.8.: *The CMB temperature power spectrum for O(2) (left) and O(3) (right). The plot shows the total (black region) plus the decomposition into scalar (red region), vector (blue region) and tensor (green region). In those regions the bright lines correspond to mean spectra while the pale regions represents 1σ and 2σ confidence limits obtained by bootstrapping 10 times over 5 radiation and 5 matter realizations for UETCs.*

Dataset	*Planck* 2015 CMB		
Defect	O(2)	O(3)	
Model	$\mathcal{PL}+G\mu$	$\mathcal{PL}+G\mu$	$\mathcal{PL}$
f_{10}	<0.017	<0.024	–
$10^{12}(G\mu)^2$	<0.031	<0.73	–
$-\ln\mathcal{L}_{\max}$	6472	6470	6472

Table 6.6.: *95% upper limits for $(G\mu)^2$ and f_{10} as well as best-fit likelihood values for different cosmological models for O(2) global strings and O(3) global monopoles, fitting for the Planck 2015 TT, TE, EE and low TEB data.*

using COSMOMC [91], which uses CAMB [92] as the Einstein-Boltzman solver for the primordial perturbations.

We vary the 6 base parameters of the standard ΛCDM model (see Section 1.6): ω_b ($\Omega_b h^2$), ω_c ($\Omega_c h^2$), Θ_{MC}, τ (κ), $n_{\rm s}$, ${A_{\rm s}}^2$; which we call the *Power-Law* model ($\mathcal{PL}$). In order to construct models with defects, we add to the basic $\mathcal{PL}$ model the possible contribution of the global defects individually. However, we do not consider both type of defects simultaneously in any case.

The contribution of the defects is incorporated using the power spectra presented in previous sections. We allow only to vary the amplitude of the spectra, since as for other defects their contribution is expected to be of order of about 1% of the temperature power spectrum at angular scales. The fraction of global defects and monopoles is described by the usual pair of parameters: $G\mu$ and f_{10}. As we have mentioned in (6.14), in the case of global strings μ is the tension in the string core and in the global monopole case it is related with the mass in the core of the monopole; in both cases $\mu\sim\eta^2$, where η is the symmetry breaking scale. On the other hand, f_{10} measures the relative contribution of defects to the total (defects + inflation) at multipole $\ell=10$ in TT.

We show the results for the 95% upper limits for the string fraction for O(2) and O(3) defects in Table 6.6. We only show the parameters related to models with defects, since base-model parameters do not suffer considerable variations as they are already highly constrained by *Planck*. We find that the addition of the defects to the $\mathcal{PL}$ model does not improve the fit to the data. Even though O(3) are able to improve slightly the likelihood, the improvement is not significant. In all cases the scenario with no defects $G\mu=0$ is totally compatible with the measurements.

Comparing the fits obtained here with the fits obtained in [95], where the Abelian-Higgs case was analysed, we observe that global strings give a slightly bigger contribution at $l=10$, f_{10}, compared with the Abelian-Higgs with the same symmetry-breaking scale, while the contribution that global monopoles give is the biggest. However, even though global monopoles slightly improve the global fit to the data, the fitting process in general does not show any significative preference for models with defects.

[2] It has to be noted that we also vary the nuisance parameters inherent to the experiments used in the analysis, 27 in this case. They are not shown in this work due to their lack of physical significance in terms of our investigations.

6.7. Discussion and conclusions

In this paper we have computed for the first time the CMB power spectra for global strings and monopoles using field theory simulations. In order to obtain the power spectra, we have computed the source functions obtained from UETCs extracted from our simulations, which also capture the effect of transition from radiation dominated cosmology to matter dominated one. The source functions were used to obtain CMB temperature and polarisation anisotropy power spectra. Finally we compared our predictions with the latest *Planck* data [12] so as to put limits on models that include O(2) or O(3) defects.

We investigated the scaling regime with simulations performed in pure radiation and matter eras. We computed length estimators of defect networks using global field estimators as well as direct length measurements. The results obtained for the slope of the correlation length of the scaling networks show that both method are compatible (see Table 6.2). Moreover, the values of scaling parameters for global strings as well as for global monopoles can be compared with scaling parameters obtained by other analysis (in [101] for local strings and in Chapter 4 for global monopoles). Our results for the scaling parameters which are obtained using bigger simulations and have smaller errors validate the values of scaling parameters obtained in the previous analysis.

The UETCs obtained in matter dominated era for global strings and global monopoles can be seen in Figure 6.3 and 6.4. The amplitudes of the UETCs for global strings are somewhat higher than those for the Abelian-Higgs strings, which is a direct consequence of more energy per horizon volume in the global case. Due to the same reason, the amplitudes for global monopole UETCs are much lower compared with the local string case. Nevertheless, the overall shape is similar in all cases.

The radiation-matter transition is particularly important for the accurate computation of CMB perturbations at around the degree scale. On the contrary, the effects of matter-Λ transition are rather small [95], and we do not consider them. The fixed-k UETC interpolation method [45] ensures that the effect of the radiation-matter transition is well modelled. However, it requires the calculation of the interpolating functions for each defect type considered. Therefore, in order to compute those interpolating functions, we have performed simulations at cosmological transitions, using 5 different patches that covered most of the transition period. We have obtained that the form of the transition function (see Eq. 6.13) coincides with previous analysis and the value of γ is compatible with the values found for AH strings [45] and for global defects in the large-N limit [54]. Nevertheless, the value of the exponent, κ, differs from model to model, which confirms that the transition function is not universal for every kind of defect. As we have pointed out, however, it would be interesting to determine from which N on this parameter κ will reach the value proposed in [54].

After obtaining the source functions that capture the radiation-matter transition we have computed the CMB power spectra. We have compared the power spectra with the power spectra obtained for the Abelian-Higgs case [95] and for the large-N limit [54]. The overall shape for all the cases under study is fairly similar. The signal coming from the global string case has a somewhat higher amplitude than the signal coming from the Abelian-Higgs strings, whereas the amplitude of the power spectra of global monopoles is the smallest. The origin of this difference comes from the energy per horizon volume for each defect network, which is the biggest for global strings, while smallest for global monopoles. Although the overall shape is the same, the power spectra for global monopoles show a more bumpy shape which is more similar to the shape of the power spectra obtained in the large-N limit. However, comparing the values we have obtained with the values obtained in the large-N limit at two points of the power spectra, we have shown

that the large-N limit underestimates the values of the power spectra and that the details of the shape are not well described (at least for so low N). From Table 6.5 we can observe a tendency that for bigger values of N the ratio between the measured power spectra and the one obtained using the large-N approaches one. Even so, we have demonstrated that the large-N limit fails to correctly capture the dynamics of the system for $N < 4$, validating the result obtained in [56] using GW predictions.

Finally, comparing the power spectra predictions with the latest CMB data released by the *Planck* collaboration [12] we put limits on the allowed fraction of those defects. We have seen that the global strings could give a slightly bigger contribution compared with the Abelian-Higgs case, while global monopoles could give the biggest contribution between these three models. Nevertheless, none of the models studied in this work improved significantly the fit to the data.

Using these constraints we can also estimate the amplitude of the gravitational wave spectrum created by global strings and global monopoles following the calculations presented in [56]. Using the upper limits on $(G\mu)^2$ that we have found (see Table 6.6), we obtain that the upper limit for the amplitude of the GW spectrum is similar in both cases (global strings and global monopoles), which is $\Omega_{GW} \sim 10^{-15}$. Comparing this value with the expected sensitivity curved of eLISA [23, 37] we can say that the gravitational wave backgrounds created by global strings and global monopoles lay below the observability window of eLISA.

7 General Conclusions

The central objective of this Thesis has been to characterise the properties of cosmic defects and explore their observational effects. In order to accomplish this task we have performed both static and dynamical analysis of properties of different types of cosmic defects.

In Chapter 3 we have investigated field theoretical models for cosmic strings with flat directions in curved space-times. More precisely, we consider minimal models with semilocal, axionic and tachyonic strings, respectively. In flat space-time, isolated static and straight cosmic string solutions in the Bogoml'nyi limit admit a uniparametric family of solutions with the same energy, which is related with the zero mode. We have shown that the zero modes survive the minimal coupling to gravity. Moreover, we have also shown that the variation of the free parameter related with the zero mode affects the energy density distribution but the total energy remains constant. In other words, the variation of the parameter changes the field solutions due to the fact that Einstein equations depend on local quantities. But as the total energy is the same, the deficit angle remains constant.

After the static analysis of the gravitational properties we have started the dynamical analysis of defect networks. Firstly, in Chapter 4 we have measured the global monopole velocity using field theory simulations. Before our novel procedure was introduced the velocities were measured using local-field estimators which only give average network velocities. However, our method lets us measure velocities of individual monopoles. In our work, we have implemented three different procedures to measure monopole velocities. On one hand, we have used two different local-field estimators, and on the other hand, we have used our new method that follows each one of the monopoles in the box. We have shown that our method validates the procedures that use local-field values to compute an average network velocity. We have been able to determine that the global monopole velocities are $v_r = 0.76 \pm 0.07$ and $v_m = 0.65 \pm 0.08$ for radiation and matter dominated eras, respectively. For the first time we have shown that global monopole velocities are subluminal. The detailed characterisation of global monopoles we have performed gave us the opportunity to calibrate the VOS-type analytical model for global monopoles in detail, where the subluminal branch of solutions is favoured. We have hinted directions in which to improve the VOS-type analytical model.

In the same way, in Chapter 5, we have characterised in detail the network of semilocal strings. Using what we had learned form the global monopole case and introducing some new algorithms, we have been able to give a one dimensional representation of the semilocal segments, where the segment ends have been located as monopoles. This new characterization has allowed us to measure the segment length and velocities, as well as monopole velocities, directly from the evolution of the network. For the first time we have measured the segment length in a specific time following the one dimensional path from one segment end to another. Moreover, we could

follow each one of the segments in the box during its evolution, as well as each one of the segment ends. Thanks to the possibility to track segment evolutions we could analyse in detail the peculiar behaviour of the semilocal segments. We have obtained information to build the whole history of each one of the segments on the box. This information can be used to analyse the VOS-type analytical models. In a future work we will use this information to analyse the viability of the already presented models, and in the case that the hypothesis used to construct them are correct we will use the data obtained here to calibrate them.

Finally in Chapter 6 we have presented the cosmic microwave background (CMB) power spectra from numerical simulations of cosmological defects in the global O(N) model, with $N = 2, 3$. In order to compute the CMB power spectra we have obtained source functions from UETCs that capture the radiation-matter transition. We showed that the interpolation function that mimics the transition is not the same as for other defects models, confirming the non universality of the interpolation function. The CMB power spectra for global strings and global monopoles have the same overall shape as the power spectra obtained for Abelian-Higgs strings and obtained in the large-N limit. However, the amplitudes for global strings power spectra are much bigger than the ones for global monopoles. In the same way, the amplitudes for global strings power spectra are somewhat bigger than those for Abelian-Higgs strings. A detailed comparison of the power spectra for global strings and global monopoles with the one obtained in the large-N limit have shown that this limit with $N < 4$ fails to correctly capture the dynamics of the system. Finally we have compared the CMB power spectra with the latest CMB data in order to put limits on the allowed fraction of these defects. We found that even though the addition of global monopoles improves slightly the likelihood, the improvement using global strings or global monopoles is not significant.

Bibliography

[1] A. A. Abrikosov. On the Magnetic properties of superconductors of the second group. *Sov. Phys. JETP*, 5:1174–1182, 1957. [Zh. Eksp. Teor. Fiz.32,1442(1957)].

[2] F. S. Accetta and L. M. Krauss. The stochastic gravitational wave spectrum resulting from cosmic string evolution. *Nucl. Phys.*, B319:747–764, 1989.

[3] A. Achucarro and J. Urrestilla. The (In)stability of global monopoles revisited. *Phys. Rev. Lett.*, 85:3091–3094, 2000.

[4] A. Achucarro and T. Vachaspati. Semilocal and electroweak strings. *Phys. Rept.*, 327: 347–426, 2000. [Phys. Rept.327,427(2000)].

[5] A. Achucarro, K. Kuijken, L. Perivolaropoulos, and T. Vachaspati. Dynamical simulations of semilocal strings. *Nucl. Phys.*, B388:435–456, 1992.

[6] A. Achucarro, J. Borrill, and A. R. Liddle. Semilocal string formation in two-dimensions. *Phys. Rev.*, D57:3742–3748, 1998.

[7] A. Achucarro, J. Borrill, and A. R. Liddle. The Formation rate of semilocal strings. *Phys. Rev. Lett.*, 82:3742–3745, 1999.

[8] A. Achucarro, P. Salmi, and J. Urrestilla. Semilocal cosmic string networks. *Phys. Rev.*, D75:121703, 2007.

[9] A. Achucarro, A. Avgoustidis, A. Leite, A. Lopez-Eiguren, C. Martins, et al. Evolution of semilocal string networks: Large-scale properties. *Phys.Rev.*, D89(6):063503, 2014.

[10] R. Adam et al. Planck 2015 results. I. Overview of products and scientific results. *Astron. Astrophys.*, 594:A1, 2016.

[11] P. A. R. Ade et al. Planck 2015 results. XIV. Dark energy and modified gravity. *Astron. Astrophys.*, 594:A14, 2016.

[12] P. A. R. Ade et al. Planck 2015 results. XIII. Cosmological parameters. *Astron. Astrophys.*, 594:A13, 2016.

[13] N. Aghanim et al. Planck 2015 results. XI. CMB power spectra, likelihoods, and robustness of parameters. *Astron. Astrophys.*, 594:A11, 2016.

[14] A. Albrecht, R. A. Battye, and J. Robinson. The Case against scaling defect models of cosmic structure formation. *Phys. Rev. Lett.*, 79:4736–4739, 1997.

[15] A. Albrecht, R. A. Battye, and J. Robinson. Detailed study of defect models for cosmic structure formation. *Phys. Rev.*, D59:023508, 1999.

[16] B. Allen and E. P. S. Shellard. Cosmic string evolution: a numerical simulation. *Phys. Rev. Lett.*, 64:119–122, 1990.

[17] B. Allen, R. R. Caldwell, S. Dodelson, L. Knox, E. P. S. Shellard, and A. Stebbins. CMB anisotropy induced by cosmic strings on angular scales ¿ approximately 15-minutes. *Phys. Rev. Lett.*, 79:2624–2627, 1997.

[18] N. D. Antunes, L. M. A. Bettencourt, and M. Kunz. The Role of point - like topological excitations at criticality: From vortices to global monopoles. *Phys. Rev.*, E65:066117, 2002.

[19] U. Ascher, J. Christiansen, and R. D. Russell. A Collocation Solver for Mixed Order Systems of Boundary Value Problems. *Math. Comput.*, 33(146):659–679, 1979.

[20] D. Austin, E. J. Copeland, and T. W. B. Kibble. Evolution of cosmic string configurations. *Phys. Rev.*, D48:5594–5627, 1993.

[21] N. A. Bahcall and P. Bode. The Amplitude of mass fluctuations. *Astrophys. J.*, 588:L1–L4, 2003.

[22] N. A. Bahcall et al. The Cluster mass function from early SDSS data: Cosmological implications. *Astrophys. J.*, 585:182–190, 2003.

[23] N. Bartolo et al. Science with the space-based interferometer LISA. IV: Probing inflation with gravitational waves. *JCAP*, 1612(12):026, 2016.

[24] R. A. Battye, J. Robinson, and A. Albrecht. Structure formation by cosmic strings with a cosmological constant. *Phys. Rev. Lett.*, 80:4847–4850, 1998.

[25] D. P. Bennett and F. R. Bouchet. High resolution simulations of cosmic string evolution. 1. Network evolution. *Phys. Rev.*, D41:2408, 1990.

[26] D. P. Bennett and S. H. Rhie. Cosmological evolution of global monopoles and the origin of large scale structure. *Phys. Rev. Lett.*, 65:1709–1712, 1990.

[27] K. Benson and M. Bucher. Skyrmions and semilocal strings in cosmology. *Nucl. Phys.*, B406:355–376, 1993.

[28] N. Bevis, M. Hindmarsh, and M. Kunz. WMAP constraints on inflationary models with global defects. *Phys. Rev.*, D70:043508, 2004.

[29] N. Bevis, M. Hindmarsh, M. Kunz, and J. Urrestilla. CMB power spectrum contribution from cosmic strings using field-evolution simulations of the Abelian Higgs model. *Phys.Rev.*, D75:065015, 2007.

[30] N. Bevis, M. Hindmarsh, M. Kunz, and J. Urrestilla. Fitting CMB data with cosmic strings and inflation. *Phys. Rev. Lett.*, 100:021301, 2008.

[31] N. Bevis, M. Hindmarsh, M. Kunz, and J. Urrestilla. CMB power spectra from cosmic strings: predictions for the Planck satellite and beyond. *Phys. Rev.*, D82:065004, 2010.

[32] J. J. Blanco-Pillado and K. D. Olum. The Form of cosmic string cusps. *Phys. Rev.*, D59: 063508, 1999.

[33] J. J. Blanco-Pillado, G. Dvali, and M. Redi. Cosmic D-strings as axionic D-term strings. *Phys. Rev.*, D72:105002, 2005.

[34] S. I. Blinnikov and M. Yu. Khlopov. ON POSSIBLE EFFECTS OF 'MIRROR' PARTICLES. *Sov. J. Nucl. Phys.*, 36:472, 1982. [Yad. Fiz.36,809(1982)].

[35] E. B. Bogomolny. Stability of Classical Solutions. *Sov. J. Nucl. Phys.*, 24:449, 1976. [Yad. Fiz.24,861(1976)].

[36] C. G. Callan, Jr. and S. R. Coleman. The Fate of the False Vacuum. 2. First Quantum Corrections. *Phys. Rev.*, D16:1762–1768, 1977.

[37] C. Caprini et al. Science with the space-based interferometer eLISA. II: Gravitational waves from cosmological phase transitions. *JCAP*, 1604(04):001, 2016.

[38] S. R. Coleman. The Fate of the False Vacuum. 1. Semiclassical Theory. *Phys. Rev.*, D15: 2929–2936, 1977. [Erratum: Phys. Rev.D16,1248(1977)].

[39] E. J. Copeland, R. C. Myers, and J. Polchinski. Cosmic F and D strings. *JHEP*, 06:013, 2004.

[40] R. A. C. Croft, W. Hu, and R. Dave. Cosmological Limits on the Neutrino Mass from the Lya Forest. *Phys. Rev. Lett.*, 83:1092–1095, 1999.

[41] T. Damour and A. Vilenkin. Gravitational wave bursts from cosmic strings. *Phys. Rev. Lett.*, 85:3761–3764, 2000.

[42] T. Damour and A. Vilenkin. Gravitational wave bursts from cusps and kinks on cosmic strings. *Phys. Rev.*, D64:064008, 2001.

[43] T. Damour and A. Vilenkin. Gravitational radiation from cosmic (super)strings: Bursts, stochastic background, and observational windows. *Phys. Rev.*, D71:063510, 2005.

[44] D. Daverio, M. Hindmarsh, and N. Bevis. Latfield2: A c++ library for classical lattice field theory. 2015.

[45] D. Daverio, M. Hindmarsh, M. Kunz, J. Lizarraga, and J. Urrestilla. Energy-momentum correlations for Abelian Higgs cosmic strings. *Phys. Rev.*, D93(8):085014, 2016.

[46] M. R. DePies and C. J. Hogan. Stochastic Gravitational Wave Background from Light Cosmic Strings. *Phys. Rev.*, D75:125006, 2007.

[47] K. Dimopoulos. Primordial magnetic fields from superconducting cosmic strings. *Phys. Rev.*, D57:4629–4641, 1998.

[48] S. Dodelson. *Modern Cosmology*. Academic Press, Amsterdam, 2003. ISBN 9780122191411. URL `http://www.slac.stanford.edu/spires/find/books/www?cl=QB981:D62:2003`.

[49] M. Doran. CMBEASY: an object oriented code for the cosmic microwave background. *JCAP*, 0510:011, 2005.

[50] R. Durrer, M. Kunz, and A. Melchiorri. Cosmic microwave background anisotropies from scaling seeds: Global defect models. *Phys. Rev.*, D59:123005, 1999.

[51] G. Dvali and A. Vilenkin. Formation and evolution of cosmic D strings. *JCAP*, 0403:010, 2004.

[52] G. Dvali, R. Kallosh, and A. Van Proeyen. D term strings. *JHEP*, 01:035, 2004.

[53] V. R. Eke, S. Cole, C. S. Frenk, and J. P. Henry. Measuring omega(0) using cluster evolution. *Mon. Not. Roy. Astron. Soc.*, 298:1145, 1998.

[54] E. Fenu, D. G. Figueroa, R. Durrer, J. Garcia-Bellido, and M. Kunz. Cosmic Microwave Background temperature and polarization anisotropies from the large-N limit of global defects. *Phys. Rev.*, D89(8):083512, 2014.

[55] D. G. Figueroa, R. R. Caldwell, and M. Kamionkowski. Non-Gaussianity from Self-Ordering Scalar Fields. *Phys. Rev.*, D81:123504, 2010.

[56] D. G. Figueroa, M. Hindmarsh, and J. Urrestilla. Exact Scale-Invariant Background of Gravitational Waves from Cosmic Defects. *Phys. Rev. Lett.*, 110(10):101302, 2013.

[57] A. S. Goldhaber. Collapse of a 'Global Monopole.'. *Phys. Rev. Lett.*, 63:2158, 1989.

[58] J. H. Goldstein et al. Estimates of cosmological parameters using the CMB angular power spectrum of ACBAR. *Astrophys. J.*, 599:773–785, 2003.

[59] J. Goldstone. Field Theories with Superconductor Solutions. *Nuovo Cim.*, 19:154–164, 1961.

[60] K. Griest. The Search for dark matter: WIMPs and MACHOs. 1993. [Annals N. Y. Acad. Sci.688,390(1993)].

[61] A. H. Guth. The Inflationary Universe: A Possible Solution to the Horizon and Flatness Problems. *Phys. Rev.*, D23:347–356, 1981.

[62] E. R. Harrison. Fluctuations at the threshold of classical cosmology. *Phys. Rev.*, D1: 2726–2730, 1970.

[63] E. Hawkins et al. The 2dF Galaxy Redshift Survey: Correlation functions, peculiar velocities and the matter density of the universe. *Mon. Not. Roy. Astron. Soc.*, 346:78, 2003.

[64] P. W. Higgs. Broken symmetries, massless particles and gauge fields. *Phys. Lett.*, 12: 132–133, 1964.

[65] M. Hindmarsh. Private communication.

[66] M. Hindmarsh. Existence and stability of semilocal strings. *Phys. Rev. Lett.*, 68:1263–1266, 1992.

[67] M. Hindmarsh. Semilocal topological defects. *Nucl. Phys.*, B392:461–492, 1993.

[68] M. Hindmarsh, C. Ringeval, and T. Suyama. The CMB temperature bispectrum induced by cosmic strings. *Phys. Rev.*, D80:083501, 2009.

[69] M. Hindmarsh, S. Stuckey, and N. Bevis. Abelian Higgs Cosmic Strings: Small Scale Structure and Loops. *Phys.Rev.*, D79:123504, 2009.

[70] M. Hindmarsh, C. Ringeval, and T. Suyama. The CMB temperature trispectrum of cosmic strings. *Phys. Rev.*, D81:063505, 2010.

[71] M. Hindmarsh, R. Kirk, and S. M. West. Dark Matter from Decaying Topological Defects. *JCAP*, 1403:037, 2014.

[72] M. Hindmarsh, R. Kirk, J. M. No, and S. M. West. Dark Matter with Topological Defects in the Inert Doublet Model. *JCAP*, 1505(05):048, 2015.

[73] M. Hindmarsh, J. Lizarraga, J. Urrestilla, D. Daverio, and M. Kunz. Scaling from gauge and scalar radiation in Abelian Higgs string networks. 2017.

[74] M. B. Hindmarsh and T. W. B. Kibble. Cosmic strings. *Rept. Prog. Phys.*, 58:477–562, 1995.

[75] G. Hinshaw et al. Nine-Year Wilkinson Microwave Anisotropy Probe (WMAP) Observations: Cosmological Parameter Results. *Astrophys. J. Suppl.*, 208:19, 2013.

[76] C. J. Hogan and M. J. Rees. Gravitational interactions of cosmic strings. *Nature*, 311: 109–113, 1984.

[77] E. Hubble. A relation between distance and radial velocity among extra-galactic nebulae. *Proc. Nat. Acad. Sci.*, 15:168–173, 1929.

[78] K. Jones-Smith, L. M. Krauss, and H. Mathur. A Nearly Scale Invariant Spectrum of Gravitational Radiation from Global Phase Transitions. *Phys. Rev. Lett.*, 100:131302, 2008.

[79] K. Kajantie, M. Karjalainen, M. Laine, J. Peisa, and A. Rajantie. Thermodynamics of gauge invariant U(1) vortices from lattice Monte Carlo simulations. *Phys. Lett.*, B428:334–341, 1998.

[80] M. Kamionkowski. WIMP and axion dark matter. In *High-energy physics and cosmology. Proceedings, Summer School, Trieste, Italy, June 2-July 4, 1997*, pages 394–411, 1997. URL `http://alice.cern.ch/format/showfull?sysnb=0260730`.

[81] M. Kawasaki, K. Saikawa, and T. Sekiguchi. Axion dark matter from topological defects. *Phys. Rev.*, D91(6):065014, 2015.

[82] T. W. B. Kibble. Topology of Cosmic Domains and Strings. *J. Phys.*, A9:1387–1398, 1976.

[83] T. W. B. Kibble. Evolution of a system of cosmic strings. *Nucl. Phys.*, B252:227, 1985. [Erratum: Nucl. Phys.B261,750(1985)].

[84] A. A. Klypin, I. A. Strukov, and D. P. Skulachev. The Relikt missions: Results and prospects to detect the microwave background anisotropy. 1991.

[85] J. B. Kogut and L. Susskind. Hamiltonian Formulation of Wilson's Lattice Gauge Theories. *Phys. Rev.*, D11:395–408, 1975.

[86] P. Laguna and D. Garfinkle. Space-time of Supermassive U(1) Gauge Cosmic Strings. *Phys. Rev.*, D40:1011–1016, 1989.

[87] M. Landriau and E. P. S. Shellard. Fluctuations in the CMB induced by cosmic strings: Methods and formalism. *Phys. Rev.*, D67:103512, 2003.

[88] M. Landriau and E. P. S. Shellard. Large angle CMB fluctuations from cosmic strings with a cosmological constant. *Phys. Rev.*, D69:023003, 2004.

[89] A. Lazanu and P. Shellard. Constraints on the Nambu-Goto cosmic string contribution to the CMB power spectrum in light of new temperature and polarisation data. *JCAP*, 1502 (02):024, 2015.

[90] A. Lazanu, E. P. S. Shellard, and M. Landriau. CMB power spectrum of Nambu-Goto cosmic strings. *Phys. Rev.*, D91(8):083519, 2015.

[91] A. Lewis and S. Bridle. Cosmological parameters from CMB and other data: A Monte Carlo approach. *Phys. Rev.*, D66:103511, 2002.

[92] A. Lewis, A. Challinor, and A. Lasenby. Efficient computation of CMB anisotropies in closed FRW models. *Astrophys.J.*, 538:473–476, 2000.

[93] A. D. Linde. A New Inflationary Universe Scenario: A Possible Solution of the Horizon, Flatness, Homogeneity, Isotropy and Primordial Monopole Problems. *Phys. Lett.*, B108: 389–393, 1982.

[94] A. D. Linde. Decay of the False Vacuum at Finite Temperature. *Nucl. Phys.*, B216:421, 1983. [Erratum: Nucl. Phys.B223,544(1983)].

[95] J. Lizarraga, J. Urrestilla, D. Daverio, M. Hindmarsh, and M. Kunz. New CMB constraints for Abelian Higgs cosmic strings. *JCAP*, 1610(10):042, 2016.

[96] A. Lopez-Eiguren, J. Urrestilla, and A. Achúcarro. Measuring Global Monopole Velocities, one by one. 2016.

[97] C. J. A. P. Martins and A. Achucarro. Evolution of local and global monopole networks. *Phys. Rev.*, D78:083541, 2008.

[98] C. J. A. P. Martins and E. P. S. Shellard. Quantitative string evolution. *Phys. Rev.*, D54: 2535–2556, 1996.

[99] C. J. A. P. Martins and E. P. S. Shellard. Extending the velocity dependent one scale string evolution model. *Phys. Rev.*, D65:043514, 2002.

[100] P. McDonald et al. The Linear theory power spectrum from the Lyman-alpha forest in the Sloan Digital Sky Survey. *Astrophys. J.*, 635:761–783, 2005.

[101] J. N. Moore, E. P. S. Shellard, and C. J. A. P. Martins. On the evolution of Abelian-Higgs string networks. *Phys. Rev.*, D65:023503, 2002.

[102] K. J. M. Moriarty, E. Myers, and C. Rebbi. Dynamical Interactions of Flux Vortices in Superconductors. *Phys. Lett.*, B207:411–418, 1988.

[103] H. B. Nielsen and P. Olesen. Vortex Line Models for Dual Strings. *Nucl. Phys.*, B61:45–61, 1973.

[104] A. S. Nunes, A. Avgoustidis, C. J. A. P. Martins, and J. Urrestilla. Analytic Models for the Evolution of Semilocal String Networks. *Phys. Rev.*, D84:063504, 2011.

[105] S. Olmez, V. Mandic, and X. Siemens. Gravitational-Wave Stochastic Background from Kinks and Cusps on Cosmic Strings. *Phys. Rev.*, D81:104028, 2010.

[106] K. D. Olum and J. J. Blanco-Pillado. Field theory simulation of Abelian Higgs cosmic string cusps. *Phys. Rev.*, D60:023503, 1999.

[107] K. D. Olum and J. J. Blanco-Pillado. Radiation from cosmic string standing waves. *Phys. Rev. Lett.*, 84:4288–4291, 2000.

[108] M. E. Ortiz. A New look at supermassive cosmic strings. *Phys. Rev.*, D43:2521–2526, 1991.

[109] U.-L. Pen, D. N. Spergel, and N. Turok. Cosmic structure formation and microwave anisotropies from global field ordering. *Phys. Rev.*, D49:692–729, 1994.

[110] U.-L. Pen, U. Seljak, and N. Turok. Power spectra in global defect theories of cosmic structure formation. *Phys.Rev.Lett.*, 79:1611–1614, 1997.

[111] L. Perivolaropoulos. Instabilities and interactions of global topological defects. *Nucl. Phys.*, B375:665–693, 1992.

[112] S. Perlmutter et al. Measurements of Omega and Lambda from 42 high redshift supernovae. *Astrophys. J.*, 517:565–586, 1999.

[113] P. Peter and J.-P. Uzan. *Primordial Cosmology*. Oxford University Press, Oxford, 2009. ISBN 978-0-19-920991-0.

[114] J. Polchinski. Dirichlet Branes and Ramond-Ramond charges. *Phys. Rev. Lett.*, 75:4724–4727, 1995.

[115] W. H. Press, B. S. Ryden, and D. N. Spergel. Dynamical Evolution of Domain Walls in an Expanding Universe. *Astrophys.J.*, 347:590–604, 1989.

[116] A. Refregier, A. Amara, T. D. Kitching, A. Rassat, R. Scaramella, and J. Weller. Euclid Imaging Consortium Science Book. 2010.

[117] D. M. Regan and E. P. S. Shellard. Cosmic String Power Spectrum, Bispectrum and Trispectrum. *Phys. Rev.*, D82:063527, 2010.

[118] S. H. Rhie and D. P. Bennett. Global monopoles do not 'collapse'. *Phys. Rev. Lett.*, 67: 1173, 1991.

[119] A. G. Riess et al. Observational evidence from supernovae for an accelerating universe and a cosmological constant. *Astron. J.*, 116:1009–1038, 1998.

[120] R. J. Scherrer and A. Vilenkin. 'Lattice-free' simulations of topological defect formation. *Phys. Rev.*, D58:103501, 1998.

[121] E. P. S. Shellard. Cosmic String Interactions. *Nucl. Phys.*, B283:624–656, 1987.

[122] X. Siemens, J. Creighton, I. Maor, S. Ray Majumder, K. Cannon, and J. Read. Gravitational wave bursts from cosmic (super)strings: Quantitative analysis and constraints. *Phys. Rev.*, D73:105001, 2006.

[123] X. Siemens, V. Mandic, and J. Creighton. Gravitational wave stochastic background from cosmic (super)strings. *Phys. Rev. Lett.*, 98:111101, 2007.

[124] G. F. Smoot et al. Structure in the COBE differential microwave radiometer first year maps. *Astrophys. J.*, 396:L1–L5, 1992.

[125] L. Sousa and P. P. Avelino. Revisiting the VOS model for monopoles. 2017.

[126] M. Tegmark et al. Cosmological parameters from SDSS and WMAP. *Phys. Rev.*, D69: 103501, 2004.

[127] J. Urrestilla, N. Bevis, M. Hindmarsh, M. Kunz, and A. R. Liddle. Cosmic microwave anisotropies from BPS semilocal strings. *JCAP*, 0807:010, 2008.

[128] J. Urrestilla, N. Bevis, M. Hindmarsh, and M. Kunz. Cosmic string parameter constraints and model analysis using small scale Cosmic Microwave Background data. *JCAP*, 1112: 021, 2011.

[129] T. Vachaspati and A. Achucarro. Semilocal cosmic strings. *Phys. Rev.*, D44:3067–3071, 1991.

[130] T. Vachaspati and A. Vilenkin. Formation and Evolution of Cosmic Strings. *Phys. Rev.*, D30:2036, 1984.

[131] T. Vachaspati and A. Vilenkin. Gravitational Radiation from Cosmic Strings. *Phys. Rev.*, D31:3052, 1985.

[132] L. Van Waerbeke et al. Cosmic shear statistics and cosmology. *Astron. Astrophys.*, 374: 757–769, 2001.

[133] G. J. Verbiest and A. Achucarro. High speed collision and reconnection of Abelian Higgs strings in the deep type-II regime. *Phys. Rev.*, D84:105036, 2011.

[134] P. T. P. Viana, R. C. Nichol, and A. R. Liddle. Constraining the matter power spectrum normalization using the SDSS/RASS and reflex cluster surveys. *Astrophys. J.*, 569:L75, 2002.

[135] A. Vilenkin. Gravitational radiation from cosmic strings. *Phys. Lett.*, B107:47–50, 1981.

[136] A. Vilenkin. Gravitational Field of Vacuum Domain Walls and Strings. *Phys. Rev.*, D23: 852–857, 1981.

[137] A. Vilenkin and E. P. S. Shellard. *Cosmic Strings and Other Topological Defects*. Cambridge University Press, 2000. ISBN 9780521654760. URL `http://www.cambridge.org/mw/academic/subjects/physics/theoretical-physics-and-mathematical-physics/cosmic-strings-and-other-topological-defects?format=PB`.

[138] E. Witten. Cosmic Superstrings. *Phys. Lett.*, B153:243–246, 1985.

[139] M. Yamaguchi. Scaling property and peculiar velocity of global monopoles. *Phys.Rev.*, D65: 063518, 2002.

[140] V. Zacek. Dark Matter. In *Proceedings, 22nd Lake Louise Winter Institute: Fundamental Interactions (LLWI 2007): Lake Louise, Alberta, Canada, February 19-24, 2007*, 2007. URL `http://inspirehep.net/record/754834/files/arXiv:0707.0472.pdf`.

[141] Ya. B. Zeldovich. A Hypothesis, unifying the structure and the entropy of the universe. *Mon. Not. Roy. Astron. Soc.*, 160:1P–3P, 1972.

[142] W. H. Zurek. Cosmological Experiments in Superfluid Helium? *Nature*, 317:505–508, 1985.

[143] W. H. Zurek. Cosmological experiments in condensed matter systems. *Phys. Rept.*, 276: 177–221, 1996.

A Semilocal String Network figures, at different β

Figures analogous to the ones in the main part of the text of Chapter 5, but for different β:

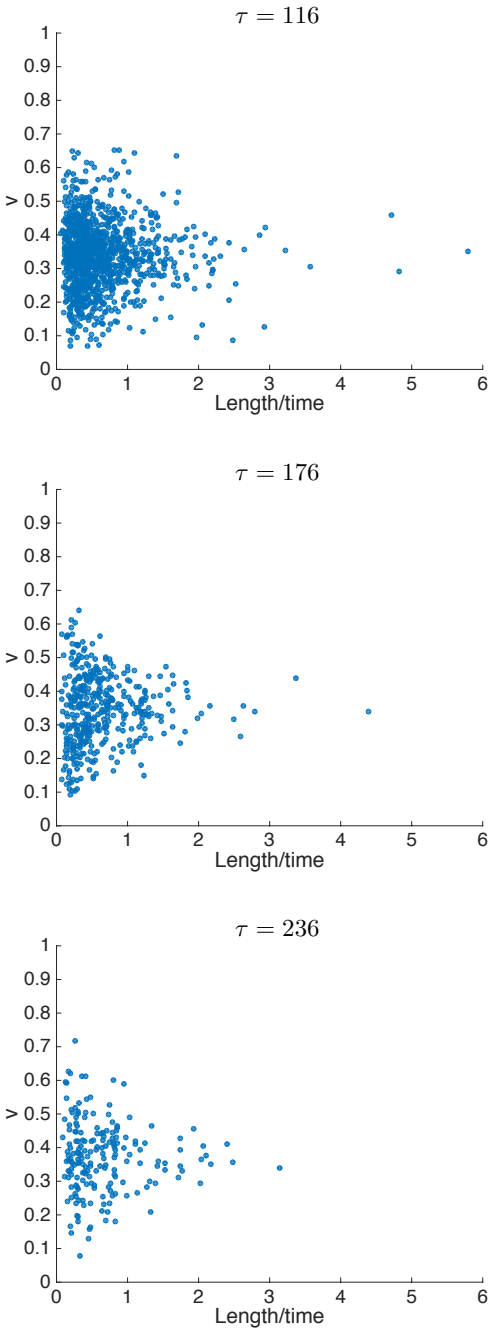

Figure A.1.: *This plot shows the distribution of segments with respect to velocity for simulation in radiation domination and $\beta = 0.20$. Each point represents a segment in the network, where the length of the segment divided by time is shown in the x-axis and its velocity in the y-axis. This is the case where segments flow through the network, i.e., they do interact with any other segment in the next time step. Note that the segments are shorter on average, as expected for higher β.*

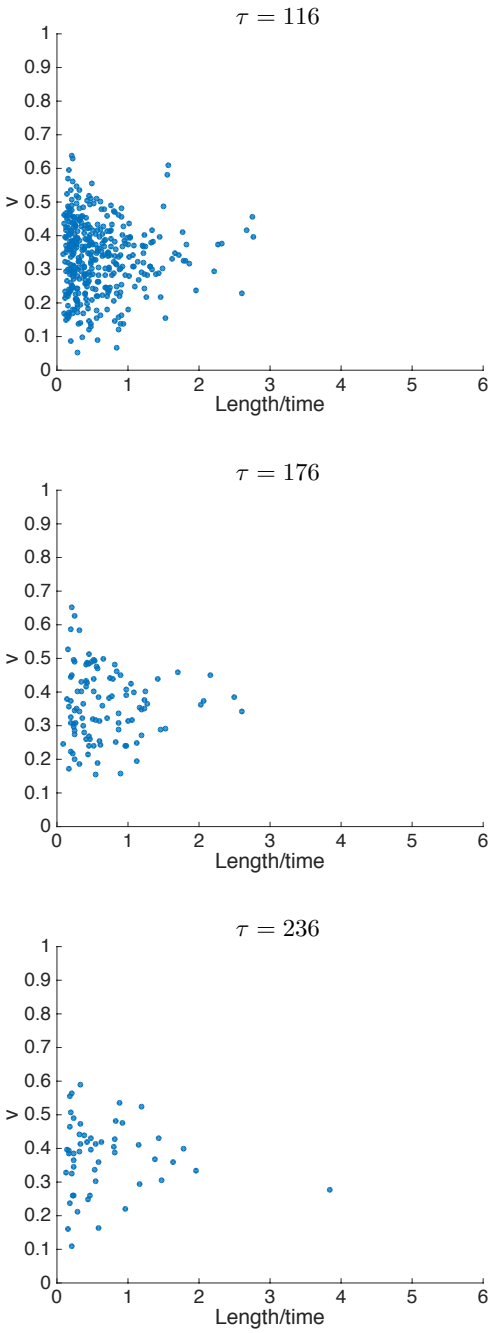

Figure A.2.: *This figure is similar to Fig. A.1, but in this case the segments that are plotted are those that merge with other segments before the next time step.*

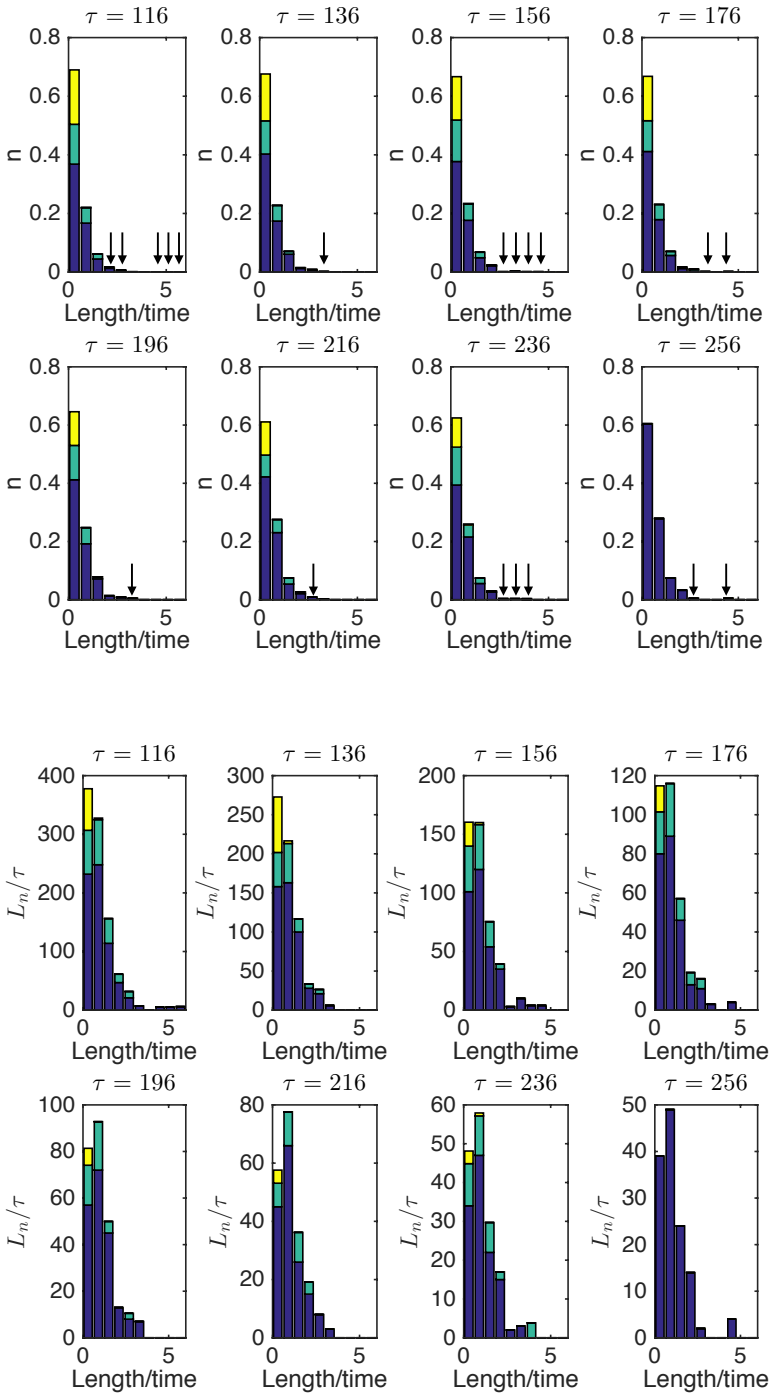

Figure A.3.: *These histograms show the distribution of the segments during the evolution for $\beta = 0.20$ in radiation domination, where the segments are binned in 10 bins with uniform width. The top figure shows the distribution of the number of segments with respect to length-per-time, whereas the bottom figure shows the same distribution, but where the total length-per-time of the segments in each bin has been added. The colors represent different type of segments, depending on their future behaviour: in blue segments which are flowing, in green segments that are merging and in yellow segments that are collapsing before the net time step. We write arrows to remark that in those instances, there are a few (one or two) segments in that bin, which are hard to see in the top plot, but can be seen in the bottom plot. Note that in the last time step we have no information whether the segments will flow, merge or collapse, so we just choose to show them as flow segments.*

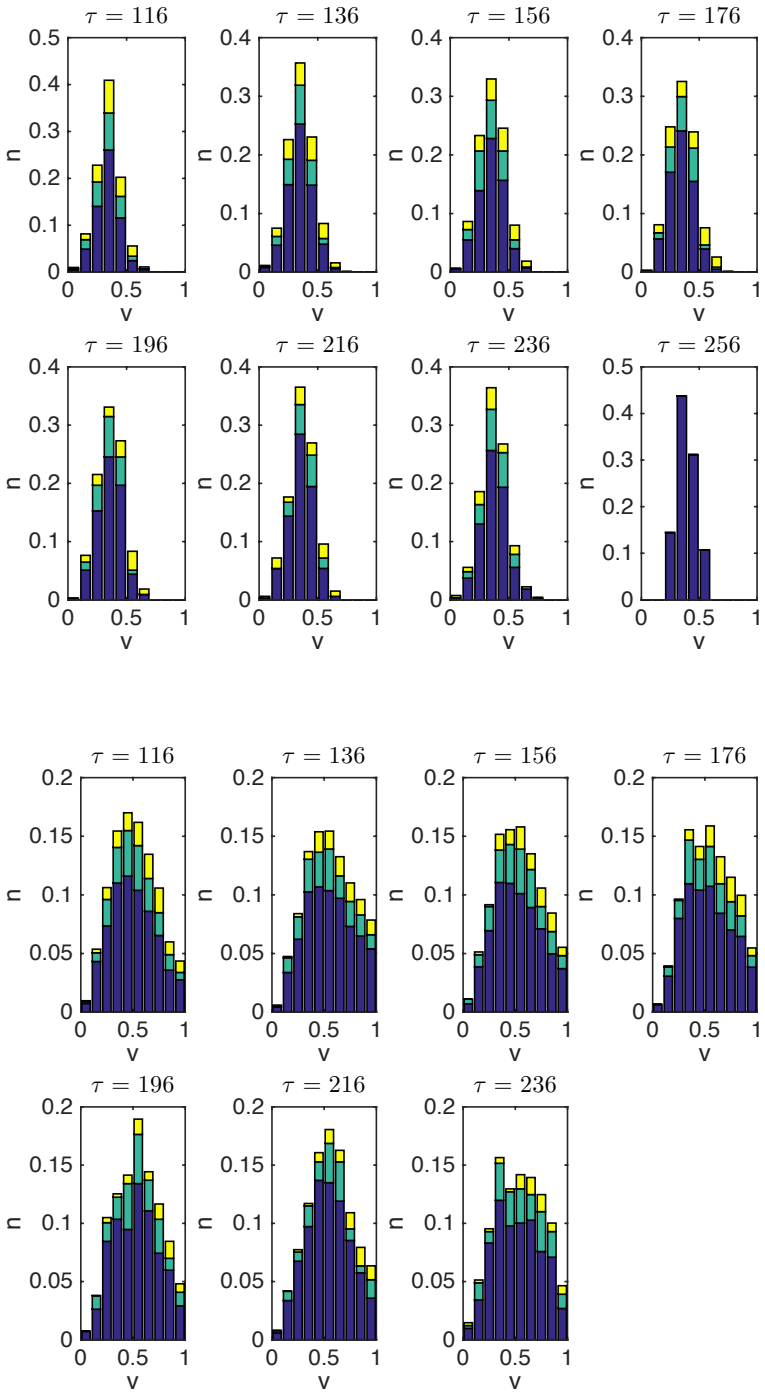

Figure A.4.: *These histograms show the velocity distribution of the segments (top) and monopoles (bottom) during their evolution, for radiation and $\beta = 0.20$. The velocities are binned in 10 bins with uniform width. The color code is analogous to the previous figure: blue corresponds to strings that do not interact with other strings before the next time step (flow), green is for strings which merge with other segments and yellow is for strings that disappear before the next time-step because the segment collapses. Note that in the last time step of segment velocities we have no information whether the segments will flow, merge or collapse, so we just choose to show them as flow segments. Note also that in the monopole velocity case we do not have information to compute the velocity at the last time step.*

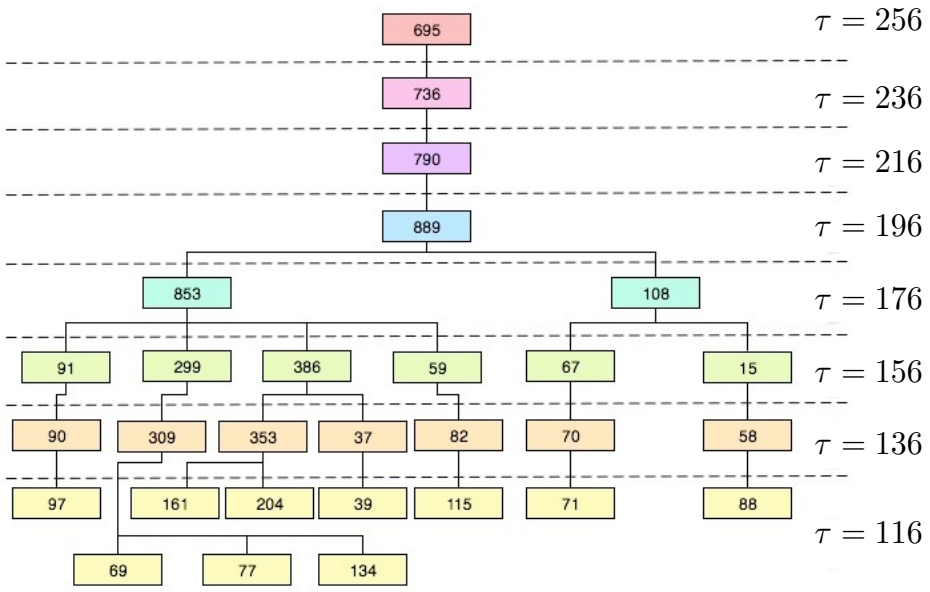

Figure A.5.: *The "family tree" of a segment for $\beta = 0.20$ in radiation. The number inside the box denotes the length of each segment, and time runs upwards.*

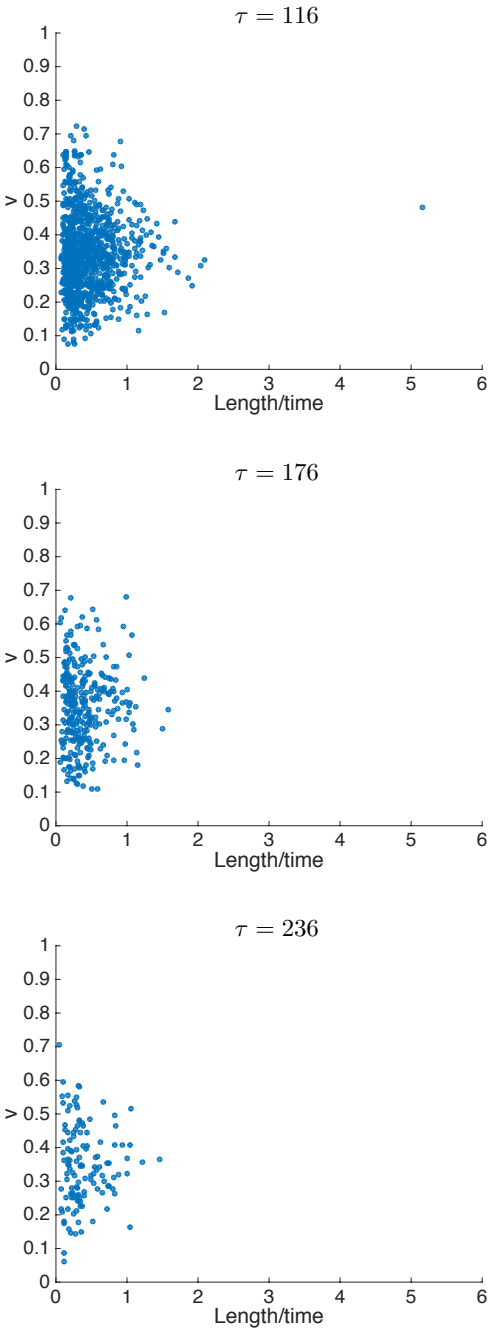

Figure A.6.: *This plot shows the distribution of segments with respect to velocity for simulation in radiation domination and $\beta = 0.35$. Each point represents a segment in the network, where in the x-axis the length of the segment divided by time is shown and its velocity in the y-axis. This is the case where segments flow through the network, i.e., they do interact with any other segment in the next time step.*

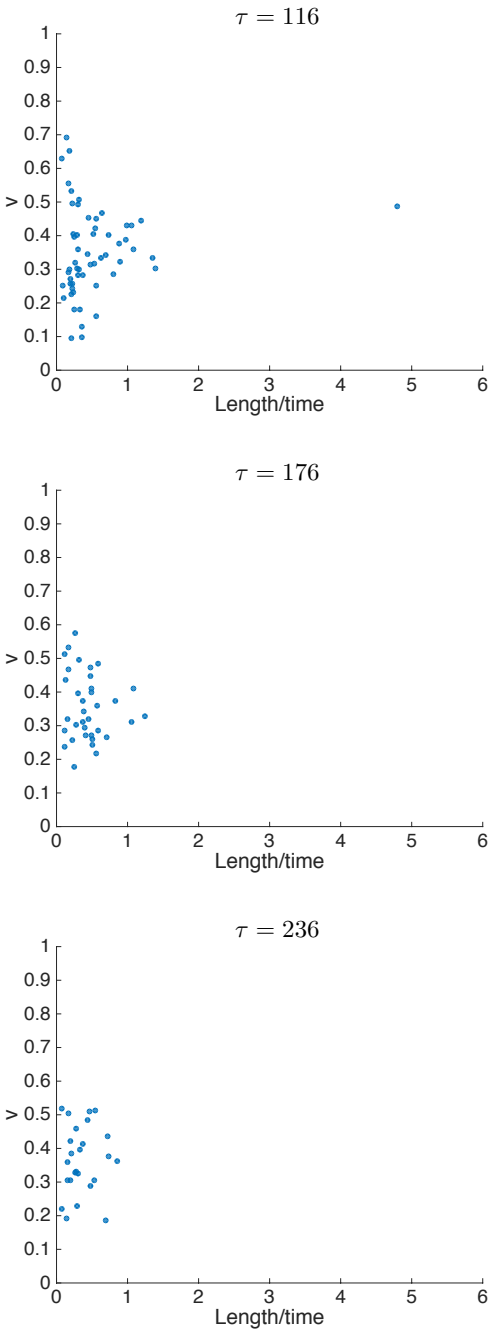

Figure A.7.: *This figure is similar to Fig. A.6, but in this case the segments that are plotted are those that merge with other segments before the next time step.*

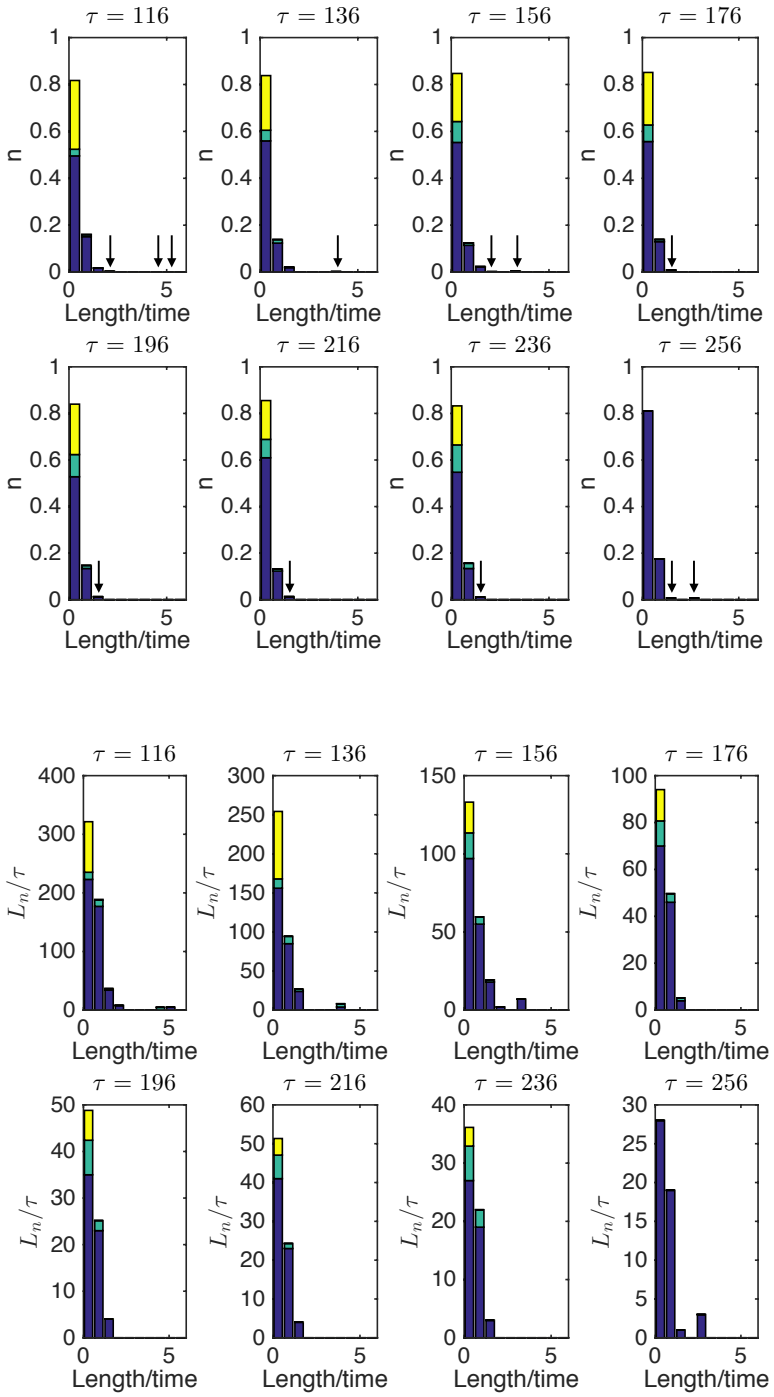

Figure A.8.: *These histograms show the distribution of the segments during the evolution for $\beta = 0.35$ in radiation domination, where the segments are binned in 10 bins with uniform width. The top figure shows the distribution of the number of segments with respect to length-per-time, whereas the bottom figure shows the same distribution, but where the total length-per-time of the segments in each bin has been added. The colors represent different type of segments, depending on their future behaviour: in blue segments which are flowing, in green segments that are merging and in yellow segments that are collapsing before the net time-step. We write arrows to remark that in those instances, there are a few (one or two) segments in that bin, which are hard to see in the top plot, but can be seen in the bottom plot. Note that in the last time step we have no information whether the segments will flow, merge or collapse, so we just choose to show them as flow segments.*

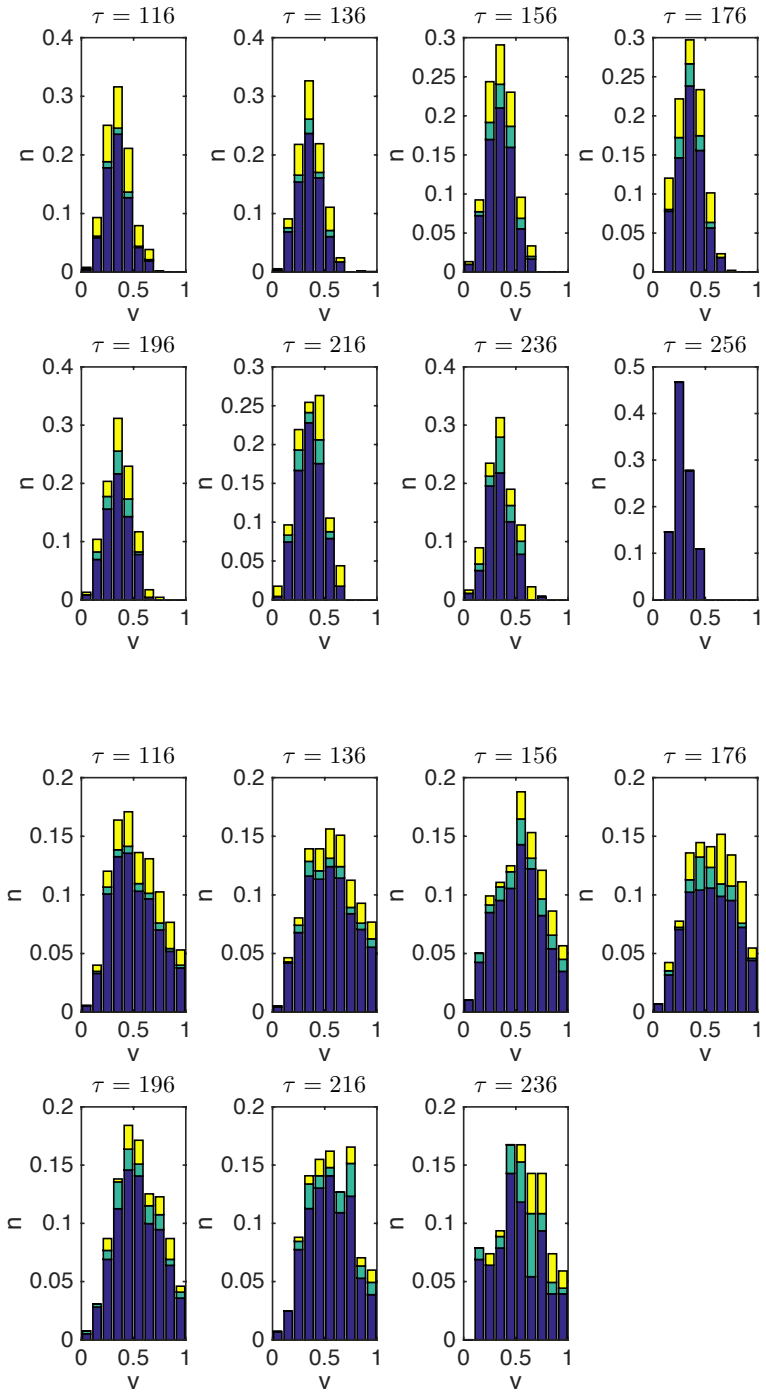

Figure A.9.: *These histograms show the velocity distribution of the segments (top) and monopoles (bottom) during their evolution, for radiation and $\beta = 0.35$. The velocities are binned in 10 bins with uniform width. The color code is analogous to the previous figure: blue corresponds to strings that do not interact with other strings before the next time-step (flow), green is for strings which merge with other segments and yellow is for strings that disappear before the next time-step because the segment collapses. Note that in the last time step of segment velocities we have no information whether the segments will flow, merge or collapse, so we just choose to show them as flow segments. Note also that in the monopole velocity case we do not have information to compute the velocity at the last time step.*

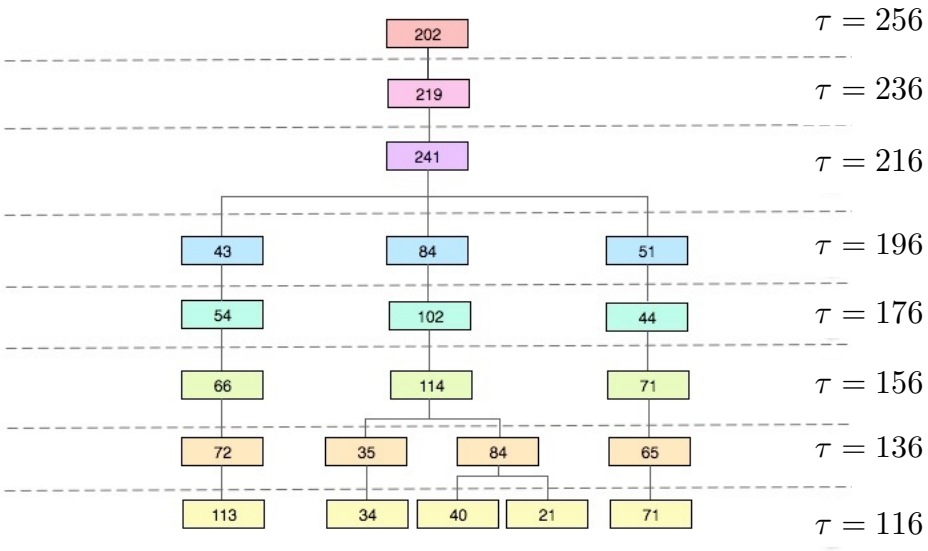

Figure A.10.: *The "family tree" of a segment for $\beta = 0.35$ in radiation. The number inside the box denotes the length of each segment, and time runs upwards.*